ABSTRACT

Title of Dissertation: TACTILE SENSING WITH COMPLIANT STRUCTURES FOR HUMAN-ROBOT INTERACTION

Ying Chen

Doctor of Philosophy, 2018

Dissertation directed by: Professors Miao Yu[1] and Elisabeth Smela[1,2]

[1] Department of Mechanical Engineering

[2] Institute for Systems Research

This dissertation presents the research on tactile sensing with compliant structures towards human-robot interaction. It would be beneficial for robots working collaboratively with humans to be soft or padded and have compliant tactile sensing skins over the padding. To allow the robots to interact with humans via touch effectively and safely and to detect tactile stimuli in an unstructured environment, new tactile sensing concepts are needed that can detect a wide range of potential interactions and sense over an area. However, most highly sensitive tactile sensors are unable to cover the forces involved in human contacts, which ranges from 1 newton to thousand newtons; to

implement area sensing capabilities, there have been challenges in creating traditional sensing arrays, where the associated supporting electronics become more complex with an increasing number of sensing elements. This dissertation develops a novel multi-layer cutaneous tactile sensing architecture for enhanced sensitivity and range, and employs an imaging technique based on boundary measurements called electrical impedance tomography (EIT) to achieve area tactile sensing capabilities.

The multi-layer cutaneous tactile sensing architecture, which consists of stretchable piezoresistive strain-sensing layers over foam padding layers of different stiffness, allows for both sufficient sensitivity and an extended force range for human contacts. The role that the padding layer plays when placed under a stretchable sensing layer was investigated, and it was discovered that the padding layer magnifies the sensor signal under indentation compared to that obtained without padding layers. The roles of the multi-layer foams were investigated by changing stiffness and thickness, which allows tailoring the response of multi-layer architectures for different applications. To achieve both extended force range and distributed sensing, EIT technique was employed with the multi-layer sensing architecture. Machine and human touch were conducted on the developed multi-layer sensing system, revealing that the second sensing skin is required to detect the large variability in human touch.

Although widely applied in the medical field for functional imaging, EIT applied in tactile sensing faces different challenges, such as unknown number and region of tactile stimuli. Current EIT tactile sensors have focused on qualitative demonstration. This

dissertation aims at achieving quantitative information from piezoresistive EIT tactile sensors, by investigating spatial performance and the effect of sensor's conductivity. A spatial correction method was developed for obtaining consistent spatial information, which was validated by both simulation and experiments from our stretchable piezoresistive EIT sensor with an underlying padding layer.

TACTILE SENSING WITH COMPLIANT STRUCTURES FOR HUMAN-ROBOT INTERACTION

by

Ying Chen

Dissertation submitted to the Faculty of the Graduate School of the
University of Maryland, College Park, in partial fulfillment
of the requirements for the degree of
Doctor of Philosophy
2018

Advisory Committee:
Professor Miao Yu, Chair and advisor
Professor Elisabeth Smela, advisor
Professor Srinivasa R. Raghavan, (dean's representative)
Professor Sarah Bergbreiter
Professor Abhijit Dasgupta
Professor Don L. DeVoe

DEDICATION

To my parents, Donglei, and Olivia

ACKNOWLEDGEMENTS

I first would like to thank my advisors, Prof. Miao Yu and Prof. Elisabeth Smela. It is their insights, encouragements, and patience that guided me through the five years of this research. I would also like to thank Prof. Hugh A. Bruck for consistently providing me valuable advice and immediate help. I am thankful to other professors in my committee for guiding me to improve this dissertation. I am very thankful to Prof. Abhijit Dasgupta, who was very generous to agree serving on my committee in the last minute.

I also want to thank my colleagues in Sensors and Actuators Lab: Dr. Haijun Liu, Dr. Hyungdae Bae, Dr. Zhijian Zhang, Dr. Yongyao Chen, and Dr. Hyuntae Kim, for providing me valuable advice since I started this research; Kashav Rajasekaran and Yahan Liu, for help in my research. I want to thank my colleagues in Lab for Microtechnologies: Dr. Deepa Sritharan and Dr. Timir Baran Datta-Chaudhuri, for providing me valuable academic guidance; Benjy Levi, Ephraim Zegeye, and Yonatan Saadon, for help in my research. I want to thank my colleagues in Multiscale Measurements Laboratory: Nelson Quispe for accommodating my use of Prof. Bruck's lab; Dr. Ariel Perez-Rosado for teaching me the technique of Digital Image Correlation; and Elizabeth Sauerbrunn for lab training.

I would like to acknowledge the support received from NSF research funding of the National Robotics Initiative (NRI) under award number IIS1317913 and the Clark School's 125th Anniversary Challenge.

My deepest gratitude goes to my parents and my husband. I could not start or reach the end of my Ph.D. study without the support and understanding from my parents. My life would not be so enjoyable and valuable over the past decade without the company of my husband, Donglei.

TABLE OF CONTENTS

LIST OF TABLES

LIST OF FIGURES

Chapter 1. Introduction

1.1 Background and Motivation

Although robots have been widely applied in industry [1-3], robots involved in unstructured environments, such as working in proximity to humans [4] or exploring an unknown terrain [5], are relatively new. A robot that is used for physical human-robot interaction is also called a co-robot.

Physical human-robot interaction favors soft robots, which provide a soft contact sensation to the human body [6,7]. Soft robots can be created by covering the surface of conventional robots that are made of rigid structures with a soft material. **Figure 1.1** shows an example of a soft robot, RI-MAN [8], designed for working collaboratively with humans. The entire surface of RI-MAN is covered with foam (Figure 1.1). Soft whole-body covering materials on other robotic platforms for human-robot interaction include silicone [9], rubber [10,11], soft urethane foam [12], and fur [13].

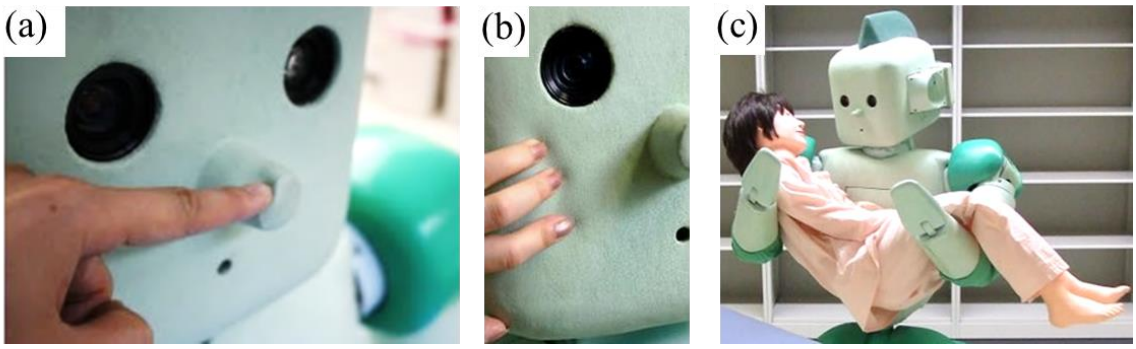

Figure 1.1: An example of a co-robot, RI-MAN, from the Bio-Mimetic Control Research Center of RIKEN, Japan [8]. A human touches the soft robot by pressing a) a finger on its nose or b) multiple fingers pressing on its cheek. c) The robot is supporting a dummy patient.

Researchers have found that touch sensing is indispensable for human beings to conduct dexterous manipulation [14] and to build emotional attachments [6]. In order to establish an effective human-robot communication, provide robots with an environmental awareness, and guarantee a safe interaction, a tactile sensing skin is necessary. However, development of artificial tactile sensing for robots has been slower than that for vision [15] because it is more difficult to mimic the human skin since human organs for touch sensing are not localized but are over the entire human body [15].

Soft tactile sensing skins are favorable for physical human-robot interaction. In early designs, rigid tactile sensors were mounted on robots, and these rigid sensors were usually covered with or embedded in an elastic material [16,17]. However, signal blurring and spatial filtering caused by the elastic covering is inevitable [18]. Prof. Fearing analyzed the effect of the thickness of covering on the sensitivity of an embedded capacitive sensor in the 1990s [19]. Non-rigid tactile sensors that can be in direct and conformal physical contact with interacting objects are therefore

important to achieve fidelity to tactile stimuli. Numerous soft touch sensors have emerged [20-23].

Practical issues rise in utilizing soft tactile sensors on robots. Is it feasible to fabricate new designed sensors on existing robotic platforms? Is it cost-effective to cover whole-body robots? Is wiring simple enough when increasing the number of mounted sensors? It is a pity if a high-performance sensor cannot be utilized on a robot due to fabrication limitations and scalability issues. In early designs, tactile sensors used on whole-body robots are simple binary switch sensors [24]. One striking example that soft and large-scale tactile sensors are mounted on a humanoid is described in reference [25]. The soft sensors were assembled in modular printed circuit boards, and are able to provide hundreds of sensing points over the robot's arms and hands [25].

This dissertation aims to understand the performance of a compliant sensing skin over padding materials, to improve tactile sensing capabilities by developing new sensing structures, and to investigate an area-sensing scheme. These efforts contribute to the field of tactile sensing for physical human-robot interaction.

1.2 Desirable Features for Tactile Sensors

In this dissertation work, we are interested in the following features of tactile sensors: compliance, sensitivity, force sensing range, and area sensing.

Based on the level of compliance, soft tactile sensors can be divided into two groups, flexible but not stretchable and stretchable. Stretchable tactile sensors are not only able to bend over non-flat surfaces, like flexible tactile sensors do, but also able to respond to inplane stretch.

Sensitivity and force sensing range together set a requirement on tactile sensors. Sensitivity should be high enough to detect a gentle human touch. Force range should be wide enough to cover the forces involved in human-robot interaction. Sensitivity and force sensing range are considered together in this dissertation because requirements on sensitivity depend on sensing ranges. Higher sensitivity is required at low force range: the distinction between very light and light touches is important. The requirement on sensitivity in high force range is not as strict as that for low force range, but the maximum force coverage is more important. The reason can be explained that it is more important for sensors to distinguish strong contacts that are safe to humans and strong contacts that are dangerous, than to accurately tell the difference between two strong contacts with similar strengths.

Area sensing is necessary to detect multiple stimuli that occur at different locations. A basic criterion for area tactile sensors is to obtain consistent information over the sensing medium, e.g. sensitivity and spatial resolution. Consistent spatial information makes it possible to compare stimuli conducted at different locations. For robot tactile sensing, the criterion on spatial performance is recommended to be set properly, not the high the better. Compared with rapid advancements in sensor designs, the relatively slow developments in implementable tactile sensors for robots have been blamed on much focus on pursuing highest performance in every

aspect [26]. For large-area tactile sensing, e.g. whole-body coverage for a robot, spatial resolution is suggested to vary at different parts of a robot. Because whole-body sensing skin with highest resolution everywhere would significantly increase signal complexity [7] and hardware wiring [25]. Even on the human body, spatial resolution is low on the torso [27] and high on the fingertips [28].

1.3 Previous Work on Compliant Tactile Sensors

Conductive sensing materials that have been made into compliant tactile sensors include fluids, fabrics, thin metal films, and polymer composites.

1.3.1 Conductive Fluids

Soft sensing materials that are inherently stretchable have been used for creating soft sensors. For example, conductive materials that are in a liquid state at room temperature, e.g. eutectic gallium-indium (EGaIn), can be embedded into patterned stretchable micro-channels as shown in **Figure 1.2** [29]. Features (e.g. minimum size) of the micro-channel rely on fabrication method [29].

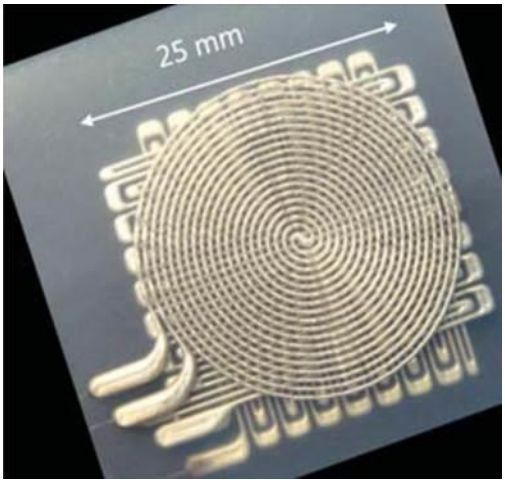

Figure 1.2: Conductive EGaIn liquid embedded in stretchable micro-channels [29].

1.3.2 Conductive Fabrics

Fabrics allow stretchability due to the way the fibers are structured[30]. **Figure 1.3** shows a stretchable fabric sensing glove [31] in which the fibers are coated with conductive polymers. Fabric-based tactile sensors can be readily incorporated into clothing. Fabric-based tactile sensors have outstanding fatigue resistance and high damage tolerance [30].

Figure 1.3: A sensing glove made of conductive fabrics [31].

1.3.3 Conductive Thin Films

Another inherent stretchable sensing materials are carbon nanotube (CNT) thin films. When stretched, aligned nanotube films fracture into islands connected by thin nanotube bundles (**Figure 1.4**) [32]. The resistance change of nanotube films under tactile stimuli depends on the strain history. It is typical that a previous stretch of the sensing material defines its subsequent ranges of reversible stretches [33].

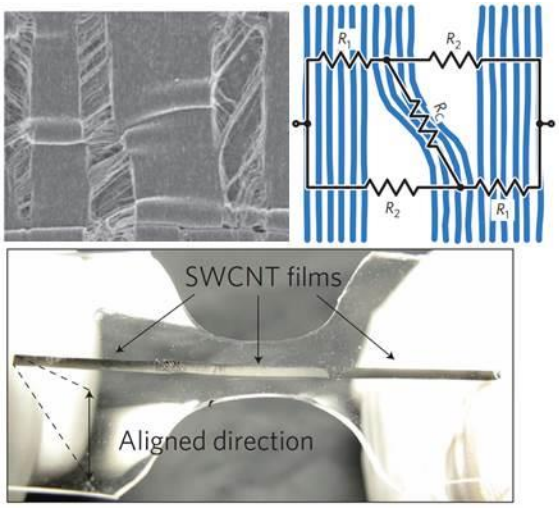

Figure 1.4: Carbon nanotube thin films are conductive under stretch due to the connected islands [32].

Un-stretchable bulk materials can improve compliance by thinning [34,35]. For example in **Figure 1.5**a, large and out-of-plane deformation is allowed by evaporating a thin gold film onto a soft substrate [35]. Mechanical buckling can add [36,37] or increase [38] stretchability. In Figure 1.5b, a non-stretchable thin metal film is bonded to a pre-strained substrate; the thin film buckles when the pre-strain is released. Buckled structures allow higher levels of deformation [36,37]. Buckling, however, prevents conformal contact between the sensor surface and interacting objects [20].

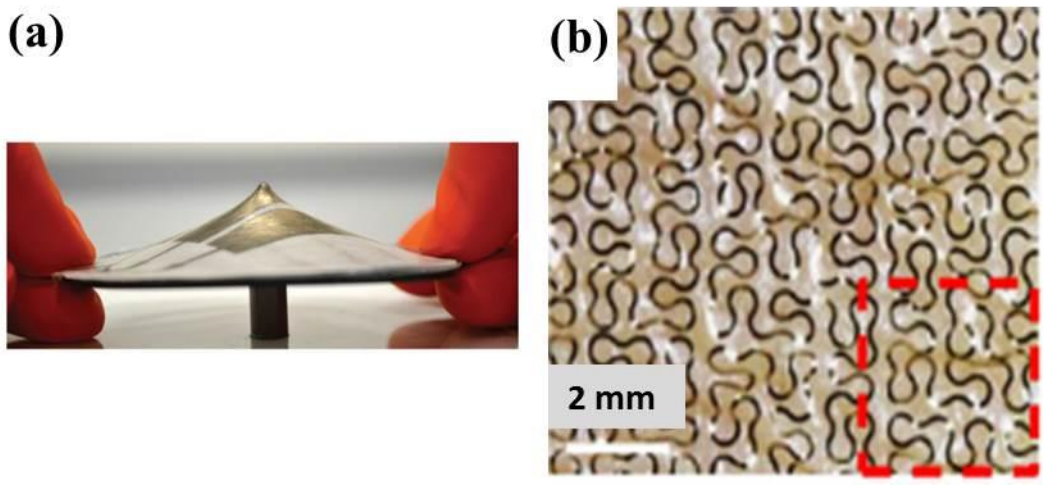

Figure 1.5: (a) A thin metal film evaporated over foam [35]. (b) A buckled thin film with improved stretchability [36].

1.3.4 Conductive Polymer Composites

Conductive polymer composites are made by blending conductive particles, such as carbon black [39-43], carbon nanotubes [44,45], graphite [46-48], or metallic particles [49], into an insulating host elastomer, such as polydimethylsiloxane (PDMS) or Ecoflex [45]. A conductive polymer composite takes advantage of its components: The conductive particles contribute to the composite's electrical impedance, and the elastomer host contributes to the composite's mechanical compliance. **Figure 1.6** [50] shows a soft sensor array made of a carbon black in PDMS host, i.e. CB/PDMS. The stretchable sensing material utilized in this dissertation a conductive polymer composite made of exfoliated graphite mixed in an elastomer [51]. The advantage of using conductive polymer composites as tactile sensing material includes simple fabrication technique, both stretchable and robust mechanical property, suitable for small or large area [23]. However, such material shows hysteresis problem, which represents a difficulty in sensing application.

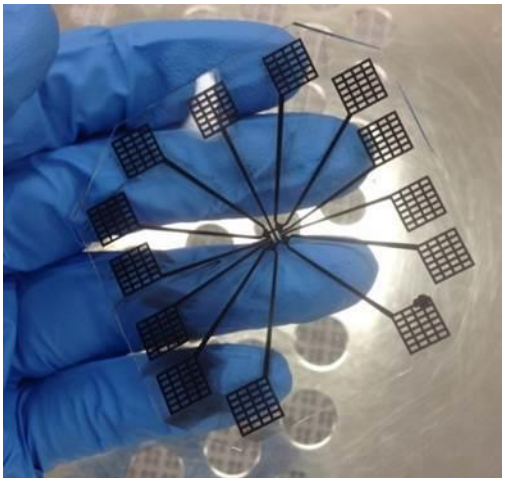

Figure 1.6: A conductive polymer composite made by dispersing carbon black into PDMS [50].

1.3.5 Electrical Behavior of Conductive Polymer Composites

The electrical conductance G of a conductive polymer composite is characterized by a power law in percolation theory [52]:

$$G \propto (x - x_c)^t \tag{1.1}$$

where x is volume fraction of the filler, x_c is percolation threshold, and t is a critical component to be fitted with experimental data. When the content of the filler reaches the percolation threshold, the composite becomes conductive. Higher filler content increases the conductivity of the composite, but decreases its compliance. The conductivity changes with deformation due to destruction and reconstruction of conducting pathways inside the composite.

Figure 1.7 shows a typical resistance response under a step-pressure input. Resistance increases instantly when the pressure is loaded, drops (relaxes) as the pressure is held steady, and

decreases instantly when the pressure is released. After the pressure is released, resistance slowly recovers. The performance of conductive polymer composites depends on the elastomeric host and fabrication conditions. Experimental studies [39] show that the electrical behavior of the composites can be analyzed using rheological models in viscoelasticity [53]. Such models typically consist of a series of linear elastic springs and linear viscous dashpots [54]. The spring models the instantaneous response to a load. The dashpot models a slowly building up response as a load is applied and an un-recovered response after the load is released. Empirical viscoelastic models [55] have been employed to characterize specific conductive composites [41,56-58].

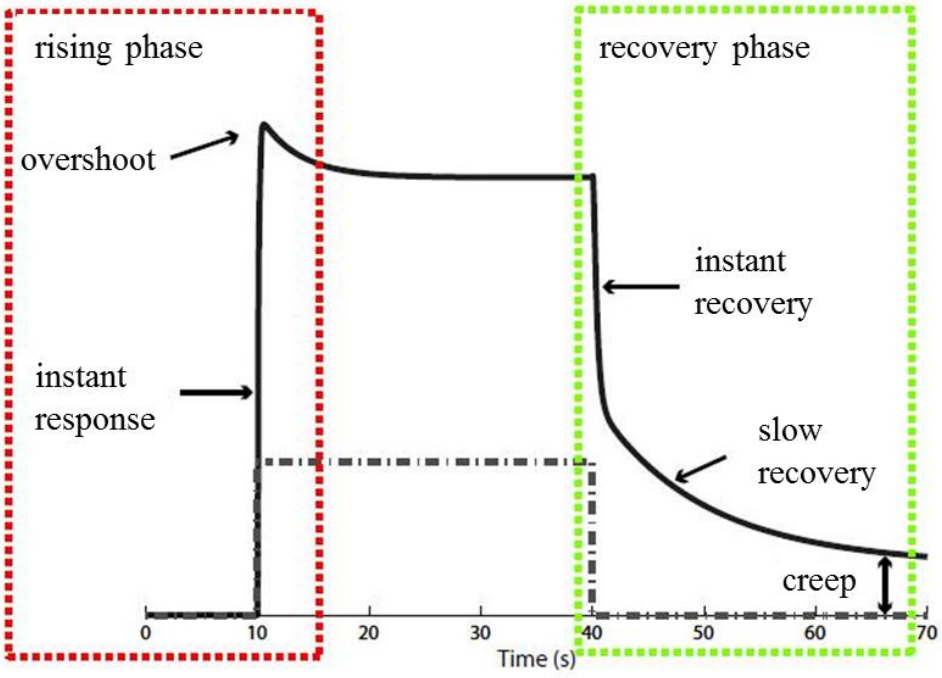

Figure 1.7: A typical waveform of resistance response (solid line) to a step-pressure (dashed line) stimuli from a conductive polymer composite, lightly modified from [56].

Stretchability demonstrated in conductive polymer composites is attractive for soft tactile sensing, although their electrical responses are varied. The challenge in characterizing

conductive polymer composite is understanding the memory effects, i.e. hysteresis, rate-dependency, and loading-history dependency.

1.4 Previous Work on Sensitivity and Force Range

1.4.1 Sensitivity

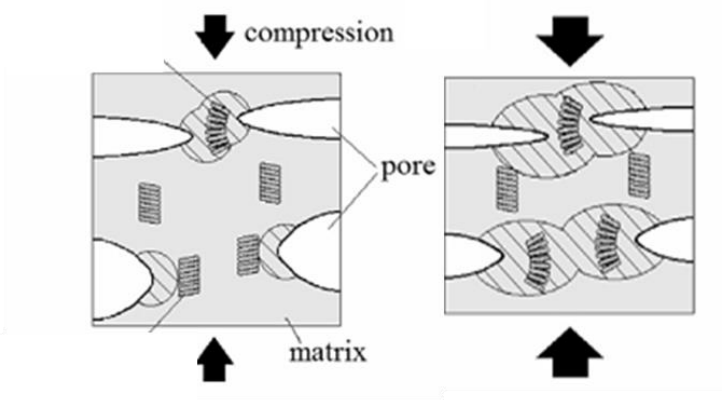

Figure 1.8: Sensitivity enhanced by pores, which were created in a conductive composite [59].

Compliant sensing systems have made use of soft or porous structures to increase sensitivity [60]. **Figure 1.8** shows a soft sensor made of a conductive composite with pores. The sensitivity of the sensor increased under compression due to improved piezoresistivity [59]. In **Figure 1.9** [35], sensing elements, which are made with softer materials show higher sensitivity. A similar way to increase compliance and thereby sensitivity is by engineering the sensor surface into microstructures [61].

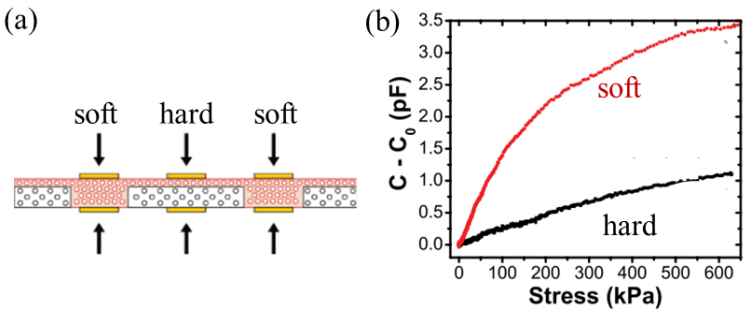

Figure 1.9: Softer material enhances sensitivity. (a) Sensing elements made with soft and hard materials. (b) Sensitivity is higher for the sensing elements made with soft materials [35].

There are limited studies on evaluating role of soft materials on sensor performance. Investigations have shown that gels withstand high impact force and high conformability [62]. Maiolino et al. compared different dielectric materials, elastomers and foams, for a capacitive sensor (see **Figure 1.10**a) [63]. They found that sensitivity of the sensors were similar to each other, based on the slope of sensor response (Figure 1.10b). They also found that material stability as an issue since the signal changed substantially after six months. They concluded that selection of soft materials should depend on a specific application.

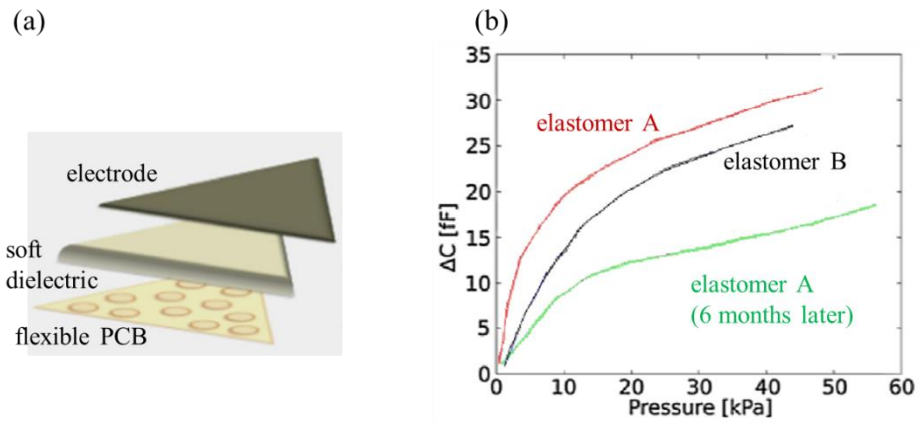

Figure 1.10: Role of different materials. (a) Schematic of a capacitive sensor with a soft dielectric. (b) Sensitivity for using different dielectric materials and sensitivity from elastomer A six months later [63].

For a robot with a padding material, e.g. RI-MAN, it is straightforward to put a sensing skin on top of the padding. However, the role of padding materials has not been investigated. Chapter 2 of this dissertation focuses on the evaluation of various padding materials that are placed underneath a sensing skin.

1.4.2 Force Range

Force sensing with a wide enough range is necessary for a robot to be aware of how weak or strong a human touch is. Force sensing range should be able to cover the forces involved in human touches. **Figure 1.11** shows forces involved in human contact, ranging from 1 N when a finger touches a screen to 2000 N when a boxer punches. These data are compiled from literature [64-72].

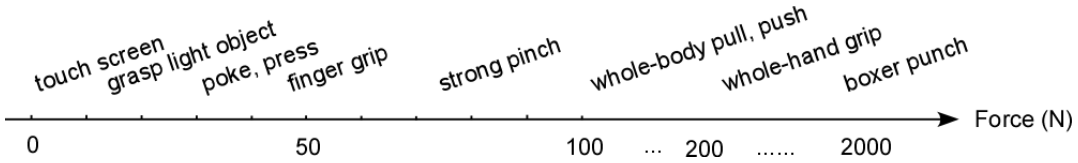

Figure 1.11: Forces involved in human contact. Data are compiled from literature [64-72].

In order to extend force sensing range, stiffer material can be effective, but decreases sensitivity as found Wettels et al. [73], who compare robot fingers made with different materials. The maximum force achieved with the stiffest material is 30 N. Therefore, the trade-off between sensitivity and force range should be considered when choosing the stiffness of a material.

1.5 Previous Work on Area Sensing

Area sensing or distributed sensing means that a sensor obtains information over an area, not a single point. In this section, various area sensing mechanisms are summarized. A specific type of area sensing scheme, called electrical impedance tomography (EIT), which is employed in this dissertation, will be introduced in detail.

1.5.1 Types of Mechanism

A straightforward way to implement area sensing is by assembling a number of individual sensors [74]. This is simple and effective when the required number of sensing elements is small. However, wiring complexity increases with the number of elements [74].

Arraying sensors is the most common way to achieve distributed sensing [75] [76-78]. The number of wires required for a sensor array is in general 2(m+n), where m and n are the number of rows and columns.

Four-wire schemes have been employed for area sensing [79-84]. One type of four-wire schemes, where two pairs of parallel line electrodes are placed along the boundary of a rectangular sensing medium, can be based on planar electric field [79] or contact electrification [80]. Such schemes have been used to detect only the position of a stimulus. To obtain both position and strength of a stimulus for four-wire schemes, data processing methods based on resistor network [82,83,85,86] has been investigated. Another type of four-wire scheme used four point electrodes, and it identified contact location based on machine learning [84]. However, none of four-wire scheme is able to identify more than one stimulus.

1.5.2 Electrical Impedance Tomography (EIT)

Electrical impedance tomography (EIT) is another type of area sensing scheme. EIT is an imaging technique used for reconstructing internal impedance by obtaining measurements only at the boundary of a sensing medium. EIT was originally applied in the medical field in the 1980s, and has been reviewed in [87-91]. Medical EIT, which is non-invasive and inexpensive, has been used to monitor the electrical conductivity of human tissue, which changes with the activity of the human body. For example, the electrical conductivity of the lung changes as the human inhales, because the air content within the lung changes [89].

1.5.2.1 Basics on EIT

Electrical potentials over a conductive medium satisfy Kirchoff's law [89]:

$$\nabla \cdot s\nabla\varphi = 0 \tag{1.2}$$

where s is the electrical conductivity of the medium. The SI unit for conductivity is Siemens per meter. For thin films with uniform in thickness, the term sheet conductivity is used and the unit is Siemens per square (S/sq) [92]. φ is the electrical potential.

Calculating electrical potentials based on the knowledge of the medium's conductivity and boundary conditions is a so-called "forward" problem. Determining the conductivity distribution based on boundary measurements is an "inverse" problem (or reconstruction problem). Inverse problems are often ill-posed, meaning that the problem does not satisfy any of the Hadamard criteria [93]:

- a solution exists,
- the solution is unique, and
- the solution changes continuously with the data.

The EIT inverse problem, i.e. reconstructing unknown conductivity from boundary measurements, is ill-posed largely due to its violation of the third criterion [89]. A small variation in the data would lead to a large fluctuation in the solution.

The objective for reconstructing internal conductivity is to find a conductivity distribution that minimizes the difference between the boundary voltage measurements and voltages calculated based on an estimation of conductivity.

$$\min ||\boldsymbol{V} - \boldsymbol{F}(\boldsymbol{s})||^2 \tag{1.3}$$

where $||\cdot||^2$ is the norm and V is voltage measured at the boundary. $F(s)$ is a forward operator, converting conductivity to voltages.

$F(s)$ is nonlinear for EIT. To simplify the minimization problem, it is common to linearize $F(s)$ around a reference conductivity s_0 [94].

$$\boldsymbol{F(s) = F(s_0) + \frac{\partial F}{\partial s}(s_0)(s - s_0) + O(||s - s_0||^2)} \quad (1.4)$$

where $J = \frac{\partial F}{\partial s}(s_0)$ is the Jacobian matrix (also called sensitivity matrix) at $s = s_0$.

Removing the second order terms,

$$\boldsymbol{F(s) = F(s_0) + J(s - s_0)} \quad (1.5)$$

This approximation is valid only when perturbation of the conductivity s is small, relative to the reference conductivity s_0.

To this end, equation (1.4) helps explain two types of EIT reconstruction: The absolute EIT (a-EIT) and the time difference EIT (td-EIT) [95]. Absolute EIT estimates absolute conductivity $\hat{s}$, which involves solving a forward problem to obtain s_0. Complete and accurate information on the physical model, e.g. shape of the medium and boundary conditions, is required for an accurate solution of s_0. Time difference EIT estimates the changes in conductivity, i.e. $\widehat{ds} = s - s_0$, based on the changes in voltage measurements from two time instants, i.e. $dV = \boldsymbol{F(s)} - F(s_0)$. Model information that does not vary with time is cancelled out in time difference EIT. It is easier to conduct time difference EIT, and, in most cases [89,95], time-difference EIT is enough to serve the purpose.

The solution of (1.4) is not stable because solving either $\hat{s}$ or $\widehat{ds}$ requires calculating the inverse of the Jacobian, which could be ill-conditioned. Many entries in the Jacobian are close to zero, so the inversion of the Jacobian results in many entries with large values. Small measurement errors lead to an amplified error in the solution. The ill-posedness of a matrix can be defined by the condition number k [96]:

$$\boldsymbol{k(J) = ||J|| \cdot ||J^{-1}|| = \frac{\gamma_1}{\gamma_2}} \tag{1.6}$$

where $\|\cdot\|$ corresponds to a matrix norm [97], γ_1 is the largest singular value of J, and γ_2 is the smallest nonzero singular value of J. The larger the condition number is, the more ill conditioned the matrix is.

Regularization has been used in solving ill-posed problems. The regularization procedure is to add a regularization term to the original least square function. In many cases, Tikhonov regularization is used, formulated as [94]:

$$\boldsymbol{\arg min_s\{\left|\left|L_1 \cdot (V - F(s))\right|\right|^2 + \alpha||L_2 \cdot s||^2\}} \tag{1.7}$$

where α is a regularization parameter or *hyperparameter*, $L_1$is a weighting term, and $L_2$is a regularization matrix. Hyperparameter α is in general unit-less. Terms $L_1$and L_2 carry appropriate units in order to balance the norm terms. The original ill-posed problem is approximated by a better conditioned one by adding the regularization term, which is tuned by α. After regularization, the ill-posed condition of an inverse problem is mitigated. By selecting a proper regularization term, the solution of the regularized problem changes continuously with the data.

In inverse theory, the error between the exact and the regularized solution s consists of two parts: one is the measurement error multiplied by the condition number of the regularized problem, which tends to infinity as α tends to zero; the other is the approximation error due to regularization, which tends to zero with α [98]. To keep the total error small, a proper α should be selected. The larger α, the more stable the solution becomes. But the mismatch between the original problem and the regularized problem is larger with larger α.

Solution of the standard Tikhonov regularized problem in the linear case is [89,94,99]:

$$\widehat{\boldsymbol{ds}} = (\boldsymbol{J^T J} + \boldsymbol{\alpha I})^{-1} \boldsymbol{J^T dV} \tag{1.8}$$

To implement the reconstruction process, EIDORS (Electrical Impedance Tomography and Diffuse Optical Tomography Reconstruction Software) is an open source toolbox developed for both 2D and 3D EIT reconstruction, released under General Public License (GUN) [100]. The toolbox is based on Matlab functions [101,102]. The toolbox provides circular or square shaped models of a sensing medium, provides forward problem solver, and is able to solve inverse problem based on boundary voltage measurements.

To obtain voltage measurements, different drive-measure strategies have been used in EIT. In the adjacent drive and adjacent measure strategy (see **Figure 1.12**), current is injected into two adjacent electrodes, and differential voltages are measured between all the other (non-current-carrying) electrode pairs. Then current is switched to the next two adjacent electrodes, and the voltage measurements are repeated. For a complete data set, current should be applied to all 16 adjacent electrode pairs, and differential voltages should be measured for each current injection

pattern. Although adjacent method is the most commonly used strategy, there are other data collection strategies (opposite method, cross method) that vary the driving and measuring electrodes [87]. Compared with opposite method and cross method, the adjacent method has been experimentally observed to have lower standard deviation in the voltage measurements [103] and lower image error [104]. There is a theoretically optimal current pattern [105] that has better ability to distinguish conductivity changes [106], but it requires multiple current generators, so the hardware design is complicated [107].

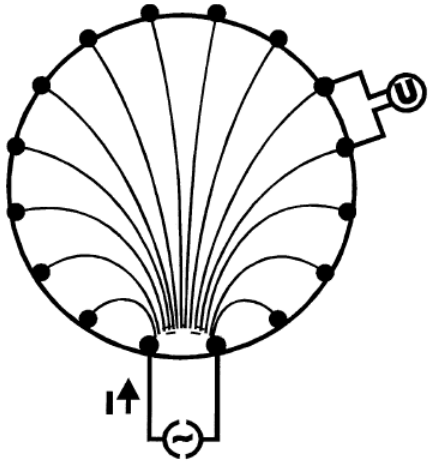

Figure 1.12: Illustration of the adjacent drive and adjacent measure strategy [89]. Current is switched around all pairs of boundary electrodes, and differential voltages are measured between all the non-current-carrying electrode pairs.

The electrodes, which are used for both current injection and voltage measurement, are in general uniformly spaced along the boundary of a medium. It might be expected that placing more electrodes would improve image reconstruction. However, in real applications, where noise is inevitable, the ill-posed condition of the inverse problem is worsened when significantly more electrodes are used [108,109]. Simulation studies [104,110] have shown that it is not necessary that more electrodes could lead to better reconstruction.

1.5.2.2 EIT Tactile Sensors

EIT was employed in tactile sensing for the first time during the 2000s [111]. **Figure 1.13**a shows an example of a compliant EIT tactile sensor placed over a dummy face. Figure 1.13b shows a reconstructed image of the conductivity change due to a tactile stimulus loaded at the cheek of the dummy face [111].

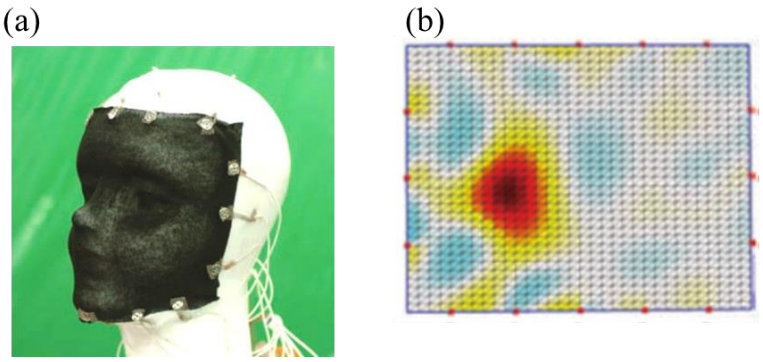

Figure 1.13: Distributed sensing based on the technique of electrical impedance tomography (EIT). (a) An EIT-based sensing skin placed over a dummy face. (b) An image of the conductivity change due to tactile stimuli loaded at the cheek [111].

Compared with the before mentioned four-wire schemes, advantage of EIT is that more information on stimuli can be reconstructed: positions, intensities, and contact area for more than one stimulus. Multiple touch points over planar [112-116] or curved surfaces [111,117,118] have been detected. Simulation study has investigated detecting contact area of a stimulus [118]. A variety of sensing materials have been used for making EIT tactile sensors, such as carbon nanotubes [119], carbon filled elastomers [116], fabric [113,115,120,121], and ionic liquids [122].

Most of the research on EIT tactile sensors focus on qualitatively demonstrating the feasibility of tactile sensing [111-120,122-124]. However, quantitative analysis in practical applications is rare [121]. Russo et al. analyzed the performance of an EIT tactile sensor under different drive-measure strategies [121].

1.6 Overview of the Dissertation Work

The goal of this dissertation is to investigate the performance of a sensing skin on padding materials for tactile sensing (not the performance of a sensing skin alone). Performance of a sensing skin alone has been extensively studied; however, a sensing skin over padding materials that undergoes large deformation has not been investigated. A sensing skin over the surface of a padded robot structure is shown in the photo of **Figure 1.14**. This dissertation includes understanding the role of a padding layer, taking advantage of padding materials, evaluating performance of sensing human touches, and exploring area sensing for a polymer composite sensing skin on padding materials.

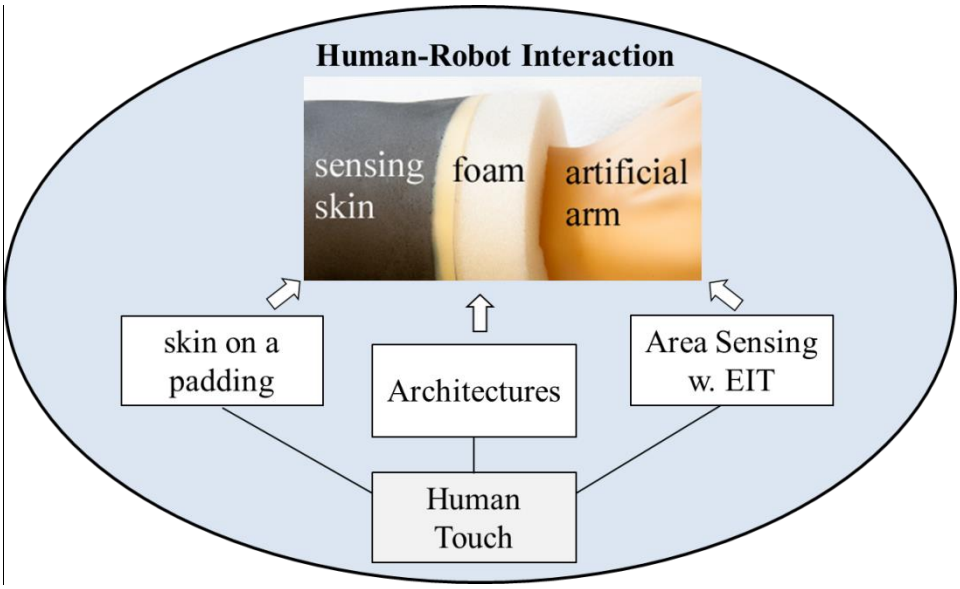

Figure 1.14: Overview of the dissertation work.

This dissertation includes following three research thrusts.

Research Thrust 1: Understanding the role of a padding layer on a sensing skin.

The role of a padding material on a polymer composite sensing skin was investigated through experiments and material's microstructures. Performance of the padded sensing skin was evaluated by using different padding materials. Requirements on padding materials were generated to obtain consistent sensor response.

Research Thrust 2: Developing new skin-padding sensing structures with improved performance.

Based on the findings from Thrust 1, Thrust 2 develops new multilayer padding sensing systems that consist of sensing skins over foam layers. Performance of multilayer architecture was evaluated by changing the stiffness and thickness of each padding layer. A soft-hard sensing

architecture was characterized with both sensitivity and an extended force sensing range. Temporal effects of the padded skins due to the viscoelastic behavior of polymer composites were experimentally evaluated.

Research Thrust 3: Investigating the performance of padded sensing skins in sensing human touches.

In this research thrust, soft-hard multilayer sensing systems were further evaluated through detecting human touches that involve a wide force range. Out-of-plane touch modalities and distributed touches were tested on multilayer sensing systems with sensing skins in strip shapes and in circular shapes aided with an area sensing technique (EIT).

Research Thrust 4: Developing and understanding the performance of EIT tactile sensors.

In this research thrust, the technique of electrical impedance tomography was employed on padded sensing skins for area sensing. Quantitative study was conducted for EIT tactile sensors made of polymer composites, including understanding reconstruction parameter, spatial performance, and the effect of material's background conductivity. A spatial correction method was proposed and validated by experiments.

The rest of the dissertation is organized as following. In Chapter 2, by utilizing a conductive polymer composite, i.e. exfoliated graphite/latex, sensing skins with different types of underlying padding materials will be investigated. The benefit of the padding material will be revealed. In Chapter 3, a soft-hard multilayer padding architecture for both high sensitivity and wide force sensing range will be proposed and characterized under out-of-plane indentation tests. In

Chapter 4, the soft-hard multilayer sensing system will be applied in identifying human touches. The benefit of the multi-layer structure on sensing wide range of forces will be revealed. Capability in identifying various touch modalities will be presented by employing the technique of electrical impedance tomography. In Chapter 5, quantitative analysis of EIT-based tactile sensing scheme will be presented. The role of reconstruction parameter, the effect of background conductivity, and a spatial correction method will be investigated. In Chapter 6, the dissertation work and contributions will be summarized and suggestions on future work will be outlined.

Chapter 2. Stretchable Touch-Sensing Skin over Padding for Co-Robots

Published in Smart Materials and Structures, 25 (5) 055006 (2016).

Ying Chen[1], Miao Yu[1], Hugh A Bruck[1], Elisabeth Smela*[1,2]
[1]Department of Mechanical Engineering, University of Maryland, College Park, MD, 20742
[2]Institute for Systems Research, University of Maryland, College Park, MD, 20742
* corresponding author: smela@umd.edu

Co-author contributions: The idea of comparing different padding materials for padded piezoresistive sensing strip comes from the discussion among all authors. Ying Chen fabricated the sensors, performed the experiments, and processed the data. All authors contributed to writing the text and making the figures.

2.1 Abstract

For robots that work collaboratively with people, often referred to as "co-robots", it would be beneficial for them to be soft or padded and to have a touch-sensing "skin" to enable tactile environmental awareness. However, a sensing skin over a padding material that undergoes large deformations requires "stretchable" materials, which may possess time-dependent or viscoelastic mechanical responses. In this work the role that a padding layer plays when placed under a stretchable sensing layer was investigated. A strain-sensing skin was formed by coating a thin film of compliant piezoresistive sensing paint, consisting of exfoliated graphite in latex, onto a rubber membrane, and the response of the skin was characterized. The change in resistance was linear with tensile strain. The role of the padding material was then investigated under

indentation by examining three foams and two elastomers. As expected, the padding enhanced energy dissipation as shown by hysteresis in the sensor response, which is linked to its protective function; the hysteresis was comparable for the five padding materials. The padding also provided an unexpected advantage: it magnified the change in resistance compared to that obtained under free displacement in air. While hysteresis in viscoelastic materials can largely be handled with an appropriate model, inconsistency cannot be, and the two elastomers were found to have unacceptably high variability because of micro-cracks and other defects in these materials. On the other hand, foams that had few defects and regular cell sizes gave good consistency across trials and different sensor positions over the padding. Combined with their lighter weight and availability in a wide range of stiffness, we conclude that foams make a better choice for padding of co-robots.

2.2 Introduction

For robots to work alongside people, provide physical assistance, or interact socially via touch, corporal contact must be safe and comfortable. These so-called co-robots are thus envisioned to be "soft," which can be accomplished by making the robot from elastomeric materials [125], by utilizing inflated air-filled structures [126,127], or by padding a rigid robot [8,62].

Also critical to the emerging field of co-robotics will be sensors that give a robot the capability of sensing touch. Tactile sensors can be placed either under a padding or over it. A conventional rigid sensor can be placed under the padding, where it is mechanically protected, but it suffers

substantial loss of resolution [128]. Here we consider a stretchable external covering or "skin" that can be placed over the padding and follow the changing conformations of a compressible soft robot (**Figure 2.1**). It should ideally cover the entire outer surface and could potentially provide information not only on touch but also on joint positions.

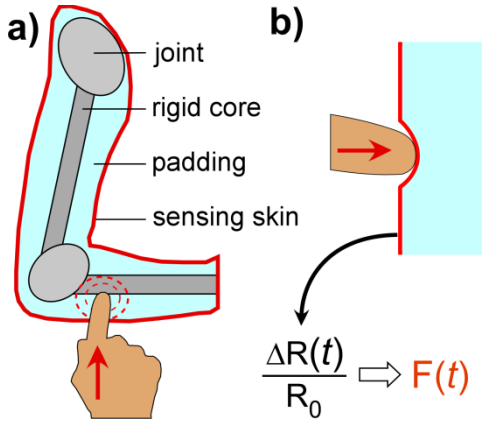

Figure 2.1: a) A sensing skin over a padded robot. b) Touch (i.e., force F(t)) can be inferred from changes in the resistance (i.e., $\frac{\Delta R(t)}{R_0}$) of a piezoresistive sensor that experiences strain over a padding.

Various flexible sensors have been demonstrated for sensing touch, as reviewed in [15,18,129,130]. Most have been either resistive or capacitive. Resistive strain sensors include those for which stretching leads to dimensional changes of a conductor, for example a thin metal film [131] or a channel filled with conductive fluid [29]. Alternatively, piezoresistive sensors are typically based on a flexible host matrix filled with conductive particles, such as carbon black or graphite [39-43,46-48], or even pockets of conductive fluid [132]. Capacitive sensors are usually based on a change in spacing between two conductors [25,63,133-135], but it is also possible to measure impedance changes through a weakly conductive medium [73,136]. Other mechanisms for sensing touch have also been demonstrated, such as changes in transistor current

[137,138] or piezoelectric [139] or optical [140] effects. Compliant sensors have been reported that are stretchable (not only flexible) [132,141] or that could cover large areas (> 10 cm) [111,117,134,135,142-145].

Piezoresistive strain sensors based on conductive carbon nanoparticles (including carbon nanotubes (CNTs), carbon black, exfoliated graphite (EG), graphene) dispersed in various insulating polymeric host materials have been the subject of considerable recent research [39-43,46-48,56,58]. In the present work, the sensing layer was a composite of EG dispersed in a latex host. Latex is a natural rubber, and the composite becomes electrically conductive at percentages of EG (loading) that do not substantially increase its stiffness, which renders the composite stretchable. This is critical because a large-area tactile sensing skin can undergo large deformations. The latex/EG composite paint used in this work has been previously characterized on bendable substrates; its static response was found to be linear with strain and its dynamic response faster than 10 Hz [48]. Another significant advantage of this sensor is its simplicity: the EG/latex dispersion is readily prepared, particularly since the relative change in resistance is largely insensitive to EG content above percolation [48], and the dispersion can be easily and rapidly applied onto various substrates as a thin film by spray or brush coating.

Padding materials have been extensively investigated for applications as diverse as footwear and automobile crash protection [146], including polymer foams [147,148] and other cellular materials, elastomers, gas pockets, springs, gels, and granular materials. For impact protection, compliance and low stiffness serve to distribute the impact force both spatially and temporally; the choice of padding depends on the range of expected forces and loading directions. Ideally,

the padding should also be lightweight, practical to apply to the structure, and relatively compact. While mechanical hysteresis is needed for energy absorption, it is unfavorable for sensing, since it complicates determination of the loading from the signal amplitude (although hysteresis can be predicted mathematically [25]).

Various types of padding have been considered for robots, with most of the focus on foams and elastomers. Hayashi et al. [149] discussed potential soft materials, and they developed a humanoid robot covered with polyurethane foam. For dexterous manipulation, padding on robot fingers renders them conformable, allowing a more secure grasp [62]. The mechanical properties of fingertips made of silicone and polyurethane have been evaluated [150]. Berselli et al. [151] considered padding material and shape for mimicking human fingers, evaluating modulus, sensitivity, and hysteresis. For robot fingertips, Shimoga et al. compared plastic, rubber, sponge, powder, paste, and gel [62]. Sponges showed the best conformity and highest energy dissipation, but gels allowed reduced padding thickness and increased stiffness, which enables the application of higher forces. Shimojo [128] examined the loss of spatial resolution due to a thin elastic covering on a rigid sensor. Maiolino et al. [63] compared soft dielectric materials for capacitive sensing in terms of sensitivity, durability, and resolution, showing that sensitivity varied with force but was similar for different materials, concluding that the choice should be specific to the application.

Although padding materials have been extensively studied alone, their use under sensing skins has not. In this chapter, we address the use of a *stretchable* sensing skin, comprising a thin film piezoresistive coating on a latex membrane, overlying a *highly deformable, energy-absorbing*

padding for sensing strains due to mechanical loading. Tensile and indentation testing showed that the sensing skin responded linearly to strain and had a recovery time on the order of 4 seconds. Three types of padding were examined: open cell foam, closed cell foam, and silicone elastomer. Under indentation, the addition of an underlying padding amplified the change in resistance, by a factor of 2 to 5 depending on the material. This is due to localized deformations associated with indentation, which results in a greater change in length of the skin. While padding increased the sensitivity, it also introduced delayed spring-back, a measure of the efficacy of a padding. The resistance hysteresis was similar for all the padding materials, regardless of their stiffness or force hysteresis, with recovery times of approximately 7 () seconds, twice as long as the sensing skin. Also important to co-robot applications is low variability in measurement results, and padding materials with uniform microstructures and few defects exhibited greater consistency.

2.3 Experimental Methods

2.3.1 Sensor Fabrication

2.3.1.1 Sensor Material

Piezoresistive strain sensors consisted of a blend of latex and conductive exfoliated graphite (EG). Microwave exfoliation of graphite (Asbury Graphite Mills, Inc.) was described previously [47]. Following this, an EG suspension was formed by sonicating (QSonica Q700, amplitude 100, power 200-300 W) EG (10 g) together with 1000 mL of deionized water, 7.5 g of surfactant

(Triton X-100, Sigma-Aldrich) and thirty drops of antifoaming agent (SE-15, Sigma-Aldrich) as detailed in [48]. To avoid over-heating the sonicating probe, the power was turned on and off for 5-minute intervals until the total energy reached 400 kJ (1 hr). Into this dispersion (12.2 g), latex (0.936 g, RD-407, ArtMolds) was added as described in [48,152]. After spray coating and drying, this dispersion leads to a piezoresistive sensing composite containing 25 wt% EG.

2.3.1.2 Sensing Skin Fabrication

To form the touch-sensitive skin, the piezoresistive paint was applied by spray-coating onto a latex membrane (ELE International, triaxial membranes, 0.3 mm thick). Sensor dimensions were defined by a stencil created from painter's tape (ScotchBlue). The substrate was placed on a flat, rigid surface to prevent the sprayed fluid from running. The EG/latex dispersion was spray-coated (10 psi air pressure) in a hood and allowed to air dry for one minute. This was repeated to deposit 10 layers, after which the stencil was removed, yielding a sensor area in the desired shape and size. The sheet resistance of the final film was 100 Ohms/square, obtained by the Van der Pauw method [153]. The film thickness was 67 ± 22 μm, obtained using calipers with a precision of 10 μm: 10 measurements of thickness of the membrane alone and 10 of the sensor+ membrane were averaged and the values subtracted. The latex composite adhered well, as determined by visual inspection and rubbing with a fingertip.

2.3.1.3 Sensor Connection and Mounting

The latex membrane, with a rectangular sensor-coated area of 11 cm x 20 cm, was cut along the 20 cm length into 25 strip-shaped sensors, each 0.8 cm wide. The two ends of each strip sensor were connected to electrical wires (single strand, 30 AWG) with silver epoxy (CircuitWorks, CW2400), and the initial resistance (R_0) and gauge factor (GF) of each sensor was measured (see the online Supplementary Information (SI)). Fifteen sensors with similar R_0 (7.0±1.5 kΩ) and GF (13.8±1.4) values were chosen for this study.

The surface of each strip was coated with a flexible insulating paint (Behr Premium Plus Ultra, black). The coating protected the sensing material from abrasion and inadvertent electrical connection. This had a smooth surface, had minimal effect on sensitivity, and showed the least variation among identically treated samples due to cracking (see Appendix D5).

A steel frame was made to suspend a set of three sensors (**Figure 2.2**). The interior edges were rounded to prevent undue stress concentrations. The ends (last 1.5 cm) of the sensors (face up) were adhered (Krylon, Repositionable Spray Adhesive 7020) to the frame. The three sensors were separated by a distance of 3 cm, a distance large enough to avoid sensing an applied local loading on the neighboring sensors. A different set of 3 sensors was used for each of the five padding materials, so the sensing strips were replaced when the padding material was changed. Sensors were readily removed from the frame with a razor blade and the next set of sensors was attached.

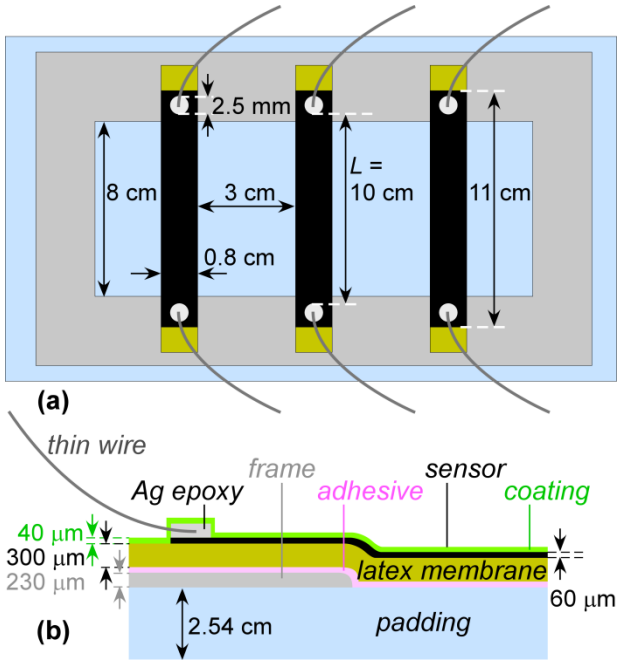

Figure 2.2: (a) Overhead schematic view of the strip sensors on the fixture, affixed to the padding. (b) Cross sectional close-up of the inner edge of a sensor.

To track the deformation reliably and reduce wrinkling, there should be no slip or gaps between the sensing skin and the padding. The sensors and the frame were fixed to the padding with the same repositionable adhesive. Adhesive was applied sparingly so that it did not harden substantially after curing and stiffen the contact interface.

2.3.2 Uniaxial Tensile Testing

To obtain the gauge factors for each sensor, they were suspended vertically and were uniaxially stretched. The experimental setup for the uniaxial testing is shown in Supplementary Information (Appendix D2) together with a more detailed description. Both ends, including the portions with the attached electrodes, were glued (Aleene's fabric glue) to a thin plastic film

(Highland701 transparency film, 0.4 mm thick). The upper end was then glued to a piece of glass (microscope slide, 25 x 75 x 1 mm) so it could be firmly clamped. A hole was punched through the transparency on the lower end to allow it to be pulled. The gauge length of the sensors (the effective initial length L_0, given by the distance between electrodes) was 100 mm.

To confirm the linearity of the strain sensitivity, found previously [48], another sensor from the same batch but different from the 15 samples used in the loading tests was used. (For this sensor, L_0 was 90 mm instead of 100 mm.) The lower end of this sensor was pulled to five positions, stretching it by 2.5, 5, 10, 15, and 20 mm (2.8, 5.5, 11.1, 16.7, and 22.2% strain, respectively) (Figure 2.6). Considering the small strains that would be experienced in the loading experiments and the linear response of these sensors, the 15 sensors used in the loading tests were stretched to only two stretch ratios, 1.030 and 1.060 (3% and 6% strain) to obtain the gauge factors. The gauge factors of these 15 sensors were normalized to the *GF* of Sensor #1.

2.3.3 Indentation Testing

A force transducer (Bose 3330 Series II) was employed to conduct constant-displacement tests (**Figure 2.3**). The transducer probe had a spherical silicone tip (dia. 1 cm) that was slightly compressible; it contacted the center of the sensing strip. To measure the force during the indentation testing, a load cell (Cooper Instruments & Systems LFS270 5 lbs (2.3 kg)) was

connected in series with the probe. To avoid potential adhesion of the probe to the sensor, the probe was covered with Teflon tape (PTFE thread seal tape).

In the loading/unloading tests, probe speeds of 2.5, 25, and 250 mm/sec were compared. Rate dependency is common in viscoelastic materials, but there was no systematic effect at these rates, as shown in the Appendix (Appendix D6). For single indentation tests, the loading/unloading speed was kept at 2-3 mm/sec. Data from the first run were discarded to eliminate variations due to the Mullin's memory effect.

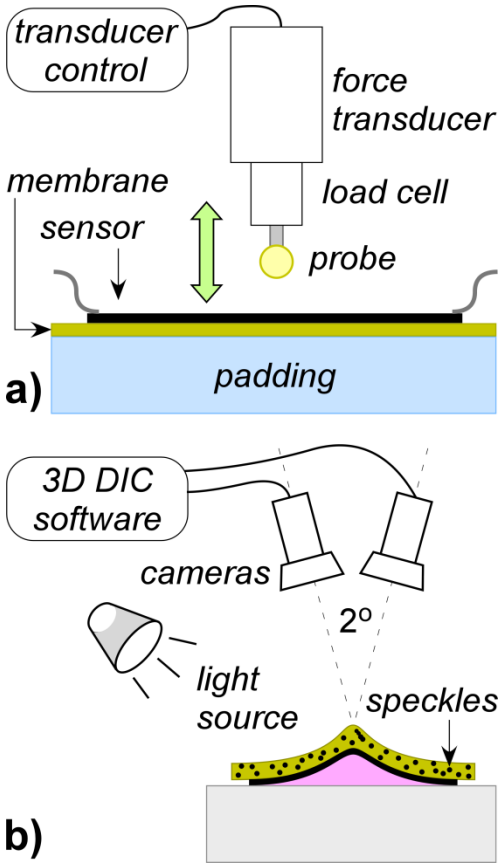

Figure 2.3: a) Experimental setup for indentation tests showing the sensing skin on the padding, the probe, and the force transducer. b) Experimental setup for the 3D-DIC experiments showing the sample, cameras, and light sources. The membrane shape was frozen by a fast-setting epoxy.

Sensor resistance was measured with a voltage divider circuit, with the sensor connected in series with a known, fixed resistor. A voltage source (Hewlett-Packard 6236B triple output power supply) applied a constant 5 V. Sensor resistance was derived from voltage measurements by a data acquisition system (DAQ) (NI USB-6009, 14 bit, 48 kS/s).

Displacement was recorded directly from the force transducer with a different DAQ. The times from the two systems were synchronized by matching the times of the peaks. Experiments were conducted in triplicate, and matching the first peak resulted in synchrony for the others also.

Three dimensional (3D) digital image correlation (DIC) [154-157] (Figure 2.3b) was employed to independently measure deformation due to indentation. A membrane sheet was painted with random speckles (Behr Premium Plus Ultra, white, speckle size 1 mm dia.). Two cameras (body: Point Grey FL2G-13S2M-C, lens: Tamron AF 75-300 mm 1:4-5.6 LD tele-macro [1:3.9]) were placed looking towards the speckles. The angle between the cameras was 2.4° . A bright light source (Lowel Pro-light) provided the illumination required for good image quality. 3D-DIC software (Vic-3D, Correlated Solutions) was used to analyze the images to obtain the membrane shape.

Conventionally DIC is performed during a loading test while the cameras look at the sample area of interest. For the indentation test performed on the sensors, the probe blocked the cameras, rendering the area underneath the probe invisible. Therefore, 3D-DIC was discontinuously performed. In order to obtain a complete shape over the entire indented area, we employed a

shape-freezing method, similar to stress-freezing [158]: after obtaining the initial speckle pattern from the undeformed membrane, the sample was indented by the probe and an uncured fluid epoxy was poured around the probe and allowed to harden, and a second speckle pattern obtained. A circular membrane, coated on one side with the insulating paint and speckled, was placed with the speckles facing the padding, and the probe was indented to a depth of 6 mm. The resin and hardener (EpoxAcas, 30 g epoxy resin (650 part A), 3.6 g hardener (101 fast hardener part B)) were mixing together (3 min) and poured onto the surface around the probe. The epoxy became rigid after 4 hours at room temperature. The deformed membrane, together with the attached probe, was removed from the force transducer. 3D-DIC was performed on the deformed membrane (Figure 2.3b).

2.3.4 Padding Materials

Foams are either open-cell or closed-cell, according to whether the gas introduced during fabrication is trapped [147], which adds rigidity. Silicone elastomers, such as polydimethylsiloxane (PDMS), have a stiffness that can be varied via the ratio of the base polymer to cross-linker [159].

We selected two commercial open-cell (OC) foams with different stiffness and one closed-cell (CC) foam, and we prepared PDMS with two ratios of precursor to curing agent (Table 2.1). Foams were obtained as sheets with 1” (2.5 cm) thickness and were cut to rectangles of 15 x 17.5

cm. PDMS was prepared in circular molds, from which they were removed after curing, giving dimensions of 14 cm diameter and 1.8 cm thickness.

Padding stiffness was characterized by indentation load deflection (ILD), obtained by measuring the load required to make a 1'' x 1'' x 1'' sample (2.5 cm cube) reduce in the thickness direction by 25%. The load was measured with the same load cell, and ILD numbers (Table 2.1) were calculated as the ratio of the loading to the area.

Table 2.1: Padding materials, in order of increasing stiffness.

Name	Code	Material	Source	ILD (N/cm^2)
open-cell foam 1	OC-1	poly(urethane-ether)	foamforyou.com	0.14
open-cell foam 2	OC-2	polyurethane	Home Depot	0.47
PDMS 1	PDMS-1	silicone, 1:1 part A: part B	Dow Corning, Sylgard 527	0.51
PDMS 2	PDMS-2	silicone, 1:3 part A: part B		0.85
closed-cell foam	CC	nitrile rubber	Armacell	0.90

Images of foams were taken with a camera and macro zoom lens (Nikon D700, Sigma EX 105 mm 1:2.8D). A microscope (Leica MZ 12.5 stereo zoom) was used to view the elastomers at higher magnification, with images captured using a digital camera (Tucsen 5MP, with software TSview). Two light paths were used for the latter: coaxial (perpendicular to surface) and ring (oblique).

Images of the five padding materials are shown in **Figure 2.4**. Comparing the two open-cell foams (top row), OC-1 was uniform, while OC-2 contained large bubbles of varying size.

Furthermore, the cells of OC-1 (bottom row) were symmetric and of consistent size, while those of OC-2 were oriented and had non-uniform size. The closed-cell foam (center) had larger cells with thin walls, compared to the struts in the OC foams, giving the surface a wrinkled look; the cell size was irregular, but there were no large defects. The elastomers were featureless on the length scale used to image the foams. Microstructures for PDMS are therefore shown, using two illumination sources; each image is at the same location. PDMS-1 had many surface defects, such as small bumps, dents, and white patches. PDMS-1 was soft and tacky, so it is unsurprising that touch may have affected the surface condition. Cracks were seen on PDMS-2, which was more brittle than PDMS-1.

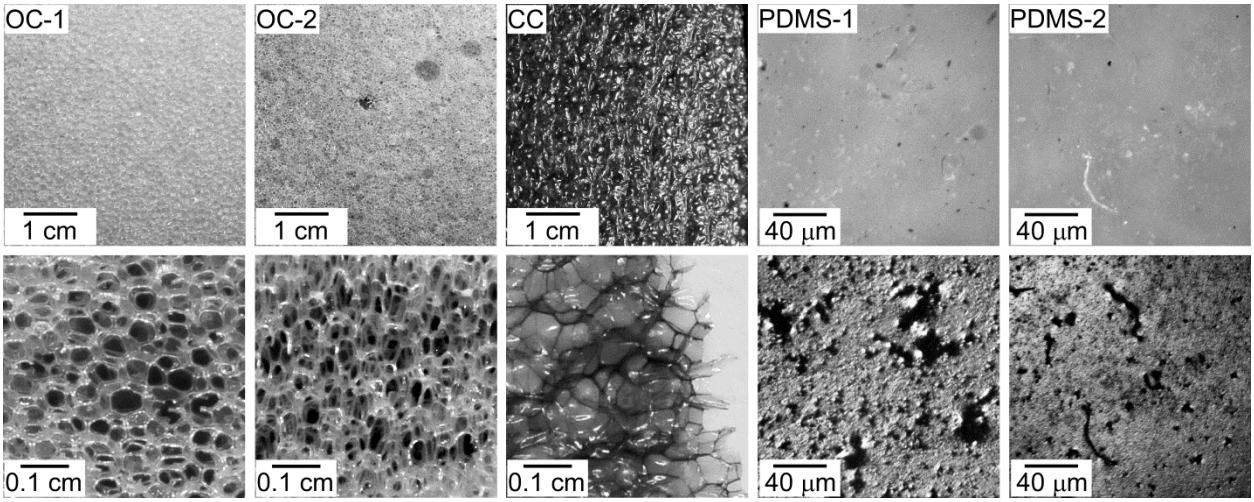

Figure 2.4: Microstructures of five padding materials at (first three foam columns) two low magnifications and (last two elastomer columns) at high magnification under (top) coaxial and (bottom) ring light illumination.

2.4 Results and Discussion

The most important performance characteristic of a sensor+membrane+padding system is the sensitivity, which for a strain sensor is the gauge factor. Also of interest are the time response, the reproducibility, and the break-in time for steady-state behavior under cyclic loading. The contributions of each component of the system to the sensing performance were determined by examining various combinations and geometries (**Figure 2.5**).

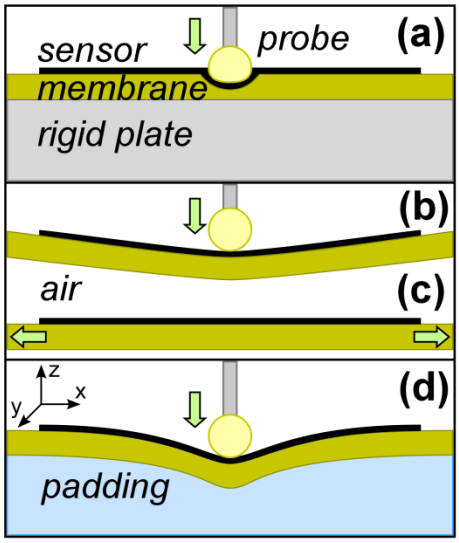

Figure 2.5: Perpendicular load applied to sensor + membrane (i.e., sensing skin) (a) on a rigid substrate (Section 2.4.2), (b) supported at the edges, over air (Section 2.4.3), (d) and over padding (Section 2.4.4). (c) Uniaxial loads applied to sensor + membrane (Section 2.4.1).

2.4.1 Uniaxial Tensile Testing

Before examining the effect of padding, the sensing skin alone was characterized and calibrated (Figure 2.5c). In prior work, the EG/latex sensor were applied on bending cantilevers, which were flexible but not stretchable, and showed a linear tensile response to 1500 microstrain [48]. Due to the hyper-elastic rubber membrane, the strains experienced in this work were orders of magnitude larger. (The calibration of the EG/latex sensor on bending cantilevers was repeated in this work, Appendix D1.)

The calibration curve of a reference sample is shown in **Figure 2.6**. The relative resistance change was substantially linear with axial tensile strain to at least 22%. A linear curve fit gave a gauge factor *GF* of 14.2, where *GF* is defined by $\Delta R/R_0 = GF\Delta L/L_0 = GF\varepsilon$, where ΔR is the change in resistance, ΔL the change in sensor length, L_0 the initial length, and ε the engineering strain. This value is larger than the typical *GF*s of 2 for metal thin film strain gauge sensors.

Before they were mounted to the frame fixture, the strain response of each sensor was obtained by uniaxial stretching to fixed displacements, in triplicate. The initial average resistance of the fifteen sensors was R_0 = 7.0 kΩ with a standard deviation of 1.5 kΩ. The variation is due primarily to non-uniform thickness of the sensing layer: the coating was manually applied in multiple layers. The average gauge factor was comparable to that of the reference sample, 13.8 ±1.4; there was no correlation between *GF* and R_0. (see Appendix D2.) The variation in the gauge factor was smaller (10%) than the variation in resistance, and this is the more important value because relative changes in resistance were evaluated.

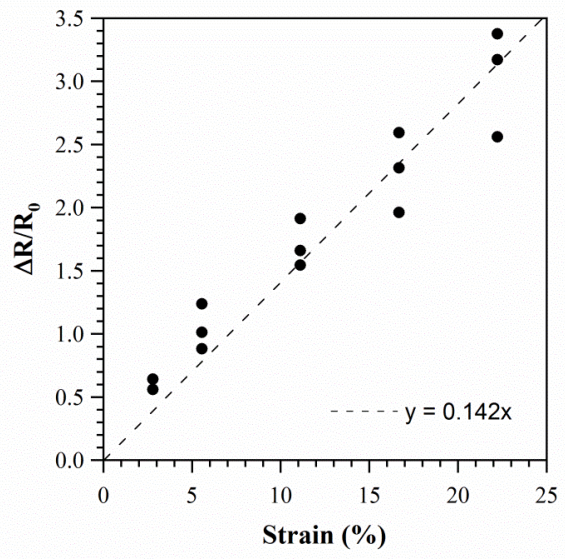

Figure 2.6: Change in resistance with strain under uniaxial stretching (illustrated in Figure 2.5c) of the reference sample. The line is a curve fit to the mean values of the three replicate measurements.

Although all the strip-shaped sensors were fabricated from the same EG/latex dispersion and were spray coated at the same time, variations in thicknesses and geometrical variations from the cutting process led to small differences in R_0 and GF. Because the GFs were constant, variations could be simply handled by calibration and normalization. (The goal of the present study was not the production of identical sensors.) The electrical responses in later experiments were normalized by the gauge factor of each sensor: the gauge factors of the sensors were divided by that of sensor #1 to give a ratio, and in future experiments the measured $\Delta R/R_0$ were divided by this ratio to normalize for variations in sensitivity.

The temporal responses of the sensor on a bending cantilever and on the latex membrane are shown in the supporting information (Appendix D1 and D3). The resistance response was

almost the same in these two cases (Figure D.7, SI). The polymer is able to follow high frequency (9 Hz) deformation in the glassy or elastic state.

2.4.2 Loading on a Rigid Substrate

Loading by a probe can introduce both compressive and tensile stress. To better understand the effect of compressive loads applied to the skin, the response of the sensing skin on a rigid substrate (a steel block), was examined upon perpendicular loading at the center (as illustrated in Figure 2.5a). In the previous section, the load was inplane tensile; here it was out-of-plane compressive, but membrane deformation in the *z*-direction leads to expansion of the sensor, located on the surface, in *x* and *y* due to Poisson's ratio. Three strips were measured in triplicate after an initial "break in cycle" indentation. A probe with a silicone tip moved downward at a fixed velocity of 2.6 mm/sec until it reached a given distance beyond the original surface, and then retracted at the same velocity (**Figure 2.7**a). Experiments were separated by time intervals of 5 minutes without contact.

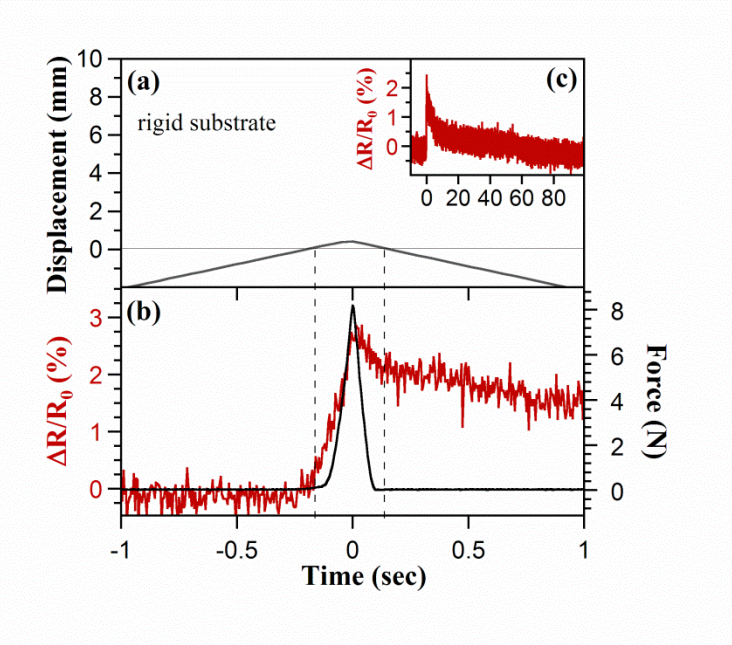

Figure 2.7: a) Displacement, b) normalized change in resistance, and force vs. time for a sensing skin supported by a rigid surface under perpendicular loading (Figure 2.5a). c) A longer time period for the sensor response. Zero displacement is where the probe contacts and leaves the surface, indicated by the dashed vertical lines.

The time course of a typical strain gauge response is shown in Figure 2.7b and c. The indentations were comparable to the membrane thickness of 0.3 mm: as illustrated schematically in Figure 2.5a, the measured indentation is a combination of membrane compression and probe tip deformation. The force over the rigid substrate reached 8 N after a short delay; this is due to "slop" in the probe mechanics of a few hundred μm, when the probe contacts the surface but does not exert force until vertical play in the system is eliminated.

Upon indentation, the resistance changed immediately, increasing due to sensor stretching around the probe. The normalized change in resistance peaked at 2.5%. Although the probe was

in contact for less than half a second, it took tens of seconds for the resistance to decay back to a stable value.

These data shed light on two important aspects of coating a thin sensing film onto a highly stretchable membrane. Firstly, the measured change in resistance is primarily due to strain, rather than force: $\Delta R/R_0$ reached only a few percent under a large compressive load in the thickness direction, compared to 300% under uniaxial tensile testing. Secondly, the sensor accurately reflected the mechanical behavior of the underlying substrate. As discussed above, a slow recovery must be expected and taken into account when working with "soft" materials. Methods for determining the applied load on viscoelastic sensors have previously been developed [56] that can reasonably predict for these effects.

2.4.3 Loading over Air

The indentation tests were run without a substrate (illustrated in Figure 2.5b) to provide the other extreme of boundary condition. The load in this case was primarily tensile, as in the uniaxial stretching tests, but there was a varying time course to the loading. The maximum displacement in these tests was fixed at 8 mm (**Figure 2.8**a), giving a total inplane strain of 1.9%. Three samples were cycled four times each, the first cycle being a break-in cycle, with 5 minute intervals between cycles. The force reached a maximum of 0.18 N, or 2.3% of that on the rigid substrate.

The increase in resistance (Figure 2.8b) closely followed the increase in force, again beginning at the point of contact, as expected. The maximum change in normalized resistance (at 8 mm) was $25.6 \pm 2.1\%$ (3 trials), roughly 10 times larger than under the compressive load. The gauge factor was 13.5, consistent with the values in the uniaxial tests, and the sensitivity was 2.1%/mm at an indentation of 6.7 mm (for comparison with values in Table 2.2). Comparing these values with those on the rigid substrate, it is again clear that the sensors respond to strain, rather than force.

While the force recovered to zero when the displacement went to zero, there was still a residual change in resistance that took longer to decay. The recovery time t_r was defined as the time it took after the indenter left the surface for the value to return to 10% of its peak. For the skin over air, this took approximately 4 seconds.

It should also be noted that deformations of the sensing skin during indentation tests (Figure 2.5b) are not unidirectional, so biaxial testing was performed (Appendix D4). The sensitivity in the *x*-direction was unaffected by the amount of stretching in the *y*-direction.

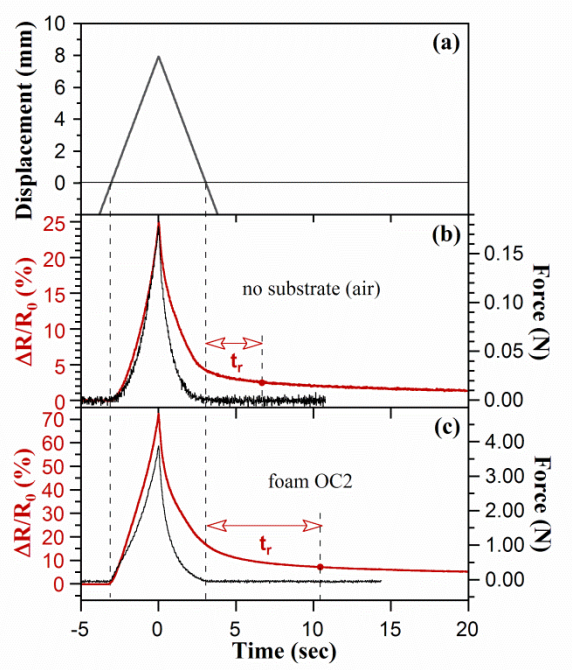

Figure 2.8: a) Displacement waveform for single loading-unloading cycle to a fixed 8 mm displacement. Corresponding changes in normalized resistance and force for b) an edge-supported sensor+membrane under perpendicular loading (illustrated in Figure 2.5b) and c) when the sensor was over a padding (open-cell foam OC-2). Dashed vertical lines indicate when probe contacted and left the surface, at zero displacement. At time t_r the resistance had dropped to 10% of its peak value. Note: *y*-axes differ in (b) and (c).

The data from this section isolate the response from just the sensing skin, without padding, under indentation loading. Combining this with information on the role of padding, presented below, it is possible to build a general understanding of the response of highly compliant sensing skin/foam systems.

2.4.4 Loading on Padding

Loading can be performed to constant force or constant displacement. The latter is more often used because it has the advantage of causing similar material deformation profiles even if their stiffness varies. For this work, it was also advantageous because the sensors principally detect strain, not force, as shown above.

2.4.4.1 Single-Indentation Loading

A single touch on a robot's skin, such as a push, might be expected to be the most common occurrence. As above, four single-indentation loading-unloading tests were conducted, separated by a time interval of 5 minutes without contact to allow recovery from memory effects in all parts of the system (sensor, membrane, padding). A five minute interval is typical in the study of mechanical responses of padding, such as polyurethane foams [148].

The 8 mm maximum displacement represented nearly one third of the 25 mm foam thickness and half of the 18 mm elastomer padding thickness; it represented a large deformation. The same loading/unloading speed of 2-3 mm/sec was again used here. Three same-sensor replicates of three sensors provided a total of nine same-padding replicates.

The force on the probe and normalized resistance change for one of the sensors on open-cell foam 2 (OC-2) are shown in Figure 2.8c. On this foam, the force on the probe reached 4 N (compared with 0.2 N over air and 8 N on the rigid surface). Resistance changes on this foam

were three times higher than those when the membrane was suspended over air: the foams produced an amplification of the strain response.

As was the case for the suspended membrane, both the force and $\Delta R/R_0$ increased with displacement, although again nonlinearly. The two curves were closely correlated upon indentation for this foam.

As in Figure 2.8b, although the force in Figure 2.8c returned to zero as soon as the probe lost contact with the surface, the resistance only gradually decreased back to R_0. The recovery time for foam OC-2 was 8 seconds, roughly twice as long as for the membrane alone, and for the other padding materials t_r was similar (Appendix D7).

Plotting the response as a function of displacement (**Figure 2.9**) better displays memory effects. At the surface (displacement $d = 0$) the force and resistance change both started at zero. The force returned to zero at $d = 0$ at the end of the cycle because the probe to which the force transducer was attached lifted off the surface. The resistance, however, stayed high because the padding and skin were still deformed, which was read by the sensor. The resistance eventually returns to its initial value (Figure 2.8) as the viscoelastic materials return to their original shapes.

The force on the probe shows hysteresis, having a lower value upon unloading because the foam was compressed. Hysteresis is defined as the maximum vertical distance between curves, normalized by the maximum range: $e_h = [\max(|y_{load} - y_{unload}|)]/(y_{max} - y_{min})$. In this case, it is the maximum difference of force during loading-unloading divided by the maximum force.

Hysteresis is a measure of the foam's ability to dissipate energy [62], and is essential in a padding. Although hysteresis complicates analysis of the sensor signals, the lack of bounce-back after compression reduces impact forces and distributes the impact load [146]. The resistance curves were typically shaped as figure-8s and did not close, since the resistance followed the long mechanical recovery times. The change in resistance was fairly linear with displacement before the turn-around point.

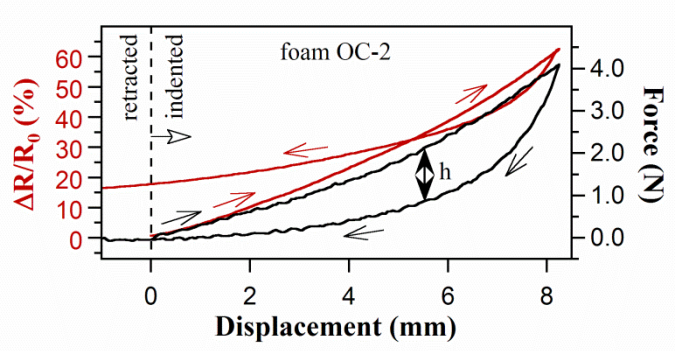

Figure 2.9: Change in resistance and force as a function of displacement for foam open cell 2. Hysteresis *h* in the force is illustrated. Arrows indicate loading and unloading.

Single-cycle loading on foam, air, and the rigid substrate are compared in **Figure 2.10**. As shown in Figure 2.10b, the padding OC-2 magnified the sensor's resistance response compared with that on air (on average by a factor of 3.8 at 6.7 mm indentation). Since the maximum normalized resistance change for the rigid substrate was 2%, this magnification is unrelated to the more concentrated compression introduced by the soft padding compared to air. The reason for the enhancement is explored in Sections 2.4.4.4 and 2.4.4.5.

The rubber membrane introduced some hysteresis in $\Delta R/R_0$, as shown by the non-closing loop over air (Figure 2.10b). This hysteresis was substantially smaller than that on the foam, however, even though the displacement was the same. The padding thus dominates the memory effects.

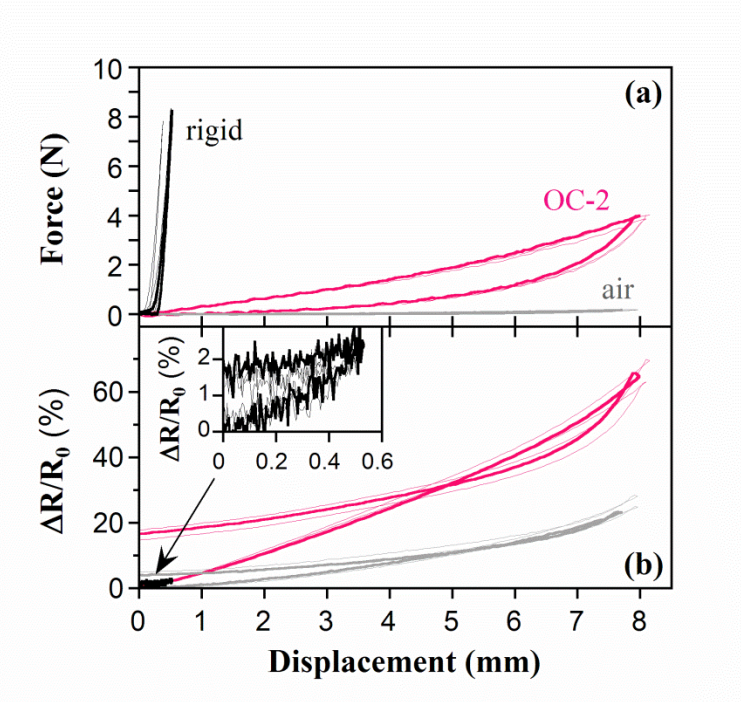

Figure 2.10: a) Force and b) normalized resistance change for the three underlying materials in single-indentation tests as a function of probe displacement.

The indentation results show that the cushioning foam, as expected, increased the displacement and lowered the forces compared with a rigid substrate. The foam also had an unexpected benefit, increasing the sensitivity to indentation. On the other hand, the foam increases the recovery time compared to the skin alone. This time is 7 seconds after complete removal of the touching object, which is still short compared to expected times between intermittent human touching of a robot.

2.4.4.2 Cyclic Loading

Cyclic loading may occur on a smart skin for repetitive motions such as walking. Under cyclic loading, the padding does not have time to mechanically recover, and its behavior reaches a steady state response after a number of cycles. For piezoresistive composites in which an insulating host is loaded with a conductive filler, the resistance response under loading is known to be history-dependent [39]: in dynamic tests a stable electrical response is obtained after several "break-in" cycles. New percolation paths are established and old ones are destroyed as the system reaches a new equilibrium [58].

Dynamic load testing was performed to determine the role played by the underlying padding in the break-in behavior. Sinusoidal constant-displacement tests (**Figure 2.11**a) were conducted on each sensor: 30 cycles at a frequency of either 0.2 or 1 Hz to a maximum displacement of 8 mm at the center of the sensor (results were insensitive to rate in this frequency range, as shown in Appendix D6). Simultaneously, the force applied by the probe and the resistance of the sensor were measured.

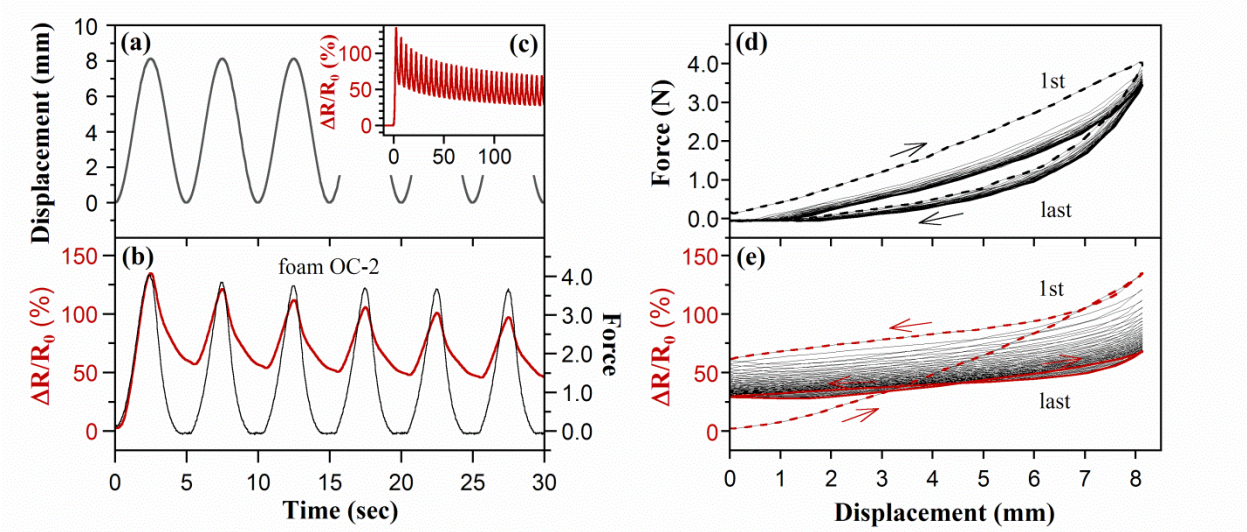

Figure 2.11: a) Sinusoidal displacement at 0.2 Hz. b) Force and normalized resistance change as a function of time under cyclic loading. c) Normalized resistance change over a longer time. d) Force and e) normalized resistance change versus displacement. (First cycle, dashed line; last cycle, heavy solid line. Data are from a sensing skin on foam OC-2.

The temporal response of the force and the relative resistance changes are shown in Figure 2.11a,b. The resistance change during the first cycle was nearly double that in the single-indentation test (Figure 2.8c). This was because the very first cycle in those tests was discarded and R_0 was set to the value at the start of the second cycle. As shown in Figure 2.11b, the peaks of the resistance curve correspond with those of the force curve, so the sensor followed the dynamic input, albeit with a reduced amplitude. The resistance did not recover to zero after the first cycle, but remained at a higher level. Figure 2.11c shows a longer time scale.

History dependence from cycle to cycle is seen even more clearly in plots against displacement (Figure 2.11d,e). The measured force generally stabilized already in the 2nd cycle, but the

resistance response took longer. The start-of-cycle resistance of the sensor decreased to a steady value, stabilizing after approximately 20 cycles.

Comparing these results with cyclic testing of the skin (Appendix D3) confirms that the padding lead to greater dissipation of energy during the 1st loading cycle, as it should. Interestingly, the steady-state resistance response to indentation over padding had less hysteresis than the skin response under tension (Figure 2.5c).

The results of this section illustrate how the padding dampens sensor readings under cyclic loading, since it does not have sufficient time to mechanically recover between cycles; this is in marked contrast to the response of the sensor painted onto a more rigid substrate [48] or the response of the sensor on the membrane, which is in the glassy (elastic) state at these frequencies. A direct mapping between signal and deformation cannot be expected in highly deformable systems, although the deformation can still be inferred by modeling [56].

2.4.4.3 Padding Comparisons

Single-Indentation

The force and resistance responses (three cycles each on three sensors) on the five padding materials are compared for single-indentation loading in **Figure 2.12**a,b. The probe started some distance above the surface, so there were variations in the final displacements on the different padding materials.

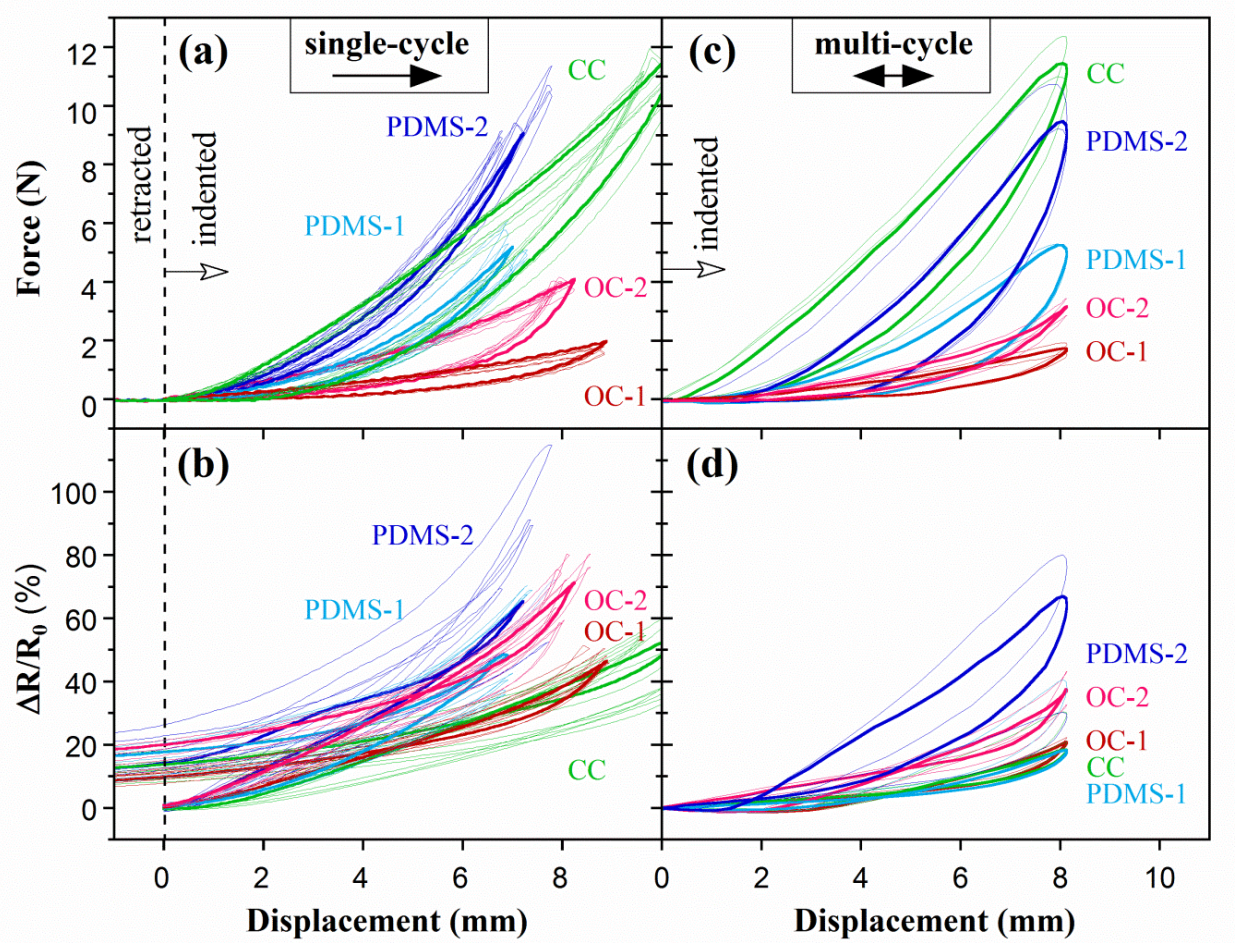

Figure 2.12: a) Force and b) normalized resistance change for all 5 padding materials in single-cycle tests as a function of probe displacement. Nine traces are from triplicate measurements on 3 samples. One trace is heavier to aid visualization. c) Force and d) normalized resistance change under cyclic loading; one steady state curve for each of the three sensors is shown, with one trace heavier to aid visualization. These curves were shifted to the same baseline: $\Delta R/R_0 = 0$ at displacement = 0 mm.

The maximum force on the probe reached between 2 and 12 N, tracking the ILD values (Table 2.1) as expected, since ILD quantifies the stiffness. For the three foams, at the start of indentation under small compressions, the force was fairly linear with displacement (Figure 2.12a) as the cell walls bent and the foams behaved as Hookian springs [146]. With increased compression the force curves turned upward, showing a rise in stiffness, as the foam cells began

to collapse, and, for the closed cell foam, as the air in the cells was compressed. (Note the greater curvature for foam CC.) The elastomer samples behaved similarly to CC. The force hysteresis (an indication of padding efficacy) was largest for the soft open-cell foams (33% for OC-1, 37% for OC-2) and smallest for the elastomers (19% for PDMS-1, 13% for PDMS-2) in the single-indentation tests.

With respect to change in resistance (Figure 2.12b), the materials split into two groups, $\Delta R/R_0$ being higher for the two elastomers and OC-2 (44-69%, Table 2.2) and lower for OC-1 and CC (31-32%). The sensitivity (slope) increased with displacement; under this loading condition, the strain experienced by the gauges rose nonlinearly with indentation. Once again, the magnitude of the resistance change did not follow the force (comparing Figure 2.12 a and b). However, it did not just follow the indentation, either: there was a dependence of sensitivity on padding type, yielding differences in $\Delta R/R_0$ at identical displacements. The deformations experienced by the gauges are further discussed in Sections 2.4.4.4 and 2.4.4.5. The resistance hysteresis was similar for all the padding materials, as were the recovery times t_r (Appendix D7).

The variation among the curves is also important. For both mechanical and electrical responses, variation among sensors was larger (typically around 2x) than between trials on the same sensor (Table 2.2). Since the sensors were placed at different locations over the foam surface, this suggests that the variation was introduced by non-uniformity of the padding material. (Recall that the gauge factors of the sensors were individually normalized, so variations in sensitivity among sensors are not responsible.) The force variation among sensors was largest for PDMS-2 (8%). More critical for sensing, the two elastomers also had a large variation in $\Delta R/R_0$ among

sensors (12% and 17%), compared with the most consistent padding, which was OC-1 (4%). Even between trials on the same sensor, the variation for PDMS-2 was large (at 12%, 3 or more times larger than the other four materials). These variations can be understood by referring to Figure 2.4. OC-1 consistently had the smallest variation in measurements, and it had regular cell sizes and no defects. The variations on OC-2 were larger, corresponding to the presence of bubble defects and irregular, anisotropic cells. CC was even less consistent, and although it had no defects, the cell structure was even more irregular. The two elastomers had many micro-scale defects and even cracks, accounting for the largest variations for these.

Table 2.2: Hysteresis, variations, stabilization cycle, and sensitivity in force and resistance measurements for the five padding materials. (Largest values are boldfaced, smallest are italicized.)

	Force					**Resistance**									
	Single-Indent			Cyclic		Single-Indent					Cyclic				
Padding	Force Hysteresis[1] (%)	Force Variation[5] (%) Between Trials	Force Variation[5] (%) Among Sensors	Force Hysteresis[3] (%)	Variation[5] (%) Among Sensors	Av. $\Delta R/R_0$ [7a] (%)	Sensitivity[8a] (%/mm)	Resistance Hysteresis[2] (%)	$\Delta R/R_0$ Variation[5] (%) Between Trials	$\Delta R/R_0$ Variation[5] (%) Among Sensors	Stabilization Cycle[6] (#)	Av. $\Delta R/R_0$ [7b] (%)	Sensitivity[8b] (%/mm)	Resistance Hysteresis[4] (%)	$\Delta R/R_0$ Variation[5] (%) Among Sensors
OC-1	33±2	1	4	40±3	4	31±1.3	4.6±0.2	*21±2*	*2*	*4*	**25±5**	*21±1*	*2.7*±0.1	21±2	*2*
OC-2	**37±1**	2	*3*	*22±2*	4	53±1.3	7.9±0.2	23±2	3	7	**25±1**	38±5	4.7±0.7	*19±2*	6
PDMS-1	19±3	2	5	50±5	*2*	44±4.0	6.5±0.6	**28±4**	4	**17**	*17±11*	30±16	3.7±2.0	30±7	**15**
PDMS-2	*13±1*	2	**8**	**47±9**	4	**69±8.8**	**10.4±1.3**	23±5	**12**	12	20±10	**59±26**	**7.4**±3.2	**34±3**	**15**
CC	24±1	2	5	34±6	3	*32±0.8*	*4.7*±0.1	25±2	4	11	*17±7*	23±6	2.9±0.8	27±6	9

[1,2,3,4] Hysteresis: At the same displacement points, the maximum difference of force (or resistance), represented by *x*, in the loading and unloading directions divided by the maximum force (resistance) value, i.e.

$$hysteresis = \frac{\max(|X_{load} - X_{unload}|)}{X_{max} - X_{min}}.$$

[1,2] The average hysteresis among the 9 tests (3 tests for each sensor, 3 sensors) on each material and its standard deviation.

[3,4] The average hysteresis among the 3 sensors (1 test for each sensor) on each material and its standard deviation.

[5] Variation between trials. The average and standard deviation among the three trials from one sensor was calculated at each point along the loading-unloading loop, resulting in two vector X_{loop} and S_{loop}. The average standard deviation is the average of the vector $\overline{S_{loop}}$.
The variation among sensors was calculated as the standard deviation of $\overline{X_{loop,sensor1}}$, $\overline{X_{loop,sensor2}}$, and $\overline{X_{loop,sensor3}}$.

[6] Stabilization Cycle: the cycle number at which the relative resistance change stayed within 1% of that of the 30th cycle.

[7] Av $\Delta R/R_0$: the normalized resistance change (%) averaged over 9 tests (single-indentation) or 3 tests (cyclic). This value was obtained at a fixed point: [a] at 6.7 mm indentation (since the maximum indentation changed, the same value was used for every padding) or [b] at 8 mm indentation (maximum displacement).

[8] Sensitivity: the normalized resistance change (%) divided by the displacement (units of mm). The average resistance data from 9 tests (for single-indentation test) or 3 tests (for cyclic tests) were used. This value does not take into account the nonlinearity of the curves, which show increasing sensitivity with displacement, but rather takes the slope at a fixed point: [a] at 6.7 mm indentation (the maximum reached by PDMS-1) or [b] at 8 mm indentation.

Foams, as expected, were more effective as energy-absorbing materials than elastomers, as shown by the greater hysteresis in the force, but the hysteresis in the sensing signal introduced by all five padding materials was nevertheless similar. The magnitude of the signal (strain) was nonlinear with indentation distance and depended on padding material. It is shown below that this is related to the local shape taken by the padding around the probe. In Section 2.4.1, we discussed variations among the sensors and how that can be handled by calibration, but in this section we show that non-uniformities in the padding microstructure introduce response variation that is difficult to compensate. Therefore, a padding with uniform microstructure is preferred.

Cyclic Loading

On multi-cycle tests (Figure 2.12c,d), the probe always loaded and retracted to the same pre-set position, so indentations for all the padding materials were exactly at the pre-set value, 8 mm. The maximum forces (Figure 2.12c) were essentially the same as in the single-cycle experiments. However, the force hysteresis on the PDMS elastomers was much larger in cyclic loading than in single-indent loading, more than doubling (going from 13% and 19% to 47% and 50%, Figure 2.12c, Table 2.2), indicating better energy absorption. It is well known that elastomers, such as rubbers, exhibit rate-dependent hysteresis due to thermodynamic effects, which are more pronounced in cyclic loading [160]. For OC-2, on the other hand, the hysteresis was nearly halved in cyclic loading (going from 37% to 22%). In foams, the energy absorbed from crushing the cells is not fully recovered by the subsequent cycle [161]. A padding material that performs well under one type of loading cannot therefore be assumed to be good for another.

For OC-1 the force hysteresis did not change substantially (33% to 40%). From the perspective of good, consistent padding ability, OC-1 is thus the best choice, and CC the next best.

Interestingly, the resistance hysteresis (approx. 24%) was not substantially different on the 5 materials for single-indentation loading, and under cyclic loading, the resistance hysteresis was again similar (although it increased for the stiffer elastomer, PDMS-2). These values would be expected to be related to spring-back (recovery time t_r), which was similar for these materials (Appendix D7).

The sensitivity under cyclic loading was smaller than in single-indentations (typically by 40%). Since the padding was continuously loaded, it never had time to recover to its original thickness, producing smaller changes. Importantly, the relative sensitivity of the padding materials remained the same (PDMS-2 > OC-2 > PDMS-1 > OC-1 ≈ CC) as in the single-indentation tests (Table 2.2).

Although the sensors on PDMS-2 had the highest sensitivity (7.4 %/mm), they also had the biggest variation (3.2 %/mm), as was the case for the single-cycle indentation. As discussed previously, the variability over the surface of the elastomers may be due to the micro-cracks observed in Figure 2.4, as well as incomplete mixing or tiny bubbles introduced during the PDMS preparation process. The lack of consistency from one part of the material to another is a serious drawback in this application.

To quantitatively evaluate at which cycle the sensors stabilized on different padding materials, the cycle number at which the relative resistance change was within 1% of that of the 30th cycle was determined (Table 2.2). There was considerable variation among the sensors on the same substrate, although all five stabilized after 17-25 cycles. With regards to consistency, the elastomers had the greatest variation in the stabilization cycle number among the three sensors.

These experiments showed that the performance of a padding used as cushioning can depend on whether it undergoes single-indentation loading or cyclic loading. In fact, both may need to be examined when choosing a material for a particular co-robotics application. However, because all the padding materials tested in this work had comparable recovery times, the signal hysteresis was also similar among them under cyclic loading. The previous finding for one of the foams that the sensitivity was lower during cyclic loading than single-cycle, was also true for the other padding materials.

None of the padding materials did well in every category. Choosing an appropriate padding therefore involves balancing energy absorption, sensor sensitivity, and variability in the context of a particular application. For example, the two open cell foams had good padding characteristics but were quite soft, and OC-1 had better consistency while OC-2 had higher sensitivity. The elastomers had several significant disadvantages: not only are they heavier and more expensive, but their responses to indentation varied too much from place to place.

2.4.4.4 Padding Placement

To gain insight into the mechanism by which the padding materials amplified the strain response in comparison with having only air under the membrane, the presence of the padding at various locations underneath the sensor was investigated. An 8 cm wide piece of foam OC-2 was cut into 5 rectangles oriented perpendicular to the axis of the sensing strip, and various pieces were selectively removed (**Figure 2.13**a). As in the previous sections, the probe was indented to a depth of approximately 8 mm and then retracted. The experiments were performed on three sensors, each in triplicate. The results from one sensor are shown in Figure 2.13b,c; the other sensors had the same behavior. Force and resistance measurements were taken during loading when the probe reached 6 mm.

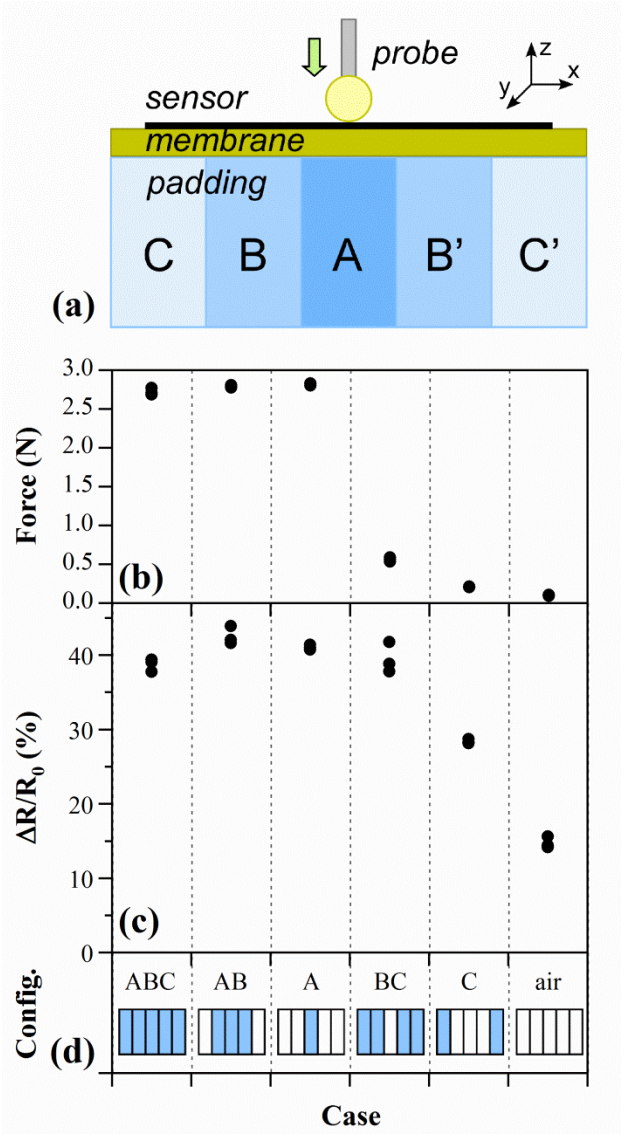

Figure 2.13: a) Padding under the membrane divided into 5 sections. b) Force and c) normalized change in resistance at a displacement of 6 mm upon symmetric removal of sections of foam OC-2 under the membrane. Points represent three measurements on one sensor.

Figure 2.13b shows that the force on the probe is due to the center (A) column of foam; when it is removed, the force falls almost to that of no foam (air). The amplification of the resistance change, on the other hand, is more complex. Like for the force, the presence of column A alone produces the amplification, with no change upon removal of B and C pieces, but removal of A

while leaving B,C in place gives the same result. Therefore, the shape of the membrane under the probe makes a difference. The shape of the membrane was therefore further examined, as outlined in the next section.

2.4.4.5 Deformed Membrane Shape

To further explore the signal amplification effect of the padding, the deformed membrane shape was measured with 3D-DIC (Section 2.3.3). The same membrane was also used, prior to that, to obtain the shape of indentation without padding (over air, as in Figure 2.5b).

Figure 2.14a shows the sample with the frozen-in indentation obtained over foam OC-2, and Figure 2.14b shows z-displacements along two perpendicular lines passing over the peaks in air and over OC-2. The deformation was more focused over the padding, wrapping around the probe. Over air, the probe pushed the center of the membrane downward, with nearly straight lines on either side. The change in length of the lines before and after indentation was obtained from the 3D DIC deformation measurements, giving an average stretch ratio of 0.0079 over air and 0.0245 over OC-2, a factor of 3 difference. This is comparable to the difference in resistance responses. The padding therefore magnifies the sensor signal through an increase in total strain.

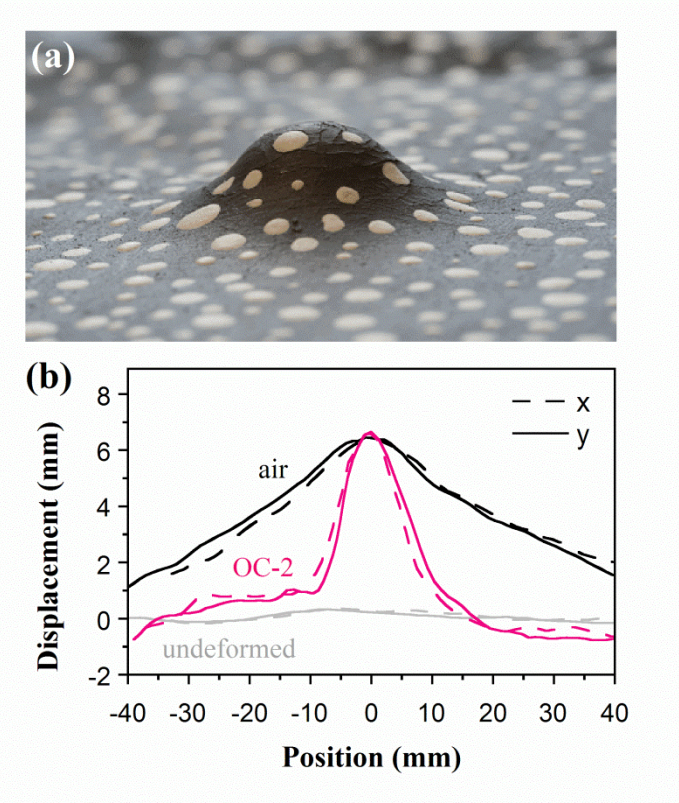

Figure 2.14: a) Frozen-in shape of membrane indented over padding. b) Displacements for no loading, loading with no underlying substrate (over air), and loading on OC-2. Two sets of data were extracted from two perpendicular lines (denoted as *x* and *y*) across the peak. To aid comparison, the positions of maximum displacement were shifted in the plot to position = 0 mm.

2.5 Discussion

An advantage of the piezoresistive sensors used in this work is the simplicity of application by spray coating. Since the fabrication was performed manually, there were variations among the sensors. However, because the relative change in resistance was fairly linear with strain, the GF could be treated as constant and variations due to fabrication inconsistencies could be handled by normalization after calibration.

For co-robotics applications, a large-area tactile sensing skin and any protective padding over a rigid robot frame will undergo *large deformations*. Inherent to stretchable coverings, such as rubber, and also to paddings, such as foam and silicon, is viscoelastic behavior. Under large deformation, the polymer chains of a viscoelastic slowly rotate and move past each other. Recovery to the original shape upon removing a stress is time-dependent, and varies with the material (chemical composition, degree of crosslinking, crystallinity). To support large deformations, the cell walls of a foam can buckle or crack, absorbing energy and providing protection. Recovery of a foam to the original shape is also time-dependent, varying not only with the material, but also with the foam structure. Therefore, the signals coming from the sensor reflect the time-varying behavior of the skin and the foam. However, the slower response will typically govern most of the system's behavior. Therefore, even if the sensor responds instantaneously, if it is placed over a padding, the signal will be time dependent.

Viscoelastic behavior has previously been reported on various polymer composite sensors. For example, the carbon black filled silicone sensor reported in [56] showed a recovery time on the order of 10 sec. Our sensing skin recovered in only 4 seconds (Figure 2.8b), while over padding signal recovery took approximately 8 seconds (Figure 2.8c). The capacitive sensor made of stretchable dielectric material reported in [25] showed an even longer recovery time, on the order of thousand seconds. Nevertheless, this behavior has not prohibited their use for strain sensing, and they have been applied in robotics[25,46].

For intermittent touch, the time-dependent effects do not significantly affect an estimate of the applied load. For continuous loading, the sensors can directly provide qualitative information on the magnitude of the load (large vs small, long vs short), which is likely to be sufficient for many co-robotics applications. Quantitative information can be obtained by performing modeling. The behavior of viscoelastic materials is often approximated by mechanical models consisting of series and parallel combinations of springs and dashpots (e.g. Generalized Maxwell or Maxwell-Weichert)(or resistors and capacitors in electrical analogs). Once the models have been obtained experimentally, the applied load can be inferred from the sensor signal [56].

2.6 Conclusions

A composite of latex and exfoliated graphite was spray-coated onto a latex membrane to form a sensing skin. The use of an elastomeric host for the nano-scale conductive particles resulted in stretchable piezoresistive thin film sensors, which are amenable to conformal wrapping of large areas, as required for co-robots. These sensors detected touch indirectly, via strain introduced by contact. The shape of the deformation was thus important, and the compressibility and localized deformation the foam resulted in amplification of the signal compared to a rigid substrate or a suspended configuration.

The use of padding under a sensing skin introduces significant time-dependent effects that need to be taken into account when interpreting the readings. The microstructure of the padding is also influential in this application: a uniform and defect-free microstucture ensures reproducible

responses from the skin. The padding should be chosen based on both the protection it imparts, through lower stiffness and energy absorption, as well as the response of the overlying sensor, including sensitivity, consistency, differences in single and multi-cycle loading, and resistance hysteresis.

Chapter 3. Characterization of a Compliant Multi-Layer System for Tactile Sensing with Enhanced Sensitivity and Range

Published in Smart Materials and Structures, 27 (6), 065005 (2018).

Ying Chen, Miao Yu, Hugh A Bruck, Elisabeth Smela

Co-author contributions: The idea of soft-hard multilayer padding architecture comes from the discussion of Prof. Miao Yu, Prof. Elisabeth Smela, and Ying Chen. Ying Chen fabricated the sensor system, performed the experiments, and processed the data. Prof. Yu, Prof. Elisabeth Smela, and Prof. Hugh A. Bruck contributed to the modeling. All authors contributed to writing the text and making the figures.

3.1 Abstract

To allow robots to interact with humans via touch, new sensing concepts are needed that can detect a wide range of potential interactions and cover the body of a robot. In this chapter, a skin-inspired multi-layer tactile sensing architecture is presented and characterized. The structure consists of stretchable piezoresistive strain-sensing layers over foam layers of different stiffness, allowing for both sufficient sensitivity and pressure range for human contacts. Strip-shaped sensors were used in this architecture to produce a deformation response proportional to pressure. The roles of the foam layers were elucidated by changing their stiffness and thickness,

allowing the development of a geometric model to account for indenter interactions with the structure. The advantage of this architecture over other approaches is the ability to easily tune performance by adjusting the stiffness or thickness of the foams to tailor the response for different applications. Since viscoelastic materials were used, the temporal effects were also investigated.

3.2 Introduction

The integration of tactile sensors is of interest for robots that may physically interact with humans. Requirements for a tactile skin can be drawn from pressures associated with human contact, as summarized in Table 3.1. The values cover a substantial range, from operating a touchscreen at 5 kPa to delivering a punch at 800 kPa. For an electronic skin, it is challenging to maintain sufficient sensitivity at the most commonly encountered low forces while still providing measurements at high forces.

Efforts on tactile sensing have focused on sensor development [130]. Flexible and stretchable sensors have been demonstrated that are highly sensitive, accurate, and linear [23,134,162-170]. For recent elastomeric resistive tactile sensors, force ranges are on the order of 2-5 N and gauge factors are 7-33, as summarized in [77]. Ultra-sensitive sensors typically have low upper limits (e.g. 5-10 kPa [170-172]), although some have reached the intermediate range in Table 3.1 (140 kPa [173], 80 N [74]). Soft, porous materials [59,171,172,174], including foams [26,172,173,175], provide a straightforward way to increase sensitivity. Mechanical compliance

enhances signals from both capacitive [172,173] and resistive sensors [59,175]. Recently, a sensing structure having soft and stiff foams side by side has been reported, with the soft foam providing higher sensitivity [35]. Another way to increase compliance is by adding spacers [31,176,177] or compressible microstructured surface features [178,179] such as pyramids [179,180], ridges [61,178], and micropillars [181].

Table 3.1: Forces involved in human contact and calculated pressures based on the assumed contact areas.

Contact Type	Force (N)	Pressure (kPa)*		Source
		Finger (2 cm^2)	Fist/Hand (20 cm^2)	
touching cell phone screen, typing on keyboard	1-2	5-10	–	[64,65]
grasping light rough object	5	25	2.5	[182]
grasping light slippery object	25	125	12.5	[182]
gripping (typical), per finger	30-60	150-300	–	[67]
poking, pressing	35-50	175-250	17.5-25	[68,69]
strong pinching	65-100	325-500	–	[68]
pulling, pushing (whole body)	100-500	–	50-250	[70,72]
gripping, whole hand	250-550	–	125-275	[68,70]
punching (novice boxer)	1600	–	800	[71]

* Forces were reported in the source references, and the corresponding pressures were calculated based on the given assumed sizes.

It has been difficult to prevent signal saturation at high pressure [73,183]. Simply increasing the stiffness of the material increases the range at the cost of sensitivity [183]. Making use of two distinct sensing mechanisms can increase the force range [184], but the signal may then be non-monotonic, changing sign as the dominant mechanism changes. Other approaches to extending the force range have included adding surface texture [73], altering the sensor geometry [185,186], and tailoring the sensing material, for example by adjusting the shape of embedded particles [187]. Thus, covering the entire potential force range in human-robot interactions remains a challenge.

To reduce the potential for harm during contact, robots can be covered with padding (**Figure 3.1**a). However, relatively little work has been done to examine the performance of sensors over soft substrates such as foams. Rigid tactile sensors are usually placed under the padding to mechanically protect them, but this comes at the cost in terms of sensitivity and spatial resolution [128,188], as well as the need to solve an inverse tactile transduction problem [15]. Embedding sensors in an elastic body has also been examined [189]. Stretchable sensors can be placed over the padding, but the signals are modulated by the compliant substrate (Figure 3.1b,c) [175]. For a strain sensor, this modulation is actually required, since the signal is due to the deformation of the padding under an applied load. There are advantages to placing an elastic sensor on a spongy surface, as described for a recently commercialized fingertip sensor: the larger deformations associated with both materials enables more energy to be absorbed during collisions and allows more time for the robot to alter its motion to prevent damage [190]. These combinations are also inexpensive to produce, have the ability to cover large and complex areas [191], have a lower rate of false positives, and lack sharp edges and "dead spots" [192,193].

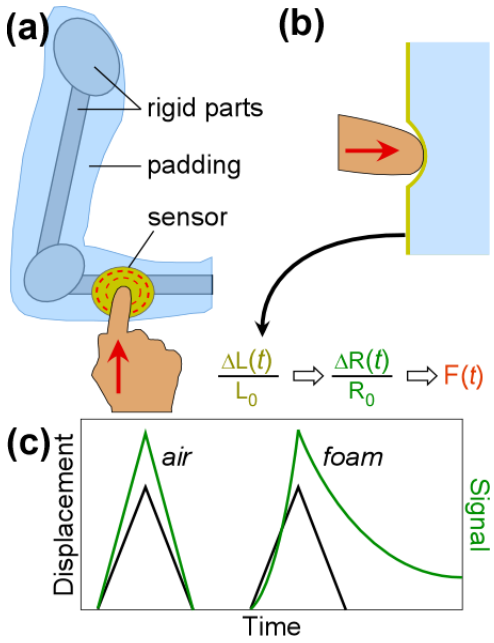

Figure 3.1: a) Schematic of a strain sensor on a padded robot arm experiencing a touch. b) The touch produces an indentation in the foam, leading to a strain in the sensor and thus a change in its resistance, from which the applied force can be inferred. c) A sensor with a linear response to displacement will have a different response on foam, reflecting the viscoelastic mechanical properties of the foam.

Mammalian skin is multi-layered, with several sorts of mechanoreceptors, overlapping and located at different depths; tactile sensors are located at the surface (SA-I Merkel cells) for high resolution and deeper within it (SA-II Ruffini corpuscles) for more distributed sensation [20,182,194-196]. Yet, there has been little research on artificial multi-layered tactile sensors. Human skin is also stretchable and viscoelastic, experiencing relaxation, creep, and hysteresis [197]. Since skin provides a desirable tactile response, its characteristics suggest an architecture for electronic skins to mimic.

In this work, we present and characterize a compliant multi-layer sensing structure with both enhanced sensitivity at low pressure and a sufficient range to cover most of the forces

encountered in Table 3.1. Our multi-layer architecture employs two strata, each consisting of a skin-covered foam (**Figure 3.2**d). We had previously reported on the performance of touch-sensing "skins" made by applying piezoresistive films onto rubber membranes, which were then placed over various padding layers [47,175]. Fabrication of the sensing skins is simple, consisting of spray-coating an aqueous mixture of exfoliated graphite (EG) and latex onto a latex membrane. We use EG/latex because it is paintable and has a reasonably high gauge factor, *but the focus of this work is the multi-layer architecture, for which other sensors could be used just as well*. The construction of multi-layer structures is also straightforward, and this layering approach is advantageous because it allows one to separately optimize the sensing skins and the foams for particular applications.

While many other tactile sensors have much higher sensitivity [168-171,173], the aim of this work was to investigate a new architecture that delivers a balanced combination of low pressure and high pressure performance in a simple and tailorable way. We have employed a piezoresistive film to demonstrate the feasibility of the sensing architecture, but we emphasize that the sensing architecture could in principle employ any stretchable "soft" sensor [168-170].

3.3 Experimental Methods

3.3.1 Sensing Skin Fabrication

Compliant piezoresistive strain sensing skins (Figure 3.2a) were made by blending conductive exfoliated graphite (EG) particles into a flexible matrix and coating the mixture onto a rubber membrane. The graphite (Asbury Graphite Mills, Inc.) exfoliation process [47], preparation of the composite [48], and spray-coating of the composite onto the latex membrane (ELE International, 0.3 mm thick) [175] have been reported previously. In summary, an EG dispersion was prepared from 10 g of EG prepared in a microwave oven, 1 L of water, 7.5 g of surfactant (Triton X-100, Sigma-Aldrich), and thirty drops of antifoaming agent (SE-15, Sigma-Aldrich). To the 12.2 g of the dispersion was added 0.936 g of natural rubber latex (RD-407, ArtMolds). The coating pattern, a rectangle of 11 cm x 19.2 cm was formed by spraying over a template formed of painter's tape (ScotchBlue). A total of 10 layers were applied, air-drying for one minute between layers. The coated membrane was scissor cut along the 10.4 cm length into 24 strip-shaped pieces, each 0.8 cm wide. The resistance of the sensing strips was 2.37±0.21 kΩ between the two edges. In this work the sensing layer was not covered by a protective coating, but we have shown that spraying an additional layer of mask-making latex over the surface can prevent damage due to rubbing [198].

The amount of EG in the sensing layer (25%) is above the percolation threshold, yet the layer remains stretchable. Under tensile strain, the distance between nanoparticles increases in the stretch direction, breaking some of the percolation pathways and resulting in an increase in

resistance. The gauge factor (GF), defined as the relative change in resistance per unit strain, was 8 for these skins (Appendix E1) due to the inherent resistivity changes caused by disrupting percolation, compared with GF = 2 obtained from geometric effects. The skin's behavior, alone and on foam, was characterized in [175]. (The skins are compared with two commercially available compliant materials, carbon filled silicone and conductive fabric, in Appendix E2).

Electrical connections to the composite sensing layer were formed with carbon fiber braids (The Composites Store, braided sleeves, 0.1'' diameter). Carbon fibers have a smaller diameter and are more flexible than fine multi-strand metal wire, and they have a low contact resistance to the composite, resulting in superior adhesion and good electrical contact. The braid was cut to the required length and two bundles of carbon fibers were pulled from it. A 1 cm length at the end of the bundle was spread out and laid over the strip. Drops of the EG suspension were applied by pipette onto the overlapping area and air dried. The carbon fibers were completely embedded in the latex/EG composite after applying 8 drops, forming a robust connection (Appendix E3). The carbon fiber was in turn connected to multi-strand Cu wire (Alpha Wire Corp., 26 AWG, PVC insulation) with heat shrink tubing (NTE Electronics, Inc. 1/16'', HS-ASST-10), applying hot air (Aoyue, 852A++ repairing system) for 1 minute. The total resistance of the strip, including the connections, was 2.43±0.22 kΩ. The resistance of the connections was small compared to that of the sensing layer (3%).

3.3.2 Foams

Two foam combinations were used in this work. In foam pair A (Figure 3.2b), the top foam was an open-cell poly(urethane-ether) (thickness d_1 = 12.5 mm, "standard medium foam", foamforyou.com, Foam N' More and Upholstery Inc., Clawson, MI), and the bottom one was an ethylene-vinyl acetate (EVA) foam (d_2 = 12.5 mm, BalanceFrom BFPM-01GY, puzzle exercise mat). In foam pair B, the top foam was an open-cell poly(urethane-ether) ("plush/soft foam", foamforyou.com, Foam N' More and Upholstery Inc., Clawson, MI), and the bottom one was a closed-cell nitrile rubber. In the *soft-hard* configuration with foam pair B, the thickness of the soft foam was d_1 = 12 mm and the thickness of the hard foam was d_2 = 19 mm. In the s*oft-soft* configuration, the soft foam of pair B was used with d_1 = 12 mm, d_2 = 25 mm. In the *hard-hard* configuration, the hard foam of pair B was used with d_1 = 9 mm, d_2 = 19 mm.

Foam stiffness was characterized by indentation load deflection (ILD), obtained by measuring the load required to reduce the thickness of a 1 cm x 1 cm x 1 cm sample by 25%. The load was measured with the force transducer (Bose 3330 Series II), and ILD numbers were calculated as the ratio of loading to area (N/cm^2). For foam pair A, the ILD of the top layer was 0.4 N/cm^2, and that of the bottom layer was 6.3 N/cm^2, meaning that the bottom layer was nearly 15 times stiffer. For foam pair B, the ILD of the soft foam was 0.14 N/cm^2, and that of the hard foam was 13.34 N/cm^2, meaning that the hard foam was nearly 100 times stiffer.

3.3.3 Indentation Tests

The sensing strips were attached to the foams using adhesive (Krylon, Repositionable Spray Adhesive 7020) to keep them from moving during testing (Figure 3.2c). The skin+foam strata were aligned so that the 8 mm wide strips were positioned directly over each other. The two strata were held together by clamping at the four corners to a rigid support. To prevent the clamp from penetrating into the soft foam, rigid plates were placed between the soft foam and the clamps.

Out-of-plane indentation tests were performed with a force transducer (Bose 3330 Series II) outfitted with a polytetrafluoroethylene (PTFE) probe with either a circular flat bottom (dia. = 1, 2, and 4 cm) or a spherical shape (dia. = 0.95 cm). The force and indentation were obtained from the output of the transducer (2048 pts/30 sec scan time). Pressure was calculated from the force and the probe cross-sectional area.

Sensor resistance was measured with a voltage divider circuit, with the sensor connected in series with a known, fixed resistor (5 kΩ). A voltage source (Hewlett-Packard 6236B triple output power supply) was used to apply a constant 5 V, and the voltage over the sensor was measured using a data acquisition (DAQ) system (NI USB-6009, 14 bit, at 5 kHz sampling rate). The two sets of measurements were synchronized by aligning the peaks of the signals, as previously described [175]. The resistance data were smoothed by averaging 20-point intervals.

Unless specified otherwise, the flat-bottom probe with a diameter of 1 cm was used in the indentation tests. Four cycles were performed sequentially at a constant speed of 4.5 mm/sec, separated by 5 minute intervals.

3.3.4 Tensile Tests

The same force transducer (Bose 3330 Series II) was used for tensile tests, and the same voltage divider circuit was used for recording the sensor signal. The sensing strips were held vertically, with one end being attached to the moving part of the transducer and the other end fixed (for details, see Appendix E1). Four scans were performed on each sensing strip, and results from the 2^{nd} to 4^{th} scans are shown in section 3.4.3. All the tests were repeated on another set of sensing strips; similar behavior was obtained.

3.4 Results and Discussion

3.4.1 Response Characterization

3.4.1.1 Response to Indentation

As illustrated in Figure 3.2d, the multi-layer sensing system consisted of two layers of foam (Figure 3.2b) having different stiffness, each surmounted by a strip-shaped sensing skin (Figure 3.2a). Basic indentation tests were performed to obtain the mechanical and electrical responses. Figure 3.2g shows the pressure and force as a function of probe depth. (Unloading curves are

shown in Appendix E4) Up to an indentation of 10 mm, nearly up to the d_1 = 12.5 mm thickness of the upper soft foam layer (foam1), the pressure increased linearly, to 38 kPa (3 N). The slope then increased as the probe began to deform the lower hard foam layer (foam2). The maximum indentation was 20 mm, which is 80% of the 25 mm original total foam thickness and more than half-way into the d_2 = 12.5 mm thickness of the lower hard foam. All four scans were similar, as evident from the overlapping curves. Thus, the membranes and foams did not exhibit mechanical first-cycle memory effects. The noise (Figure 3.2g inset) is due to the limited force resolution when the widest range setting is used for the force transducer ($\pm$ 3000 N) (With a 10 bit digitization of the signal, the force resolution was limited to approximately 3 N.)

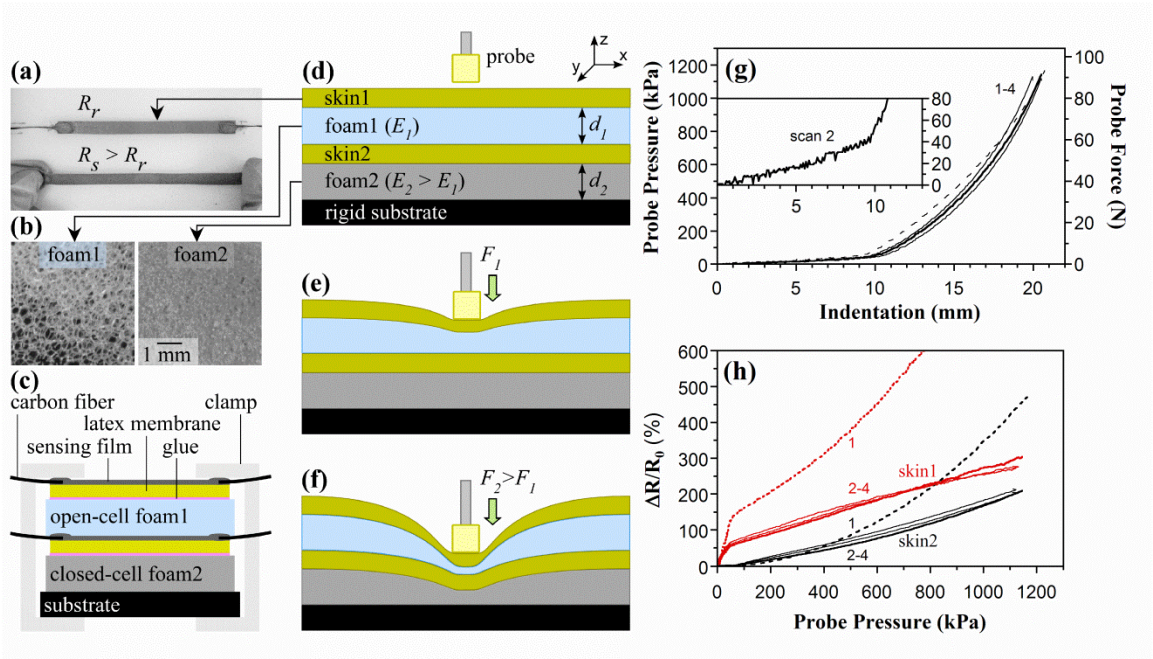

Figure 3.2: The multi-layer sensing system consists of a stack of skin+foam pairs ("strata"), with the foam stiffness (elastic modulus, *E*) increasing with depth. a) Overhead photos of a sensing strip attached to a layer of soft foam and a second sensing strip being manually stretched. The stretched resistance R_s is greater than the relaxed resistance R_r. b) Close-up photos of the soft open-cell foam1 and the harder closed-cell foam2. c) Schematic of the multi-layer system. d) A stack of two strata was used in this work. e) When light force is applied, the upper foam deforms. f) When a larger force is applied, the soft upper foam is completely crushed and the bottom layer deforms, but it is able to sustain a larger force before being crushed. g,h) Performance of the 2-strata soft-hard system (foam pair A) under increasing indentation. The first scans are represented by dashed lines and the 2nd to 4th scans by solid lines; the line for scan 2 is heavier. Scan numbers are indicated. g) Pressure (contact area 0.8 cm^2) as a function of indentation. Inset: close-up showing pressures in the range of 0-80 kPa for the 2nd scan. h) Normalized change in resistance of the two sensing skins vs. pressure. The signal from the upper skin1, over the soft foam, is shown in red, and the signal from the lower skin2, over the hard foam, is in black.

The relative change in resistance of the two sensing skins is shown in Figure 3.2h as a function of pressure. The resistance increases because electrical conduction is by percolation in the EG nanoparticle network, and some percolation paths are disrupted when the particles separate under strain. This is in contrast with materials whose resistance decreases with strain, such as

conductive fabrics, in which the fibers in the weave make better electrical contact under stretching. However, it is important to note that conductive fabrics and other sensors can still be used in place of the EG sensing material, since the architectural principle does not depend upon whether the gauge factor of the sensing material is positive or negative.

The signal was larger during the first scan (due to memory effects, section 3.4.3.1), and then it was similar in the remaining three scans. (See Appendix E4 for a discussion of first cycle effects.) This behavior can be attributed to break-in during the first cycle in viscoelastic materials such as foams and elastomers, which is known as the Mullins effect [199] in filled rubbers. For skin1 at low pressure (up to 38 kPa, 0-10 mm), the sensitivity was high and substantially linear (initial slope = 1.3 %/kPa or 17.6 %/N in the 2^{nd} scan), and the relative change in resistance was an easily measurable 60%. The sensitivity then gradually decreased, and above a turnover region it became linear again (above 250 kPa, slope = 0.2 %/kPa or 2.9 %/N for scan 2). At 1125 kPa, the change in resistance was over 250%. The utility of a monotonic, bilinear relationship should be emphasized.

For skin2, which was sandwiched between the foam layers, the output was almost zero at low pressure, since it remained unstrained while only the upper foam experienced compression. At the turnover point for skin1, corresponding to the corner in the force-indentation curve, the resistance of skin2 began to increase as the foam under it was indented. Its slope was similar to that of skin1, since both signals followed the deformation of foam 2.

The piezoresistive latex/EG sensors respond to strain [175], so the resistance of the skins reflects the surface deformations of the foams. The higher sensitivity at low forces is due to deeply indenting the soft foam1 without much pressure (Figure 3.2b). The signal from skin1 does not saturate after foam1 is completely crushed because the membrane continues to stretch as indentation of foam2 begins (Figure 3.2c). Because foam2 is stiffer, there is less strain per unit force, and thus a relatively smaller change in resistance. The similar slopes for the signals from the two skins indicates that they undergo similar net changes in strain once foam2 starts to collapse.

Comparing sensitivity with other sensing systems is challenging because of the variety of metrics reported (V, N, %, Ω/Pa, A/Pa, %/Pa [130]). A conducting polymer array showed 0.1%/kPa up to 30 kPa [200] and a conductive network of carbon nanotubes on PDMS reported 360 %/kPa to 0.1 N [201]. The difficulty of balancing sensitivity and range is demonstrated by these examples, as is the utility of our approach for achieving both (1.9%/kPa up to 31 kPa and 0.055%/kPa to 1.2 MPa). The sensitivity in our system could be further increased simply by using an even softer top foam.

The displacement resolution of the measurement setup was derived from the noise level of the signal. The resolution is commonly determined by using the root mean square (RMS) noise of the signal [202]. We obtained the RMS noise by taking the standard deviation of $\Delta R/R_0$ over a 5 second period with no indentation, and it was 0.0055. From the $\Delta R/R_0$ versus pressure and pressure versus indentation curves (Figure 3.2g, h), the displacement resolution in terms of variation in indentation was determined as 0.1 mm (i.e., the indentation level corresponds to the

$\Delta R/R_0$ noise level of 0.0055). This is not a limit of the sensing system, but of the measurement system.

3.4.1.2 Effect of Contact Area

The contact area for human-robot interactions may be as small as a fingertip or as large as a hand. The effect of contact area on the sensing signal is thus examined here. In this system, strip-shaped sensors were used whose width w = 0.8 cm was less than the probe diameter d. We hypothesized that the piezoresistive signal would be independent of probe area if, for $d > w$, the strips are only strained at the probe edges, not underneath the probe (see section 3.4.2.3).

Three flat-bottom probes were used with diameters of 1, 2, and 4 cm (areas of 0.8, 3.1, and 12.6 cm^2, respectively). **Figure 3.3** shows results from the second to the fourth cycles. As expected, while larger probes generated larger forces at the same indentation (Figure 3.3a), they produced the same pressures (Figure 3.3b). Figure 3.3c shows the normalized change in resistance of skin1 and skin2 as a function of force; $\Delta R/R_0$ for both were greater when the contact area was larger. When plotted as a function of pressure, the electrical responses overlapped (Figure 3.3d) for all three probes. These results indicate that the architecture can be used effectively as either an indentation sensor or a pressure sensor with strip-shaped sensors.

It may seem surprising that a strain sensor can be used as a pressure sensor. This is a consequence of $w < d$, making the sensing system quasi-one dimensional (1D) so that the strip is

always deformed by just the two edges of the probe (see sections 3.4.2.2 and 3.4.2.3), and also of the sensor's stretchability.

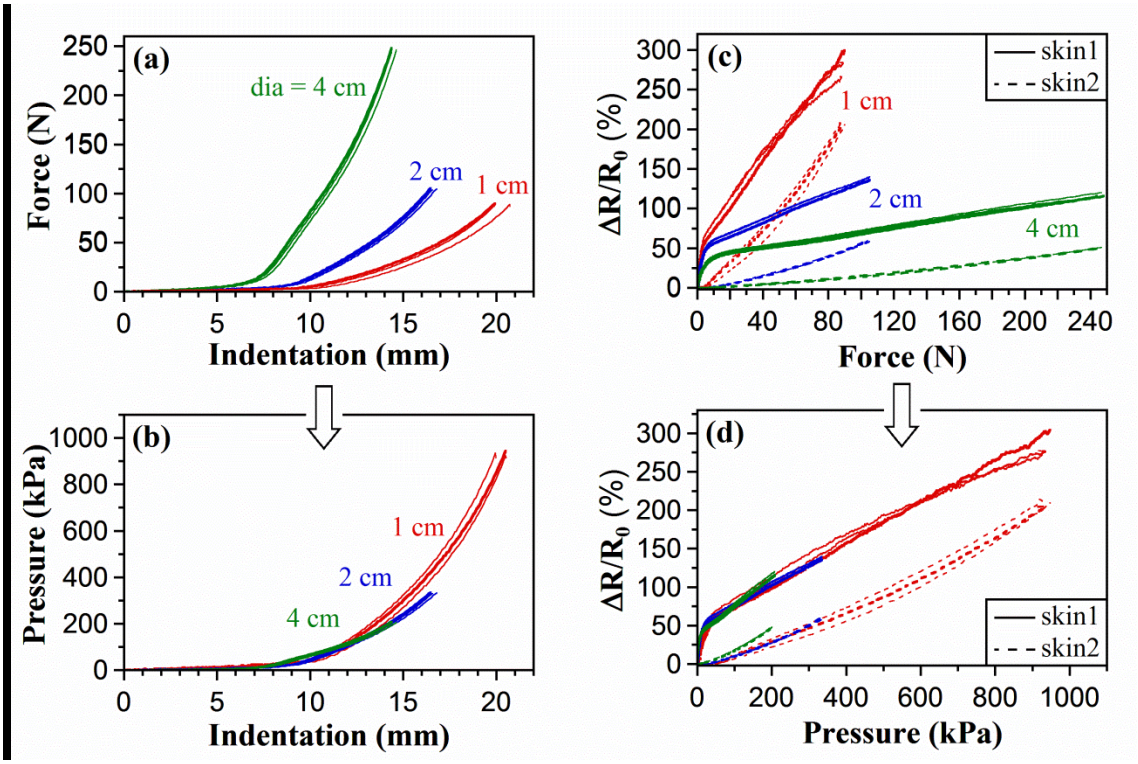

Figure 3.3: Effect of contact area. a) Force vs. indentation replotted as b) pressure vs. indentation for three probe sizes. c) Corresponding normalized resistance change as a function of c) force and d) pressure for the two sensing skins. (scans 2-4, foam pair A)

3.4.2 Understanding the Sensor Response

In this section the reasons for the behaviors observed above are examined. First, the postulated roles of the foams are confirmed. Next, the deformed shapes of the membranes and foams are examined. Finally, the foam behaviors are modeled.

3.4.2.1 Comparison with Other Configurations

The question may be raised, is it necessary to have foams of different stiffness, or can two strata with the same foam stiffness achieve a similar result? In order to determine the benefit of using a combination of foam stiffnesses (soft-hard), three other foam combinations were examined (**Figure 3.4**a): two layers of the soft open-cell foam (*soft-soft*, d_1= 12.5 mm, d_2 = 12.5 mm), two layers of the stiff closed-cell foam (*hard-hard*, d_1 = 12.5 mm, d_2 = 12.5 mm), and a thin layer of soft foam with no second foam (*soft-rigid*, d_1 = 12.5 mm).

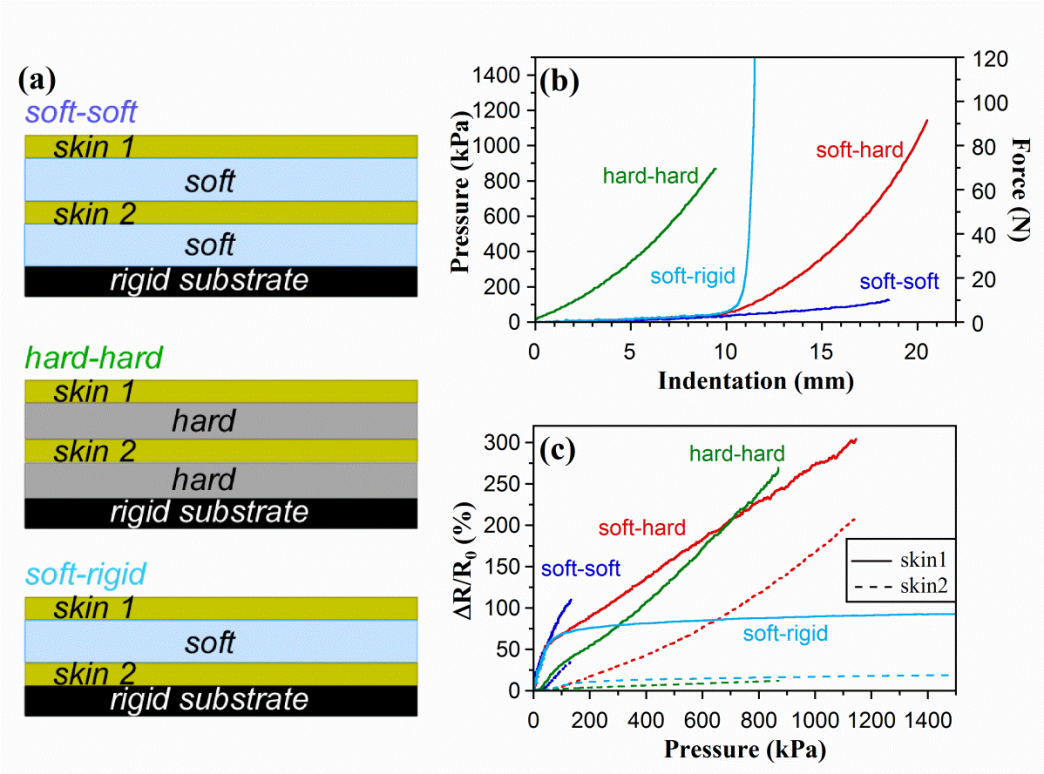

Figure 3.4: Comparison of the performance of four configurations. a) Schematic representations of the three new configurations. b) Pressure as a function of indentation. c) Relative change in resistance as a function of pressure from the upper (solid line) and lower (dashed line) skins.

The pressure vs. indentation curve for the soft-rigid system (Figure 3.4b, light blue) followed the one for the soft-hard system (red) to an indentation of almost 10 mm (the thickness of the foam), but then shot up rapidly as the probe made contact with the rigid substrate. The signal from skin1 over soft-rigid, shown in Figure 3.4c, had a high initial slope, like those of the soft-soft and soft-hard systems, but it then saturated once the thin layer of foam was crushed, for a maximum $\Delta R/R_0$ of 90%. As expected, this system demonstrated relatively high sensitivity but low range. The response of skin2 was small across the entire range (< 20%) since it rested directly on the rigid substrate and experienced negligible strain.

The pressure-indentation curve for the soft-soft system (dark blue) also followed the one for the soft-hard system to an indentation of almost 10 mm, but then instead of increasing, the pressure remained low. The signal also initially followed that of the soft-hard system, but the higher sensitivity range was extended. Skin2 began responding when the second foam layer began to deform (above 37 kPa).

The force-indentation curve for the hard-hard system (green) was similar to that of the soft-hard system, but shifted leftward toward the origin because the indenter touched the harder foam surface immediately. The initial slope of the skin1 signal was, as expected, substantially lower than that of soft-hard due to the much smaller strain under the same force. The signal from skin2 was smaller than from skin 1, and also smaller than the signal from skin2 in the soft-hard system, since the high stiffness of the overlying foam in the hard-hard system induced a smaller strain in this sandwiched skin.

Comparing the various curves, the behavior of the soft-hard system combined the sensitivity of the soft foam and the wide range of the hard one. The indentation tests were repeated on duplicate sensing skins (Appendix E7). The curve shapes and the distinct behaviors were repeated, although the amplitudes varied, mainly due to the different loading histories of the skins, whose viscoelastic behavior has been widely recognized [39,56] (see section 3.4.3.1).

These experiments confirm that a soft-hard combination is required and that the force range for each layer is determined by its thickness. By adjusting the absolute and relative thicknesses and stiffnesses of the foam layers, one can adjust the slopes and corner of the bilinear curve. A combination of foams is therefore a good approach to prevent the padding thickness on a robot from becoming unwieldy. Although the concept for enhancing the performance of the sensing system has been demonstrated using two layers, it is possible to use additional layers or even employ a continuous stiffness gradient.

3.4.2.2 Deformed Shape from Sensor-Indenter Interaction

Section 3.4.1.2 showed that the sensor response was independent of probe area, suggesting that at a given indentation the net strain of the sensing skin was the same, since the GF is almost constant with strain. In order to validate this hypothesis, the deformations of latex membranes over a soft foam (from pair A) under an applied indentation were "frozen" using epoxy. Since epoxy soaks into foam, a square latex membrane was used instead of strips; we assumed the deformation, although somewhat different, would nevertheless provide insight.

Membranes deformed around flat-bottomed probes of 1 and 4 cm diameter are shown in **Figure 3.5**. (For further discussion of the deformation, see Appendix E6) Since the membrane area in contact with the probe bottom remains flat, the curved edges were compared by overlaying the images. The shapes were found to be equivalent (Figure 3.5c). This accounts for the piezoresistive signals (Figure 3.3d) being the same.

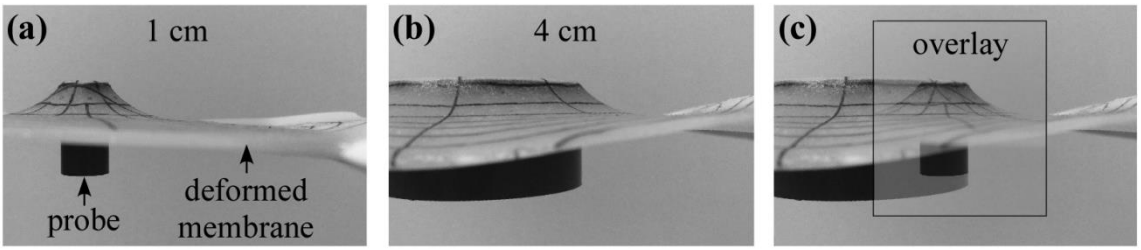

Figure 3.5: Deformed shape using an indenter with a diameter of a) 1 cm and b) 4 cm. c) Overlay of the two images.

3.4.2.3 Modeling

In order to design the sensing architecture for obtaining a desired performance, it is necessary to understand the signal vs. pressure result in Figure 3.3d and the responses of the different foam systems in Figure 3.4. Since the resulting strain in the skin depends on how the interaction between the indenter and the foam affects the shape of the foam surface, we begin by modeling that shape.

Determination of Surface Strain

The shapes of the deformed foams were determined using photographs taken at a series of indentations (**Figure 3.6**). For this work, foam combination B was used with the spherical probe (0.95 cm dia.).

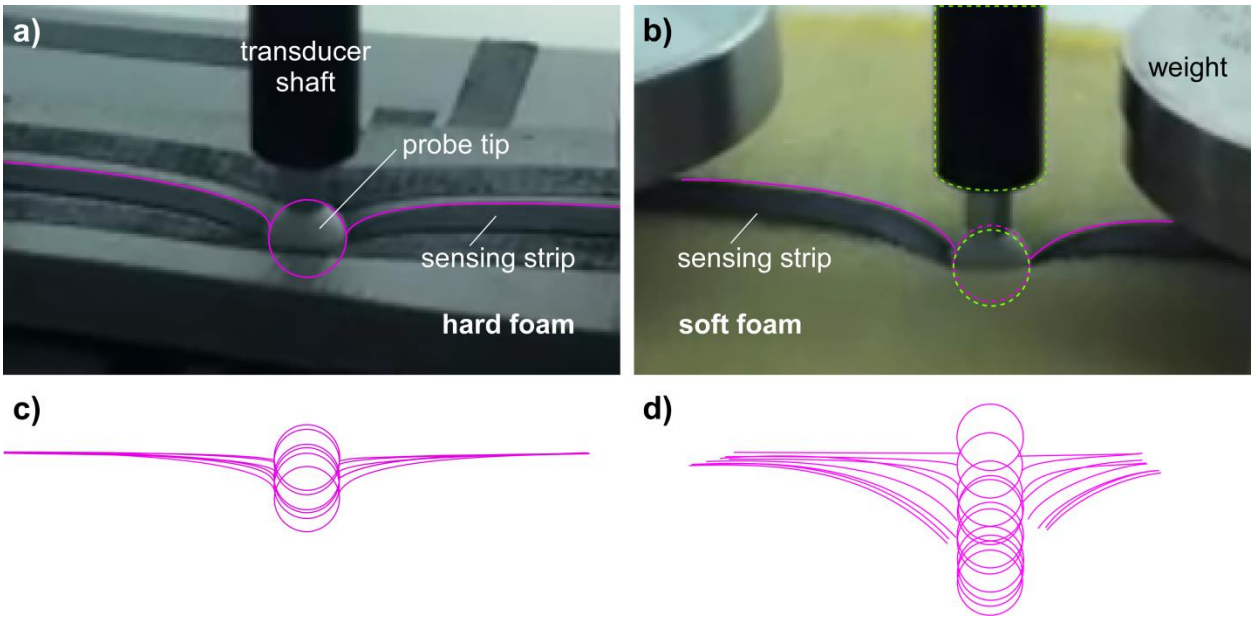

Figure 3.6: Photographs were taken at various stages during indentation on the four foam systems; two are shown here: a) hard-hard and b) soft-soft. The deformed strip shapes were fit visually (pink lines). For indentations so deep that the probe tip disappeared from view, the known position of the probe tip relative to the probe shaft (green) was used. c, d) Overlaid positions of the probe tip and surface contours from different indentations. The deeper surface contours in (d) are incomplete because the strip disappeared from the view of the camera.

Once the surface was traced, these curves were fit to a function. For elastic bodies under line (knife-edge) loading, derived for bodies that are large compared with the contact area, the theoretical decrease in stress intensity with distance x from the knife-edge goes as $1/x$ [203]. We therefore used

$$f(x) = A\frac{x_0}{x + x_0} \tag{3.1}$$

where the outer edge of the probe is at x_0, A is the indentation at x_0, and $f(x)$ is the indentation of the foam at a distance x distal from x_0. At the edge, $x = 0$ and $f(x) = A$. Far from the edge, $f(x) = 0$. Using a value of $x_0 = 0.4$ cm provided the best fit to the experimental curve shape for both foams: their surface shapes were similar at the same indentation. It also fit the shape of the membranes shown in Figure 3.5, confirming that the foam deformation determines the sensor strain.

Hard Foam Surface Strain Model

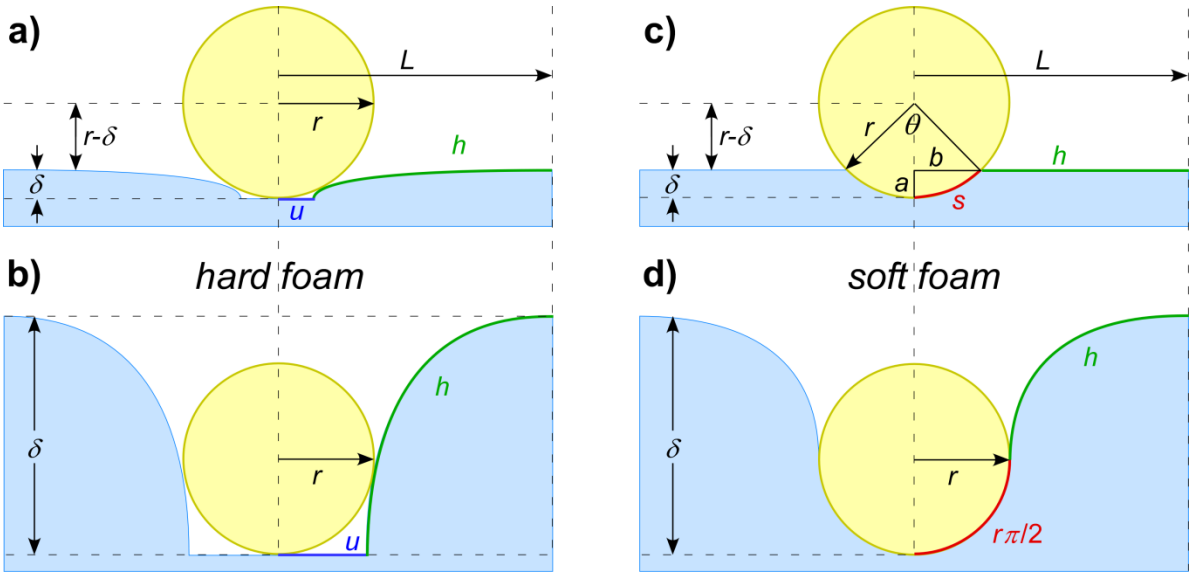

Figure 3.7: Surface strain model for hard (a, b) and soft (c, d) foams. Illustration of hard foam cases when a) δ < r and b) δ > r. c) For soft foam, when the indentation δ is less than the probe radius *r*, the surface deforms by wrapping around the spherical indenter. d) When $\delta > r$, the surface beyond the indenter is also pulled downward.

The second step in the modeling was to obtain the strain associated with the shape change. For simplicity we assumed that there was no strain under the probe tip itself, as illustrated in **Figure**

3.7a, b, i.e. the probe merely pushes the surface under it downward. The deformation is symmetric around the probe, so only a half-space was considered. The total strain ε at an indentation $\delta = 1$ was determined by summing the strains along the curve of equation 0, resulting in an increase in arc length $\Delta h = 0.3$. The strain occurred entirely within a distance of $x = 3$ cm from the edge of the probe. A linear relationship was postulated between strain ε and indentation δ (**Figure 3.8**a):

$$\frac{\Delta L}{L_0} \equiv \varepsilon = \frac{0.3}{L_0}\delta \tag{3.2}$$

where L_0 is the original sensor length (5 cm measured from the center of the probe).

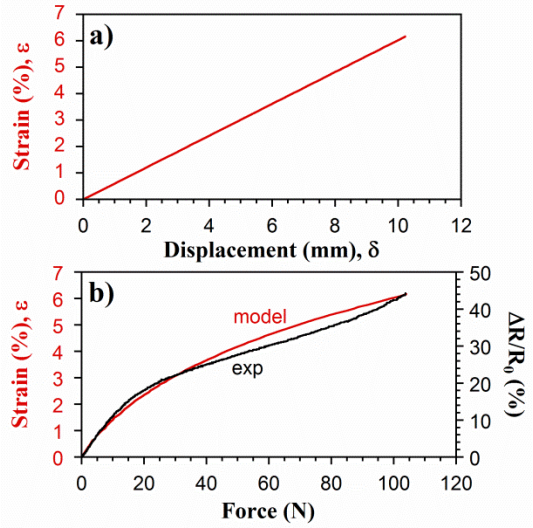

Figure 3.8: Model strain (red) for the hard foam as a function of a) displacement (indentation) and b) force, compared with the experimentally observed change in resistance (black).

The third step was to relate the strain to the force. The measured displacement-force relationship for the hard foam was employed to display the model strain as a function of force. The model is compared to the experimental signal in Figure 3.8b, where the maximum values were matched

across the two axes. Prior work [175] on the sensing skins had shown that $\Delta R/R_0$ is proportional to uniaxial strain, as expected for a constant gauge factor. For these strips GF = 8 (Appendix E1), so a normalized resistance change of 44 corresponds to a strain of 5.5%, close to the 6% predicted by the model. The agreement of the model and experimental curve shapes was excellent given the simplicity of the model and the fact that it had one fitting parameter, x_0.

Soft Foam Surface Strain Model

Applying the hard foam model to the soft foam results, the fit was not as good, as shown by the red curves ("1/x") in **Figure 3.9**: the experimental data ("exp") had a steeper initial rise and a more defined corner. (The noise in the experimental curves was due to the limited force resolution when using a large force range on the transducer.)

A revised model was therefore explored, based on the observation (Figure 3.6d) that for indentations of the probe up to half the probe radius, there was little downward motion of the surrounding surface. It appeared that the foam was conformal around the tip and only with greater indentations showed the $1/x$ behavior. The soft foam model is illustrated in Figure 3.7c,d. For this case, a separate treatment is required for indentations less than and greater than the radius.

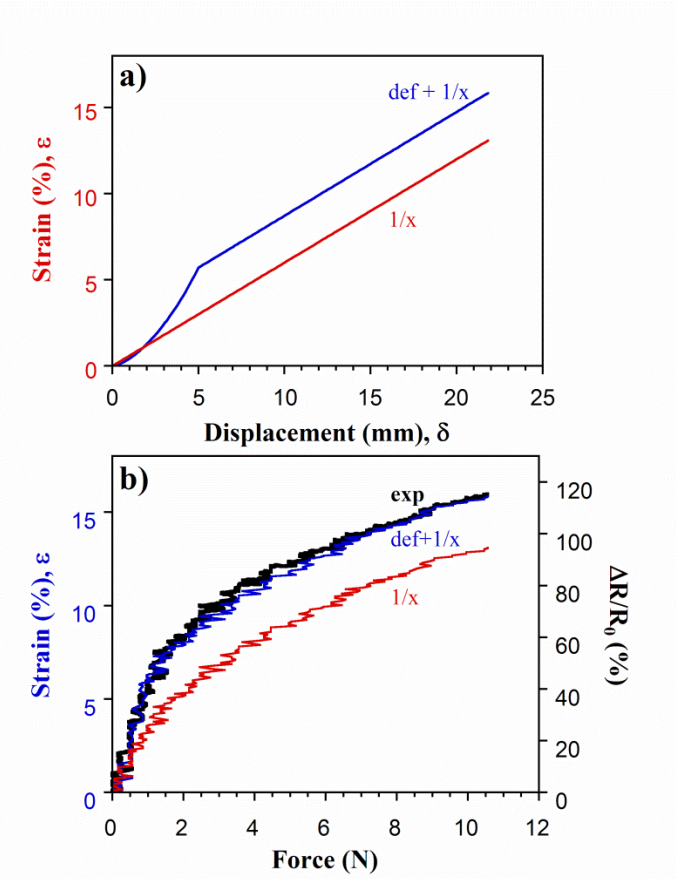

Figure 3.9: Model strains (red and blue) for the soft foam as a function of a) displacement and b) force, compared with the experimentally observed change in resistance (black). The red line represents the simple 1/*x* model, the blue line a model that takes into account deformation around the probe tip.

Indentation less than the probe radius, $\delta < r$

When the displacement δ is small the deformation of the soft foam can be treated as occurring solely around the indenter, which has radius *r* (Figure 3.7c). By symmetry we considered the half plane. The length along the surface is approximated by the sum of two pieces: a linear segment *h* between the probe and the edge of the strip at *L*, and an arc *s* around the indenter. The strain ε is then given by

$$\varepsilon = \frac{\Delta L}{L} = \frac{s + h - L}{L} \qquad (3.3)$$

where L is the length of the sensor. When the displacement is less than the probe radius, using the definition of the arc length,

$$s = r\theta / 2 \tag{3. 4}$$

Next find θ by relating it to the height of s and the radius r,

$$\begin{aligned} r - a &= r\cos\left(\theta / 2\right) \\ \theta &= 2\cos^{-1}\left(\frac{r-a}{r}\right) \end{aligned} \tag{3. 5}$$

where $a = \delta$. Substituting,

$$s = r\cos^{-1}\left(\frac{r-\delta}{r}\right) \tag{3. 6}$$

Next find h.

$$h = L - b \tag{3. 7}$$

Again use geometry to find b:

$$\begin{aligned} r^2 &= \left(r-a\right)^2 + b^2 \\ b &= \sqrt{r^2 - \left(r-\delta\right)^2} \end{aligned} \tag{3. 8}$$

Then, substituting and simplifying,

$$h = L - \sqrt{2r\delta - \delta^2} \tag{3. 9}$$

The strain is then given by:

$$\begin{aligned} \varepsilon = \frac{s+h-L}{L} &= \frac{r\cos^{-1}\left(\frac{r-\delta}{r}\right) + L - \sqrt{2r\delta-\delta^2} - L}{L} \\ &= \frac{r\cos^{-1}\left(\frac{r-\delta}{r}\right) - \sqrt{2r\delta-\delta^2}}{L} \end{aligned} \tag{3. 10}$$

Indentation greater than probe radius, $\delta > r$

The foam wraps around the indenter for half the radius and is pushed downward the remaining fraction, $\delta - r$, as shown in Figure 3.7d. The segment *s* has a constant length of $r\pi/2$. The shape of the segment *h* is again given by equation 0. The strain is then given by:

$$\varepsilon = \frac{s+h-L}{L} = \frac{r\left(\pi/2\right)+L-r+0.3\left(\delta-r\right)-L}{L} = \frac{0.27r+0.3\delta}{L} \tag{3. 11}$$

This prediction of this model is shown by the blue lines ("def+1/x") in Figure 3.9, and it provided a good shape fit. The soft and hard foam models are identical above 5 mm, but the soft-soft foam undergoes greater strain at small indentations.

Two-Layer Modeling

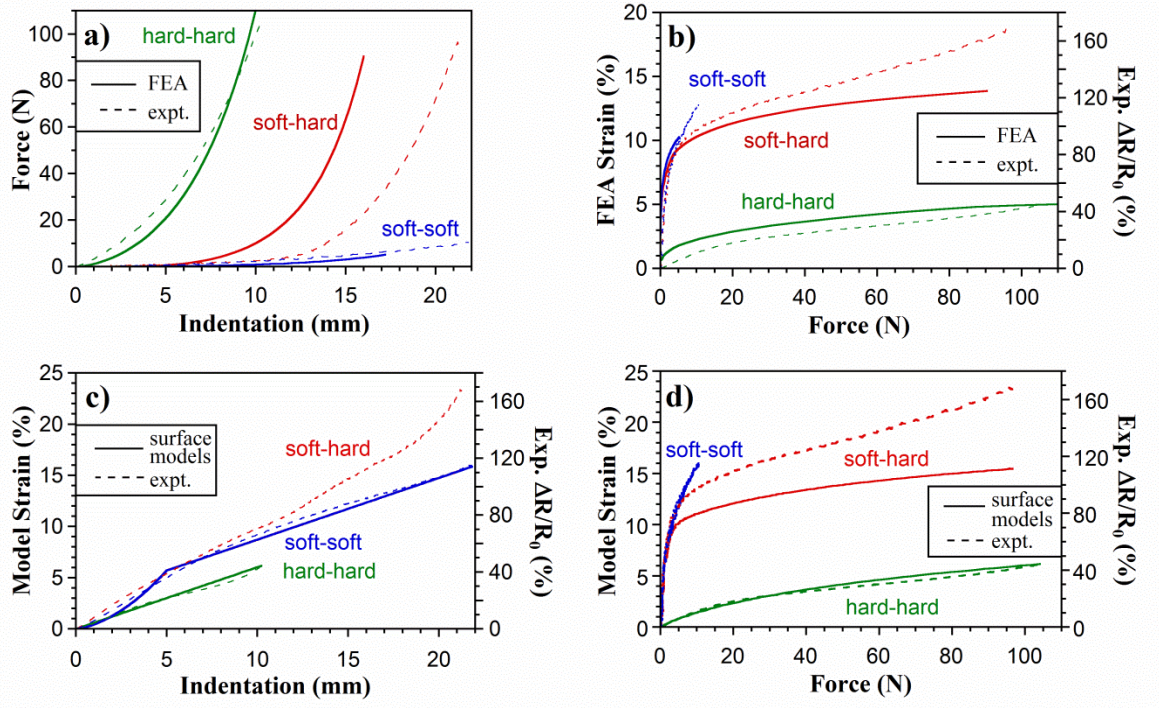

Figure 3.10: a) Force vs. displacement curves from FEA simulations of three configurations (solid lines): soft-hard, hard-hard, and soft-soft compared with the experimental results (dashed lines). b) Strain vs. force FEA results. c) Strain vs. indentation from 1/x surface shape models (solid lines) compared with the experimental results (dashed lines). d) Strain vs. force using 1/x model and experimental force vs. indentation curves.

Analytical Model

The strain for the soft-hard model is the sum of the strains in the soft and hard foams. This is equal to the strain in the soft foam when the indentation is less than the soft foam thickness, and the maximum strain in the soft foam plus the strain in the hard foam when the indentation is greater. The predicted surface strains for the three foam configurations are shown as a function of indentation in **Figure 3.10**a, together with the experimental signals. Since the strain-

indentation curves were the same for the soft and hard foams for $\delta > r$, the soft-hard model was identical to the soft-soft model, as shown by the overlayed solid red and blue curves in Figure 3.10a. However, this model did not account for the behavior. The soft-hard signal deviated from model above 12 mm (the location of the interface), showing an unexpected increase in sensitivity. The soft-hard system behaved (black curve) as if, after a total indentation of 10 mm, the strain at the surface of the hard foam was twice as great as usual, i.e., as if the hard foam stiffness was reduced. The Supporting Information (Appendix E7 and E8) shows that this change in slope of the skin1 signal also occurred at the interface of a hard-hard system, suggesting that the interface is responsible. The behaviors of the three systems are shown as a function of force in Figure 3.10b.

FEA

Taking another approach, an axisymmetric two dimensional (2D) finite element analysis (FEA) model (SolidWorks, Dassault Systèmes) was used to model three of the configurations. The top layer thickness was set to 10 mm and the bottom layer thickness to 20 mm. The material behavior was assumed to be hyperelastic and incompressible under biaxial compressive stress and described by the Mooney-Rivlin model.

The force vs. displacement curves predicted by the model at the top surface are compared with the experimental curves in Figure 3.10c. Again, the behaviors matched fairly well for the soft-soft and hard-hard pairs, but the predicted force for the soft-hard combination was higher than that from the experiment. Strain on the top surface versus force was also obtained from the FEA simulation (Figure 3.10d). The model again showed reasonable agreement for the soft-soft and

hard-hard configurations, but the predicted slope of the signal was too low for the soft-hard configuration because of the over-prediction of the stiffness. Again, the hard foam in this configuration behaved as if it were softer. Thus, neither the FEA method nor the surface model could account for the soft-hard behavior, possibly because they did not account for interfacial effects.

3.4.3 Temporal Effects

Now that the quasi-static behavior of the skins on the foams has been examined for a base-case time interval and loading rate, we turn to an examination of temporal effects. Human-robot interactions may occur at different time scales (e.g., a robot bumps into a hard object at high speed or experiences repeated touches at short time intervals). Due to the viscoelasticity of the sensing membranes and the foams, the response of the sensing structure will be rate and history dependent. This is not fatal: even sensors with very long relaxation time constants can be successfully applied in robotics [25,46].

3.4.3.1 Memory Effects

In the previous sections, $\Delta R/R_0$ was presented, where R_0 was the resistance *at the beginning of each cycle*. Here we directly examine the voltage drop V_s over skin1in the soft-hard system, which was in a voltage divider circuit (section 3.3.3). The sensor had never been strained before and had an initial voltage reading V_0.

Figure 3.11 shows the voltage in response to a first indentation of 22.5 mm followed by two smaller indentations of 17 mm. There was an immediate increase in the voltage when the probe indented the surface. After the probe left the surface in the first cycle, the voltage initially dropped rapidly, but it did not return to the original baseline V_0, instead gradually settling at a new, higher baseline V'_0. After the next indentations, the voltage again returned to the new baseline V'_0, at the same rate as for the first indentation. (We have previously fit the recovery response using a generalized Maxwell model with two time constants; see SI for [175]). After the baseline shift, the subsequent cycles were relatively stable. The higher baseline resistance after the first cycle explains the smaller signals $\Delta R/R_0$ in later scans seen in Figure 3.2h.

All three signals had comparable amplitudes above the *new* baseline. This result suggests that memory effects could be substantially mitigated by using the resistance baseline *after* an event as R_0, rather than the one before it (see Appendix E9), although such an approach may not be practical in some real-time applications. Alternatively, prior work has shown that empirical models based on sensor characterization can be developed for viscoelastic materials, allowing accurate estimates of applied pressure [56].

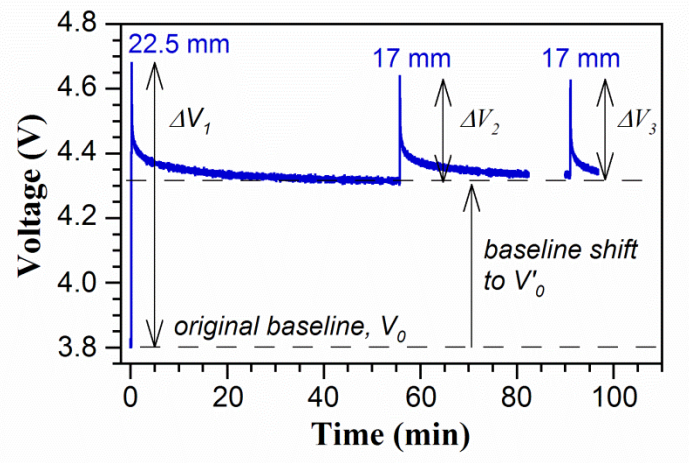

Figure 3.11: Voltage from the data acquisition system over skin1 of a soft-hard system (foam pair B) to the indicated depths were performed using the transducer (spherical probe, 4.5 mm/s).

3.4.3.2 Effect of Time Interval

Because of the relaxation time (Figure 3.11), the time interval between loading events changes the signal amplitude. Four consecutive indentation loading cycles with short to long intervals between cycles were performed on the multi-layer sensing system. To examine the response of the sensing membrane alone, tensile tests were also performed with varying time intervals.

Figure 3.12a shows pressure as a function of probe indentation for the second to the fourth cycles. The mechanical responses were independent of the interval: the results overlap. Figure 3.12b shows the corresponding signals from the two sensing skins. The signals from skin1 for time intervals of 2-10 minutes were almost the same, but for the shorter time interval of 30 seconds the signal from skin1 was lower. The region of the skin1 curve that was affected by the time interval was the high-slope region (which decreased from 1.6 to 1.2 %/kPa) at pressures less

than 50 kPa, associated with the compression of foam1. The slopes associated with foam2, for both skin1 and skin2, were unaffected by the time interval, suggesting that the time-interval dependence arises from foam1.

Figure 3.12c shows force as a function of strain in the tensile tests on the sensing skin alone. All the curves overlapped, showing that the mechanical recovery is faster than the shortest interval (15 seconds). Figure 3.12d shows the piezoresistive responses. These curves did not stop overlapping until 15 sec. Thus, the soft foam is the main contributor to recovery effects in this system and the behavior of the sensing skin on a foam is dominated by the foam to which it is attached.

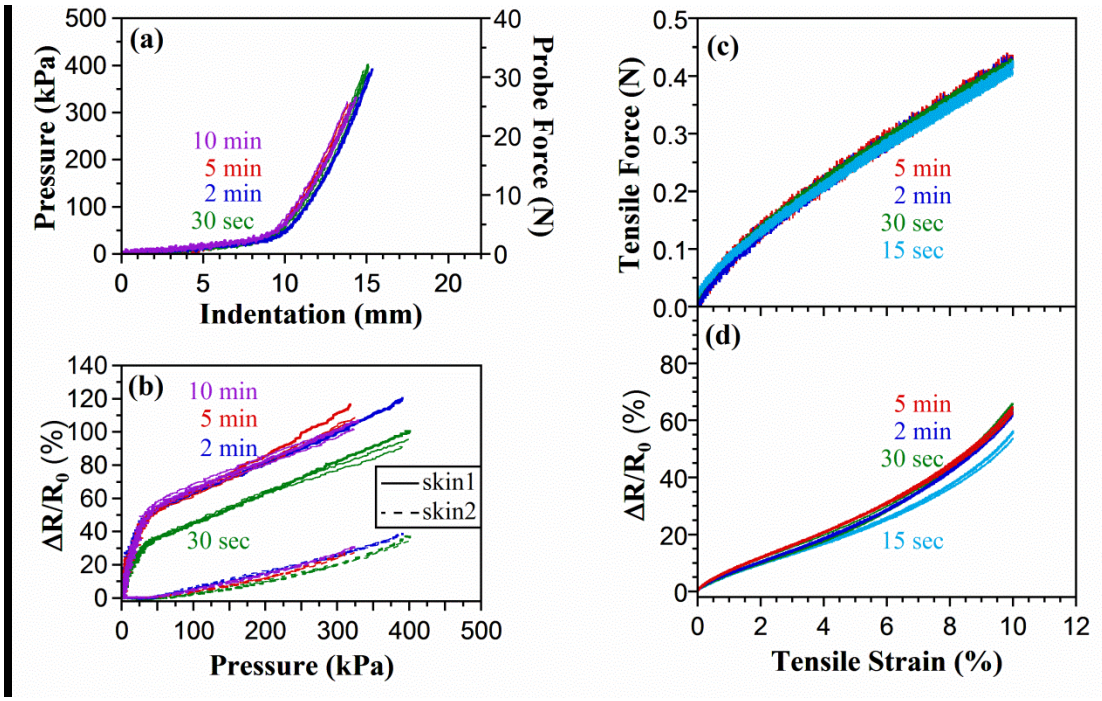

Figure 3.12: Effect of interval time between loading cycles. a) Pressure vs. probe indentation (4.5 mm/sec) for the foam pair A soft-hard system. b) Normalized change in resistance of the two sensing skins vs. indentation pressure. c, d) Tensile tests on a stand-alone sensing skin (1 mm/sec). c) Tensile force vs. tensile strain. d) Normalized change in resistance of the two sensing skins vs. tensile strain.

3.4.3.3 Effect of Loading Rate

Loading rates would likewise be expected to affect the response. Loading rates were therefore compared for both the soft-hard system and the sensing skin alone. Four cycles were performed at each rate, with time intervals between cycles of 5 minutes.

The faster loading rate resulted in a slightly higher pressure on the multi-layer system (**Figure 3.13**a) and a correspondingly larger signal from skin1 (Figure 3.13b). Just as in Figure 3.12b, the part of the curve responsible for the dependence was the low-pressure region corresponding

to the compression of foam1. Above 50 kPa, associated with compression of foam2, there was no change in slope with rate, and the slope was similar for skin2.

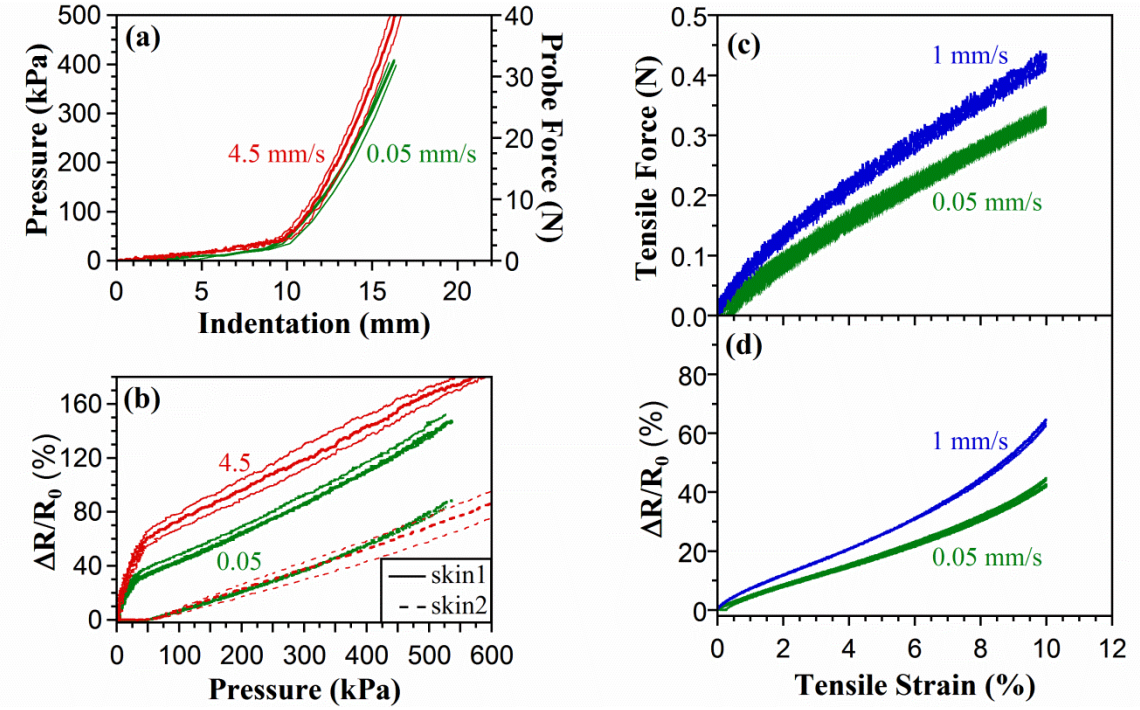

Figure 3.13: The effect of loading speed during indentation of the multi-layer system (2nd to 4th scans). a) Pressure vs. probe indentation. Add force to y axis. b) Normalized change in resistance of the two sensing skins vs. pressure. In a stand-alone membrane, c) tensile force and d) normalized change in resistance vs. tensile strain.

The responses of a stand-alone skin are shown in Figure 3.13c and d. The mechanical stiffness was greater at the higher rate, as was the $\Delta R/R_0$ signal. Interestingly, the performance of a compliant sensor on a foam may be less rate dependent than it would be alone, as evidenced in Figure 3.13b by the nearly identical curves at the two loading rates for skin2.

3.5 Conclusions

Compliant sensing skins face the challenge of achieving both reasonably high sensitivity and a sufficiently large sensing range. The multi-layer foam system investigated in detail in this chapter offers a simple solution by splitting the two goals so that each is handled by a different stratum. The upper stratum, having a softer foam, provides higher sensitivity at light touch, while the bottom stratum, having a stiffer foam, extends the range. This approach allows the sensitivity and range to be separately tailored for a given application: by tuning the stiffness and thickness of the foam layers, the pressure vs. indentation curve and the associated resistance versus pressure curve can be manipulated. This simple sensing concept is remarkably effective. The benefit of the multi-layer approach was validated by comparison with three other foam stiffness combinations. Due to the quasi-1D shape of the piezoresistive strain-sensing skins, their stretchability, and their placement on foam, they behaved as pressure sensors.

The compliant components of the multi-layer sensing structures are all inherently viscoelastic, rendering the signal time- and history-dependent. First-cycle effects were due to a long-term shift in the baseline resistance of the skin after the first touch. Memory effects were primarily contributed by the soft open-cell foam. Even with these viscoelastic properties, the simplicity of the design and the ability to tailor the response to the pressure ranges of interest make the multi-layer approach attractive for robot tactile skins that cover the robot body.

Chapter 4. Compliant Multi-Layer Tactile Sensing for Enhanced Identification of Human Touch

To be submitted

Ying Chen, Miao Yu, Hugh A Bruck, Elisabeth Smela

Co-author contribution: The idea of developing EIT multi-layer sensor system comes from the discussion among all authors. Ying Chen implemented multi-layer EIT tactile sensors, performed the experiments, and analyzed the data. All authors contributed to writing the text and making the figures.

4.1 Abstract

Tactile sensing is viewed as essential to a co-robot to facilitate their interactions with humans. Two approaches are suggested here to aid the interpretation of contact: the use of a multi-layer cutaneous tactile sensing architecture, to provide ancillary information and an expanded force range, and the technique of electrical impedance tomography (EIT), for distributed sensing. The multi-layer system consists of two stretchable sensing skins alternating with two foam layers of different stiffness. Machine and human touch are compared, revealing that, because of a large variability in human touch, although the topmost skin over a soft foam is able to recognize light contacts, a second underlying skin over a hard foam is required to gauge stronger contacts. Out-of-plane touch modalities, such as tapping and punching, could be identified using strip-shaped skins with the multi-layer system, each strip having just two electrodes. Distributed touch

modalities, such as multi-point finger presses and sliding, were distinguished from one-finger pressing using EIT with larger-area skins having electrodes around the perimeter. The differences between contact generated by a machine versus a human were shown for the first time.

4.2 Introduction

Interactive robots, called co-robots, work in the same physical space as humans, for example for manufacturing [204], housekeeping [205], entertainment [138], or care-giving [15,129,206-208]. For safety and comfort, soft robots [209-212] reduce collision impact [213]. Softness can be achieved in various ways, such as by employing mechanically compliant assemblies [214,215], inherently soft materials, or padding applied over hard structures. The latter option is explored here.

In addition to softness, robots working in unstructured situations around humans may require tactile information to know if they have made physical contact with a person or object, not only to modify their actions to reduce the probability of harm, but also to enable them to communicate with humans via touch. Tactile sensing has been the subject of a number of literature reviews [7,18,129,195,205,216-218]. For covering the robot body with tactile sensors [15,24,117,167,219], the sensors may be discrete [220] or in the form of a continuous artificial skin [111,117,219,221] [80,83]. Discrete sensing elements, such as array, have been commonly used to implement distributed sensing [75] [76], while the number of wires directly related to the

number of rows and columns. Continuous distributed sensing has been achieved based on boundary measurements and associated data processing, such as four-wire schemes [79-84] and the technique of electrical impedance tomography (EIT). Four wire schemes are limited to detect single stimulus [82,83,85,86], while EIT technique is able to detect not only multiple stimuli but also their amplitudes [111-124]. In this work, single sensing element and continuous sensors based on EIT technique are employed.

Sensors with high accuracy and resolution have been developed [192,193,201,216,222]. However, taking a task-centered approach [129], a robot may not require exact force values for operational success, but simply an ability to determine the nature and location of contacts: whether it has been gently touched by a person, is being pulled in a particular direction by someone, or has fallen onto its knees. Qualitative information is effective in the mammalian sensing system and has been deemed sufficient for robots to acquire bodily awareness [15,24,219]. The skin of mammals is viscoelastic, demonstrates stress relaxation and creep, and fails to recover to its initial position; furthermore, the signal from biological mechanosensors decreases over time in response to closely spaced repetitive stimuli [223]. Nevertheless, the mammalian sensing system works very well. Continuing to take a task-oriented approach, although extremely sensitive tactile sensors have been demonstrated (e.g. to detect insects walking on the surface [171] or acoustic stimuli [224]), cost [129,206,225] and integration issues [18,24,192,219] have proven to be more important than sensitivity and precision, especially at large scales, such as whole-body coverings [26]. The development of a robust [26] and inexpensive tactile sensing system that can qualitatively distinguish the strength and location of contacts could be transformative for robotics.

The ability to identify touch modality is thought to be particularly important for robots that interact closely with humans. This has been achieved in prior work by examining signal time profiles [61,174,224,226-228]. For example, a single sensor embedded in foam has been used to identify push, pinch, and stroke [140]. Touch modality identification has also been done by examining spatial profiles obtained with a sensor array to register distributed contact [171,173,229] and an area sensor to image pinch and grab [111]. Feature extraction has been employed to automate the classification of touch modalities [117]. Identification of various touch modalities has been investigated in the context of robots [117,230-232]. Touch modalities include both gentle and strong touches, such as pat, slap, stroke, beat, and punch. This again requires tactile sensors being able to cover wide force range.

Here we employ a compliant multi-layer sensing structure that simultaneously achieves relatively high sensitivity and extended force range [175]. Multi-layer sensing structures are rare. A four-layer sensor inspired by the multiple layers of sensors found in the human finger was suggested in [233] but not realized. Our multi-layer sensing system employs two skin+foam strata, each consisting of an elastic sensing skin on a foam pad [175]. A stratum with a soft foam is placed on top of a stratum with a stiffer foam. Since sensor response over pads is tailored by the foam stiffness [35], this "soft-hard" structure confers relatively high sensitivity via large indentations of the soft upper layer and an extended force range via the stiff bottom layer.

In this paper we present initial results to demonstrate the feasibility of employing a multi-layer sensing architecture in human touch scenarios. We contrast the use of 2-point resistance

measurements for rapid signals with the use of electrical impedance tomography (EIT) for spatial discrimination. The ease and tailorability of these approaches for future human-robot interaction is promising.

4.3 Results

4.3.1 Multi-Layer Sensing Structure

A piezoresistive strain sensing material was used in this paper, a composite consisting of a latex host elastomer filled with electrically conductive exfoliated graphite (EG), as employed previously [Chen, 2018 #13881;Wissman, 2013 #241;Barnett, 2017 #632;Chen, 2016 #446;Kujawski, 2010 #238]. The amount of EG in the sensing layer (25%) was above the percolation threshold, yet the material remained rubbery, which has been applied in our previous publications [48,175,198]. Tensile strain reduces the number of percolation pathways, resulting in increasing resistance. The sensitivity or gauge factor is defined as GF = $(\Delta R/R_0)/(\Delta L/L_0)$, the relative change in resistance $\Delta R/R_0$ per unit strain $\Delta L/L_0$. For these sensors GF is approximately 8 [234] due to the inherent resistivity changes of percolation, compared with GF = 2 obtained from geometric effects. Nano-carbon filled elastomers have been extensively studied and are not the subject of this work, which could have employed other stretchable sensing materials.

Fabrication was simple, as described previously in detail [48]. **Figure 4.1** illustrates a typical preparation procedure. The electrically conductive EG particles were expanded in a microwave oven, horn sonicated in an aqueous solution to separate the layers, and blended with latex. The

dispersion was sprayed onto a latex rubber sheet to form the sensing skin. (The term skin is used to distinguish the combination from the sensing material alone.) Carbon fiber bundles, serving as compliant electrodes, were adhered to the sensing layer. Carbon fibers have chemical compatibility with the polymer matrix and low contact resistance. The skins can readily be made (e.g. Spray the dispersion directly to a padded robotic structure.) to cover large areas and arbitrary shapes. When affixed to a layer of foam, the conformal skins report touch-induced deformations; the skin's behavior, alone and on foam, was previously characterized in [175]. "Compliance" as used here means that the skin is stretchable and the foam padding structure is compressible; the foam is always mounted on a rigid substrate and does not undergo stretching or twisting

In previous investigations, elastomers loaded with EG were studied as stretchable and durable piezoresistive sensing materials [47], used to monitor wing deformation for flapping wing micro air vehicles [48], and engaged to create images of braille dots [198]. They compare favorably to commercial compliant conductive materials (see the Supporting information of [234]). We also found that the use of a foam padding under a sensing skin enhances strain during indentation, resulting in a larger signal [175]. Recently, our skins were employed on a padded hugging robot to determine when a hug had been started and stopped [235].

Figure 4.1: Formation of the sensing skin. Acid-intercalated graphite is expanded, the layers are separated in an aqueous solution (not shown), and latex is added to form a paintable dispersion that is spray-coated onto a rubber membrane to form an EG/latex piezoresistive sensing skin. Large areas are possible. Electrical connections are made with carbon fiber bundles using additional EG/latex as an adhesive. The skin can be placed over a layer of foam to form a skin+foam stratum.

In this work, both strip-shaped (**Figure 4.2**a) and circular-area skins (Figure 4.2c) were produced (see Section 4.6). For the multi-layer system with strip-shaped sensors (Figure 4.2b), two nominally identical strips (11 x 0.8 cm x 300 μm) were aligned directly over each other, with skin1 glued to the upper soft foam1 (d_1 = 12.5 mm) and skin2 glued to the stiff lower foam2 (d_2 = 12.5 mm). The two skin+foam strata (total thickness 25.6 mm) were placed over a rigid substrate and clamped at two edges (Figure 4.2b). The sensing skins were highly stretchable (Figure 4.2a); a substantially linear strain sensing range of at least 25% was obtained in our previous work [175]. This allows the skins to follow the deformation of the foam under touch.

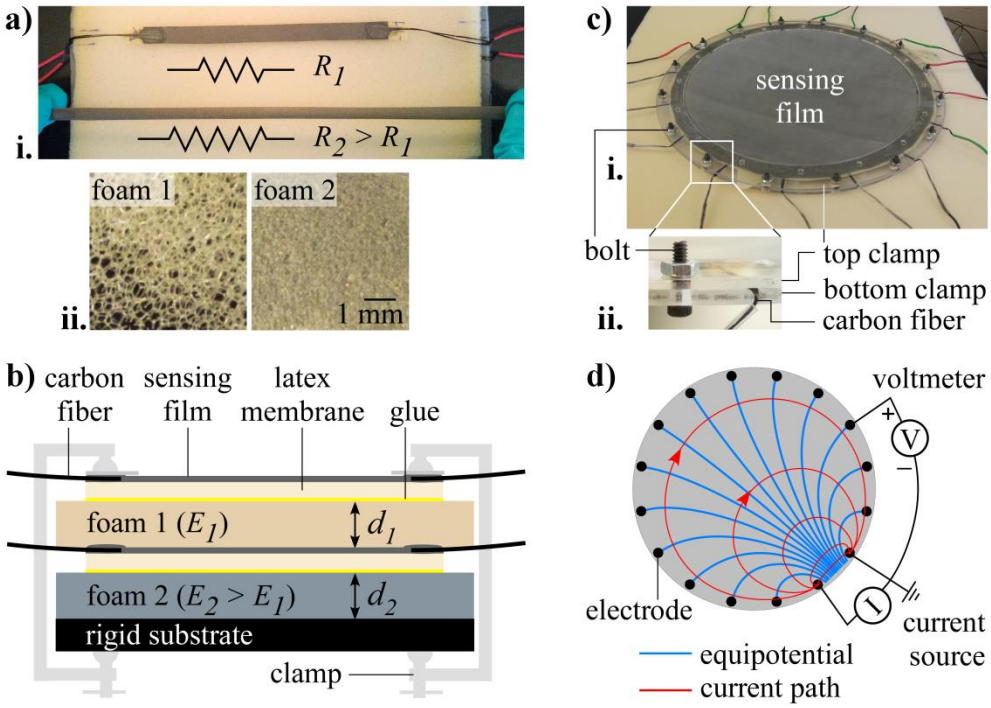

Figure 4.2: a) i. Strip-shaped sensor with carbon fiber electrodes glued to foam1 (top). Demonstration of the stretchability of the sensing skins (bottom). ii. Close-up of the two foams showing their open and closed cell structures. b) Cross-sectional schematic of the multi-layer sensing system with strip-shaped sensing skins. c) i. Circular continuous sensor used with EIT, clamped at the perimeter. ii. Close-up of the clamp fixture, edge-on view. d) Schematic of the method for collecting data to create EIT images [111].

When the multi-layer system was used with circular skins (dia. = 20 cm), they were clamped on the perimeter in a fixture (Figure 4.2d) to provide mechanical support and electrical connections to 16 carbon fiber electrodes. Due to instrumentation limitations, only one distributed skin could be measured at a time. The fixture was placed i) over the combination of foam1 and foam2 to serve as skin1 or ii) between the two foams to serve as skin2.

Images of indentation-induced strains were produced using EIT. [123] EIT involves injecting current into two electrodes and measuring the voltage at all the other electrodes, then moving the injection point to the next electrode and repeating the measurements, rotating completely around

the circle (Figure 4.2d). (See also Section 4.6) A map of conductivity changes over the sensing area is reconstructed from measurements made at the boundary.

4.3.2 Machine Touch

Before examining the performance of the multi-layer system under human touch, its behavior in controlled experiments with an indention probe and a force transducer is presented. The multi-layer system with strip shaped skins was characterized with out-of-plane indentation to 20 mm depth using a rigid 1 cm dia. cylindrical probe (**Figure 4.3**). Four loading-unloading cycles at 4.5 mm/sec were performed, separated by 5 minute intervals. (Further characterization was reported in Chapter 3.)

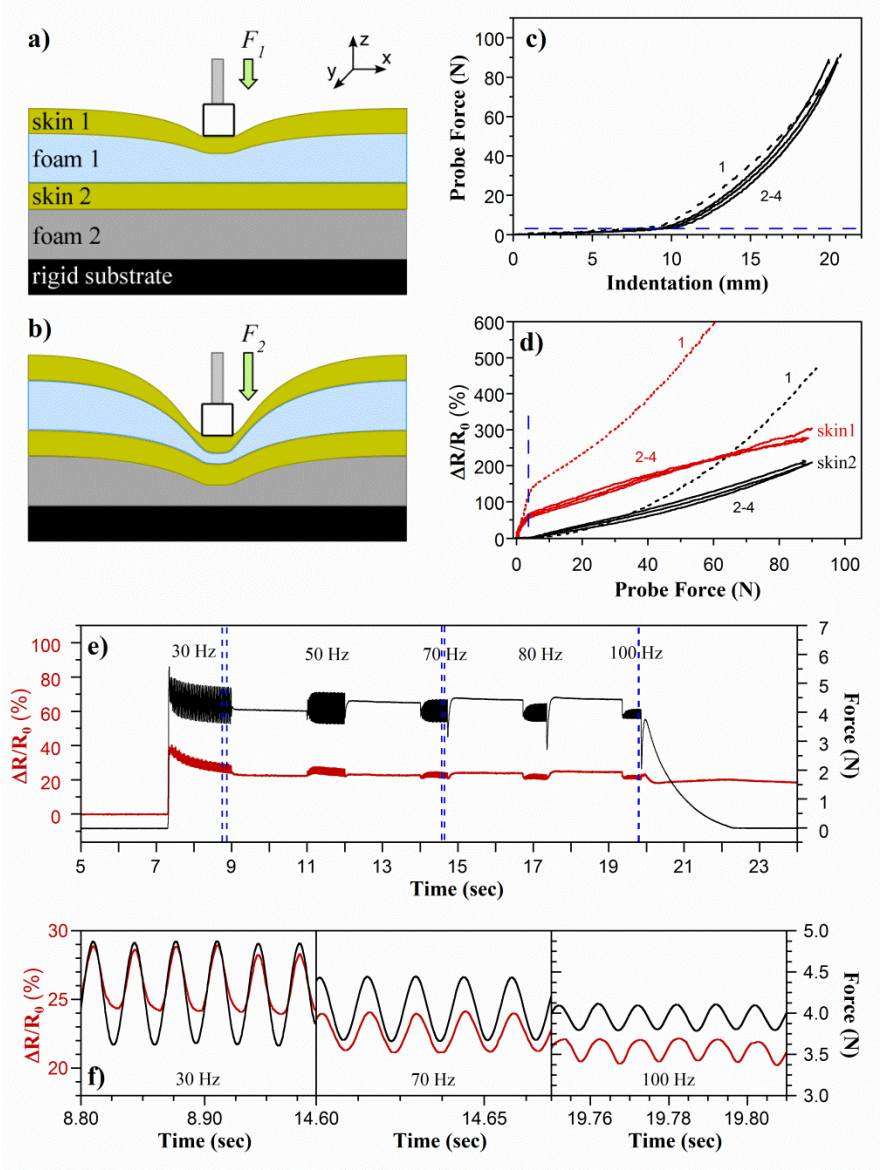

Figure 4.3: a) When a light force is applied, only the upper skin1+foam1 stratum deforms. b) When a large force is applied so that foam1 is nearly crushed, the lower stratum, which is able to sustain a larger force, begins to deform. c) Force experienced by the multi-layer system under increasing rigid probe indentation. The first scan is represented by a dashed line and the 2nd to 4th scans by solid lines. Scan numbers are indicated. d) Normalized change in resistance of the two strip-shaped sensing skins as a function of probe force. The signal from skin1 is shown in red and the signal from skin2 is in black. The contact area between the probe and the sensing system is constant during the entire loading process due to the flat bottom of the probe. e) Dynamic response of skin1+foam1 under cyclic constant-displacement tests. f) Close-ups taken at the indicated times in (e).

Figure 4.3c shows force as a function of probe indentation, measured downward from the un-deformed surface of skin1. Up to an indentation of 10 mm, nearly to the thickness of soft foam1, the force remained below 3 N (dashed horizontal blue line), corresponding to the scenario shown in Figure 4.3a. The force then increased nonlinearly as the probe began to deform the hard foam2 layer (scenario shown in Figure 4.3b). At the maximum indentation of 20 mm, the probe indented half-way into the hard foam2, and the force reached 90 N. All four scans had similar mechanical responses, as evidenced by the overlapping curves.

The normalized change in resistance $\Delta R/R_0$, where ΔR is the change in resistance and R_0 is the initial resistance, is shown as a function of force in Figure 4.3d for both sensing skins. The changes were larger during the first scan (dashed lines), but were then similar in the remaining three scans. This behavior was expected because viscoelastic materials such as foams and elastomers experience break-in effects during the first cycle, known as the Mullins effect [199] in filled rubbers. For skin1 at low force (up to 3 N, indicated by the dashed vertical blue line), the sensitivity was high and substantially linear. In this force range the probe indented only the soft foam (0-10 mm) and thus only strained the top sensing layer (Figure 4.3a), leading to a corresponding increase in its resistance. The $\Delta R/R_0$ was an easily measurable 60%. Beyond 10 mm, the sensitivity decreased, and above a turnover region it became substantially linear again up to the maximum force. The sensitivity dropped because of the greater stiffness of foam2: a unit increase in force corresponds to a smaller displacement, and thus smaller strain. At 90 N, the change in resistance reached 300%. The slopes of these curves directly reflect the foam stiffness and the turnover point the foam thickness, so the performance of the system can readily be tailored to meet particular application requirements.

For skin2, the output was essentially zero at low force, since it remained unstrained while only the upper foam was compressed. At the turnover point for skin1 (i.e., the corner in the force-indentation curve, Figure 4.3c), the soft foam1 was crushed, foam2 began to deform (Figure 4.3b), and the resistance of skin2 began to increase. Above 10 N, its slope was comparable to that of skin1.

The dynamic response of skin1+foam1 on a rigid substrate was then characterized by indenting the probe to a depth of 5 mm and applying a sinusoidal waveform with a nominal displacement amplitude of 1 mm. Five frequencies between 30 and 100 Hz, 50 cycles of each, were applied from low to high, with 2-second intervals between frequencies during which the probe was held at 5 mm indentation (Figure 4.3e). The maximum frequency was limited by the instrumentation. At the end of the test, the probe was raised from the surface.

Figure 4.3e shows both the force resulting from the displacement waveform and the relative change in resistance of skin1 throughout the test. Figure 4.3f shows three close-ups, taken at the indicated times in Figure 4.3e. The peak-to-peak amplitude of the force decreased as the frequency increased, which may be due to the inability of the transducer to reach its full displacement distance at these frequencies. Correspondingly, the peak-to-peak amplitude of the sensing signal decreased. At 30 Hz the distortion of the sensing signal shape was due to the system's memory effects [175], but by 70 Hz it was sinusoidal. There was no phase lag between the force and resistance signals, even up to 100 Hz. The lack of diminution in amplitude relative

to the force and lack of phase lag show that the skin-padding system was able to reliably respond to dynamic indentation, with the sensor accurately reporting the force.

4.3.3 Human Touch

4.3.3.1 Multi-Layer System with Sensing Strips

Human touch, unlike contact in a force-strain transducer, is not well controlled in strength. For finger touches, not only are there variations between individuals, but even for the same person the part of the finger making contact may vary in shape and stiffness, and the angle between the finger and the sensor will vary from touch to touch. The response of the multi-layer sensing strip was thus measured as it was pressed with a single finger in repeated trials by six people at a position they judged to be in the middle of skin1. They aimed to achieve force levels that they subjectively judged to be light, medium, and strong, pressing three times each, holding for 1 or 3 seconds and then waiting 30 seconds before the subsequent touch.

Figure 4.4a-c show the results as a function of time from one representative individual. Results from other individuals did not substantially differ. The curves are color-coded based on the individual's stated intentions and correspond to forces of approximately 2, 5, and 13-20 N. (Detecting ultra-gentle tactile stimuli is not the focus of this paper.) The force showed unsteadiness and inconsistency between finger touches, which was typical for the human contacts (Figure 4.4a). Figure 4.4d shows maximum $\Delta R/R_0$ of all test results from the six people as a function of corresponding finger forces. As expected from the characterization data, these

force levels could be discriminated. Skin1 showed a clear 15% $\Delta R/R_0$ response to light touch that increased further to 25% at medium force and 38% at strong force. However, $\Delta R/R_0$ was not proportional to the force. Rather, at high force the $\Delta R/R_0$ signal reflected the lower sensitivity above the turnover point (Figure 4.3d). In contrast, skin2 showed essentially no response to the light touch, but had a 1% signal for medium touch and 3-5% for strong touches, with responses proportional to the force above the turn-on point. The 2nd stratum therefore became useful in the high force range. Figure 4.4b and c also exhibit the memory effects demonstrated by these viscoelastic materials: the baseline resistance was higher after removal of the force.

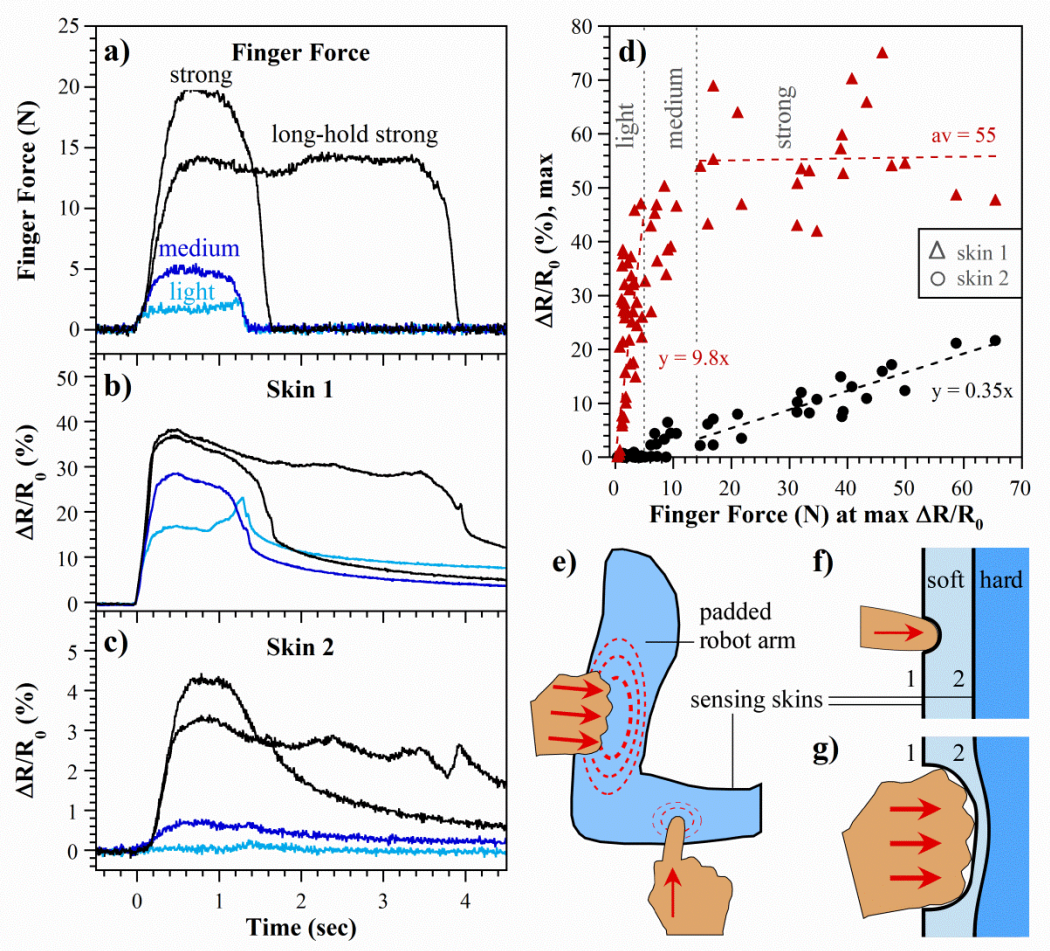

Figure 4.4: a) Force vs. time in response to light, medium, and strong finger presses, as judged qualitatively by the person. The corresponding $\Delta R/R_0$ responses of b) skin1 and c) skin2; resistance scales differ. d) Peak values of the relative change in resistance as a function of applied force for 6 people pressing 3x each for 1-4 sec at each force level. Slopes of linear curve fits are shown; strength of touch is indicated by labels. The time interval between presses made by the same individual was 30 seconds. Note that the contact area of the fingertip is changing during pressing. Concept of a sensing skin on a padded robot arm experiencing different human touches. f) A light finger touch in a multi-layer cutaneous sensor produces an indentation in the soft upper layer of foam, leading to a strain in the topmost skin1 and thus a change in its resistance. g) A hard punch deforms the underlying harder layer of foam, leading to a strain in skin2.

Figure 4.4d shows the peak normalized resistance change $\Delta R/R_{0,\max}$ for all the tests from the six people as a function of the corresponding finger-press force. Note that the contact areas in the finger press and probe indentation tests were different, the former increasing as the compressible

finger pressed harder. Thus, while these data resemble the calibration curves (Figure 4.3d) in shape, they cannot be directly compared because of the different test conditions, including, among other things, different mechanical properties of fingers and probes, different contact areas, touching at different loading speeds, and different loading history. Larger contact areas and slower loading speeds decrease the slope in plots of $\Delta R/R_0$ vs. force (see Figure 3.3 a and c and Figure F.1). The changing contact area of the finger accounts for much of the flattening of the signal at high force. The scatter in the data reflects variability in the touches.

Skin1 readily detected light presses (< 5 N). Both skin1 and skin2 were able to distinguish light from medium (5-14 N) and medium from strong (>14 N) touches. Unlike in the calibration curves, the signal from skin1 plateaued under strong forces (linear curve fit shown, giving y = constant 55% for strong presses) and showed substantial scatter, while the signal from skin2 kept increasing (linear fit, R = 0.9) and had less scatter. The high scatter from skin1 at higher forces is likely explained by variable lateral distortions of skin1 on the soft foam at relatively large deformations, and the lack of lateral distortions of skin2 on the stiff foam, which deforms less. (The scatter in the skin1 signal persisted even when it was covered by a second layer of soft foam to prevent direct finger contact.) Thus, in real-world touch scenarios skin2 helps identify the onset of medium touch and extends the dynamic range for identifying strong touch. The multi-layer sensing structure proved even more useful than initially expected. For a robot to take an action based on presses, one scenario for decision-making could be to apply a threshold test to determine whether to use data from skin 1 or skin 2. For example, when the signal from skin 1 exceeds 0.3, switch to skin 2, and when the signal from skin 2 drops below 0.6, switch back to skin 1.

It is important to point out the difference in the response of the multi-layer sensing architecture to machine and human touch. For the machine touch in Figure 4.3, the normalized change in resistance with force was similar between the two sensing skins when the applied force level was above 10 N. However, for human touch, skin1 showed large variability in response to strong touches, likely because the human touches were less controlled and the finger is deformable. This has an implication for the ability of any sensor on a compressible substrate to give quantitative information about human touch.

For human-robot interactions, an example application scenario can be a padded robot arm equipped with the multi-layer sensing structure (Figure 4.4e) that can distinguish a light finger press (Figure 4.4f) from a hard punch (Figure 4.4g). Furthermore, the two layers of foam increase the comfort and safety of interaction.

Given the enriched force information from finger presses provided by the multi-layer strip sensing system, its response to five other touch modalities was explored: tap, punch, pinch, slide, and rub. Press, tap, and punch (**Figure 4.5,** top row) are indentation-type (out-of-plane) touches with different time signatures and forces. Presses have a relatively slow onset, long hold period, and slow release. Tapping results from faster and repetitive finger motion at a lower force. Punches are impulse-like stimuli at high force covering a larger, fist-size area.

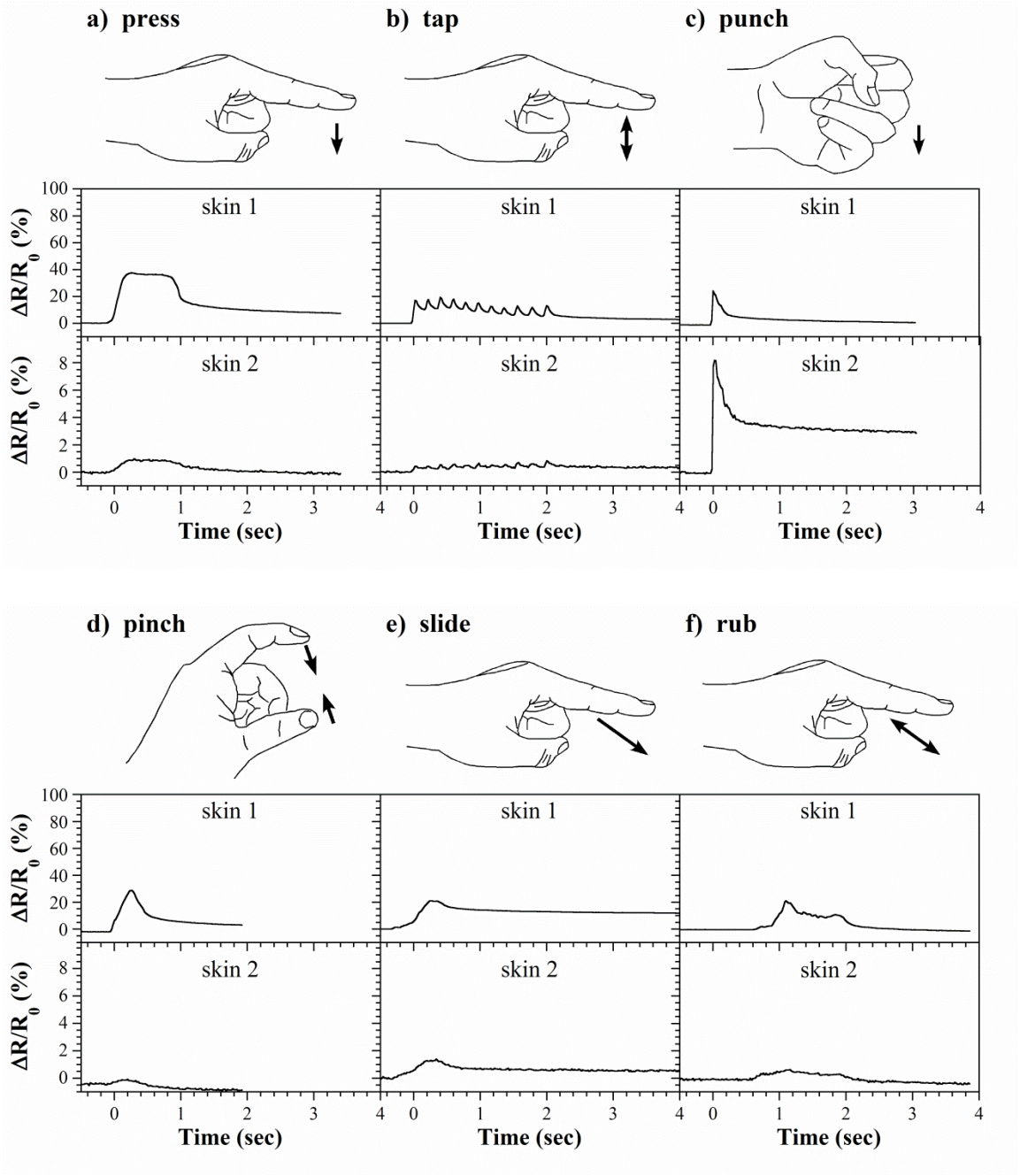

Figure 4.5: Sensing various touch modalities with the multi-layer strip system. Note that the lower panels for skin2 responses have a different scale (magnified 10x). a) Press and release with index finger (medium). b) Rhythmic tapping with index finger (medium). c) Single punch with fist (hard). d) Single pinch with thumb and index finger (light). e) Slide in one direction along the surface with index finger (light). f) Rub surface repeatedly back and forth with index finger (light).

The time responses of the sensing skin permit straightforward discrimination among these three. Both sensing skins reliably recorded the onset and release of each contact. As expected, the signal amplitudes from skin2 were always smaller than from skin1. Signals from skin1 were at similar levels for press, tap, and punch, despite punch being harder. This is due to the larger contact area of the fist (20 cm^2 vs. 2 cm^2, see Figure 3.3 a and c). On the other hand, the signal from skin2 was small for press and tap (Figure 4.5a,b), but relatively large for punch (Figure 4.5c): foam2 was indented little by the former and significantly more by the latter. The ability of skin2 to help differentiate touch strength was again useful for identifying out-of-plane touch modality.

Pinch, slide, and rub are primarily inplane motions, accompanied by a relatively small pressure. Thus, skin2 was not expected to contribute substantially, which was borne out by the results. Even for skin1, pinches (Figure 4.5d) were hardly distinguishable from presses (Figure 4.5a), except that the onset of pinches was more gradual (the initial slope was less steep). Sliding (Figure 4.5e), likewise looked virtually identical to pressing – the inplane motion was undetectable with this system. Unlike sliding, rubbing (Figure 4.5f) could be classified because it produced wrinkling on the surface, resulting in sporadic signal fluctuations.

4.3.3.2 Multi-Layer System with Distributed Skins

In the multi-layer system tested above, the sensors were long, narrow strips, and resistance was measured along their length. As a result, they behaved as single point sensors able to distinguish

touch modalities based only on the overall strain and the time response. Modalities in which only surface position changed but not the indentation level, such as sliding, could not be differentiated. In order to obtain more enriched information about human touch, a continuous large-area sensor was employed to image finger-press, multi-point touch, fist-punch, and sliding. To eliminate viscoelastic memory effects from the signal, different touch modalities were tested on different days.

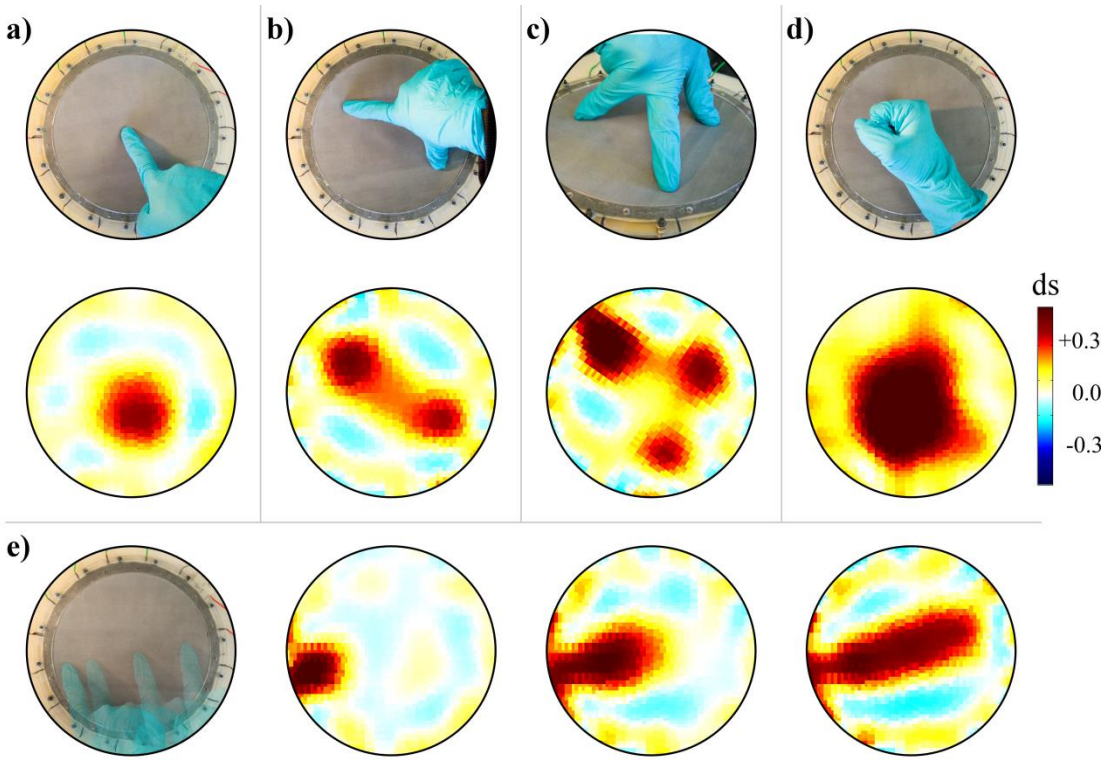

Figure 4.6: Demonstration of (top row) a) single-point, b) two-point, and c) three point finger presses, and d) a light fist-punch, together with (center row) EIT images from the skin1 position in the multi-layer distributed sensing system , where *ds* represents the conductivity change (see Section 4.6). e) Demonstration of finger sliding from left to right and EIT images recorded at different times (t = 1.0, 1.6, and 2.2 sec) during similar finger sliding.

Figure 4.6 shows EIT images adjacent to demonstrations of the touches that produced the data. The 2D EIT images present a representation of the spatial distribution of changes in conductivity (ds), the difference taken between a baseline reference conductivity distribution over the sensing layer before touch and the conductivity distributions at the times of the measurements. Pixels are evident in the images, but the resolution is significantly higher than could be obtained using a 4x4 grid sensor with the same number of electrodes (16).

Single, two-point, and three-point touches at similar levels of force were applied with the distributed sensor in the position of skin1, i.e. placed on top of the combination of foam1 and foam2. The results are shown in Figure 4.6a-c. The number and location of the contact points are readily observable. When the sensor was positioned between the foams, in the position of skin2, it was insensitive to these gentle presses (data not shown). The result of a fist punch is shown in Figure 4.6d: the larger contact area is evident. Figure 4.6e shows images obtained at different times during a finger sliding from left to right: at the start, middle, and end. The images reliably show the initiation of the contact and the history of the sliding motion. This example illustrates that the viscoelastic memories of the sensing system components can be exploited to advantage, producing an obvious lingering trace along the finger sliding trajectory. Compared with previous work by Russo et al. [236], where conductive fabrics was employed as sensing material, fast recovery of the fabrics generated images with no left-over sliding trajectory (see supporting video of Russo et al. [236]). Sliding trajectory from fast recovery material can be obtained by looking at different time stamps; sliding trajectory from slow recovery material, like the one we used here, can be seen at each time stamp. EIT image production takes a fraction

of a second, but because of the viscoelastic relaxation time, the signal does not decay too fast and fleeting touches can still be recorded.

To compare the response of the distributed sensing system to light, medium, and strong touches, it was punched in the center. Each punch was conducted on a different day, with the sensing skin fixture placed either in the position of skin1 or skin2. The system registered the light punch (60 N) in the skin1 position (**Figure 4.7**a, previously shown in Figure 4.6d), but not in the skin2 position (Figure 4.7d). At 110 N (medium), the peak value from skin1 was larger (Figure 4.7b), and skin2 showed a small response (Figure 4.7e). At 240 N (strong), the response of skin1 was not significantly larger (Figure 4.7c), but that of skin2 was (Figure 4.7f). The benefit of skin2 for extending the measureable force range is visually obvious from the images. Figure 4.7g plots the maximum value in the image as a function of force. As skin1, the sensor shows a higher sensitivity at low to medium forces, but again the signal plateaus for the stronger punches. As skin2, the sensor shows the extended range enabled by the stiffer foam.

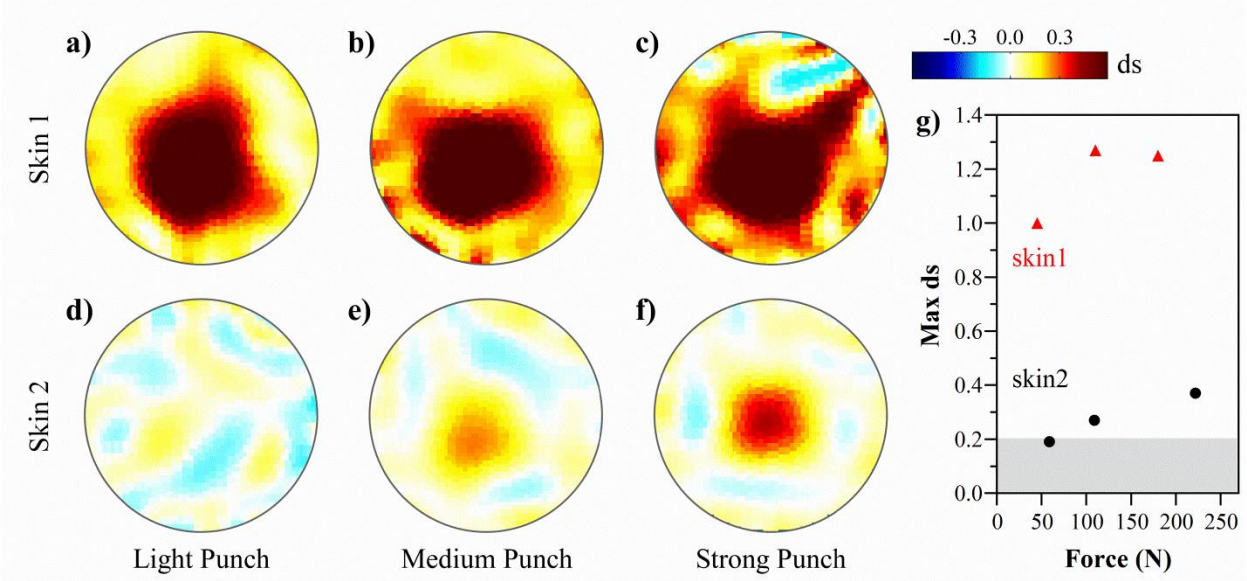

Figure 4.7: Reconstructed images of light (a, d), medium (b, e), and strong (c,f) punches with the distributed sensor above the soft foam (skin1 position) and between the foams (skin2 position). g) Peak values in the images (i.e., the maximum conductivity change, Max ds) as a function of applied force.

4.4 Discussion

The concept of soft-hard multi-layer padded sensing system enhances both sensor sensitivity and force sensing range. For specific design requirement, the turnover point for low and high sensitivity can be tuned by the thickness of top soft padding, and the sensitivity of each slope can be adjusted by the stiffness of the soft and hard padding layer.

The multi-layer system can employ two-point resistance readings across sensing strips for rapid response (dynamic responses to at least 100 Hz without noticeable amplitude attenuation and phase lag). Out-of-plane touch modalities can be determined without complex data processing. The multilayer system with strip-shaped sensors has been demonstrated to provide sensitivity to

light touch and to extend the force-sensing range [234]. However, piezoresistive sensors are inherently amenable to distributed sensing over larger areas and the use of sophisticated imaging like EIT. Combining EIT with the multilayer system, we demonstrate the imaging of touch modalities that involve spatial variation, such as multi-point contacts, variation in contact area, and sliding. The viscoelastic memories of the elastomeric sensing material and the foams proved to be advantageous for relatively slow imaging methods such as EIT, resulting in changes in resistance that last long enough to be recorded. While the technique of EIT has been used in tactile sensors [111,119,121,123], enhanced identification of the time trace of finger sliding and high forces with EIT tactile sensors has not been previously shown.

It is envisioned that a multi-layer tactile sensing system could be used for covering the limbs and torso of a robot, providing sensing and protective padding simultaneously. While tactile sensing has typically focused on high performance over small areas, e.g. for use on fingertips, the approach presented here is appropriate for body coverings, from which qualitative information is sufficient. While the concept was demonstrated using a specific stretchable piezoresistive carbon-latex composite because of its ease of fabrication, other sensing materials can in principle be used instead, such as conductive fabrics or stretchable capacitive sensing materials.

Few prior studies have been performed to evaluate the sensing of human touch by robots incorporating soft materials on their surfaces. Future studies involving larger populations and more varied touch scenarios are required to evaluate how well the concepts presented here can perform, and additional work is required to determine how best to apply the skins and padding conformally on a robot and without excess bulk. Nevertheless, the initial work here has shown

that the variability in high-force human touch can be large, for as yet incompletely understood reasons, and that this can be mitigated by the use of a second, buried sensing layer.

4.5 Conclusions

The concept of using a simple-to-construct multi-layer tactile sensing system for obtaining information about human touch has been presented. A first upper sensing skin over a soft foam provides sensitivity to light touch, while a second skin over an underlying hard foam extends the force-sensing range. The second sensing skin, while not needed for classifying touch strength in a mechanical testing instrument, proved essential for gauging human touch force because of the high variability in the way those touches are delivered. Measuring the resistance across strip-shaped sensors allows determination of rapid out-of-plane motions, such as tapping, while the use of EIT with area sensors permits the identification of touch modalities that contain spatial information, such as multi-finger presses, and spatial-temporal information such as finger motion. We have been able to study the differences between contact generated by a machine and a human. This new sensing architecture has potential for enriching tactile sensing for co-robots, and machines in general, by distinguishing human touch forces and modalities and by enhancing the safety of contact with humans.

4.6 Methods

Sensing Skin Fabrication: Microwave irradiation [237,238] was used to exfoliate acid-washed graphite flake (Asbury Graphite Mills, Inc.) in an air atmosphere in a standard microwave oven (Kenmore, 1100 W). The flake was placed into a glass vial and the power turned on for 60 seconds, leading to a several hundred-fold increase in volume in one dimension, producing worm-like particles several mm in length [47]. To 10 g of expanded flake was added 1 L of deionized water together with 7.5 g of surfactant (Triton X-100, Sigma-Aldrich) and 30 drops of antifoaming agent (SE-15, Sigma-Aldrich). The mixture was stirred, the container was placed in an ice water bath, and horn sonication (QSonica, Q700) was performed for 19 min at 100% amplitude with a ½" probe tip (solid, tip 201) while the mixture was magnetically stirred. This procedure produces plate-like particles with an average diameter of 10 μm and thicknesses of 10–200 nm [47]. To 12.2 g of the dispersion was added 0.94 g of natural rubber latex (RD-407, ArtMolds).

The stretchable piezoresistive strain sensors were made by spray-coating the aqueous EG/latex mixture onto a rubber membrane with 0.3 mm thickness (sensing strips: ELE International, circular-shaped sensing skins: McMaster Carr, part number: 8611K14). In this work, sensing strips of 11 x 0.8 cm and also larger distributed sensor of 20 cm diameter were produced. For the former, a rectangle of 11 cm x 10.4 cm was formed by spraying (Badger basic spray gun set, model 250-2) over a shadow mask made from painter's tape (ScotchBlue). A total of 10 layers was applied, air-drying for one minute between layers. The coated membrane was scissor-cut

along the 10.4 cm length into 13 strip-shaped pieces, each 0.8 cm wide. Their resistance was 2.37±0.21 kΩ between the two endpoints.

Electrical connections at the two ends of the sensing strip were made with carbon fiber braids (The Composites Store, braided sleeves, 0.1 inches in diameter). Two bundles of fibers (tows) were pulled from a piece of braid, and 1 cm at the end of the combined tows was spread out. The spread area was positioned over the strip and eight drops of the EG/latex suspension were applied by pipette and air dried 7 minutes between drops [175]. The carbon fiber was connected to multi-strand Cu wire with the heat shrink tubing (NTE Electronics, Inc. 1/16'', HS-ASST-10). The total resistance of the strip, including the connections, was 2.43±0.22 kΩ; the resistance of the connectors was < 100 Ω. The gauge factor was measured to be GF = 8.

The sensing strips were glued to each layer of foam (Krylon, Repositionable Spray Adhesive 7020) to keep them from moving during testing, and the skin+foam combinations were stacked so that the strips were positioned directly over each other. The foams were clamped at the four corners to a rigid support, with rigid plates placed between the foam and the clamps.

A circular-shaped sensing skin was fabricated (dia. d = 20 cm) following the same method. The base conductivity of the skin was 0.005 S/sq. The boundary of the skin was glued (on the non-sensor side) onto a rigid ring-shaped fixture (acrylic sheet, 1/16" thick). To a second identical fixture, 16 carbon fiber braid electrodes with uniform spacing were taped onto the ring; a portion of the fiber braid was not taped to allow it to be in contact with the conductive side of the skin. The skin and the electrodes were clamped together by screw-securing the two halves of the

fixture. The skin, together with the fixture, was placed directly over the foam padding (without glue) (Figure 4.2d).

Foams: The soft foam used in this work was an open-cell poly(urethane-ether) (thickness d =1/2 inch, "standard medium foam", foamforyou.com, Foam N' More and Upholstery Inc., Clawson, MI); the stiffer one was an ethylene-vinyl acetate (EVA) foam (d = 1/2 inch, BalanceFrom BFPM-01GY, puzzle exercise mat). The stiffness of the paddings was characterized by indentation load deflection (I.L.D.) [175]. The I.L.D. of the softer padding was 0.4 N/cm^2, and that of the stiffer padding was 6.3 N/cm^2, meaning that the bottom layer was nearly 15 times stiffer.

Distributed Sensing: Electrical impedance tomography (EIT) was employed for distributed sensing. EIT is an algorithm for creating an image showing the electrical conductivity of a bounded area based on voltage measurements made at the boundary [89]. Measurement were made using a current-drive/voltage-measure pattern: a constant current (3 mA, Keithley 2612 source meter) was injected into a pair of adjacent electrodes, and the voltage at the other 14 electrodes was measured (DAQ, NI USB-6225) relative to common ground. To reduce noise, at each position 50 data points were taken at 5 kHz and averaged. For a complete measurement, a 16-channel multiplexer (CD74HC4067, Texas Instruments) switched the current injection location among the 16 electrodes. It took approx. 300 msec to obtain one complete set of data. Multiplexers with faster switch speed may speed up data acquisition. Image reconstruction was performed off-line using the open source code EIDORS (Electrical Impedance Tomography and Diffuse Optical Tomography Reconstruction Software) [101]. A one-step linearized

reconstruction algorithm with a Laplace prior was employed, and 1024 triangular finite elements were used. The baseline conductivity was assumed to be 1 S/sq, and the hyperparameter was set to be 0.3. It took another approx. 400 msec to solve inverse problem and 250 msec to display image under our hardware environment. Note that the speed for image reconstruction is not only related to computer speed, but also programming language. The EIDORS is based on Matlab functions, and C/C++ is recommended for faster reconstruction in final applications [101]. Fast data collection and image reconstruction speed can reach 60 Hz [113].

Characterization with Rigid Probe: Out-of-plane indentation tests were performed with a force transducer (Bose 3330 Series II) outfitted with a polytetrafluoroethylene (PTFE) probe with a circular flat bottom (dia. 1 cm). The force in response to a programmed vertical displacement waveform was measured by the force transducer (force range 3000 N). Simultaneously, the resistance over the sensing strip was measured using a voltage divider and a DAQ (NI USB-6009, 14 bit, at 5 kHz sampling rate). The resistance data were smoothed to reduce noise by averaging 20-point intervals.

Human Touch Tests: Preconditioning has been recommended for conductive polymer composite sensing materials [39] because their response is history-dependent. This was done by applying a force at least as large as the greatest force in subsequent tests using the protocol of three “strong” presses, as judged by the person, waiting 30 seconds between presses. Touch test data were collected immediately after preconditioning. The sequence of presses was from low to high force and from short to long hold time. The resistance change in response to different touch

modalities was recorded in another set of experiments. Rubbing and sliding were along the length of skin1.

Chapter 5. Quantitative Information (Intensity and Size) from Piezoresistive EIT Tactile Sensors

In Preparation
Ying Chen, Miao Yu, Hugh A Bruck, Elisabeth Smela

Co-author contributions: The idea of quantitatively analyzing EIT tactile sensing comes from the discussion among all authors. Ying Chen conducted simulation analysis, proposed spatial correction method, conducted the experiments, and analyzed the data. All authors contributed to writing the text and making the figures.

5.1 Abstract

Compliant tactile sensing has received significant attention in physical human-robot interaction. The primary interest for tactile sensing is to know how many touches are there and how strong are they. However, there have been challenges in implementing tactile sensor in traditional "sensing arrays", where the associated supporting electronics become more complex with an increasing number of "pixel" elements. An alternative approach to implementing area tactile sensing capabilities is to employ an imaging technique based on boundary measurements called electrical impedance tomography (EIT). However, current efforts on EIT tactile sensing have focused primarily on qualitative demonstration. To better understand how to achieve quantitative information from EIT tactile sensors, we investigate the effect of a reconstruction parameter known as the *hyperparameter*, and we propose to select an optimal hyperparameter based on the number of artifacts in the image. The approach we have taken is based on using

piezoresistive tactile sensors, which we have been used to obtain quantitative information by investigating spatial dependency, effect of background conductivity, and memory effects associated with components involved in tactile sensing. We propose a spatial correction method to truthfully detect the intensity and the size of a stimulus at different locations, which is validated from both simulation and experimental results using a piezoresistive tactile sensor. For area sensors that are fabricated with non-uniform background conductivity, we determined that correct results can be obtained by using the actual background conductivity for reconstruction. For materials with memory effect, we investigate the impact of the non-recovered conductivity change from a previous stimulus on a subsequent one, which are at the same or a different location.

5.2 Introduction

Compliant touch sensors have received wide attention in physical human-robot interaction. To allow robots to detect tactile stimuli in an unstructured environment, touch sensors should be able to function over an area. However, there have been challenges in implementing them in traditional "sensing arrays" to obtain details of the discrete touch information over large area, where spatial resolution requires a large number of "pixel" elements. The associated supporting electronics become difficult to implement due to increased sensing elements, especially if the sensing array has to be mechanically flexible for minimized contact forces or for better conformity to contact surfaces. Recently, a continuous area sensing technique called electrical

impedance tomography (EIT) has been employed in tactile sensing as an alternative to overcoming some of the limitations using conventional sensing arrays [123].

EIT is an imaging technique originally developed for reconstructing internal conductivity change of a sensing medium from measurements that are made only at the boundary. The most common use of EIT is to reconstruct the difference in conductivity distribution of a sensing medium between two time instances, also called time-difference EIT [95]. EIT was originally applied in the medical field in the 1980s. Medical EIT is used to monitor the change of electrical conductivity of a human tissue by placing electrodes on the surface of the body. For example, EIT has been used for monitoring ventilation by detecting air content of the lung [239], whose conductivity changes as a human inhales. Comprehensive reviews on EIT technique can be found in references [87-90,95].

Attracted by its non-invasive boundary measurement style, EIT was first introduced in compliant tactile sensing in the 2000s by Nagakubo et al. [240]. Since then, compliant EIT tactile sensors, which were made of various conductive materials, have emerged [123]. Conductive compliant sensing materials that have shown successful implementations of EIT sensors include fabrics [111,113,115,121], rubber [112,114], carbon particles [116,119], exfoliated graphite [152], and ionic liquids [122]. Capability of EIT tactile sensors for area sensing has been shown by detecting the number and position of multiple stimuli [112,113,124], demonstrating image amplitudes varied by touch strength [116,117,122], mounting sensors over robot surfaces for area sensing [111,117,240], and identifying touch modalities directly based on reconstructed images [111,124,240] or by a classification method [117].

However, quantitative analysis on EIT tactile sensors is rare, and investigation of spatial dependency of tactile information (e.g. intensity and size) from EIT sensors has not been done. Visentin et al. experimentally observed different boundary signals under loads with different sizes from an EIT tactile sensor [118]. Russo et al. quantitatively compared the performance of different EIT measurement strategies on detecting various loading conditions from a touch sensor [121]. Although EIT has been used extensively for a long period of time in the medical field, practical considerations on EIT reconstruction in the context of tactile sensing have not been fully investigated.

EIT reconstruction is inherently an ill-posed problem, and proper selection of a reconstruction parameter, known as the *hyperparameter*, is important for solving ill-posed problems. The hyperparameter should be small enough to get an accurate solution, but should be large enough at the same time to get a stable reconstruction [99]. Different methods have been proposed for selecting a proper hyperparameter [99,241], including heuristic methods, L-curve, noise figure, and a method based on the best resolution. Research has shown the following: (1) The heuristic method is most commonly used, but is less repeatable; (2) The L-curve fails in certain cases; (3) The noise figure leads to a wide range of optimal hyperparameters [242]; (4) The method based on the best resolution is to select hyperparameter when an "onset of stability" is present [99]. The method based on the best resolution is beneficial for tactile sensing, because best image resolution can be obtained and artifacts that are not true tactile stimuli can be ruled out. However, this method is not applicable when multiple stimuli are present. The selection of hyperparameter is generally not clearly specified in research of EIT tactile sensors. However,

image quality differs significantly with hyperparameter, so understanding its influence on tactile sensing is important.

To obtain consistent information across an EIT sensing medium, uniform spatial performance is important for tactile sensing. EIT reconstruction is known to be spatial dependent in the medical field [242-245]. To address the spatial dependency issue, Adler et al. proposed a unified approach to provide uniform performance over a list of figures of merit for lung EIT [243]. Researcher in the field of touch sensing have also been aware of [115,240] [111]. Reconstructed images from EIT tactile sensors have demonstrated spatial dependency: Spatial resolution close to the edge of a sensing medium is better than that in the center [240]; sensitivity is higher close to the boundary than that in the center [111,115]. Spatial correction on intensity and resolution is important for tactile sensing, but to the knowledge of the authors no such research exists for EIT touch sensors.

The effect of background conductivity of sensing materials on EIT reconstruction has also not been fully understood. Even in the medical field, the background conductivity is usually vaguely assumed to be a fixed value during EIT reconstruction [246]. For most of the time such assumption is satisfactory, because only the change of conductivity is of interest. For example, for pulmonary monitoring, the relationship between conductivity change and the air volume within the lung was first calibrated, and then the air volume can be estimated based on the calibration [239]. However, the effect of background conductivity becomes significant when a comparison is made among different locations. Grychtol et al. pointed out that an incorrect background conductivity assumption would lead to a misleading reconstruction result: they

showed that the sensitivity at a more conductive region is higher than that at a less conductive region [246]. Tactile sensors that are fabricated by laminating conductive materials usually have a variation in the conductivity distribution. Such variation is more severe when a sensor is made into a large size for EIT area sensing. In addition, tactile sensors that are made of different sensing materials have different background conductivities. The effect of non-uniformity and variations in the magnitude of conductivity on EIT touch sensors has not been studied, and it will be for the first time investigated in this dissertation.

In this chapter, we analyze obtaining quantitative information – spatial dependency of intensity and size – from piezoresistive EIT tactile sensors. We propose to select an optimal hyperparameter that is the minimum value to obtain an image without artifacts. Dependency of optimal hyperparameter on noise level and background conductivity is illustrated. Figures of merit for EIT imaging that are important for interpreting tactile stimuli are developed. Previous work on EIT tactile sensing has demonstrated detection of number of touches and magnitude varied by touch strength [111,112,114,116-119,122,124]. Here, we focus on spatial dependency of tactile information, e.g. touch intensity and contact size. To obtain consistent spatial information, a spatial correction process performed on the intensity and size of a reconstructed stimulus is proposed and evaluated. The spatial correction method is validated from a piezoresistive EIT tactile sensor. The effect of background conductivity of the sensing material on EIT reconstruction is investigated in terms of the uniformity of the background and the memory effects of the sensing material.

5.3 Results

5.3.1 Metrics

Image quality of EIT reconstruction has been evaluated in aspects of spatial resolution, reconstruction amplitude, position error, etc. Figures of merit have been proposed in many groups [243,244] [245]. Here, we define metrics that are important for EIT tactile sensing.

To better illustrate the metrics, we assume a tactile stimulus that is simplified as a solid circle is added in the center of a circular sensing medium, as shown in **Figure 5.1**a. The radius of the sensing medium is r = 1. The stimuli that is centered at $C_{stim.}$ (coordinates: $\rho = 0.5, \theta = 0$) has a radius of 0.2, and its area is labeled as A_t. The conductivity of the stimulus (assuming the change relative to the background as $ds = 0.4S_0$) is different from the conductivity of the sensing medium (S_0), mimicking the conductivity change caused by a tactile stimulus over a piezoresistive sensing medium.

To obtain boundary data, adjacent drive strategy was used in this dissertation. Figure 5.1b illustrates one of the current injection patterns, where the driving current is injected into a pair of adjacent electrodes. The boundary voltages are measured at the rest electrodes. The position of the driving current rotates around all pairs of adjacent electrodes for a complete boundary voltage measurement.

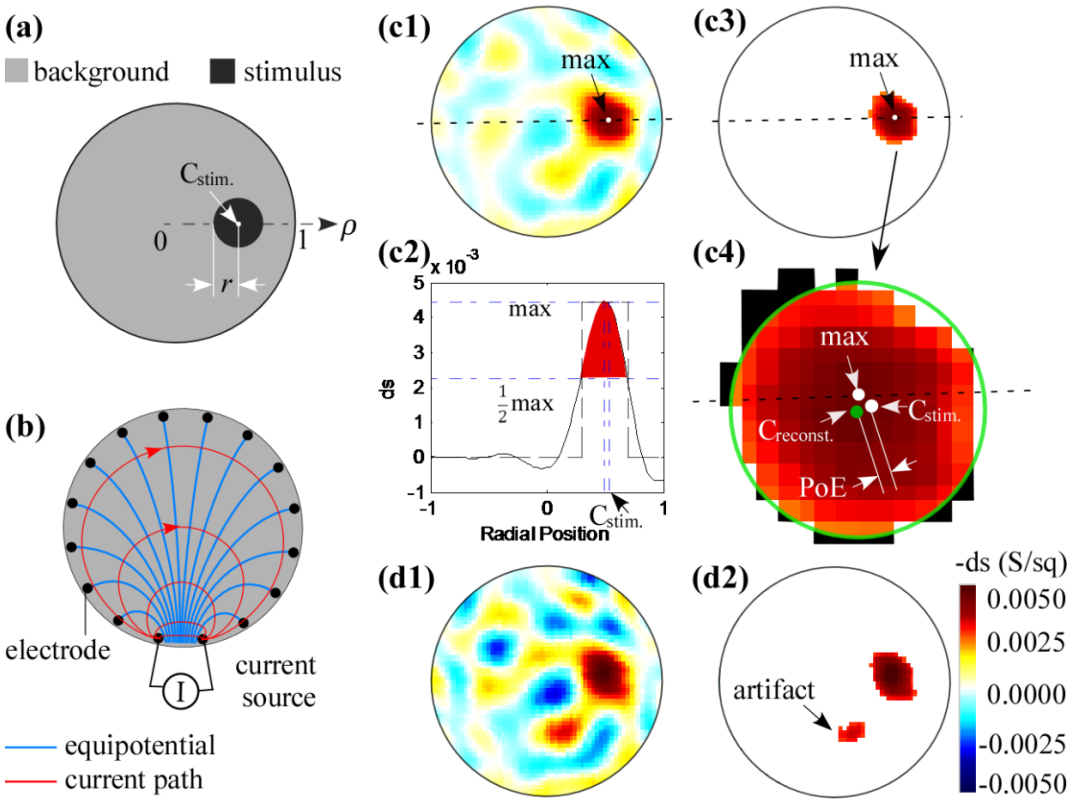

Figure 5.1: Metrics. (a) A circular EIT-based sensing medium with 16 electrodes at the boundary. Current is injected through two adjacent electrodes. (B) An example of simulation: a target with different conductivity from the sensing medium is placed at (x, y) = (0.5, 0). (c) Reconstruction result with a proper reconstruction parameter. (c1) reconstructed image. (c2) cross section profile through the location of the peak. (c3) half amplitude image. (c4) zoom-in of the reconstructed target in the half amplitude image. (d1) Reconstruction result with an improper reconstruction parameter and (d2) its half amplitude image with artifacts.

To simulate the noise in EIT measurement, different levels of noise are added to the boundary measurements. The noise level in this chapter is defined by root mean square (RMS) of n values$\{x_i\}$ $i = 1, 2, \dots, n$, $RMS = \sqrt{\frac{1}{n}\sum_1^n {x_i}^2}$. In this chapter, x_i represents the subtraction of boundary differential voltages between a current state and a reference state, and n = 16x13 = 208 non-zero data used for EIT reconstruction. Three noise levels were selected as low noise with RMS = $3\text{x}10^{-5}$ (V), medium noise with RMS = $1\text{x}10^{-4}$ (V), and high noise with RMS = $3\text{x}10^{-4}$

(V). White noise with the selected RMS value was added to noise-free data in simulation, using MATLAB function wgn. Figure 5.1(c1) shows a reconstructed image based on the case of Figure 5.1a with medium noise. The color indicates the conductivity change due to performing tactile stimuli on a piezoresistive sensing medium.

- *Peak Value*: Peak value is defined as the maximum value (conductivity change) in the reconstructed image. The location of the peak value is indicated in Figure 5.1(c1). The cross section profile through the peak value is plotted in Figure 5.1(c2). The area with reconstructed value that is higher than half peak value is shown in Figure 5.1(c3).
- *Size*: Size of the reconstructed stimulus is determined based on Figure 5.1 1(c3). To evaluate the size relative to the sensing medium, size, S_1, is defined as the area of the reconstructed stimulus ($A_{1/2}$) (Figure 5.1 1(c3)) divided by the area of the sensing medium (A), i.e. $S_1 = \frac{A_{1/2}}{A}$. To evaluate the size relative to the simulated case, size, S_2, is defined as the area of the reconstructed stimulus ($A_{1/2}$) (Figure 5.1 1(c3)) divided by the area of the simulated stimulus (A_t), i.e. $S_2 = \frac{A_{1/2}}{A_t}$.
- *Position Error (PoE)*: Position error is defined as the distance between the center of the simulated stimulus C_{stim} and the center of the reconstructed stimulus $C_{reconst}$ (Figure 5.1(c4)). $C_{reconst}$ is defined as the weighted center of the reconstructed stimulus in Figure 5.1 1(c3), which is calculated from $C_{reconst} \cdot \sum_{i=1}^{n} V_i = \sum_{i=1}^{n} C_i V_i$, where i=1, 2, …, n indicating the elements constructing the half maximum image in Figure 5.1(c3), V_i is the reconstructed value, and C_i is the coordinate of the reconstructed value, the the sum is performed over the area of the reconstructed stimulus in Figure 5.1 1(c3). The sign of PE is defined as: positive (+) means the reconstructed center is away from the center of the

medium, and negative (-) means the reconstructed center is approaching the center of the medium.

- *Shape Deformation (ShD)*: Shape deformation is used to evaluate the skewness of the reconstructed stimulus from the circular simulated one. In Figure 5.1(c4), the circle (in green) centered at $C_{reconst}$ has the same area as the reconstructed target area, i.e. $A_{1/2}$. The area of the reconstructed stimulus that is outside this circle is indicated in black, whose area is $A_{outside}$. Thus, shape deformation is defined as $SD = \frac{A_{outside}}{A_{1/2}}$.
- *Artifacts*: Selection of hyperparameter in EIT is important to the quality of the reconstructed image. Figure 5.1(d) shows a reconstructed image under assumption of Figure 5.1a using a hyperparameter ($\alpha = 0.005$) that is too small to produce a stable image, compared by the image using a proper hyperparameter ($\alpha = 0.05$) in Figure 5.1(c1). Figure 5.1(d2) shows the image whose conductivity change is higher than half peak value. Except the simulated stimulus, an artifact that is not true stimulus exists in the image. To obtain useful information for tactile sensing, in this chapter, the optimal hyperparamter is determined as the minimum value when the number of artifacts is zero (detailed procedure is in section 5.3.2.1).

5.3.2 Simulation Results

5.3.2.1 Optimal Hyperparameter

The hyperparamter α adjusts the weight of the regularization term for an ill-posed problem. The value of α balances the trade-off between the accuracy and robustness of the solution. Proper

selection of α is important to image quality. This section demonstrates the procedure of selecting an optimal α based on the number of artifacts and investigate the effect of background conductivity and noise level on the selection.

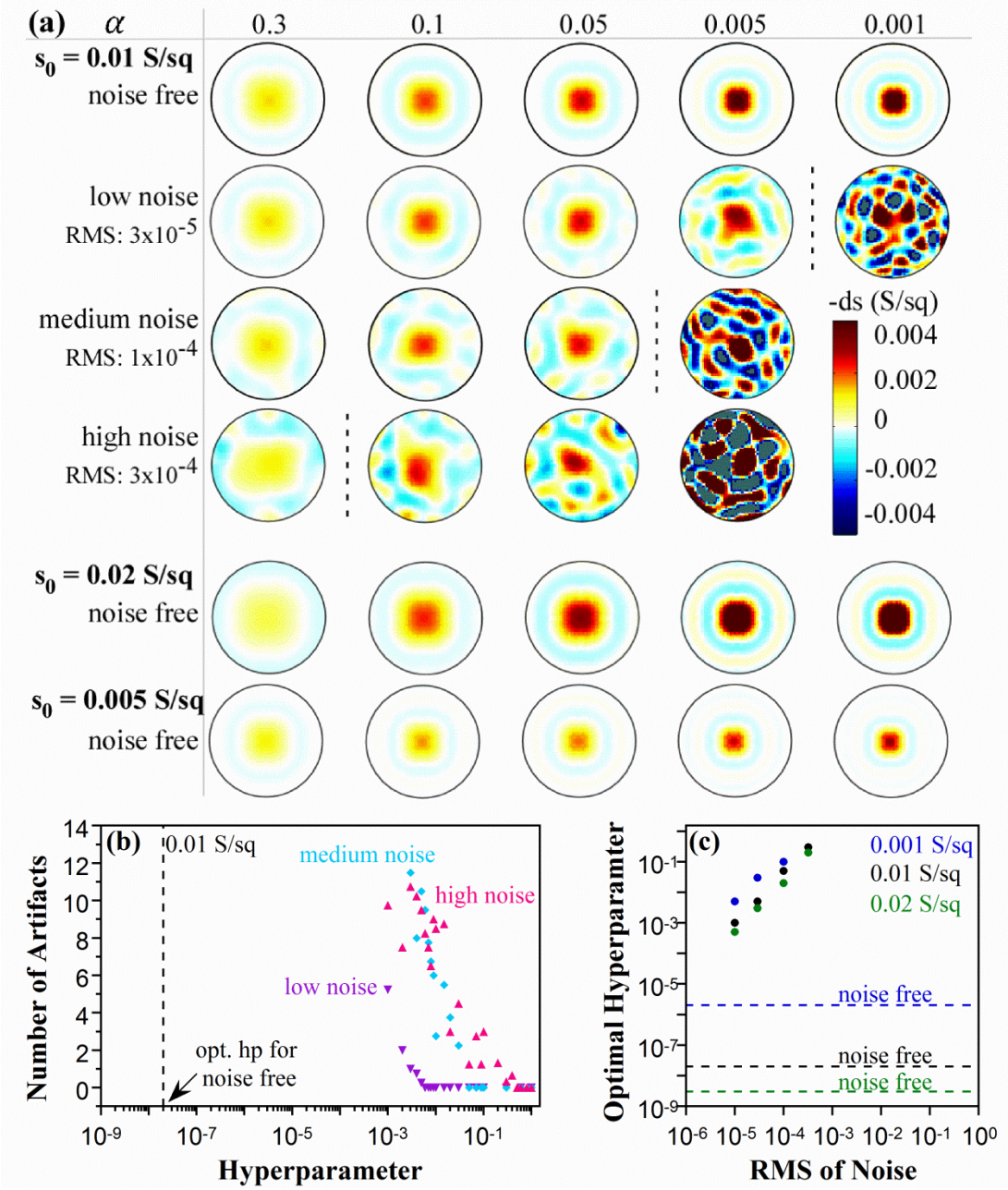

Figure 5.2: (a) Reconstructed images while using different hyperparameters for background conductivities of 0.01 S/sq in cases of noise free, low noise, medium noise, and high noise. Images at noise free case for background conductivities of 0.02 and 0.005 S/sq are also shown. (b) Number of artifacts as a function of hyperparameter for background conductivity of 0.01 S/sq with low, medium, and high noise. The optimal hyperparamter for noise free is indicated by arrow. Below this value, the reconstructed image is broken. (c) Optimal hyperparameter as a function of noise level for background conductivities of 0.001, 0.01, and 0.02 S/sq. The optimal hyperparamters for these three background conductivity at noise free case are indicated by the horizontal dashed lines.

To explicitly show the effect of α on image quality, reconstructed images of a circular stimulus centered at the center of the medium using different values of α are shown in **Figure 5.2**a. The stimulus has a radius of 0.2, and its conductivity change is ds = $0.4S_0$. α varies from high 0.5 to low 0.001, and the noise level varies from noise free, low noise, medium noise, and high noise for background conductivity S_0 = 0.01 S/sq. In Figure 5.2a, without noise, the reconstructed images for all hyperparameters show a relatively clean reconstructed stimulus. The overall intensity decreases as α is decreasing, and the size of the circular reconstructed stimulus is increasing. The blue rings around the reconstructed target are the ringing effect of EIT reconstruction [243]. At low noise, the reconstructed images show more scatters, especially when α is small. A distinct threshold (indicated by a dashed black line in Figure 5.2a) occurs between $\alpha = 0.001$ and 0.005 , above which it is easy to see the stimulus and below which the image shows artifacts that are not the stimulus. Simulation results show that $\alpha = 0.005$ is the smallest hyperparameter that no artifacts exist in the image, which we defined as the optimal hyperparameter. Above optimal α, images for low noise cases resemble the noise free case. Increasing the noise level, the threshold moves towards larger α, and simulation study shows that the optimal α for medium noise is 0.05 and for high noise is 0.3. Scattering is more severe for high noise cases, and larger α is required to obtain a robust solution. More investigation on optimal hyperparameter for stimuli with various intensities is presented in Appendix G 2.

The optimal α selected by the proposed method is not affected by the number of stimuli. Figure 5.3 shows the selection of α for one stimulus, two stimuli, and three stimuli, with the same level of noise level and stimuli intensity. With α not lower than 0.05, reconstructed images show

correctly the number of simulated stimuli; with α not higher than 0.005, reconstructed images are unstable, with un-desired artifacts. Note that the optimal α for the three cases may differ by refining the selection of hyperparameters.

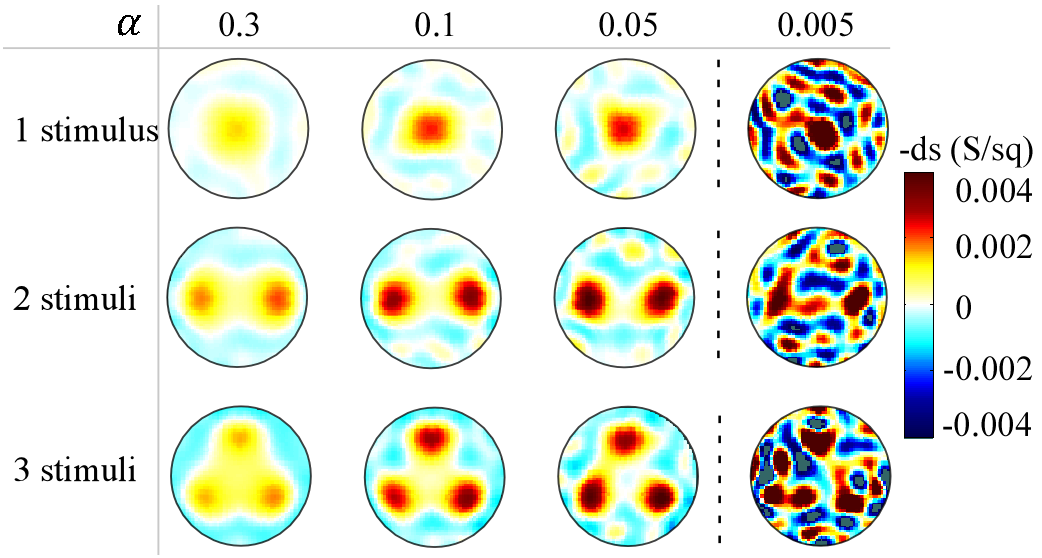

Figure 5.3: The effect of one stimulus, two stimuli, and three stimuli on the selection of optimal hyperparameter.

Reconstructed images from different background conductivities of S_0 = 0.02 S/sq and S_0 = 0.005 S/sq are also shown in Figure 5.2a. The same *relative* conductivity change, i.e. $\frac{ds}{S_0} = 0.4$, of the stimulus is simulated for different cases. The range of the background conductivity investigated in this chapter is based on the conductivity that is practical for compliant tactile sensors [113,115,175]. The intensity of the images, i.e. conductivity change, is higher for larger background conductivity. This is because the simulated change of conductivity is larger for high conductivity background, and the image just shows the change of conductivity.

The number of artifacts as a function of hyperparameter at different noise levels for background conductivity of $S_0 = 0.01\ S/sq$ is shown in Figure 5.2b. Optimal α is the minimum hyperparamter when the number of artifacts is zero. The optimal α for noise free case is $2x10^{-8}$, which is indicated by the dashed line. Larger optimal α is required at high noise levels.

Optimal α as a function of noise levels at different background conductivities is shown in Figure 5.2c. Corresponding reconstructed images are shown in supporting information (Appendix G1). Larger optimal α is required when the noise is higher, for all cases of background conductivities. The optimal α required for smaller background conductivities is higher than that for larger background conductivities. Considering that higher value of α leads to bigger mismatch between the regularized problem and the original problem, background conductivity should be low enough that a relative small α can be used for reconstruction. This behavior is important to while selecting sensing material for tactile sensors. Optimal α for noise free cases follows the same trend that a larger optimal α is required for lower background conductivity. The value of optimal α for noise free is much smaller than for noisy cases.

Understanding the effect of α on image reconstruction is a basic step towards EIT application. The method to select optimal α based on the number of artifacts comes from the needs in tactile sensing that correctly identifying the number of targets is more important than achieving higher resolution. Optimal α is related to noise levels, background conductivities, and simulation settings.

5.3.2.2 Spatial Sensing

Spatial Dependency and Correction Method

EIT tactile sensors detect changes of electrical conductivity caused by tactile stimuli in the sensing medium. Consistent detection of the tactile stimuli, e.g. intensity and area, throughout the sensing medium is important. To investigate the spatial performance for the purpose of developing a spatial correction method, we conducted a simulation study in this section, and then conducted experimental validation of the correction method from our piezoresistive EIT tactile sensor in section 5.3.3.

To illustrate the spatial performance along the radial direction of a circular EIT sensing medium (r = 1 and $S_0 = 0.01\ S/sq$), a stimulus (r = 0.2, $ds = 0.4S_0$) is added at nine different positions, from the center towards the boundary of the medium, i.e. ρ = 0, 0.1, 0.2, 0.3, 0.4, 0.5, 0.6, 0.7, and 0.8. Medium noise is added in simulation, and the optimal $\alpha = 0.05$ is used. For comparison, cases without noise is also simulated, and the optimal α for noise free cases is $2x10^{-8}$. **Figure 5.4** a1 and b1 selectively illustrate when the stimuli are added at the center (ρ= 0) and at half way from the center (ρ= 0.5) respectively.

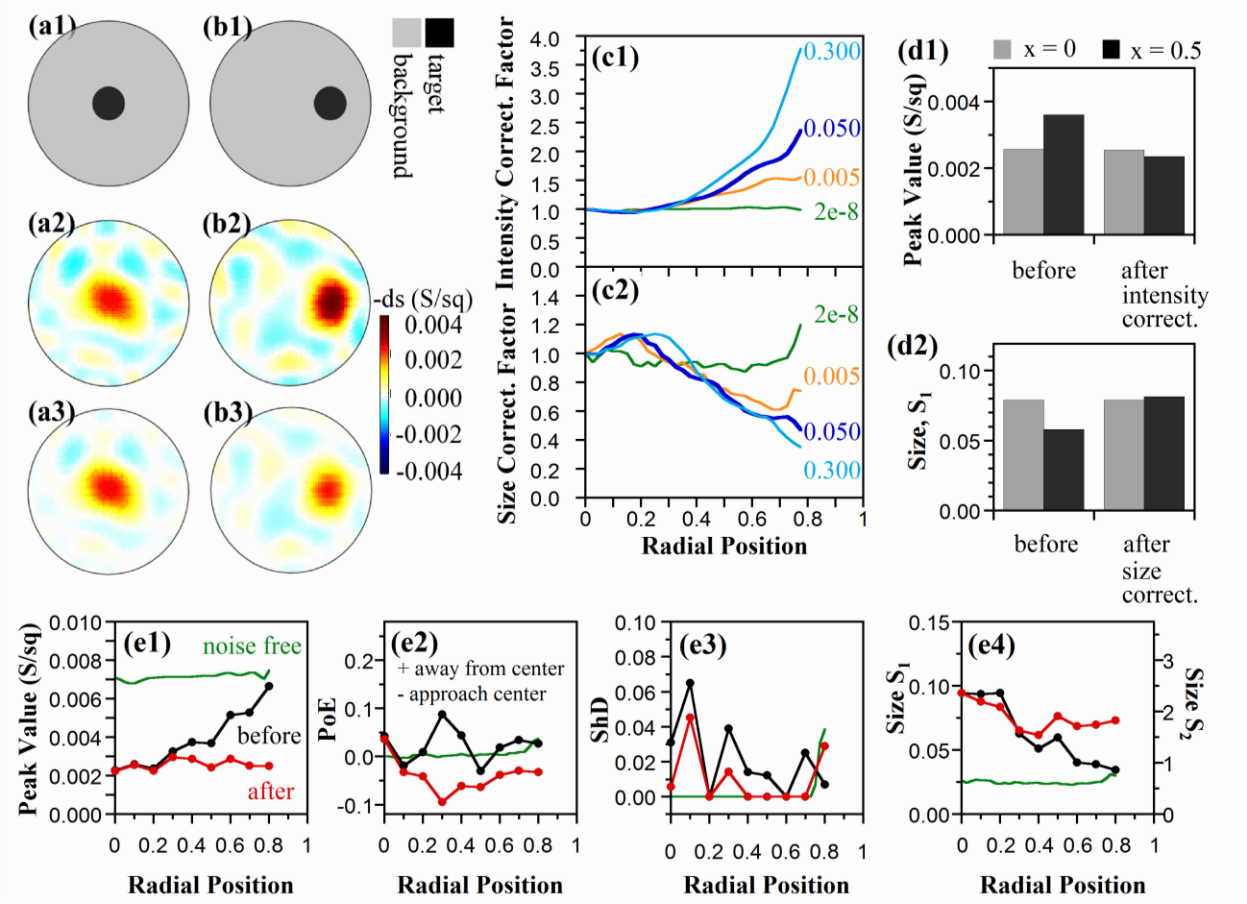

Figure 5.4: Targets at (a1) center and (b1) off-center. Reconstructed images for (a2) center target and (b2) off-center target without correction with medium noise. After intensity correction, reconstruction images for (a3) center target and (b3) off-center target. Comparison of (ci) peak value and (cii) size before and after intensity or size correction for center and off-center targets. (d1) Peak value, (d2) size, (d3) position error, and (d4) shape deformation for noise free (green), before (black) and after (red) scaling of medium noise (hp=0.05). Scaling matrix for (e1) intensity and (e2) size by using different hyperparameters.

Figure 5.4 a2 and b2 show the reconstructed images selected from stimuli at the center and 0.5 away from center. The peak value of the reconstructed image is higher and the size is smaller for the case of ρ= 0.5 than that of ρ = 0. The spatial performance in terms of peak value, position error, shape deformation, and size for all the nine positions is shown in Figure 5.4e, black curves for medium noise and green curves for noise free. Peak value (Figure 5.4 e1) and size (Figure

5.4 e4) along the radial direction is relatively uniform for noise free case compared with that of medium noise case. Position error (Figure 5.4 e2) and shape deformation (Figure 5.4 e3) is much smaller for noise free cases than that of noisy case. In the noisy case, peak value increases and size decreases towards the boundary of the medium.

To investigate the spatial dependency on hyperparameters, the spatial performance is obtained in noise free cases but using different hyperparameters. For better comparison, the spatial performance is scaled to the center position for peak value and size, as shown in (Figure 5.4 c). Higher spatial dependency exists while using higher α. The spatial performance for both intensity and size in different directions are essentially similar (see Appendix G 3 for more information). To correct the spatial dependency, a straightforward way is to correct the reconstruction by its position. To correct the intensity, the curve for the scaled peak value in Figure 5.4 e1 is served as intensity correction factor, that every value in the image is divided by the factor at the same radial position. In Figure 5.4 e2, size correcting factor along the radial direction is non-linear and non-monotonic. From the center to the edge, reconstructed size first increases a bit and then decreases towards the boundary. The curve of the scaled size is smoother for higher α. This can be explained by the function of hyperparameter that larger α generates more robust solution. To correct size along the radial direction, the reconstructed size can be corrected by dividing by the factor for the corresponding α.

For the noisy cases, peak value, position error, and shape deformation after intensity correction is shown in Figure 5.4e1-3 red curves, and size after size correction is shown in Figure 5.4 e4 red curve. Both peak value and size is corrected into a more uniform performance. Position error is

higher after intensity correction, and the reconstructed center is approaching the center of the medium. This is because intensity correction scales down more for the region that are close to the boundary. The reconstructed center (calculated as the weighted center) after intensity correction is pushed towards the center of the medium. Shape deformation is slightly smaller after intensity correction. Reconstructed images after intensity correction for stimuli at the center and at ρ= 0.5 are shown in Figure 5.4 a3 and b3. A comparison before and after correcting intensity or size is shown in Figure 5.4d.

Non-uniform spatial performance comes from the regularization process over the ill-posed problem. When the hyperparmeter is large, e.g. for the medium noise case, obvious non-uniform behavior is observed for reconstructed intensity and size reconstruction. When the hyperparameter is small, e.g. the value used in the noise free case, spatial performance is uniform. Smaller hyperparameter leads to fewer mismatches between the regularized problem and the original one. Therefore, the level of spatial dependency is related to the value of the hyperparameter.

Correction Factor

Tactile stimuli with unknown intensity and contact area complicate EIT tactile sensing. It is of interest to investigate the effect of different touch stimuli on the proposed spatial correction method. In addition, background conductivity of tactile sensors is varied by using different

sensing materials and fabrication. The spatial dependency on background conductivity is also interested.

Spatial correction factor for intensity and size is obtained for stimuli with different strengths, different sizes, and different background conductivities. To investigate how the correction factor vary with touch strength, stimuli with three different relative conductivity changes $\frac{ds}{S_0} = 0.2, 0.4, and\ 0.6$ was selected. The size of stimuli and background conductivity in this case is $r = 0.2$ and $S_0 = 0.01\ S/sq$. To investigate how the correction factor varies with size, stimuli with three different sizes $r = 0.1, 0.2, and\ 0.3$ were selected. The relative conductivity change and background conductivity in this case is $\frac{ds}{S_0} = 0.4$ and $S_0 = 0.01\ S/sq$. To investigate how background conductivity affects the correction factor, three background conductivities $S_0 = 0.005, 0.01, and\ 0.02\ S/sq$ were selected. The target intensity and size is chosen to be $\frac{ds}{S_0} = 0.4$ and $r = 0.2$ with a hyperparameter of 0.05.

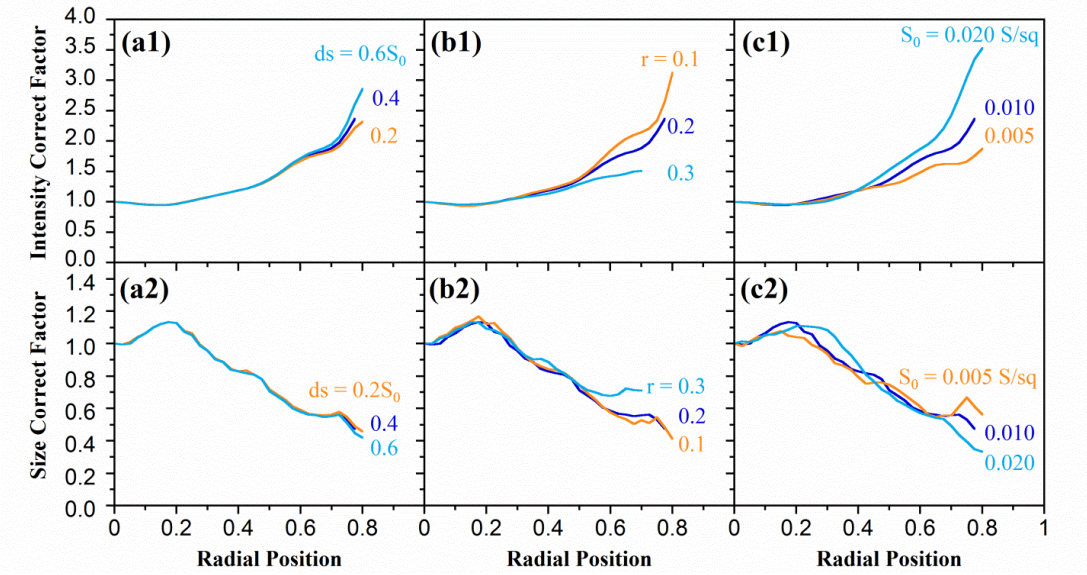

Figure 5.5: Scaling matrix for different (a) target intensity, (b) target size, and (c) background conductivity.

Figure 5.5 shows the intensity and size correction factor along the radial direction. Factors are obtained by dividing the peak value and size of the reconstructed images by the value at the center. Figure 5.5 a shows the dependency of correction factor on intensity of the stimuli. Curves of intensity and size correction factor for all three target intensities overlap, except a small portion close to the edge. Figure 5.5 b shows the dependency of correction factor on size of the stimuli. Curves of intensity and size correction factor overlap for different sizes of stimuli between radial position $\rho = 0 - 0.5$. Figure 5.5 c shows the dependency of correction factor on background conductivities. Curves of intensity correction factor overlap from center to $\rho = 0.4$ for all three background conductivities, and separate beyond $\rho = 0.4$. Intensity correction factor for higher background conductivity is higher than that of lower background conductivity. This is because the relative conductivity change of the stimuli for different background conductivities was the same, and the reconstructed value reflects the change in conductivity. Therefore, the intensity of the image is larger for higher background conductivity. Curves of size correction

factor roughly overlap for all three background conductivities. Curves of size correction factor demonstrate more fluctuation than that for intensity correction factor. This explains why the result of size correction is not as good as intensity scaling (section 5.3.2.2).

The proposed intensity and size correction method is invariant to different intensities of stimuli. This is good because the intensity and size of touch stimuli is unknown, yet the same correction method can be used. The intensity correction factors depend on sizes of stimuli and background conductivities. The size correction factors show higher variation than intensity correction factors for different stimuli sizes and background conductivities. Information on the background conductivity of tactile sensors is important when comparing results from different sensors.

5.3.2.3 Effect of Background Conductivity

Non-Uniform Conductivity on Reconstruction

Tactile sensors that are fabricated by deposition would result in a non-uniform distribution of background conductivity. Non-uniformity is more severe when sensors are fabricated in large area. Information on background conductivity may or may not be available for EIT reconstruction, so the effect of non-uniform background conductivity on EIT reconstruction is investigated in cases that users either know or not know the actual background conductivity.

Assume a circular EIT piezoresistive sensor has non-uniform background conductivity, as shown in **Figure 5.6** a1. The left and right half of the sensing medium have different conductivity,

$S_1 = 0.01\ S/sq$ and $S_2 = 0.002\ S/sq$ respectively. To mimic the situation that identical tactile stimuli are performed over different conductivity regions, relative conductivity changes that are induced by identical stimuli should be the same. This means that gauge factor is assumed to be the same across the sensing medium. Figure 5.6 a2 shows two identical tactile stimuli (r = 0.2) are added at the left ($\rho = -0.5$) and the right ($\rho = 0.5$) half of the sensing medium. Relative conductivity change of the stimuli are the same $\frac{dS_{left}}{S_1} = \frac{dS_{right}}{S_2} = 0.4$. Figure 5.6 a3 shows the across section profile for background conductivity and conductivity after stimuli are performed on the sensor. Due to the different background conductivities, the difference in conductivity before and after adding stimuli is larger for the left than that for the right. Optimal hyperparameter for uniform background conductivities is determined in section 5.3.2.1. The hyperparameter used in this case is selected to be the larger value of optimal hyperparameters among different conductivity regions at medium noise, which was a value of 0.05.

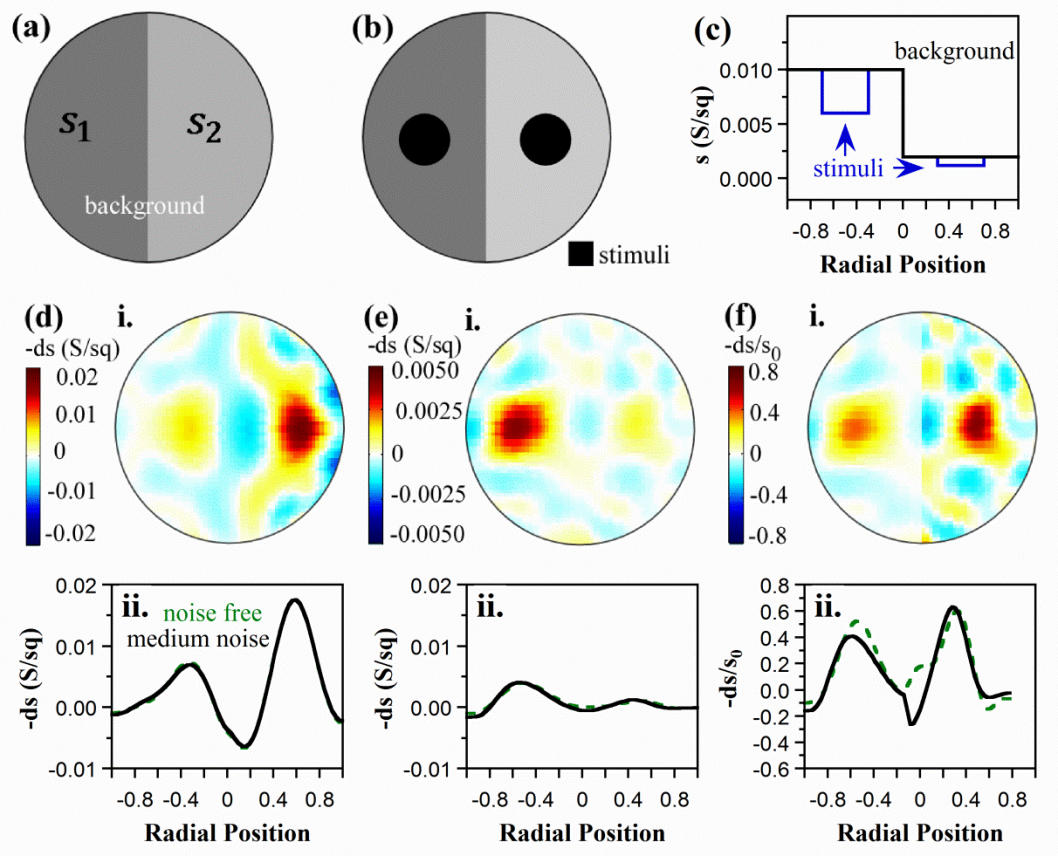

Figure 5.6: Non-uniform s of the skin on image reconstruction. (Keep same gauge factor) (a) non-uniform initial conductivity map, s1 = 0.01 S/sq, s2= 0.002 S/sq. (b) two identical loadings added at different background conductivity. (c) Profile of conductivity before (black) and after (blue) adding the loads. Reconstructed image and profile by (d) assuming background conductivity $S_0 = 0.01\ S/sq$, (e) using actual non-uniform s map, and (f) process the results from (e) to obtain relative s change, ds/s.(hp=0.05).

Figure 5.6 di shows the reconstructed image that the users do not know the actual background conductivity. The background conductivity that is used for reconstruction (Jacobian calculation) is assumed to be $S_0 = 0.01\ S/sq$. Based on the reconstructed value of conductivity change in Figure 5.6 dii, reconstructed stimulus on the right side shows larger change in conductivity, which is not true from Figure 5.6 a3. Figure 5.6 ei shows the reconstructed image that the users apply the actual background conductivity for reconstruction. From Figure 5.6 eii, conductivity change of the left stimulus is larger than that of the right one, which is compatible with Figure

5.6 a3. Therefore, images are more reliable when correct information on background conductivity is used during the reconstruction.

Since the stimuli in simulation mimic touches with identical strength, it would be ideal to obtain relative conductivity change from the reconstruction. Figure 5.6 fi shows the image reflecting the relative conductivity change by dividing the original reconstruction values (in Figure 5.6 ei) with the corresponding background conductivity. The area outside the right-hand reconstructed stimulus shows more scatter because of the dividing process. Cross section profile along the center of the stimuli in Figure 5.6 fii shows that the amplitudes of relative conductivity change, i.e. ds/s0, for the two identical stimuli are not the same. Result from noise free simulation also shows a difference in the amplitudes. This can be explained that regularization applied during EIT reconstruction is an approximation to original ill-posed problem. The solution from a regularized problem is no longer the same with the original one. In addition, since a single hyperparameter is applied for the case with 2-half non-uniform background conductivity, the approximation generated to the two conductivity regions are not the same.

The simulation study shows that information on non-uniform background conductivity is not necessary if only qualitative information of the stimuli is of interest. However, it is important for obtaining quantitative information of the stimuli. To further investigate obtaining quantitative information from non-uniform background conductivity, regularization with multiple hyperparameters corresponding to different conductivity regions might be helpful.

Materials' Memory Effect on Reconstruction

Compliant sensing materials made of conductive polymer composite show memory effect [56]. The memory effect means the conductivity is not recovered to initial value after stimuli are released. Section 0 has shown that the uniformity of background conductivity affects reconstruction results. Non-recovered conductivity due to previous stimuli affects the reconstruction of subsequent stimuli. In this section, the memory effects is investigated for cases that subsequent stimuli are either performed at the same or different locations as the previous stimuli.

Figure 5.7a shows a stimulus (r = 0.2, ρ= 0.5, $ds = 0.4S_0$) performed over an EIT sensor with uniform background conductivity ($S_0 = 0.01\ S/sq$). Assume that the amount of non-recovered conductivity change after releasing the stimulus is $0.5ds$. Figure 5.7 bi and ci show that an identical stimulus as the one in Figure 5.7 ai is loaded at a different location ρ = -0.5 and at the same location ρ = 0.5 respectively. For sensors with memory effect, an identical stimulus performed on a non-recovered background does not produce the same amount of relative conductivity change, but leads to the same final conductivity. Our previous study on sensor signal under identical stimuli over a piezoresistive sensing strip has shown that the same final resistances were obtained independent of whether a stimulus is performed over a sensor without memory from previous loads or over a sensor with non-recovered resistances. Here, we assume that a subsequent identical stimulus leads to the same final conductivity, no matter the location of the stimulus, as shown in Figure 5.7 bi and ci. Medium noise is added to simulation, and the

optimal hyperparamter used for $S_0 = 0.01\ S/sq$ is $\alpha = 0.05$. For reference, simulation is also run without adding noise and using the same hyperparameter $\alpha = 0.05$.

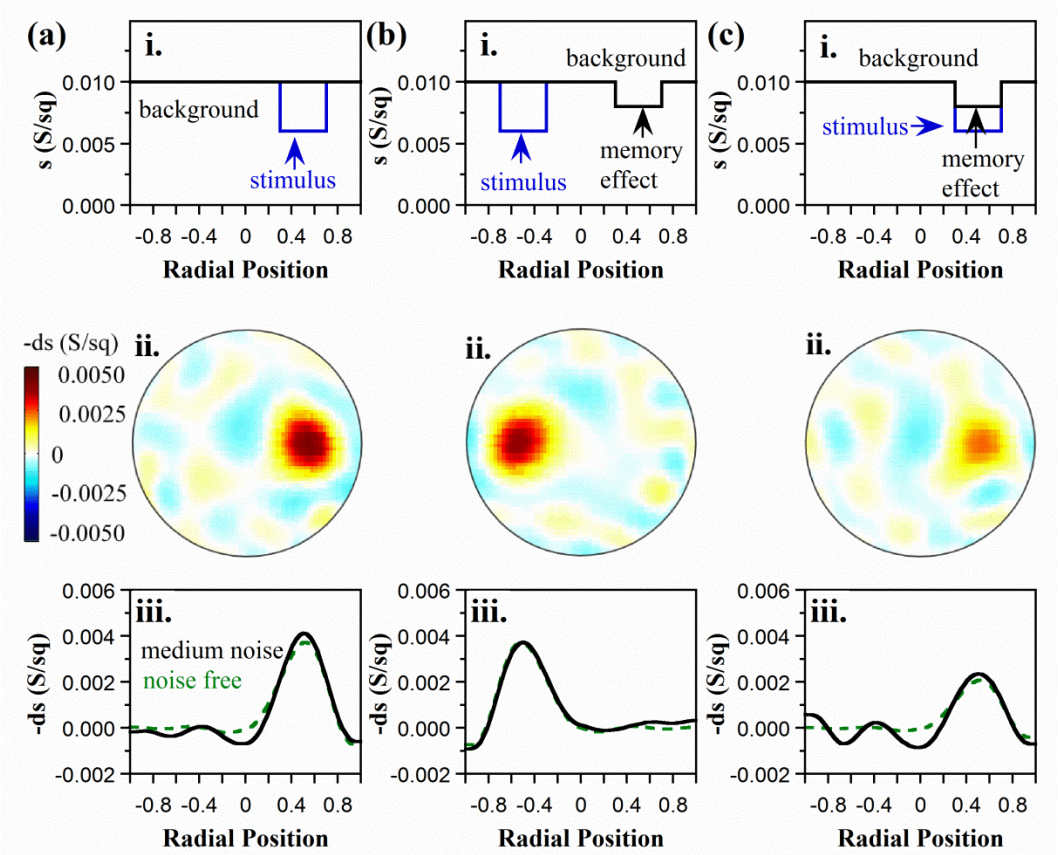

Figure 5.7: Material's memory effect on image reconstruction (Keep same final conductivity). (ai) Case 1: A stimulus added at $\rho = 0.5$ of a sensing medium with uniform background conductivity without memory effect. ii. The reconstructed image with medium noise (hp=0.05) and iii. its cross section profile (black), compared with that from noise free (green) simulation (hp = 0.05). (bi) Case 2: An identical stimulus added at $\rho = -0.5$ of the sensing medium, with non-recovered conductivity change after case 1. (ci) Case 3: An identical stimulus added at $\rho = 0.5$ of the sensing medium, with non-recovered conductivity change after case 1. (a-c) ii. The reconstructed image with medium noise (hp=0.05) and iii. its cross section profile (black), compared with that from noise free (green) simulation (hp = 0.05).

Figure 5.7 a ii. and iii. show the reconstructed image and the cross section of conductivity change for case ai. Figure 5.7 bii shows the reconstructed image for a subsequent stimulus at a

different location as Figure 5.7a. The non-recovered conductivity is at the location of the stimulus in Figure 5.7a. Compared with Figure 5.7 aiii, the cross section profile of conductivity change for the subsequent load at a different location is similar, which means that memory effect does not affect subsequent stimuli at different locations. Figure 5.7 cii shows the reconstructed image for a subsequent stimulus at the same location as that in Figure 5.7 a. The cross section profile in Figure 5.7 ciii is lower than that of Figure 5.7 aiii and biii. This means that sensor's sensitivity is lower for subsequent loads compared with the first load, which is typical behavior for viscoelastic materials such as conductive polymer composites [39].

From these results, it is clear that the non-recovered conductivity change (memory) of sensing material affects detecting subsequent stimuli that are loaded at the same location. However, the EIT reconstruction is able to reflect different conductivity changes under identical loads when the memory effect of the sensing material is considered.

5.3.2.4 Resolution

Section 5.3.2.1 has shown that the hyperparameter affects the size of reconstructed stimulus. Small hyperparameter produces better spatial resolution as long as the noise level is low enough that a smaller hyperparameter can be used. In this section, we investigate the relation between reconstructed cross section profiles and sizes of stimulus, and illustrates the ultimate spatial resolution for EIT reconstruction.

To investigate the relation between cross section profiles and sizes of stimuli, we used stimuli with five different sizes $r = 0.1, 0.2, 0.3, 0.4, and\ 0.5$. The conductivity changes of the stimuli

are the same $ds = 0.4S_0$, and the background conductivity is $S_0 = 0.01\ S/sq$. For the purpose of understanding the limit of EIT reconstruction, no noise is added to the simulation. The optimal hyperparameter is used $\alpha = 2x10^{-8}$.

Figure 5.8a i, ii, and iii show selected reconstructed images of stimuli with radius $r = 0.1, 0.2\ and\ 0.5$. The size of the reconstructed image increases with the size of the stimulus. Figure 5.8iv shows the cross section profile for all stimuli. The slopes of the side profiles are identical for all cases, and the width increases monotonically with the size of the stimulus. Fluctuations exist inside the stimulus. Therefore, noise-free EIT reconstruction reliably reflects the size of a stimulus.

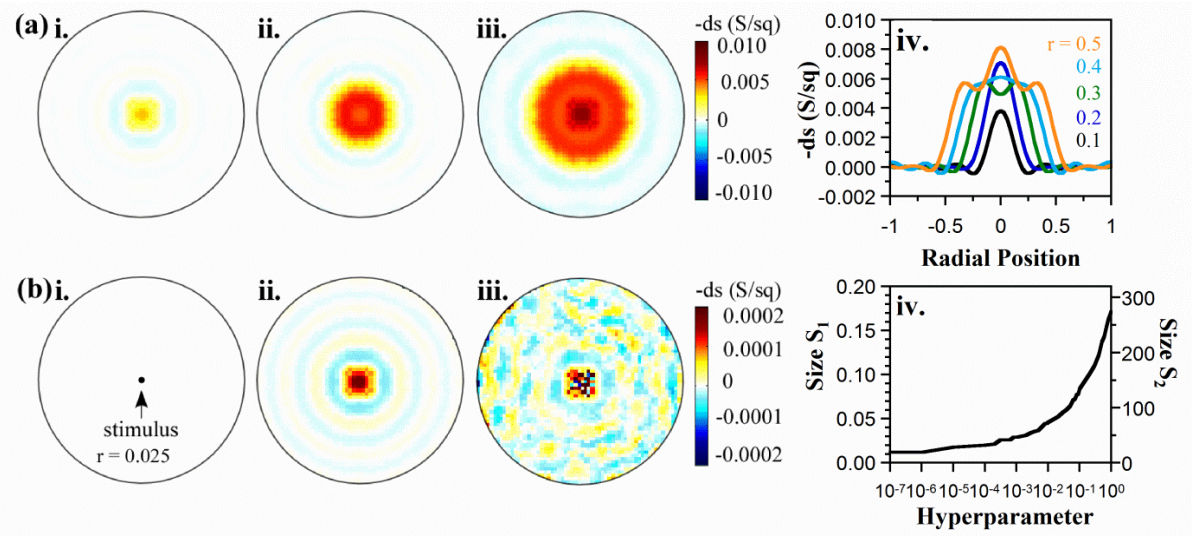

Figure 5.8: (a) Images of center stimuli in noise free case at optimal hyperparameter $2x10^{-8}$ for radius i) 0.1, ii) 0.2, and iii) 0.5. iv. Cross section profiles for increasing radius from 0.2 to 0.5. (bi) A center stimulus with a of 2.5 % of the medium radius. Reconstructed images using hyperparameter ii) $1x10^{-8}$ and iii) $2x10^{-8}$. iv) Reconstructed size by decreasing hyperparameter.

To investigate ultimate spatial resolution, a circular stimulus with radius of $r = 0.025$ is placed at the center of a sensing medium, shown in Figure 5.8bi. The size is the minimum one which is constrained by the finite element model. Intensity of the stimulus, i.e. conductivity change, is $ds = 0.4S_0$, and background conductivity is $S_0 = 0.01\ S/sq$. For the purpose of understanding the limit of EIT reconstruction, no noise is added. Hyperparameters varying from large to small number are used. Figure 5.8 bii shows the reconstructed image at optimal hyperparameter of $2x10^{-8}$, and biii shows the image at hyperparameter of $1x10^{-8}$, which leads to an unstable result. Figure 5.8biv shows the size of the reconstructed image while decreasing hyperparameter till the optimal one. The reconstructed size decreases rapidly when hyperparameter decreases from 1 to $1x10^{-3}$, and the size decreases slower when hyperparameter decreases from $1x10^{-3}$ to $1x10^{-7}$.

5.3.3 Experimental Results

To implement EIT for area tactile sensing, we developed a piezoresistive EIT tactile sensing skin. To quantitatively analyze EIT reconstruction on real tactile sensors, the spatial performance is evaluated. Validation of the correction method proposed in section 5.3.2.2 on the tactile sensor is also presented.

In **Figure 5.9**a, tactile stimuli is conducted on a padded piezoresistive sensing skin with a radius of 10 cm by a cylinder polytetrafluoroethylene (PTFE) indenter (dia. = 1 cm). To investigate the spatial performance, out of plane indentation of 5 mm into the padded sensing skin was controlled by a force transducer (Bose 3330 Series II), and the loading locations were manually

controlled by moving the sensor in horizontal direction. In Figure 5.9b, the boundary of the sensing skin is clamped between two pieces of rigid ring-shaped plates (acrylic sheet, 1/16" thick). Locations of stimuli vary along a radial direction from the center to the edge. Distances between the center of the stimulus and the center of the sensing medium normalized by the medium size are $\rho = 0, 0.1, 0.2, 0.3, 0.4, 0.5, 0.6, 0.7, and\ 0.8$. Six radial directions were tested.

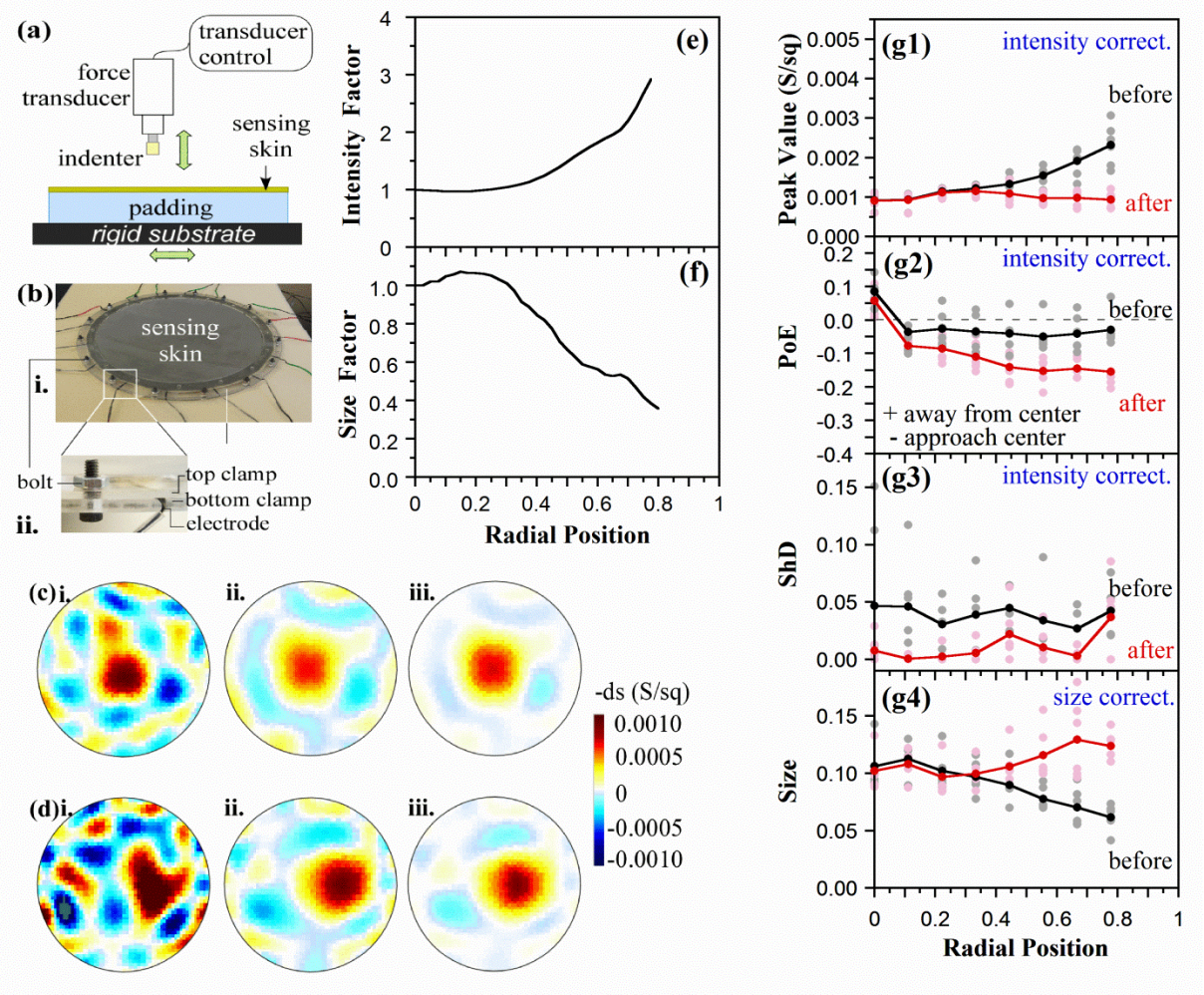

Figure 5.9: Experiments. a) setup. b) sensing mechanism. c,d) scaling matrix e,f) before scaling using hp = 0.05 and optimal hp=0.2, after scaling hp=0.2, g) metrics before and after scaling.

Figure 5.9c and d show examples of EIT reconstructed images for indentations at the center ($\rho = 0$) and off the center ($\rho = 0.5$) respectively. Figure 5.9ci and di are images reconstructed with a hyperparameter of 0.05, which is below the optimal hyperparamter (0.2) for the experimental setup. Artifacts exist in the images. Figure 5.9cii and dii are images reconstructed at optimal hyperparameter with no artifacts. Intensity, i.e. conductivity change, in image dii is higher than that of cii. Spatial performance for all eight loading locations along the radial direction is shown in Figure 5.9g (black) for peak value, size, position error, and shape deformation. Peak value increases and size decreases as the loading location moves from center to edge.

To correct spatial performance, correction factors for intensity and size are obtained from a noise-free simulation for a stimulus with a radius of 0.2. The same hyperparameter of 0.2 from the experimental reconstruction was used for the simulation. Figure 5.9e and f show the intensity correction factor and size correction factor, which are normalized by the value at the center. Intensity and size correction are performed independently, based on the correction process described in section 5.3.2.2. After intensity correction, the peak value, position error, and shape deformation is shown in Figure 5.9g1-g3(red). The peak value is successfully corrected to be uniform along the radial direction. Position error is worsened after intensity correction. Because intensity of the region closer to the edge is corrected more than that closer to the center, and considering that weighted center is calculated to obtain position error, after intensity correction the center of the target is approaching the center. Shape deformation is better after intensity correction, which is similar as simulation. After size correction (Figure 5.9

g4), the mean value for size is better, but the standard deviation is high for those close to the boundary.

This section shows that spatial dependency is also present in an actual piezoresistive EIT tactile sensor, and the proposed method is helpful for obtaining consistent information along the radial direction of the circular sensor. Performance of an actual EIT tactile sensor is more complex compared with simulation. For example, actual loading condition on a stretchable sensor with a padding layer is different from an ideal circular region as is assumed in simulation.

5.4 Conclusions

The application of electrical impedance tomography (EIT) to tactile sensing has been investigated for the purpose of obtaining more quantitative information from the image reconstruction. A method for selecting optimal reconstruction parameter, i.e. hyperparameter, is proposed based on number of artifacts in the reconstructed image. Relation between optimal hyperparameter and the background conductivity of tactile sensors is demonstrated at different noise levels. Results show that a larger optimal hyperparameter is required for lower background conductivity. When noise is present, a larger hyperparameter is also necessary to obtain images with low artifacts. For tactile sensing, we suggest considering the material electrical conductivity and the noise level of hardware in order to successfully employ the EIT technique. Applying the actual conductivity distribution for reconstruction helps in obtaining more accurate information about the tactile stimuli. It was also determined that the spatial

resolution of EIT technique is affected by the noise level of hardware. Since regularization is required to solve an ill-posed problem, a larger regularization parameter is necessary when noise is high.

Performance of the EIT reconstruction has been demonstrated on the problem of spatial dependency by using a piezoresistive sensing skin we have developed. A spatial correction method was proposed and validated through both simulation and experimental data from the piezoresistive touch sensor. For viscoelastic tactile sensing materials, e.g. conductive polymer composites, non-recovered conductivity changes after releasing previous stimuli will also affect the detection of subsequent stimuli that are loaded at the same location. However, there is no effect when subsequent loadings are in a different location.

5.5 Methods

5.5.1 Simulation Tools

Image reconstruction in this work is produced from an open source code EIDORS (Electrical Impedance Tomography and Diffuse Optical Tomography Reconstruction Software) [101], released under General Public License (GUN) [100]. The reconstruction algorithm applied in this chapter is a one-step linearized reconstruction.

5.5.2 Experimental Methods

A piezoresistive sensing film made of a conductive polymer composite, i.e. exfoliated graphite/latex, is fabricated by the method described in [175]. The exfoliated graphite/latex sensing film with a thickness of 67 ± 22 μm was spray coated on a latex membrane (ELE International, 0.3 mm thick) to be a tactile sensing skin. The tactile sensing skin was placed over a padding (2.54 cm thick, open-cell poly(urethane-ether) foam, foamforyou.com, Foam N' More and Upholstery Inc., Clawson, MI), and the padded sensing skin was placed on a rigid substrate.

A circular shaped sensing skin with a radius of 10 cm was made for EIT tactile sensing. 16 electrodes were uniformly spaced along the boundary of the sensor. The electrodes are made of carbon fiber braids (The Composites Store, braided sleeves, 0.1'' diameter), and are attached to the sensor with the exfoliated graphite/latex dispersion. The background conductivity of the sensing skin is around 0.008 S/sq. Direct current with an amplitude of 3 mA from current source (Keithley 2612 source meter) is injected into all adjacent pairs of the boundary electrodes. The Voltages were measured at each electrode by DAQ (NI USB-6225) for all 16 current injection patterns.

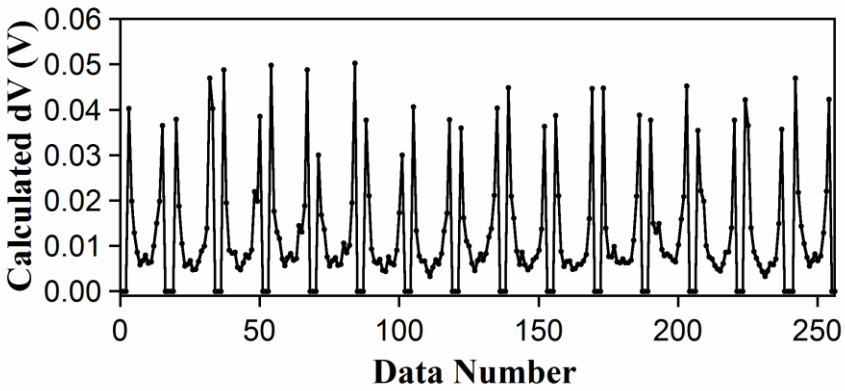

Figure 5.10: A typical set of calculated differential voltages, which is fed into EIDORS.

To obtain a complete set of EIT measurement, 50 samples of voltage are measured sequentially along the 16 electrodes under 16 current drive patterns in our hardware. Differential voltage between adjacent electrodes is calculated by subtracting mean voltages of the 50 samples. Figure 5.10 illustrates a complete set of calculated differential voltage. The data associated with the current carrying electrodes were set to zero, meaning not used by the code. The remaining non-zero data forms a series of U shapes. This set of data is fed into EIDORS for image reconstruction.

The source of noise level may come from the data acquisition equipment (16-bit DAQ used), current source, and sensor itself. Note that good insulation of the electrical wires could reduce the noise level. The standard deviation of the 50 voltage measurements at the boundary electrodes is found highest (1.3×10^{-3} V) at the location far wary from the current carrying electrodes, and lowest (0.8×10^{-3} V) at the location close to the current carrying electrodes. The standard deviation of calculated differential voltages at different loading indentations (comparable to relative conductivity change of 0.1-0.4) was found similar, meaning that target

intensity does not affect the noise. To compare the noise level defined in simulation and the noise level of our hardware setup, calculated differential voltage data without touching the sensor was analyzed over 30 sets of measurements. The range for RMS of one set of data is around $2.0x10^{-4}$ (V)- $2.5x10^{-4}$ (V), which is between the high noise and the medium noise level defined in session 5.3.1.

Chapter 6. Concluding Remarks

6.1 Summary

In this dissertation, the performance of stretchable tactile sensors with underlying compressible padding layers has been investigated, and enhanced sensing capability has been successfully implemented by developing a novel multi-layer sensing system and employing the technique of EIT for area sensing. The use of padding materials underneath a sensing skin amplifies signal under compressions. The novel soft-hard multi-layer sensing architecture ensures high sensitivity to light forces and an extended sensing range; enhanced performance has been demonstrated in both machine test and human touch. The method to obtain quantitative information from piezoresistive EIT tactile sensors has been investigated. A procedure of selecting the optimal hyperparameter for image reconstruction, which is practical for tactile sensing, has been developed. A spatial correction method and the effect of sensor's conductivity have been investigated for better understanding EIT tactile sensing.

6.2 Contributions

1. Understanding of compliant sensing skins over padding materials.

    - Discovered and experimentally explained the sensitivity enhancement by the padding material. This is a new finding that has not been pointed out in literature. The reason for the enhanced sensitivity is experimentally explained that increased strain over the skin

ensures magnified sensitivity. The knowledge on enhanced sensitivity by padding inspires a new sensor structure based on spatial filtering [198].

- A novel shape freezing method based on 3D digital image correlation for measuring surface deformation under indentation is developed. It is a challenge to measure surface shape under indentation, because indenters would block the DIC camera. By freezing the deformed sensing skin and conducting DIC, the surface deformation can be measured off-line.
- Sensitivity of sensing skins with different padding materials is found not varying broadly, but consistency in sensor signal is related to microstructures of padding material.

2. Developing a novel multi-layer padding architecture for improved sensing capability.

    - A soft-hard multilayer sensing system allows high sensitivity to gentle stimuli and extended force-sensing range. This is in principle applicable for padded system made with all types of compliant sensing skins. The system can be tailored for different applications by adjusting the stiffness and thickness of the paddings.
    - Padded sensing structures allow a strain sensor used as a pressure sensor, due to the finding that a sensing strip has the same deformation at the same indentation, regardless of indenter size.
    - Enhanced force identification of human touches in high force range proves the necessity of padding layers with different stiffness.

3. Understanding EIT technique for tactile sensing

    - Development of a soft-hard multi-layer sensing system based on EIT for the first time quantitatively distinguishes human touches in high force range. The viscoelasticity of the

padded elastomeric sensing skin is proved advantageous for EIT to display the trace of human touches. The knowledge on padded EIT tactile sensors has inspired a research work employing the developed EIT tactile sensing system to detect breast lumps.

- Development of an alternative method to select hyperparameter, which allows obtaining proper reconstructed images for more than one stimulus.
- Development of a spatial correction method allows obtaining consistent information over the whole sensor. This is a new idea which paves the way for quantitative tactile sensing, although researchers have realized the spatial dependency of EIT.

6.3 Future Work

For further improvement and applications of the padded sensing skins, future work may include following issues.

In this dissertation, spatial performance of EIT tactile sensors that has been characterized under fixed intensity and size of a stimulus. To further understand the performance of EIT tactile sensors on detecting intensity and size, characterization by varying the intensity and size of stimuli may be conducted. The limit on detecting intensity and size for EIT tactile sensors may also be investigated.

Based on the idea of developing EIT tactile sensors for area sensing, large-area EIT tactile sensing is worthwhile to investigate. Large-area tactile sensors enable providing robots with

whole-body sensing capabilities. However, limited by the theoretically low spatial resolution of EIT technique, novel data read-out schemes can be developed to compensate its low spatial resolution. For a large-area EIT sensor, it is possible to first determine a rough location of the stimulus, and then to perform EIT reconstruction over the relatively small-area region. This idea needs to design location-tunable EIT boundary electrodes, whose location are controlled based on the rough location estimation.

Another issue involved in fabricating large-area sensing skins is the level of uniformity of the conductivity, which can be measured by 4-point probes. Spray coating with controllable amount of dispersion would be helpful.

Considering that the padded piezoresistive sensing skin used in this dissertation is sensitive to stimuli that can induce inplane stretch, but not sensitive to gentle surface slide or rub. To address this problem, future work may try engineering textures on the sensor surface, which can pick up gentle inplane stimuli. This idea is inspired from papillary ridges in human skin that enhances skin's sensitivity [247]. To fabricate sensing skins with surface textures, firstly, host material can be deposited into molds with mirror-textures to form a thin layer with desired surface textures; secondly, a conventional sensing skin can be attached to the back of surface layer to form a sensing skin with surface engineered textures.

Future work can be utilizing the sensing skin for multi-functional sensing. The polymer composites used in this dissertation is not only sensitivity to strain, but also sensitive to humidity and temperature [248]. Characterization of skin's performance as a function of humidity or

temperature can be conducted. After evaluating independent effect of different types of stimuli, it would be interesting to investigate coupling effect of multiple types of stimuli.

Finally, this dissertation has already inspired other research on employing skin+padding structure for braille sensing [198], utilizing sensing skins on a huggable robot [235], and employing EIT sensing skins for detecting breast lump. More applications can be tried. For example, placing padded sensing skins inside mattresses or seats can be used to measure pressure distribution of a human body.

Appendix A Hardware Connections for EIT Setup

To obtain complete voltage measurements in EIT, the position of current injection should be switched around all electrodes. Figure A.1 demonstrates basic hardware connection while utilizing two multiplexers to switch current injections. In Figure A.1a, positive and negative ends of from current source are connected with inputs of two multiplexers. For each multiplexer, one of the 16 output channels can be selected at one time. Figure A.1b lists 16 current driving patterns and the selected output channels from the multiplexers. Figure A.1 demonstrates the hardware connection of positive and negative current injections with the 16-electrode EIT-based tactile sensors.

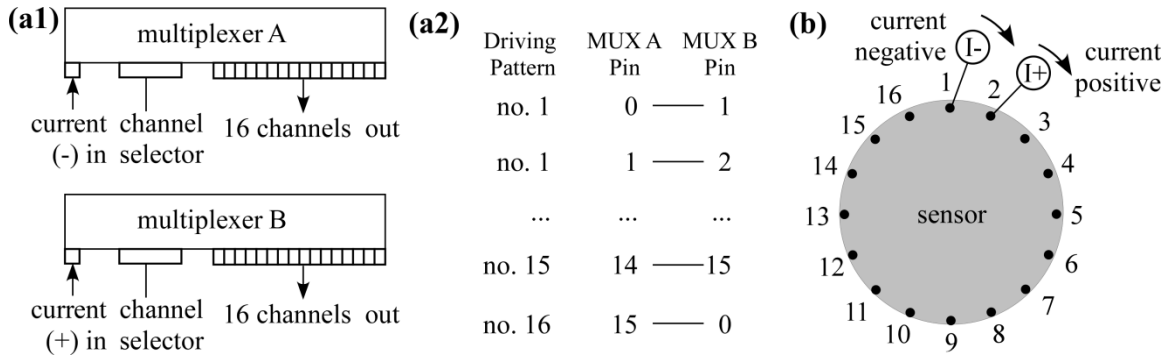

Figure A.1: Hardware connection for EIT-based tactile sensor. (a1) Connections of two multiplexers. (a2) Connections of multiplexers for 16 current driving patterns. (b) Illustration of 1st current driving pattern on a 16-electrode EIT-based tactile sensor.

Appendix B Intensity and Size Scaling

This MATLAB code was used to scale the spatial performance of the EIT-based tactile sensing, obtain metrics before and after the scaling. This code includes lines to do data process (e.g. construct EIT data structure, scaling, metrics calculation), which was written by the author, and functions necessary to solve forward and inverse problem (in bold), which is provided in EIDORS. This code should be used with EIDORS. The file name of the code: SpatialCorrectionFixNoise.m

```
n=16;  % number of electrodes
px = [0,0.1,0.2,0.3,0.4,0.5,0.6,0.7,0.8];  % x-axis position of the target
py = zeros(9,1);  % y-axis position of the target
 r = 0.2; % define radius of the target
Ps = 0;Ps_n = 0; % initialization
Ps_Ct = 0;Ps_Ct_n = 0; % initialization
TableSizePE = [0    1   7.95E-15
……
0.925   0.290441176 -0.041354892];
%  Table used to scale size, considering position error.
%  Data type for each row:  [position, size normed by center, position error]
 for m=1:1:9

imdl=mk_common_model('i2c',n);  % forward model
```

```
options = {'no_meas_current','no_rotate_meas'};   % measurement strategy
[stim, meas_select] =mk_stim_patterns(n,1,[0,1],[0,1],options,0.003);
% current driving strategy.  Current = 0.003 A
imdl.fwd_model.stimulation = stim;
imdl.fwd_solve.get_all_meas = 1;
s0 = 0.008;  %  background conductivity = 0.008 S/sq
img_1 = mk_image(imdl, s0 );  % construct initial conductivity distribution map
img_2 = img_1;  % to construct conductivity distribution map img_2 based on img_1
inclusion = sprintf('(x-%f).^2+(y-%f).^2<%f^2',px(m),py(m),r);
%  define target position and size
select_fcn = inline(inclusion,'x','y','z');
img_2.elem_data = img_1.elem_data - 0.3*s0*elem_select(img_2.fwd_model, select_fcn); %
construct conductivity distribution map img_2 by adding the target, conductivity change = -
0.3*background conductivity
vh1 = fwd_solve(img_1); %  solve forward problem img_1, obtain electrical potentials
vh2 = fwd_solve(img_2); %  solve forward problem img_2, obtain electrical potentials
data_homg = AdjacentZeroN(n,vh1.meas);
%  construct data structure of boundary electrical potentials for reference data (img_1)
data_objs1 = AdjacentZeroN(n,vh2.meas);
 %  construct data structure of boundary electrical potentials for current data (img_2)
Pnoise = -79.5;  %  power of noise level -79/5 dB
vh2_n = vh2;vh2_n.meas = vh2.meas + wgn(length(vh2.meas),1,Pnoise);
vh1_n = vh1;vh1_n.meas = vh1.meas + wgn(length(vh1.meas),1,Pnoise);
```

```
%  add white Gaussian noise to noise free data vh1 and vh2
data_homg_n = AdjacentZeroN(n,vh1_n.meas);
data_objs1_n = AdjacentZeroN(n,vh2_n.meas);
%  construct noise-present data for reference data and current data
invmdl = eidors_obj('inv_model','EIT inverse');
invmdl.reconst_type = 'difference';
imdl2 =  mk_common_model('h2c',n);
%  inverse model, different from forward model to avoid inverse crime.
invmdl.jacobian_bkgnd.value = s0;
%  background conductivity used for calculate Jacobian matrix for image reconstruction
invmdl.fwd_model = imdl2.fwd_model;
invmdl.fwd_model.stimulation = stim;
invmdl.fwd_model.meas_select = meas_select;
invmdl.solve =        @inv_solve_diff_GN_one_step; %  inverse solver
invmdl.hyperparameter.value = 0.3; %  hyperparameter
invmdl.RtR_prior =    @prior_laplace; %  prior type
img_3 = inv_solve(invmdl,data_objs1,data_homg); %  solve inverse problem, noise free
img_3_n = inv_solve(invmdl,data_objs1_n,data_homg_n);
%  solve inverse problem, noise-present
% below:  intensity scaling
scaleSensi = img_3;
% duplicate reconstructed conductivity map for intensity scaling, noise free
scaleSensi_n = img_3_n;
```

```
% duplicate reconstructed conductivity map for intensity scaling, noise present
n1 = 1;
rings = 32;  % number of rings in the FEM mesh
for k = 1:1:rings
   n2 = 4*k^2;
   if k <= 9
      scale = 0.9834+(k-1)*(-0.017)/rings;  % scale by the curve fitted results, 1st part
      if k == 9
         scaleP1 = scale;
      end
   elseif k <= 22
      scale = scaleP1 + (k-9)*3.2663/rings; % scale by the curve fitted results, 2nd part
      if k == 22
         scaleP = scale;
      end
   elseif k <= rings
      scale = scaleP + (k-22)*11.25/rings; % scale by the curve fitted results, 3rd part
   end
   scale = scale /0.9834;
   for nn = n1:1:n2
         scaleSensi.elem_data(nn)=img_3.elem_data(nn)/scale;
% scale noise-free image, img_3
         scaleSensi_n.elem_data(nn)=img_3_n.elem_data(nn)/scale;
```

```
% scale noise-free image, img_3_n
    end
    n1 = n2 + 1;
end
L = length(img_3.elem_data);
thre = 0.5*max((img_3.elem_data)); % scale noise
 [img_back,PkIndex(m),Aq,avgP]=MetricCal(img_3,thre,L); % calculate metrics
 [wx,wy,gx,gy,value_w,SD]=position(img_back,length(img_back.elem_data));
% obtain weighted center (wc), geometric center (gc), value at weighted center (value_w), and
shape deformation (SD).
D_w = sqrt((wx-px(m))^2+(wy-py(m))^2);  % position error:  weighted center
D_g = sqrt((gx-px(m))^2+(gy-py(m))^2);  % position error: geometric center
Elms_temp = img_3.fwd_model.elems(PkIndex(m),:);  % 3 nodes number of an element
P_Elms_temp = img_3.fwd_model.nodes(Elms_temp,:);  % coordinates of the 3 nodes
Peak_xy = mean(P_Elms_temp,1);  % centroid coordinates
  % below:  determine the sign of position error. + away from center, - approach to center
if sqrt(wx^2+wy^2)>=px(m)
    D_w = D_w;
else
    D_w = -D_w;
end
if sqrt(gx^2+gy^2)>=px(m)  D_g = D_g;  else  D_g = -D_g;  end
% below:  calculate metrics after scaling the noise-free case
```

```
thre = 0.5*max((scaleSensi.elem_data));
[back_sen,PkIndex_sen(m),Aq_sen,avgP_sen]=MetricCal(scaleSensi,thre,L);
[wx_sen,wy_sen,gx_sen,gy_sen,value_w_sen,SD_sen]=position(back_sen,L);
D_w_sen = sqrt((wx_sen-px(m))^2+(wy_sen-py(m))^2);
D_g_sen = sqrt((gx_sen-px(m))^2+(gy_sen-py(m))^2);
Elms_temp = scaleSensi.fwd_model.elems(PkIndex_sen(m),:);
P_Elms_temp = scaleSensi.fwd_model.nodes(Elms_temp,:);
Peak_xy_sen = mean(P_Elms_temp,1);
if sqrt(wx_sen^2+wy_sen^2)>=px(m)
   D_w_sen = D_w_sen;
else
   D_w_sen = -D_w_sen;
end
if sqrt(gx_sen^2+gy_sen^2)>=px(m)  D_g_sen = D_g_sen;  else  D_g_sen = -D_g_sen;  end
% below:  calculate metrics before scaling noisy case
thre = 0.5*max((img_3_n.elem_data));
[img_back_n,PkIndex_n(m),Aq_n,avgP_n]=MetricCal(img_3_n,thre,L);
[wx_n,wy_n,gx_n,gy_n,value_w_n,SD_n]=position(img_back_n,length(img_back_n.elem_data)
);
D_w_n = sqrt((wx_n-px(m))^2+(wy_n-py(m))^2);
D_g_n = sqrt((gx_n-px(m))^2+(gy_n-py(m))^2);
Elms_temp_n = img_3_n.fwd_model.elems(PkIndex_n(m),:);
P_Elms_temp_n = img_3_n.fwd_model.nodes(Elms_temp_n,:);
```

```
Peak_xy_n = mean(P_Elms_temp_n,1);
if sqrt(wx_n^2+wy_n^2)>=px(m)  D_w_n = D_w_n;  else  D_w_n = -D_w_n;  end
if sqrt(gx_n^2+gy_n^2)>=px(m)  D_g_n = D_g_n;  else  D_g_n = -D_g_n;  end
% below:  calculate metrics after scaling the noisy case
thre = 0.5*max((scaleSensi_n.elem_data));
[back_sen_n,PkIndex_sen_n(m),Aq_sen_n,avgP_sen_n]=MetricCal(scaleSensi_n,thre,L)[wx_se
n_n,wy_sen_n,gx_sen_n,gy_sen_n,value_w_sen_n,SD_sen_n]=position(back_sen_n,L);
D_w_sen_n = sqrt((wx_sen_n-px(m))^2+(wy_sen_n-py(m))^2);
D_g_sen_n = sqrt((gx_sen_n-px(m))^2+(gy_sen_n-py(m))^2);
Elms_temp = scaleSensi_n.fwd_model.elems(PkIndex_sen_n(m),:);
P_Elms_temp = scaleSensi_n.fwd_model.nodes(Elms_temp,:)Peak_xy_sen_n =
mean(P_Elms_temp,1);
if sqrt(wx_sen_n^2+wy_sen_n^2)>=px(m)
   D_w_sen_n = D_w_sen_n;
else
   D_w_sen_n = -D_w_sen_n;
end
if sqrt(gx_sen_n^2+gy_sen_n^2)>=px(m)  D_g_sen_n = D_g_sen_n;  else  D_g_sen_n = -
D_g_sen_n;  end
% scale size
RectPos = sqrt(wx^2+wy^2); % estimated position
RectPos = RectPos-TableSizePE(knnsearch(TableSizePE(:,1),RectPos),3);
% adjusted position based on PE
```

```
size = Aq/L/TableSizePE(knnsearch(TableSizePE(:,1),RectPos),2); );
% scaled size, noise free
RectPos_n = sqrt(wx_n^2+wy_n^2);
RectPos_n = RectPos_n-TableSizePE(knnsearch(TableSizePE(:,1),RectPos_n),3)
size_n = Aq_n/L/TableSizePE(knnsearch(TableSizePE(:,1),RectPos_n),2);
 % scaled size, noisy case
% record parameters in matrix cydata for before scaling, noise free.
cydata(m,:)=[max(abs(img_3.elem_data)) avgP  Aq/L D_w D_g value_w SD];
%  peak value, avg value around peak, normalized size, position error(wc), position error(gc),
value at weighted center, shape deformation.
cydata_n(m,:)=[max(abs(img_3_n.elem_data)) avgP_n  Aq_n/L D_w_n D_g_n value_w_n
SD_n]; %  before scaling, noisy case
cydata_sensi(m,:)=[max(abs(scaleSensi.elem_data)) avgP_sen Aq_sen/L D_w_sen D_g_sen
value_w_sen SD_sen]; %  after intensity scaling, noise free
cydata_n_sensi(m,:)=[max(abs(scaleSensi_n.elem_data)) avgP_sen_n Aq_sen_n/L D_w_sen_n
D_g_sen_n value_w_sen_n SD_sen_n]; %  after intensity scaling, noisy case
cydata_size(m,:)=[ size]; %  after size scaling, noise free
cydata_n_size(m,:)=[size_n]; %  after size scaling, noisy case
```

Appendix C EIT Metrics Calculation

The following Matlab functions are used to calculate the metrics in an EIT reconstructed image. Function MetricCal calculates number of elements that are above half peak and average reconstructed value around the peak. Function Position calculates corordinates of weighted center and geometric center, reconstructed value at the center location, and shape deformation.

```
function [ img_back,PkIndex,Aq,avgP ] = MetricCal( img,thre,L )
Ps = 0;
Ps_Ct = 0;
[temp,PkIndex]= max((img.elem_data));
img_back = img;
Aq = 0; % Aq: number of sol data in img_back
for k=1:1:L
   if (img.elem_data(k))<=thre
      img_back.elem_data(k)=0;
   else
      Aq = Aq + 1;
   end
end
% avg value around peak
% find all elements that are connected with the peak element.
for k=1:1:L
```

```
    if sum(ismember(img.fwd_model.elems(PkIndex,:),img.fwd_model.elems(k,:))) ~= 0
        Ps = Ps + img.elem_data(k);
        Ps_Ct = Ps_Ct +1;
    end
end
avgP = Ps/Ps_Ct;
 end


function [ wx,wy,gx,gy,value_w,SD ] = position(img,n)
a = sum(img.elem_data);
No = length(nonzeros(img.elem_data));
sum_w_x = 0; sum_w_y = 0;
sum_g_x = 0; sum_g_y = 0;
sum_SD = 0;
cyCount = 0; cy = 0;
SD_r = sqrt(No/n);% radius of same area circle, sqrt(Aq/L*pi*1^2/pi)
for k = 1:1: n
        if img.elem_data(k) ~= 0
            Elms = img.fwd_model.elems(k,:);% 3 node number of element.
            P_Elms = img.fwd_model.nodes(Elms,:);% coordinates of the 3 nodes
            C_ELms = mean(P_Elms,1);% centroid coordinates
            sum_w_x = sum_w_x + C_ELms(1)*img.elem_data(k);
            sum_w_y = sum_w_y + C_ELms(2)*img.elem_data(k);
```

```
            sum_g_x = sum_g_x + C_ELms(1);
            sum_g_y = sum_g_y + C_ELms(2);


        end
end
wx = sum_w_x/a; wy = sum_w_y/a;
gx = sum_g_x/No; gy = sum_g_y/No;
% find which element  [wx,wy] belongs to
for k =1:1:n
    if img.elem_data(k) ~= 0
    x = img.fwd_model.nodes(img.fwd_model.elems(k,:),1) ;
    y = img.fwd_model.nodes(img.fwd_model.elems(k,:),2) ;
            Elms = img.fwd_model.elems(k,:);% 3 node number of element.
            P_Elms = img.fwd_model.nodes(Elms,:);% coordinates of the 3 nodes
            if pdist([wx,wy;P_Elms(1,:)])>SD_r
              if pdist([wx,wy;P_Elms(2,:)])>SD_r
                 if pdist([wx,wy;P_Elms(3,:)])>SD_r
                     %sum_SD = sum_SD + img.elem_data(k);
                     sum_SD = sum_SD + 1;
                 end
              end
            end
        if inpolygon(wx,wy,x,y) == 1 % check if weighted center is inside the element
```

```
            cyCount = cyCount +1;
            cy =k;
        end
    end
end
value_w = img.elem_data(cy);
SD = sum_SD/No;
 end
```

Appendix D Supporting Information of Chapter 2

D 1 Testing of EG/Latex Sensing Film Alone

The piezoresistive sensing material is an EG/latex composite, meaning that it is also viscoelastic [54]. It was therefore separately characterized to understand its temporal responses in the absence of the underlying membrane. The sensing material was applied as a thin adherent film – too thin to be peeled off and handled alone – so it was characterized on a stiff bending cantilever as described in [48]. This limited the range of strains to a maximum of 1500 microstrain (με). The free end of the cantilever was displaced by known distances with step and sinusoidal inputs to obtain the static and dynamic responses.

D 1.1 Method

The EG/latex sensing material was applied on two cantilevers (Lexan polycarbonate, 27 mm wide x 185 mm long x 2 mm thick) by spray coating. The dimensions of the sensors were 7 mm x 25 mm. Electrical connections were made following the method described in Section 2.3.1.3 of the main text.

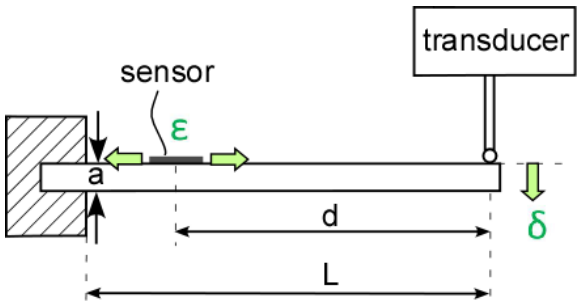

Figure D.1: Schematic for testing the EG/latex sensor alone. The cantilever tip displacement δ and the strain ε are indicated for tension. For compression, the cantilever was flipped over. (L = 155 mm, a = 2 mm, d = 135 mm.)

The end of the cantilever close to the sensor was rigidly clamped. The free end was displaced to induce either tensile (face up, as shown in Figure D.1) or compressive (face down) strain using a programmable force transducer (Bose 3330 Series II). Using small angle beam theory, the relation between the tip displacement δ and the strain ε at the center of the sensor is given by:

(1) $$\varepsilon = \frac{3da}{2L^3}\delta,$$

where L is the length of the cantilever, d is the distance from the center of the sensor to the end of the cantilever, and a is the cantilever thickness.

D 1.2 Calibration

The change in resistance was measured in both tension and compression. The cantilever tip was displaced to 8 positions for each (producing strains in the sensor of ±0.01, ±0.02, ±0.03, ±0.04, ±0.09, ±0.13, ±0.17, and ±0.22 %), in increasing order to a maximum strain of 2200 με = 0.22%. Each position was held for 2 seconds, and the resistance was measured immediately after the

deflection was reached: due to the relaxation behavior of the composite, shown below, a steady-state value could not readily be identified.

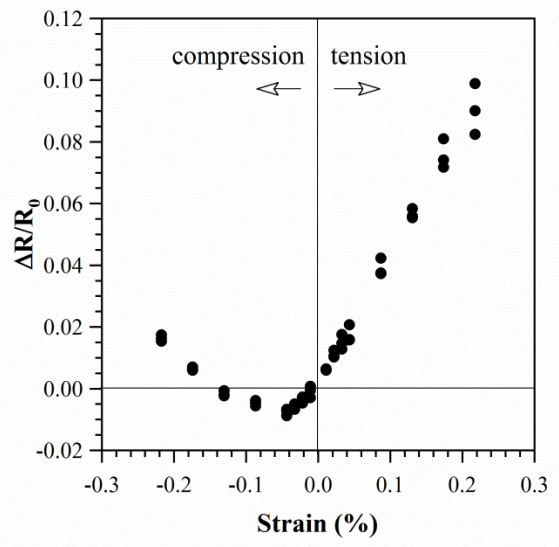

Figure D.2: Relative resistance change as a function of strain. Data from triplicate measurements are shown for one of the cantilevers.

The static response is shown in Figure D.2 for one cantilever; the behavior was identical on the second one. The sensitivity under tension and compression differed. Under tension the resistance increased linearly with the strain, as previously found in [48].

Under compression, the response was non-monotonic, decreasing at small compressive strains (up to -0.05%), and thereafter climbing. Prior reports have shown that the response under compression is highly sensitive to particle loading and shape, as discussed in [48].

D 1.3 Relaxation and Recovery

Viscoelasticity is typical for elastomeric polymer composites. To understand the performance of our EG/latex sensor, relaxation and recovery tests were also conducted on the cantilever. The sensor was rapidly placed under tension, 0.05% strain, by displacing the cantilever tip at a speed of 15 mm/sec and then holding that position for 200 sec while recording the resistance. (An ideal step input is not achievable experimentally. At rates faster than 15 mm/sec, vibration is introduced.) The strain was then released by retracting the cantilever tip at the same 15 mm/sec, and the recovery process was monitored for 100 sec.

The strain waveform and the resistive response are shown in Figure D.7 in Section 0 (left *y*-axes, black curves). The resistance changed immediately with the strain, but after that, due to the re-arrangement of the host polymer chains and guest particles, the resistance decreased gradually. When the strain was released, the resistance recovered back to its initial value, without suffering a permanent residual resistance change.

The relaxation of the resistance is related to viscoelastic stress relaxation [54]. Relaxation in polymer composite sensors has been investigated previously [41,53,58], with relaxations times of hundreds of seconds, comparable to our EG/latex sensor. This phenomenon does not prohibit applications in strain sensing application, as shown in [25,46,56].

D 1.4 Cyclic Loading

To investigate the sensor response to cyclic loading, a sinusoidal displacement was applied to the tip of the cantilever using the same apparatus. The results for a tip displacement to 5 mm at 1 Hz are shown in Figure D.3. The change in resistance was the same at 0.1 Hz and at 9 Hz, as previously shown in [48]: the sensor is able to respond quickly to the AC input because it is faster than the much slower viscoelastic (rubbery) response shown in Figure D.7, which persists for hundreds of seconds. At these frequencies, the polymer behaves substantially as a glassy material.

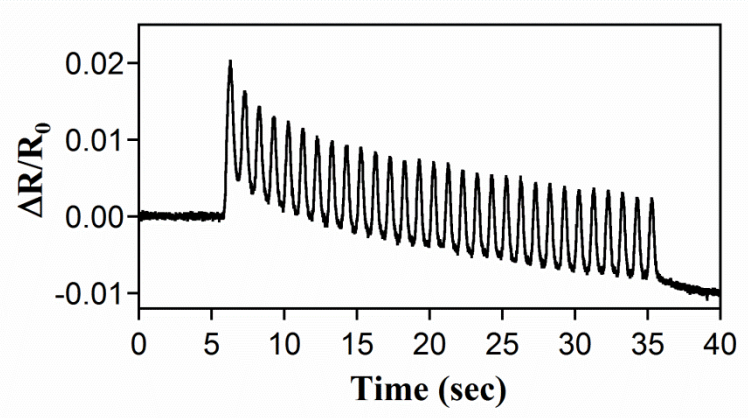

Figure D.3: Relative change in resistance due to a sinusoidal cantilever tip displacement of 5 mm starting at t = 6 sec.

D 2 Calibration of the Sensor on the Membrane

The sensitivity of each sensor to tensile strain was calibrated. The experimental configuration used for the uniaxial tensile testing is shown in Figure D.4. The sensors were suspended vertically and stretched to different positions, defined by shims of known thickness. The

reference sensor was stretched to 5 positions, stretching the 90 mm initial length by 2.5, 5, 10, 15, and 20 mm (3.2, 6.5, 13.0, 19.5, and 26.0%, respectively). The 15 sensors used in the loading tests were stretched by 3% and 6%, and linear curve fits were used to obtain the gauge factors. Calibrations were conducted in triplicate. The gauge factors for all 15 sensors are shown in Figure D.5. The gauge factors of the other 14 sensors were normalized to that of sensor #1.

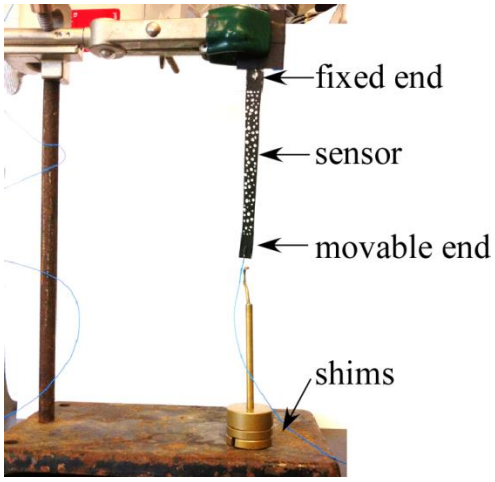

Figure D.4: Experimental setup for tensile calibration of the EG/latex sensor+membrane samples. (The white speckling was for DIC strain measurements.)

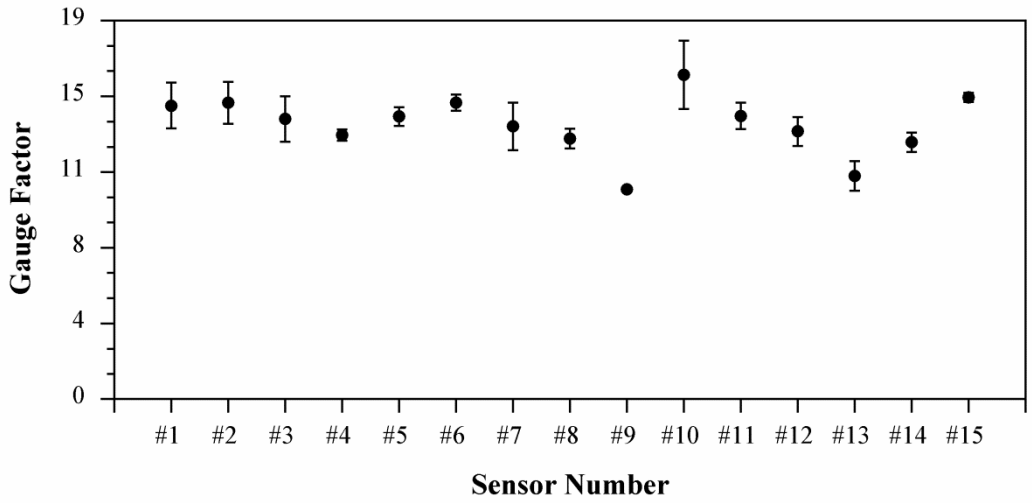

Figure D.5: Gauge factors for the 15 sensors used for load testing. Measurements were performed in triplicate; points show the average and error bars the standard deviation.

D 3 Uniaxial Dynamic Testing of Sensor on the Membrane

To further examine the behavior of the sensing skin (sensor + membrane), dynamic uniaxial tests under both static and cyclic loading were performed.

D 3.1 Method

Strip-shaped sensor skins fabricated as described in Section 2.3.1 was mounted as shown in Figure D.6. The two ends, including the electrical connections, were clamped to blocks. The bottom block was fixed, and the top block was connected in series with the transducer (Bose 3330 Series II) and the load cell (Cooper Instruments & Systems LFS270 5 lbs (2.3 kg)). The skin was strained by moving the top block as programmed by the transducer.

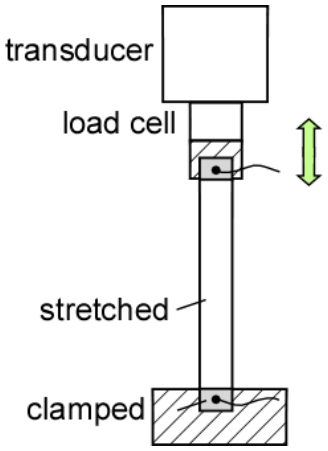

Figure D.6: Experimental setup for uniaxial dynamic test of the skin.

D 3.2 Relaxation and Recovery

The rubber membrane allows a much large strain deformation than a substrate that is only flexible, a significant benefit for a conformal skin. To investigate the effect on the dynamic response of adding the rubber membrane under the sensor, relaxation and recovery were monitored on the skin in response to a step waveform to 4% strain (Figure D.7a, right *y*-axis, red curve) using the apparatus shown in Figure D.6. The change in resistance is shown in Figure D.7b.

The sensing skin again showed the resistive relaxation expected from viscoelastic composites, and the resistance returned fully to its initial value during the recovery phase. The shape of the curve was comparable to that for the sensor alone. This is not surprising, since both the sensor and the membrane were made of latex. Significantly, the membrane did not slow down the sensor response.

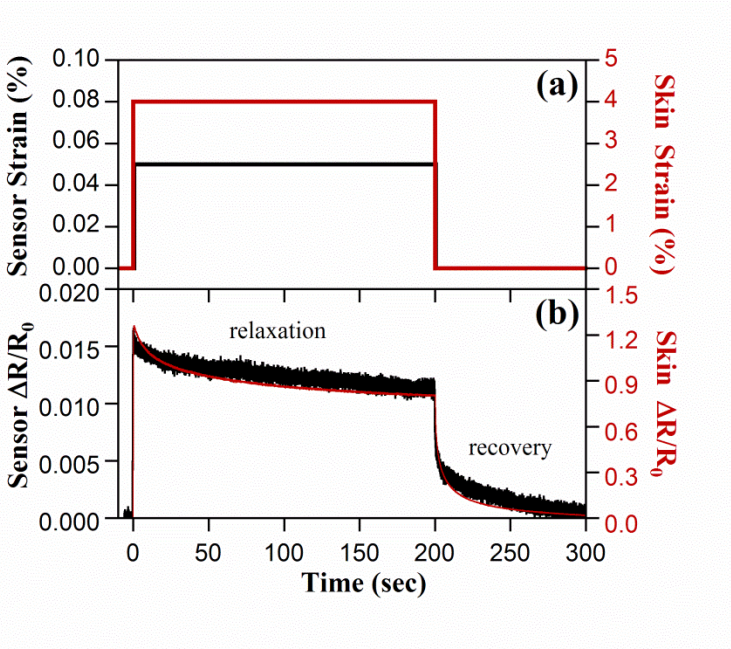

Figure D.7: Relaxation and recovery of the sensor on the rigid bending cantilever and on the rubber membrane. (a) Strain waveforms. For the cantilever, a constant strain of 0.05% was applied (relaxation) and released back to 0% (recovery). For the membrane, a strain 4% was applied and released. (b) Resistance response of the EG/latex on the cantilever (left *y*-axis) and the rubber membrane (right *y*-axis).

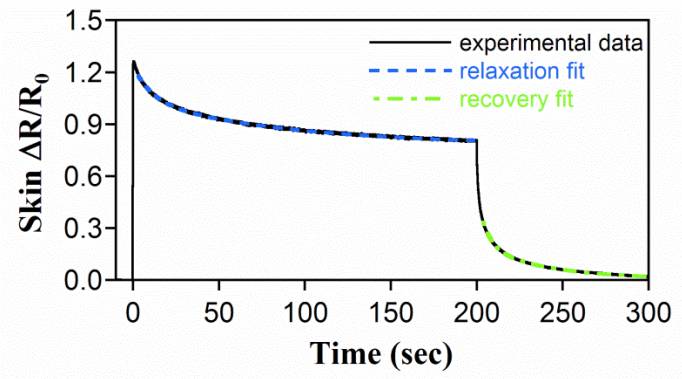

Figure D.8: Experimental step response data and fitted curves.

To determine the time constants of the skin during relaxation and recovery, we employed a Generalized Maxwell or Maxwell-Wiechert model with two time constants, fitting the relaxation

and recovery responses separately. The models often differ for relaxation and recovery, and can account for variations in the response due to variations in the structure of the material. The resistance response over time was formulated as:

(2) $\Delta R/R_0 = c_0 + c_1 \cdot e^{-t/\tau_1} + c_2 \cdot e^{-t/\tau_2}$,

where $c_0, c_1,$ and c_2 are amplitudes and τ_1 and τ_2 are time constants.

The fits are shown in Figure D.8. For relaxation τ_1 = 11 sec and τ_2 = 90 sec, whereas for recovery τ_1 = 6 sec and τ_2 = 37 sec. Note that these are not comparable to the recovery time in the main text (Figure 2.8), which was found differently. In [41,53,58], the sensors had relaxation times on the order of a hundred seconds.

D 3.3 Uniaxial Cyclic Loading

We investigated the sensing skin response to cyclic loading to compare it with the cyclic response of the skin over padding (Section 2.4.4.2). A 30-cycle sinusoidal uniaxial strain at a frequency of 0.2 Hz was exerted on the skin. The maximum strain was 4%, equivalent to the maximum strain experienced in the indentation tests over the padding.

The force response is shown in Figure D.9a; it did not change significantly over the 30 cycles. The skin maintained the same amount of hysteresis, meaning that it dissipated the same amount of energy in each cycle. The response stabilized after the 2nd cycle, which was also the case for

indentation over padding (right side, part (d)). However, over padding the shape of the first loop was different from the subsequent 29 cycles, showing that more energy was dissipated in the first cycle. The padding dominated the behavior in Figure 2.11, which is also clear from the 10x larger force amplitude.

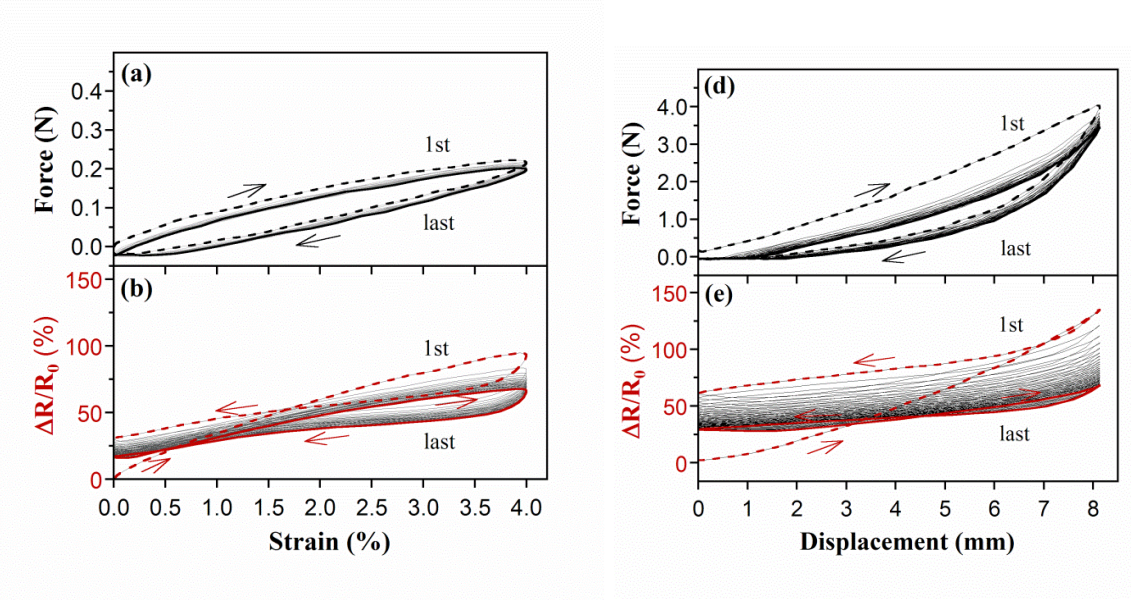

Figure D.9: (left) Sensor+membrane in cyclic tests. The input strain waveform was a 30 Hz sinusoid. (a) Force and (b) normalized resistance change versus strain. (First cycle, dashed line; last cycle, heavy solid line.) (right) Right half of Figure 2.11 showing the corresponding data from the skin over the foam. Note the differences in the axis values.

In Figure D.9b, the resistance changed in a similar manner as for indentation over padding (compare Figure 2.11e), showing a figure-8 shaped loop. The 1st cycle showed an irreversible resistance increase upon unloading. After that, the end-of-cycle resistance shifted toward a stabilized position. Over the 30-cycle loading, the hysteresis remained the same, but it was larger than in the indentation tests (Figure 2.11e).

D 4 Biaxial Tensile Testing of Sensing Skin

To more closely approximate the deformations experienced in the indentation tests (Figure 2.5b), which are not unidirectional, biaxial testing was performed to determine whether the sensitivity in the *x*-direction was affected by strain in the perpendicular *y*-direction (or lateral direction). The results showed that it is not: *the slope of the curve in the x-direction is unaffected by amount of stretching in the y-direction*. This means that the sensor is able to maintain the same sensitivity when lateral strain exists, which is a good attribute for multi-axial deformation measurements.

D 4.1 Fabrication

Biaxial tensile testing was performed on a cruciform-shaped sensor prepared using the same method as the strip-shaped sensor. The geometry of the cruciform-shaped specimen is shown in Figure D.10. The cruciform shape was formed on the latex membrane sheet (again from ELE International, 0.3 mm thick) by a stencil created from painter's tape (ScotchBlue). As with the other samples, the piezoresistive paint was applied by spray-coating onto the latex membrane (10 psi air pressure) in a hood and allowed to air dry for one minute, repeating to deposit 10 layers. After spray coating, the pattern was scissor cut along the boundary to create the cruciform-shaped specimen. Connecting wires (single strand, 30 AWG) were attached with silver epoxy (CircuitWorks, CW2400) between points 1 and 3 in Figure D.10. The four ends of the specimen (including the portions with the attached electrodes) were glued (Aleene's fabric glue) to the tops of the four arms of a biaxial testing rig, giving a stretchable length of $L_x = L_y = 30$ mm in both the

x and *y* directions. The fixed and stretchable area of the specimen are color coded in Figure D.10.

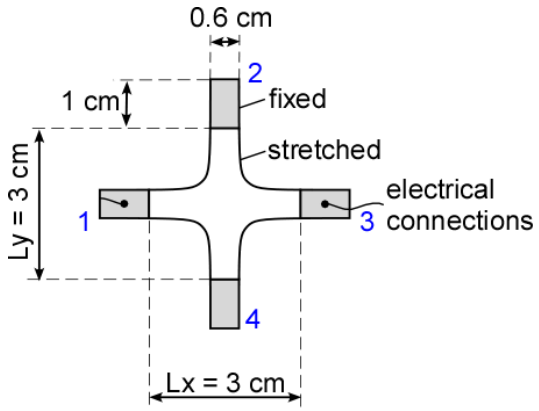

Figure D.10: Dimensions of the cruciform-shaped sensor. The fixed part is indicated by the shaded area, and the stretchable part by the white area. The resistance was measured between the points 1 and 3.

D 4.2 Experimental Setup

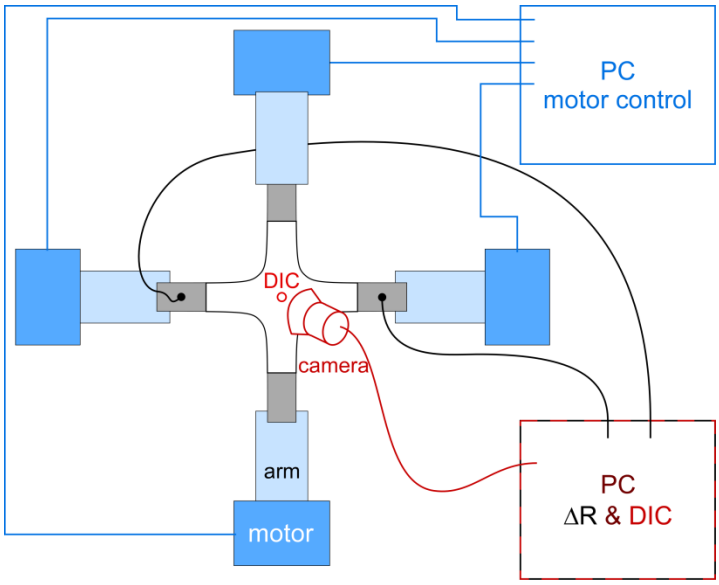

Figure D.11: Schematic diagram of the biaxial tensile testing setup. Note that the camera is looking straight towards the DIC area (red circle).

The movement of the arms was driven by four independent, linear, pneumatically-driven motors controlled by program written in LabVIEW. The resistance and local strains were measured simultaneously. In order to see the effect of lateral strain, the resistance was measured between points 1 and 3 (*x*-direction in Figure D.10) across the whole sample, and lateral strain was applied in the perpendicular *y*-direction. Figure D.11 shows an overhead view of the setup.

Local strains were obtained from two dimensional digital image correlation (2D-DIC) [154-157], which gives inplane strain information. The surface of the sensor was painted with random speckles (Rust-Oleum Quick Color aerosol paint, white; speckle size 0.02~0.24 mm dia.). One camera was positioned to look perpendicularly toward the sample and was focused on a 1 mm x

1 mm area. 2D-DIC software (Vic-Gauge 2D, Correlated Solutions) was used to collect and analyze the images and obtain the strain information.

D 4.3 Results

The inset in Figure D.12b shows where the local strains were measured using 2D DIC in the center of the sample (indicated by the red circle). Note that the local strains in the *x*- and *y*-directions differ and vary across the sample, and they are not the same as the global strains between the motorized arms. Strains at the center were highest and decreased to zero at the fixed ends of the arms, as confirmed by DIC at those positions (black circles in Figure D.12b inset). Also note that the resistance was measured across the whole sample.

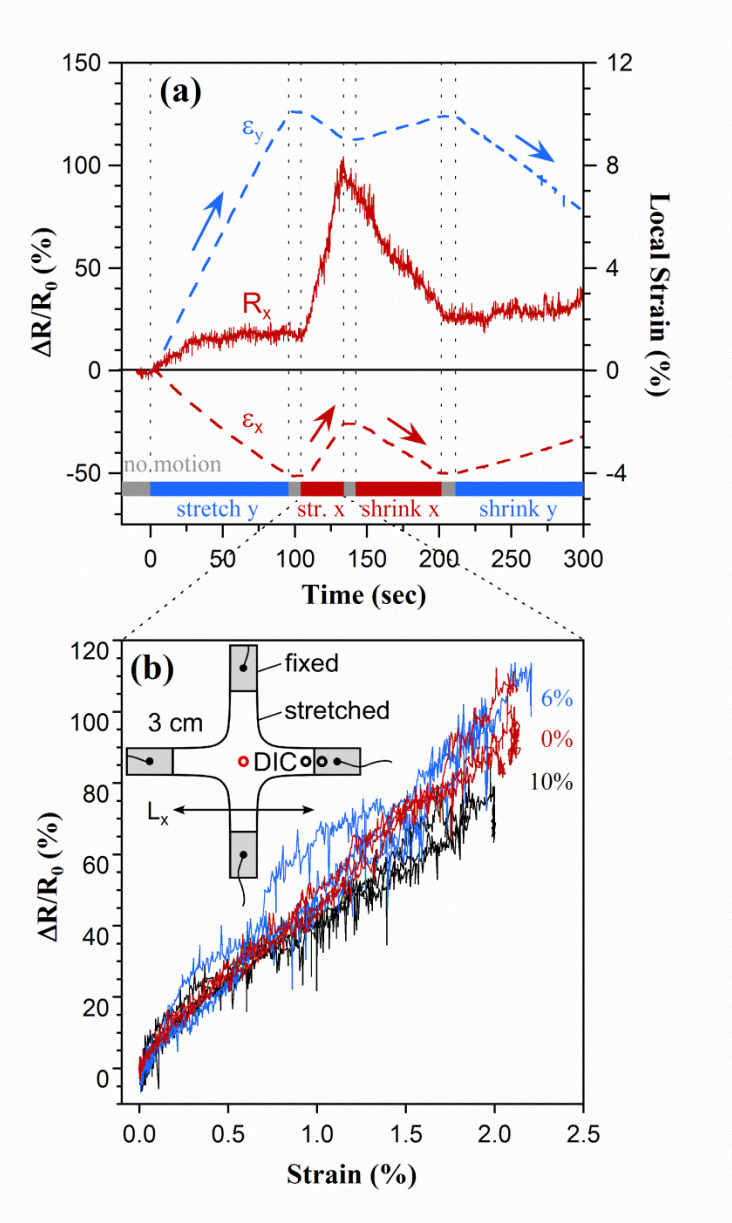

Figure D.12: a) Local strains ε_x and ε_y (dashed lines) obtained from DIC in the center of a cruciform specimen (red circle in inset in (b)) and normalized change in resistance (global) in the *x*-direction over time as the sample was sequentially stretched in *y*, stretched in *x*, relaxed in *x*, and relaxed in *y*. b) While *y* was kept fixed and *x* was stretched, the change in normalized resistance in the *x*-direction as a function of ε_x for three different ε_y, in triplicate. The starting points of all the curves were aligned at (0,0).

The experimental procedure is illustrated by the color-coded bar at the bottom of Figure D.12a.

The sample was stretched (for approximately 100 seconds, blue bar on legend) in the *y*-direction

until the local strain ε_y in the center of the sample (dashed blue line, right axis) reached 10%. At the same time, the local strain in the *x* direction, ε_x (dashed red line, right axis), decreased by Poisson's ratio. This position was next held a few seconds (gray on legend), stretched in the *x*-direction to a local strain increase of ε_x = 2%, held again, released in *x* back to the original position, held, then released in *y*. The sequences were run in triplicate at three values of ε_y, 0%, 6%, and 10%. The normalized change in resistance between points 1 and 3, R_x (solid red line, left axis), is also shown.

The three curves in Figure D.12a show the relative resistance change in the *x*-direction, as well as the local strains ε_x and ε_y in both the *x* and *y*-directions induced by the lateral stretching. Although globally there was no strain along the *x* direction, the local strain ε_x decreased by 4% due to Poisson's ratio as the *y*-direction was stretched. When stretching *y*, R_x initially increased with ε_y, but it plateaued at 17% (Figure D.12a). This also occurred for the measurements at 6% and 10% lateral strains. Since the sensing material covers the entire cruciform shape, strain within the sample can change the percolation pathways and thereby the resistance along the conductive paths. However, it is not clear why R_x increased only initially and then plateaued.

Once the central local strain in *y* was fixed at ε_y = 10%, the motor in the *y*-direction stopped stretching the specimen. Then the motor in the *x*-direction started to stretch the specimen until the central local strain ε_x increased by 2% from its starting value. During this period, R_x rose to nearly 100%, and ε_y decreased by 1%. Upon reducing ε_x, R_x decreased again. R_x was more

sensitive to strain in *x* because that affected the entire length of the strain gauge in the *x* direction, whereas strain in *y* affected only the center (and the arms connecting points 2 and 4.)

Calculating a gauge factor based on local strain, $GF = R_x/\varepsilon_x = 41$, nearly 3 times the value of 14 found in the uniaxial tests. This is reasonable because the resistance was measured over regions where the strain was much lower than the local strain at the center of the sample. Results from the second sample were similar.

Figure D.12b shows the change in resistance in the *x*-direction, R_x, as the sample was stretched up to $\varepsilon_x = 2\%$ (local strain in the *x*-direction). Three lateral strains ($\varepsilon_y = 0$, 6, and 10%) were applied to investigate their effect on the sensitivity. Triplicate measurements at each ε_y are plotted in the same color. (To facilitate comparison, the $\Delta R/R_0$ value of the 6% and 10% curves have been shifted downward by 17%, and the strain shifted by +3% and +4% respectively, so that they all have the same starting point.) R_x increased linearly with ε_x in all cases. *Most importantly, there was no notable dependence of the slopes on ε_y, so there are no evident nonlinear inplane cross-axis interactions in this range of strains.*

D 4.4 Discussion

The independence of the slopes in Figure D.12b on strain in the perpendicular direction shows that cross-axis interactions on the stretchable sensing skin were small: the gauge factor was

substantially unaffected by strain at 90°, even for strains at the center of the sample as high as10%. Strains in the *x* and *y*-directions can therefore be evaluated independently, based on the measurement direction for the resistance.

D 5 Effect of Coating

Three coatings were tested for their ability to provide abrasion protection for the sensor while not negatively impacting performance: Behr Premium Plus Ultra, Kryolan Flexible Sealor Makeup, 1481, and Zensser, Bulls Eye 1-2-3 Plus Primer. The uncoated sensors were smooth, as shown by the close-up photographs in Figure D.13. The Behr paint was viscous, as shown by the brush streaks, and it contained some small particles. It adhered well. The Kryolan coating was transparent and rendered the surface shiny; it also adhered well. The Zinsser primer coating had an inconsistent thickness and small bubbles. Stretching the sensors resulted in cracking and flaking off of the Zinsser coating.

Nine strip sensors were made from one batch of latex/EG, and their sensitivities were obtained as described above. As shown in Figure D.13, all nine sensors had similar gauge factors before coating. The sensors were coated and left to dry for 12 hours, and the sensitivity of each sensor was re-measured.

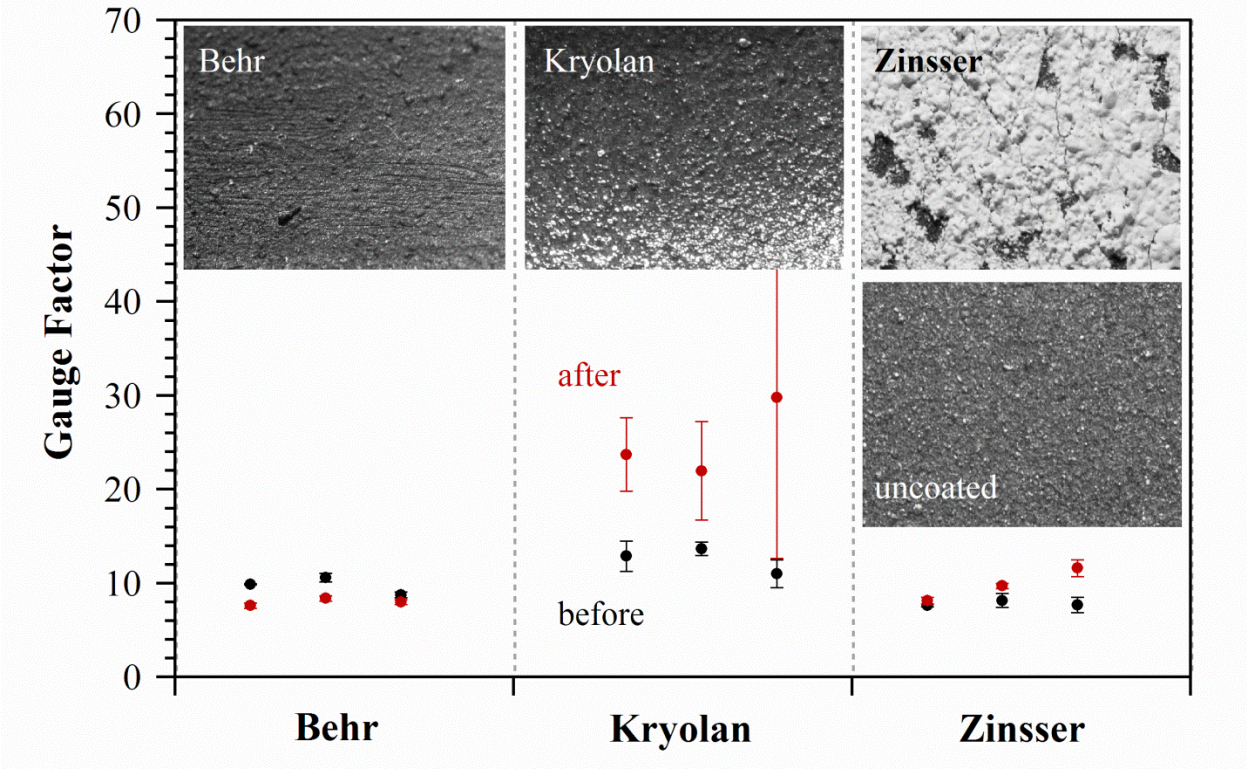

Figure D.13: The effect of the coating material on sensor appearance and sensitivity. The gauge factor before (black) and after (red) coating the sensors is shown, and the standard deviation of three replicates is indicated by the error bars. The vertical scale for the photographs is 8 mm.

Sensors coated with Kryolan experienced the largest change: the gauge factors increased, but had a large standard deviation. This was due to the high stiffness of the Kryolan coating, which cracked upon stretching and tore the sensing material, leading to a large signal change. Because such cracks in the coating are uncontrollable, the signal change was inconsistent.

The Behr and Zinsser paints were better coating materials since the gauge factors did not change much. However, there were large particles in the Zinsser coating that lead to a rough surface, and the material flaked off with mechanical contact. In contrast, the Behr coating was smooth

and capable of insulating the sensing material from conductive contacts. Therefore, the Behr coating was selected for this study.

D 6 Loading Rate Dependence

Three probe loading/unloading rates were examined. The data in the main text were from the slowest rate, 0.1 Hz (approx.2.5 mm/sec). Results on foam OC-2 and PDMS-1 are shown in Figure D.14. Neither the force nor the change in resistance showed a marked dependence on loading rate in the studied range for any of the padding materials. (The normalized resistance had less time to recover at the faster rates, so the value upon returning to zero displacement was higher, but the maximum change in resistance was the same.)

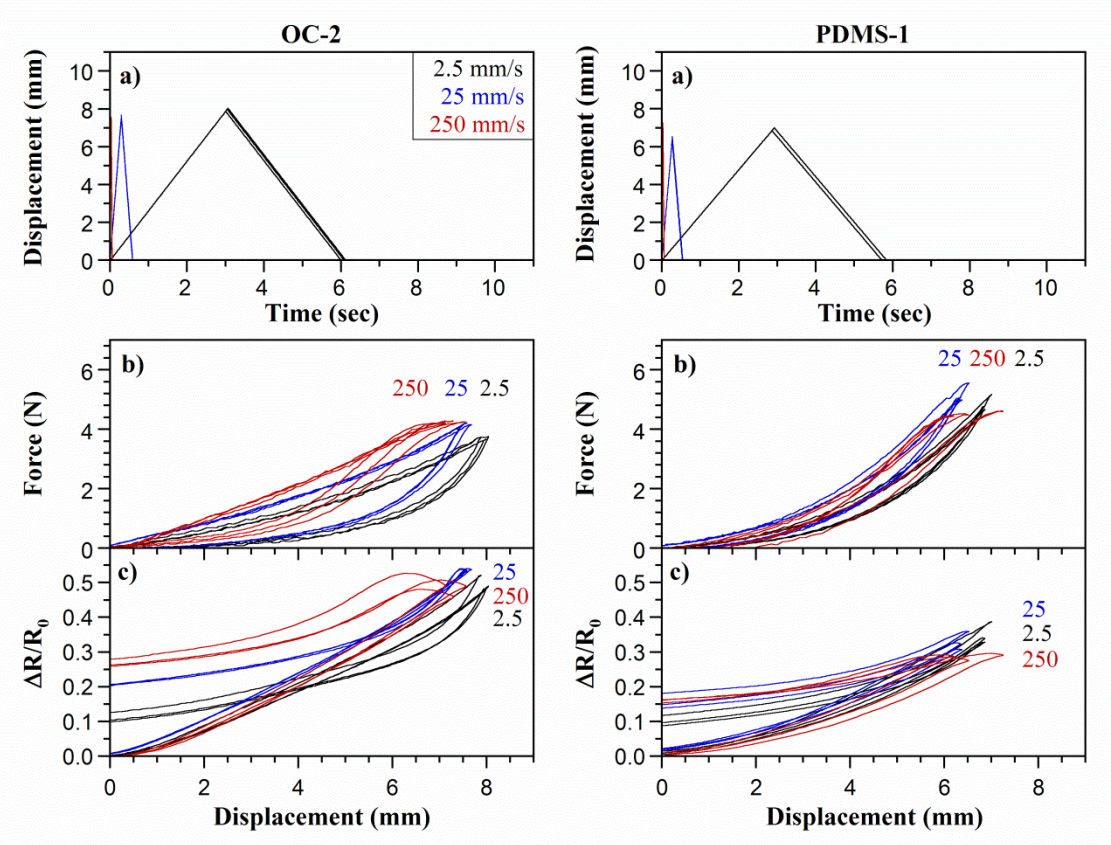

Figure D.14: (a) Displacement versus time at three loading-unloading rates: 2.5 mm/s, 25 mm/s, and 250 mm/s (frequency = 0.1 Hz, 1 Hz, and 10 Hz, respectively). b) Force and c) normalized resistance change as a function of displacement at the three indentation rates. For each padding, triplicates on one sensor are shown.

D 7 Recovery Time

Figure D.15 shows the change in resistance over time as the probe indented the skin on the various padding materials (at somewhat varying rates) and then lifted off (as in Figure 2.8). There was no substantial difference in overall behavior. (The apparent slower response of CC is due to the slower probe motion.) One difference to note is the large variation on PDMS-2.

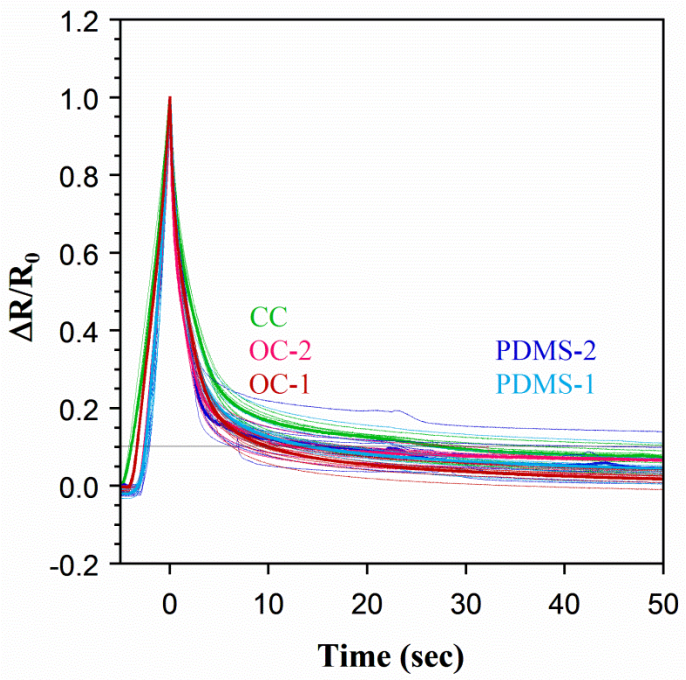

Figure D.15: Change in resistance as a function of time on the various padding materials. All 9 curves for each material are shown.

Appendix E Supporting Information of Chapter 3

E 1 Gauge Factor Measurement of Strip-Shaped Sensing Skins

The strip-shaped sensing skins used in this work were fabricated from the same batch of latex/EG dispersion and had a similar thickness of the sensing layer to reduce variations in the skins' performance. Nevertheless, to justify the comparison of the experiments discussed in the main text, it is necessary to measure the gauge factor and its variation among the sensing skins.

Ten sensing skins were randomly chosen, and their gauge factors were obtained under tensile strain. The experimental configuration used for the gauge factor measurement is shown in Figure E.1. The skins were suspended vertically, with one end being attached to the moving part of the transducer and the other end fixed. The gauge length was 90 mm. The skins were stretched at 1 mm/s to a strain of 6%, and then released back at 1mm/s. (The latex/EG sensing skin remains functional to an even higher strain [175], but that was not investigated here.) Each skin was tested twice, with a time interval between tests of 5 minutes.

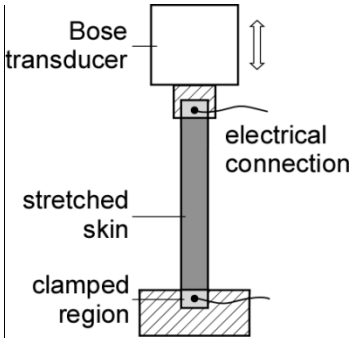

Figure E.1: Experimental setup for gauge factor measurement of the skin.

Given the known first-cycle effects (sections 3.4.1.1 and 3.4.3.1), the gauge factor for each skin was calculated from the second test, as shown in Figure E.2:. The skins had similar gauge factors (GF = 8.2 ±0.5), with a variation small enough to allow comparison of skins under different testing conditions. Assuming the maximum stretch ratio in the indentation tests was 10%, the variation in gauge factor leads to a variation in signal $\Delta R/R_0$ of 0.05. Considering the amplitude of the signal differences in the strata comparisons and under the other testing conditions in the main text, the variation of the gauge factor of different sensing skins is negligible. Since the skins here were randomly selected, it is reasonable to assume that the other skins made from the same batch and with the same amount of sensing material had similar gauge factors and variation.

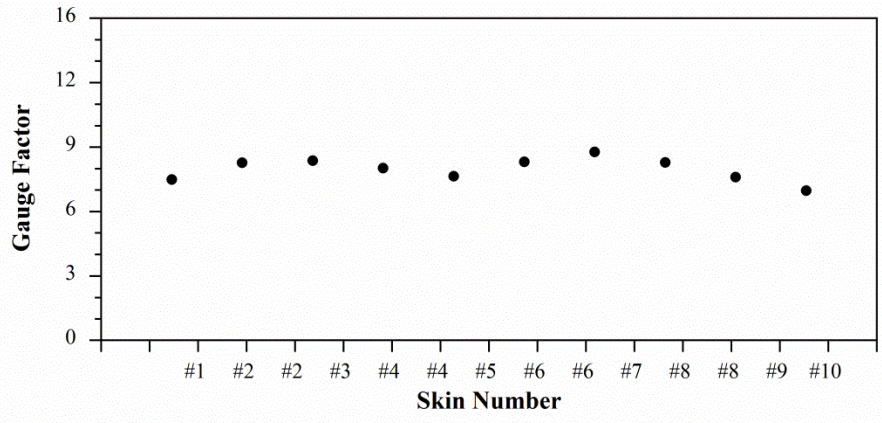

Figure E.2: Gauge factors measured from the second test for the 10 sensing skins.

E 2 Comparison with Commercial Compliant Conductive Materials

Sensors applied in soft robotics are required to be compliant and remain functional under large deformation. A large group of this type of sensor are piezoresistors made from conductive particles embedded in elastomers, such as the latex/EG sensor used in this work. Another type is piezoresistive, electrically conductive fabric, which is made by coating non-conductive fabric with conducting materials. Here, we compared the performance of our latex/EG skins with two commercial compliant conductive materials: carbon filled silicone from eShield RubberCon and EeonTex Conductive Stretchable Fabric (LTT-SLPA-20k). The materials were cut into strip-shaped samples of 0.8 cm x 11 cm. The fabric was cut along the thread. However, the thicknesses varied: it was 0.3 mm for the latex/EG sensing skin, 0.5 mm for the silicone/carbon sample, and 0.38 mm for the fabric.

The gauge factor was measured in the same way as discussed in Appendix E1, but the maximum strain was 15% (gauge length 90 mm) for the EeonTex fabric and the eShield RubberCon. Two consecutive tensile strain cycles were performed on each strip, separated by a 5 minute time interval. Figure E.3: shows the relative change in resistance of the three conductive materials during both the two cycles.

Figure E.3:a shows that $\Delta R/R_0$ decreased almost linearly as the fabric was stretched (after a small initial increase), to -7% at 15% strain. This is due to the coated fibers in the fabric making better electrical contact. The responses during both cycles were identical. The signal after release went to +2% before gradually returning to the baseline.

Figure E.3:b shows that the signal from the commercial eShield RubberCon was not only nonlinear with strain, but also non-monotonic, reaching a peak value in the stretching part of the first cycle of 33% at 7% strain. In addition, the signal dropped significantly in the 2^{nd} cycle. A clear unload peak was observed in the release half of both cycles, which was larger (48% at 9% strain in the first cycle) than the original peak. Neither signal returned to the baseline.

Figure E.3:c shows that the signal from the latex/EG sensing skin was monotonic and much larger than the other two materials, reaching 55% at only 6% strain in the first cycle. The resistance did not return to the baseline after the first test, as discussed in the main text. Therefore, the $\Delta R/R_0$ was smaller during 2^{nd} cycle, after which the signal almost returned to the baseline.

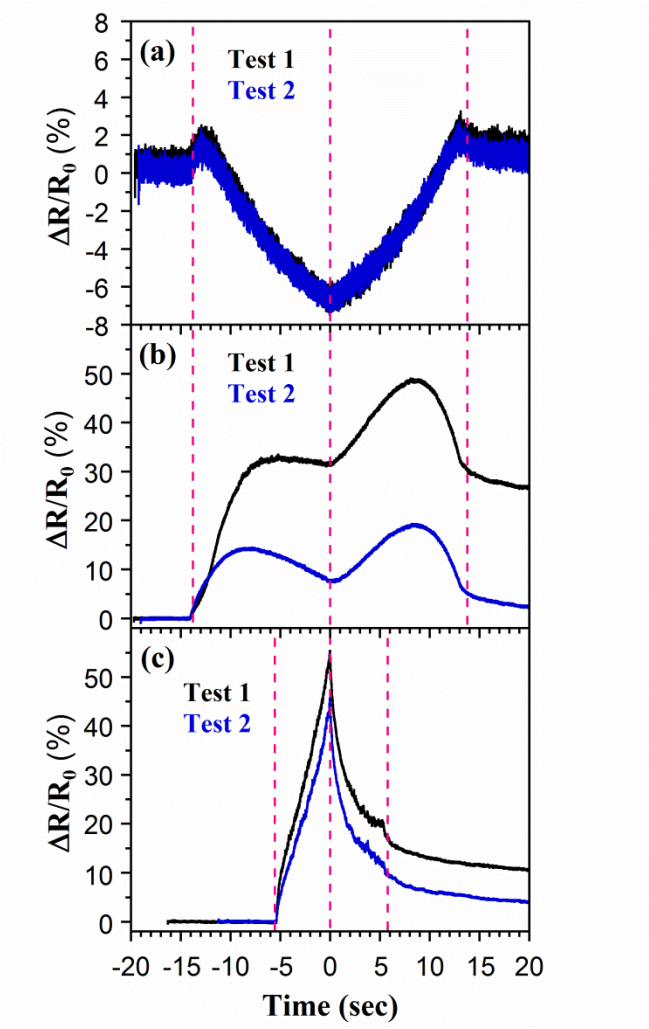

Figure E.3: Time profile during the tensile loading and unloading of the strip-shaped conductive material. a) conductive fabric, b) conductive rubber, and c) latex/EG sensing skin. Vertical scales differ. The initiation of a stretch, maximum stretch, and end of release are indicated by the dashed lines.

A comparison of the performance of the gauges is given in Table E.1:. The initial resistance of the EeonTex fabric was 200 kΩ, 100 times higher than the eShield RubberCon and 40 times higher than our latex/EG sensing skin. The gauge factor of the EeonTex fabric (0.5) was smaller than that of a conventional metallic strain gauge (2), while that of the eShield RubberCon (2) was comparable. The latex/EG sensing skin had the highest GF at 8.2. Both the fabric and

latex/EG skin showed a large linear sensing range. The eShield RubberCon material was the stiffest, having a relatively high modulus of 0.06 GPaThe moduli of other two were smaller than 0.016 GPa. The fabric showed little hysteresis, unlike the other two, which are elastomers.

Table E.1: Comparison of strip-shaped sensors made from three piezoresistive materials.

Performance	EeonTex Fabric	eShield RubberCon	EG/Latex
Initial Resistance (kΩ)	200	2	5
Gauge Factor	0.5	2.4	8.2
Linear Sensing Range	at least 15%	less than 7 %	at least 20% [175]
Modulus (GPa)	< 0.016	0.06	0.016
Hysteresis	Little	Large	Some

In conclusion, the conductive fabric had a low sensitivity, which is undesirable in a sensor. The commercial carbon/elastomer had a reasonable sensitivity but its response was non-monotic, and it was not very compliant.

E 3 Carbon Fiber Electrical Connections to Sensing Layer

Figure E.4: shows a close-up of an electrical connection to a sensing strip. As described in section 3.3, the connection between the carbon fiber bundles and the latex/EG composite is formed with a thicker layer of latex/EG, applied as droplets. The contact resistance between the carbon fibers and latex/EG is small compared to the resistance of the sensor (60 Ω). The good mechanical and electrical connection is due to the large surface area between the fiber yarns and the sensing composite.

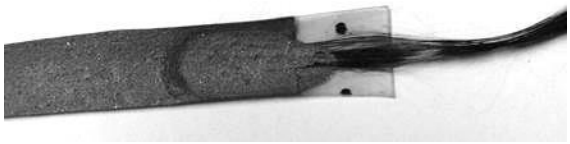

Figure E.4: Photograph showing a carbon fiber interface to a latex/EG sensor.

E 4 Loading/Unloading the Soft-Hard System

The complete loading and unloading paths for the experiment of Figure 3.2 are shown in Figure E.5:. The behavior was different for the force and resistance. For both, there was significant hysteresis in the 1st scan. The unloading path for the force was underneath the loading path, which means that a smaller force was exerted during unloading for a given indentation level. The hysteresis is due to the viscoelastic, energy-absorbing properties of the compliant membranes and the foam padding [175]: they do not spring back immediately but remain indented for a time. At the end of the scan, the force went back to its initial level of 0.

For the resistance, in the 1st scan the unloading path was higher than the loading path, which means that the resistance was slowly recovering during unloading. At the end of the scan, the resistance had not recovered to its initial level.

For the 2nd scan, the force retained the hysteretic behavior, with a slightly smaller maximum indentation. The hysteresis in the electrical signal was retained in the second scan, although the

behavior thereafter (not shown here) remained the same as for the 2nd scan. *The 1st scan acted as a preconditioning process, resulting in a more stable performance for the sensing skin.*

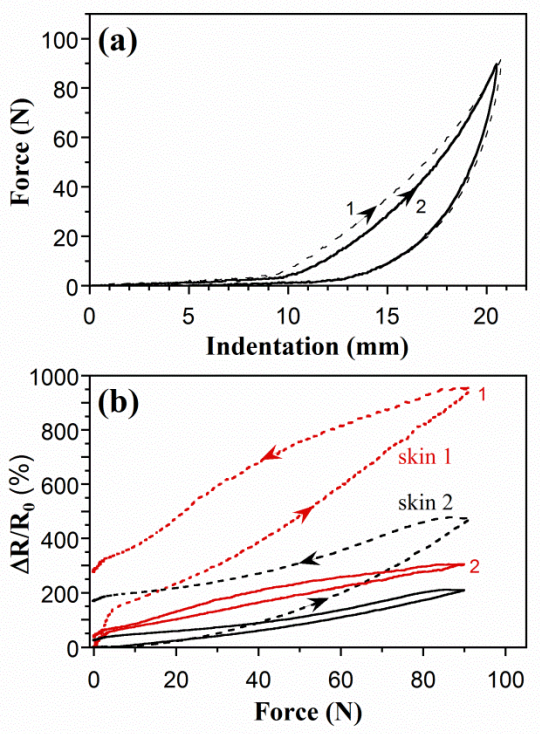

Figure E.5: Loading and unloading paths, indicated by arrows, for a) force and b) resistance during indentation. The 1st and 2nd scans are shown; subsequent scans looked like the 2nd one.

E 5 Effect of Extent of Indentation

Humans may touch a robot strongly or lightly. The effect of indentation level on the sensing signal from the soft-hard multi-layer system is investigated in this section. Two maximum indentation levels were selected: 14 mm and 20 mm. Four consecutive loading cycles were

performed for each level on the same strip using the standard test conditions (1 cm dia. flat-bottom probe, 5 minute time interval, 4.5 mm/s rate). To better understand the performance of the sensing skin alone at various stretch levels, tensile tests over the strip-shaped sensing skin were also conducted. Four consecutive tensile tests were performed to maximum strains of 10% and 20 % (5 minute time interval, 1 mm/s).

The test results from the second to the fourth loading are shown in. The mechanical response of the multi-layer system depended on the maximum indentation levels for indentations of more than 10 mm (Figure E.6:a). Looking at the sensing skin alone during tensile testing (Figure E.6:c), the tensile forces overlapped for both strains. Thus, the mechanical difference in the multi-layer system comes from the padding material, and in particular, given the point at which the signals diverge, from the hard foam.

Figure E.6:b shows that the electrical signal versus pressure depends on the maximum indentation level when the pressure is higher than 20 kPa (at the turning point of the curve). However, Figure E.6:c shows that most of the electrical response curve, except at the tip, overlaps for the two cases. Thus, the difference in electrical signal is due to the mechanical behavior of the hard foam.

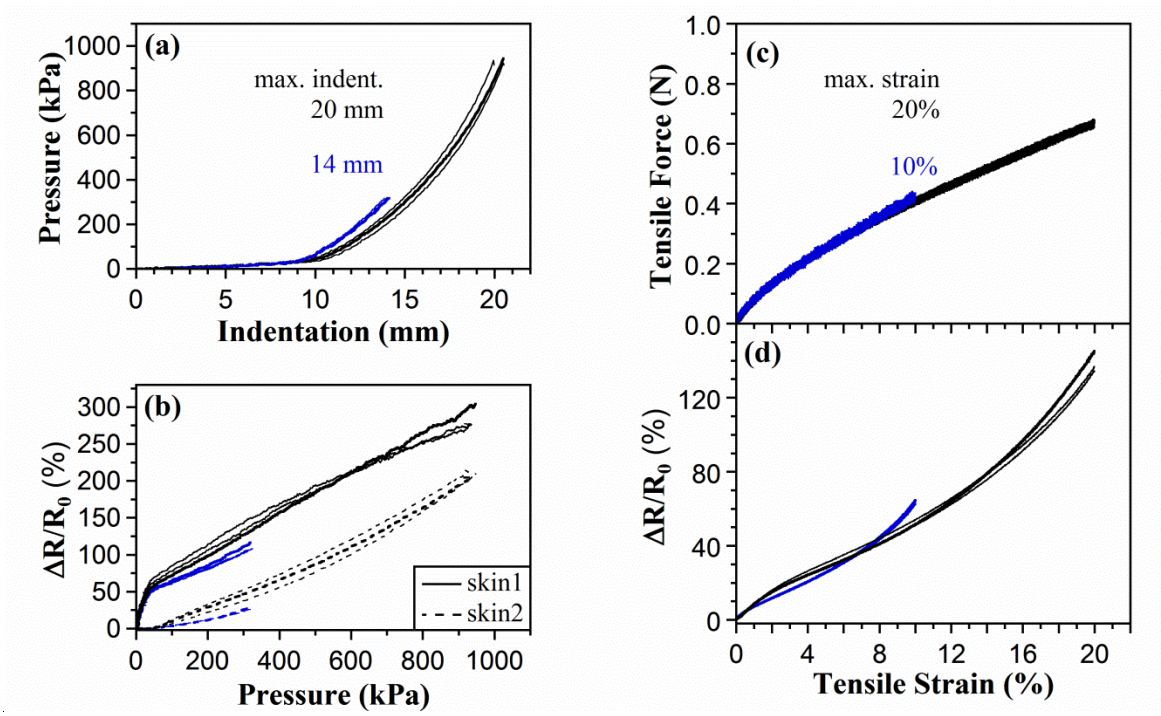

Figure E.6: Effect of maximum indentation (a and b) or tensile strain (c and d) of a strip-shaped sensing skin (2nd to 4th cycles). a) Probe pressure versus probe indentation for two maximum indentation levels. b) Normalized change in resistance of the two sensing skins vs. probe pressure. c) Tensile force vs. tensile strain for two maximum tensile strains. d) Normalized change in resistance vs. tensile strain.

E 6 Further Discussion of the Deformed Membrane Shape

The location of the deformation areas of the membrane can be determined by comparing before and after indentation, the pattern of evenly spaced radial and circular lines drawn on the surface.

Figure E.7:a shows the concentric circular pattern on the membrane. The center of the probe was aligned with the center of the circles. Since the deformation from indentation tests is 3D, the distance between the pattern and the camera is critical in evaluating the amount of deformation.

The deformed pattern was aligned with the un-deformed pattern at two locations. Figure E.7:b overlaps the area at the bottom of the probe. The 1st and 2nd rings were not deformed, while the 3rd and 4th rings were enlarged by 0.1 mm. This means that no deformation took place underneath the probe. Figure E.7:c overlaps the outmost circle in the deformed and un-deformed photos. Outside the probe area, the deformation occurs at the rings close to the edge of the probe, with less deformation occurring for the rings further from the probe. Therefore, most of the deformation occurs near the edge of the probe. These results support the conclusion from the edge-on views in section 3.4.2.2 and the strain model in section 3.4.2.3.

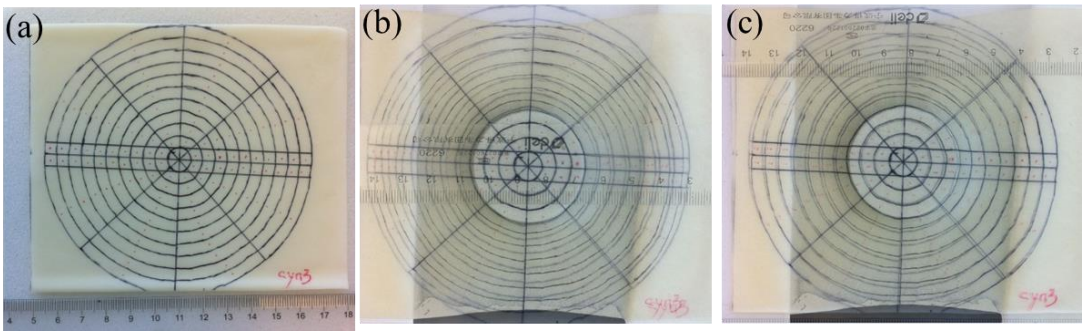

Figure E.7: a) The pattern on the undeformed latex membrane. b) Overlap image of the deformed pattern inside the probe area and the undeformed pattern. c) Overlap image of the deformed pattern at the edge of the membrane and the undeformed pattern.

E 7 Replicate Characterization

In order to corroborate the performance of the padding configurations, replicate tests were performed. As in the main chapter, the loading rate was 4.5 mm/s. Figure E.8: shows the force versus indentation and $\Delta R/R_0$ versus force for these additional samples.

Duplicate tests on the soft-hard (S-H) systems are shown at the top of Figure E.8:; the foam layers were the same, but the sensing skins differed, although they came from the same batch (i.e., they were made at the same time). The two force-indentation curves were nearly identical but for a horizontal offset, which may reflect differences at the interfaces between the two strata, which were placed together manually. The skin1 curves had the same basic shape, but a different amplitude, reflecting a different sensitivity of the sensing skin. Sensitivity depends on loading history, and in this case the loading tests were not the same for the two sets of samples. The skin2 plots overlapped. All the curves had a higher than expected sensitivity (slope) at high force (compare the H-H curves), after the probe encountered the hard foam, which was unaccounted for by the models. This is not understood, but it appears to be reproducible.

Results of re-testing of the soft-soft (S-S) system one day later are shown in the center of Figure E.8:. The force-indentation curves were identical. The amplitudes of the resistance-force curves differed, again reflecting differences in sensitivity due to memory effects, but the shapes were the same.

A duplicate sample of the hard-hard system was also tested, and the results are shown at the bottom of Figure E.8:. The force-displacement curves were identical, but the amplitudes of the resistance curves again differed, with the shapes being similar. In *sample b*, there was a pronounced change in slope at a force of 15 N, which was not seen in *sample a*. The reason for this is not yet understood, but may be related to differences in skin/probe interactions or interface effects.

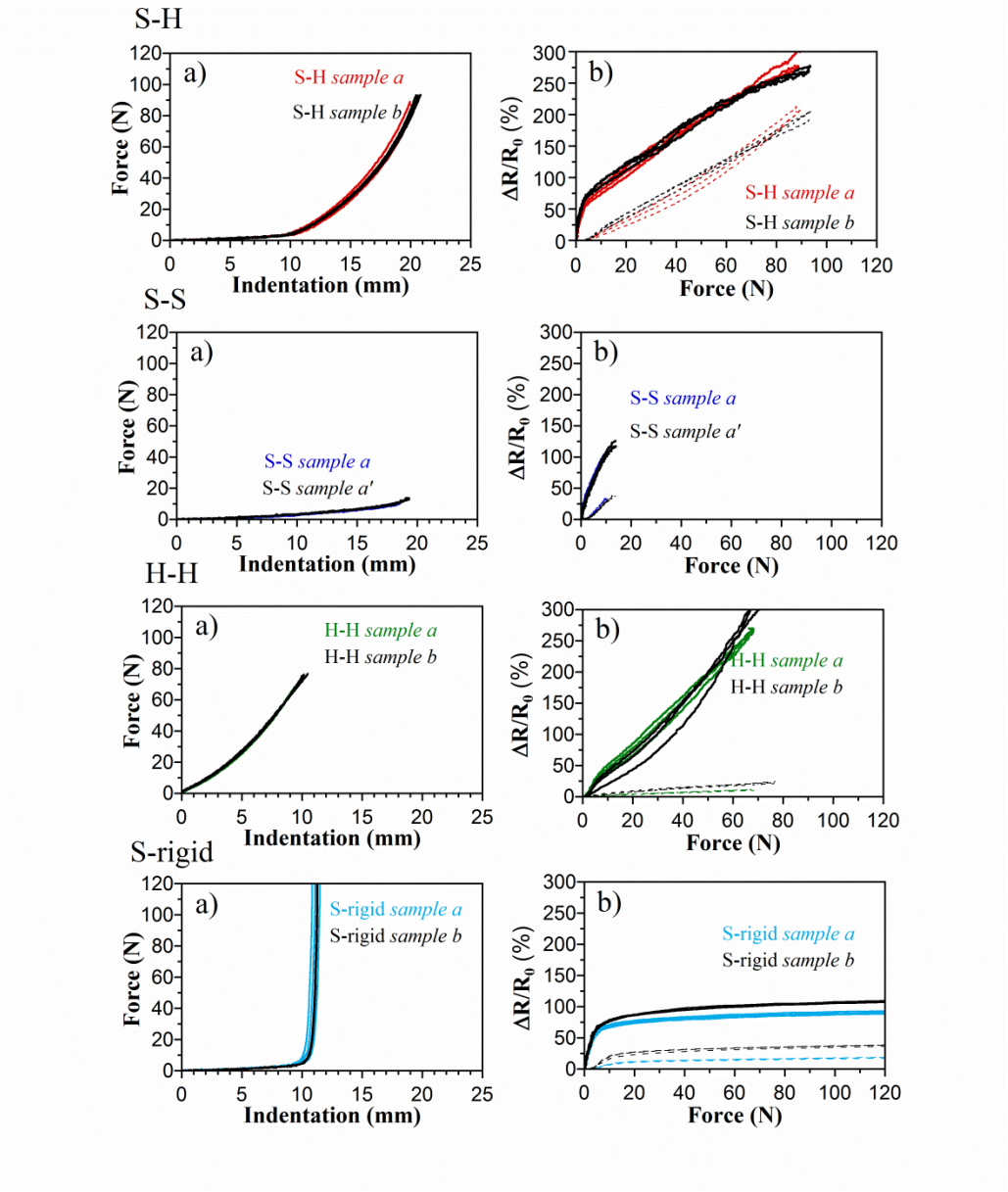

Figure E.8: Duplicate tests of the soft-hard (S-H), soft-soft (S-S), and hard-hard (H-H) configurations. *Sample a* data were previously shown in the main text (colors correspond to those used in Figure 3.4), *sample b* data (black) were obtained from a new pair of sensing skins on the same pieces of foam, and *sample a'* data (black) were taken on the day following *sample a*. a) Force as a function of indentation. b) Normalized change in resistance as a function of force (2nd to 4th scans) from skin 1 (solid lines) and skin 2 (dashed lines).

E 8 Greater Indentation of the Hard-Hard System

Section 3.4.2.3 showed that the model accounted for the experimental data for the soft-soft and hard-hard configurations, but not for the soft-hard. The experiment-model mismatch started when the probe reached the hard padding layer. In the main text, the maximum indentation on the hard-hard configuration stopped at 10 mm (Figure 3.4b, Figure 3.10c). In order to explore the source of the mismatch, greater indentation on the hard-hard configuration was tested.

Indentation tests were repeated, but this time to a depth of 20 mm. Three tests were performed sequentially, separated by 5 minute intervals, using the usual loading speed of 4.5 mm/s. The thicknesses for the hard-hard configuration were d_1 = 9 mm and d_2 = 19 mm, so the maximum indentation exceeded the thickness of the top padding layer.

Figure E.9:a shows the force as a function of indentation. At 20 mm indentation, the force exerted by the probe reached 300 N, which is 3 times that on the soft-hard structure and 30 times that on the soft-soft structure. The curve was nevertheless smooth and resembled the one in Figure 3.4b.

The response of skin 1 can be seen in Figure E.9:b. After the probe reached 11 mm of indentation (75 N), the slope of this curve increased by a factor of 3. (This was not seen at 75 N in Figure 3.4c, but it may have occurred at a higher force.) Recalling that the higher slope in the

soft-hard system also occurred when the probe reached the interface, the transition points suggests that the higher slopes may be related to the interface. When the indentation went beyond 15 mm in the H-H system, the signal reached a plateau. This is also not understood, but it implies that forces above 200 N induce no further strain in the sensing skin.

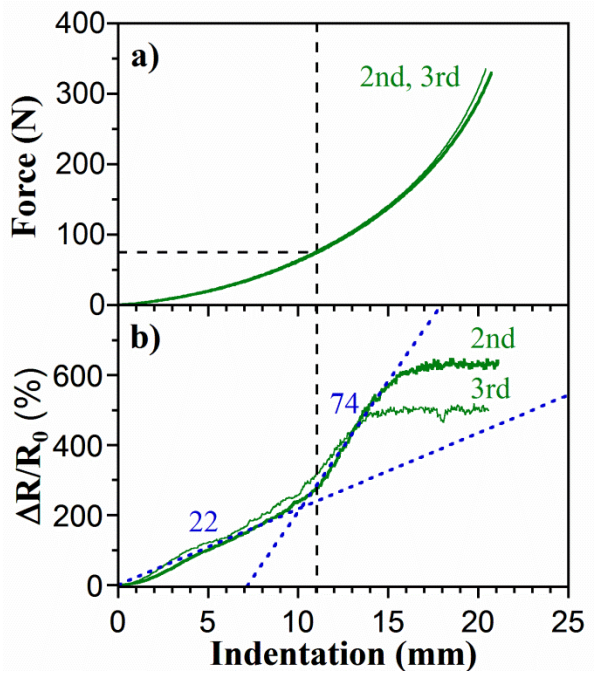

Figure E.9: Tests with greater indention on the hard-hard system (2nd and 3rd scans). a) Force and b) relative change in resistance of skin 1 as a function of indentation. Curve fits to the slopes for the two linear ranges in (b) are shown as blue dashed lines, and the slopes are provided (%/mm).

E 9 Additional Voltage vs. Time Data

Figure E.10:a shows voltage data from an experiment in which finger touches, rather than a rigid probe, were used to indent the same system. The first "pre-treatment" touch was at a force perceived as "strong". It raised the baseline (by approx. 0.2 V), which remained high during the

subsequent two presses to the same force. During a series of subsequent light touches of 1, 2, and 3 second duration, the baseline fell back to the original level over the course of 5 minutes. A medium touch raised the baseline again, and it remained raised during the subsequent medium touches. We can infer that return of the voltage to the baseline is minimally inhibited by touches that are much lighter than the baseline-shifting touch. Touches at the same strength prevent recovery. Touches that are stronger raise the baseline further.

To show the efficacy of using the trailing baseline as the "zero" level, the data of Figure E.10:a were adjusted in Figure E.10:b.

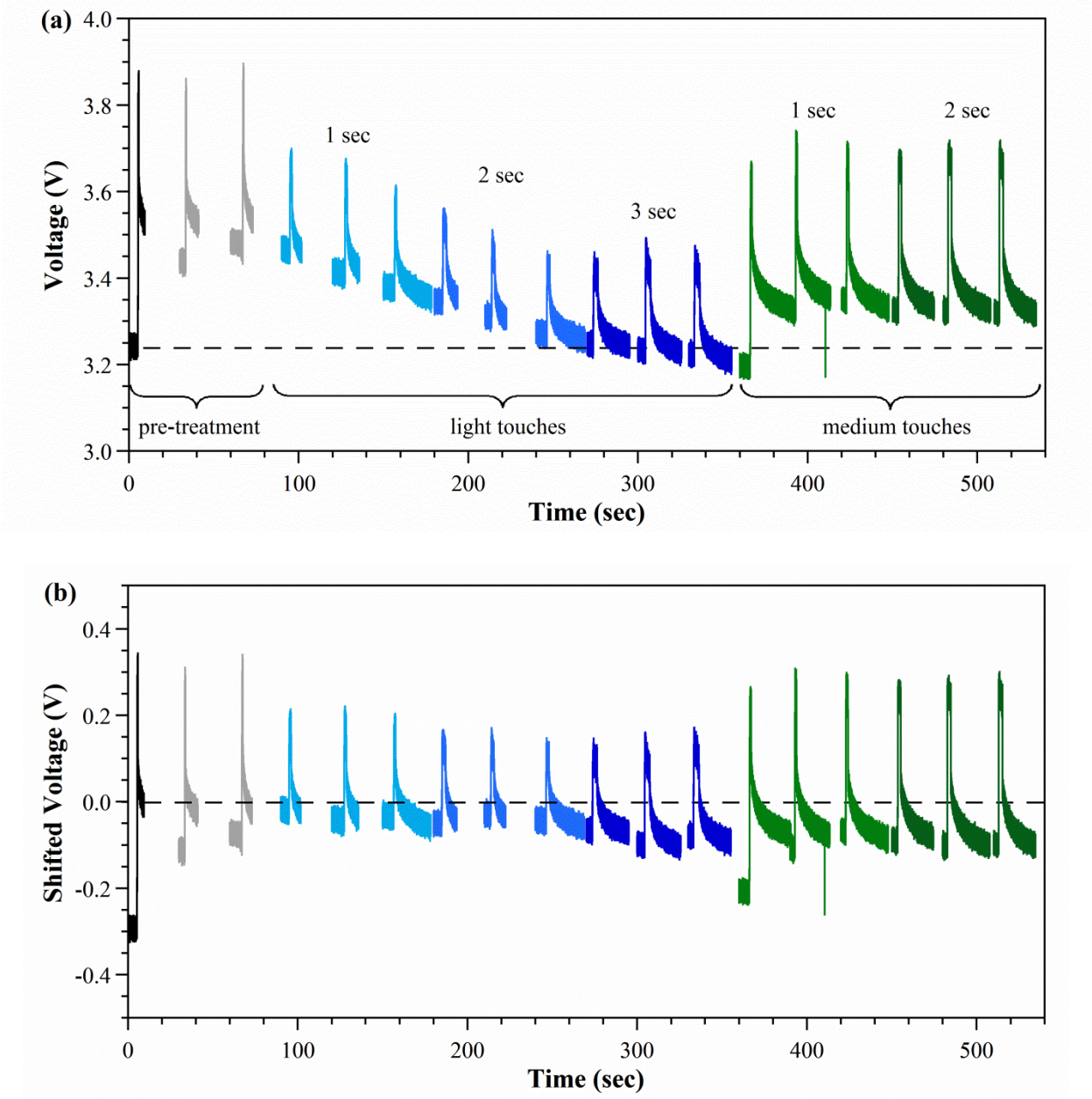

Figure E.10: a) Voltage over time recorded during strong touch pretreatment, followed by light and medium touches for different times. Time intervals between touches were approximately 30 seconds, varying by human error. The dashed line indicates the initial baseline. b) The data from (a) replotted using post-peak ("trailing") baseline subtraction, taking the average value (over 0.02 seconds) 5 seconds after the peak (the baseline after the 1st pre-treatment was taken 3 seconds after the peak due the limited available data recorded).

Appendix F Supporting Information of Chapter 4

Figure F.1 is plotted using the same data of Figure 3.13 a and b. During the experiment, probe force was directly measured from the force transducer. The 1 cm dia. cylindrical probe was used to indent the soft-hard multi-layer system at two loading speeds, 4.5 and 0.05 mm/s. Four consecutive loading tests were conducted at each rate, with a time interval between them of 5 minutes.

Test results from the second to the fourth loading cycles are shown in Figure F.1. Somewhat larger forces were measured at the higher loading speed (Figure F.1a). The electrical response (Figure F.1b) from skin1 also depended on the indentation speed: $\Delta R/R_{0.}$was greater at the faster loading rate. Skin 2, however, did not show much rate-dependency.

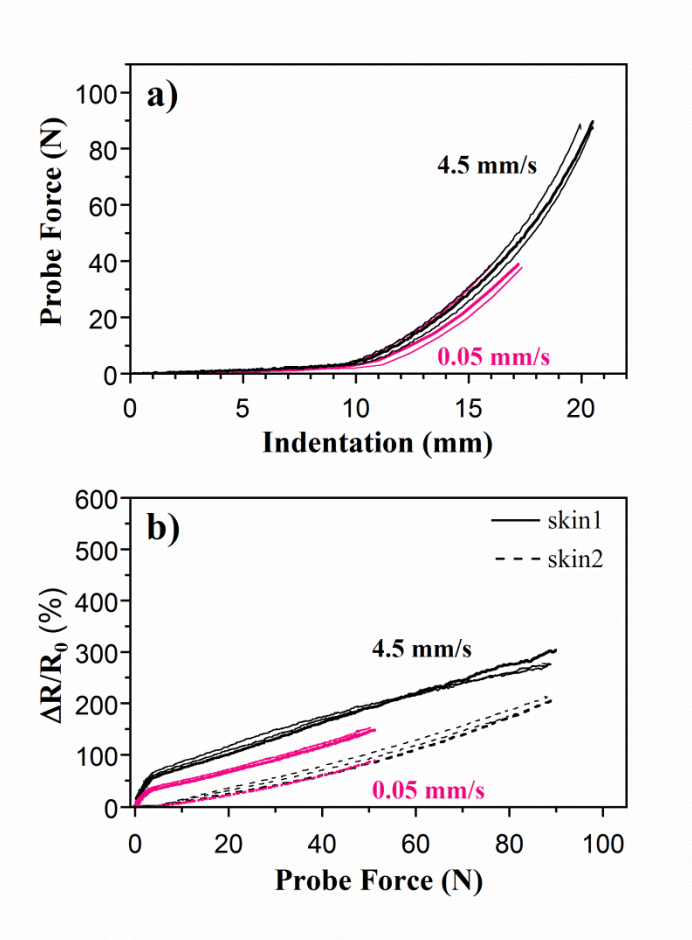

Figure F.1: The effect of loading speed from the 2nd to 4th scans for a 1 cm dia. cylindrical probe. Indentation tests conducted at loading speeds of 4.5 and 0.05 mm/s. a) Probe force vs. probe indentation. b) Normalized change in resistance of the two sensing skins vs. probe force. The curves from skin2 at 0.05 mm/sec overlapped perfectly, so only the first is shown.

The multi-layer sensing system is sensitive to loading speed, both mechanically and electrically, although the effect is smaller for skin2. For human finger presses, it takes longer to indent the sensing system when higher force is required, as shown in Figure 4.4a in which the slope (rate of press) is smaller for larger force. Therefore, in the plot of sensor signal vs. finger force, the slope for skin1 decreases for harder presses.

In addition to the effects of contact area and loading speed, other test conditions differ between the probe indentation tests and human touch tests, such as the rigidity of the probe and the loading history, which are not discussed in this chapter.

Appendix G Supporting Information of Chapter 5

G 1 Reconstructed Images and Hyperparameters

Reconstructed images at various hyperparameters for background conductivity of 0.02 S/sq and 0.001 S/sq is shown in Figure G.1.

(a)

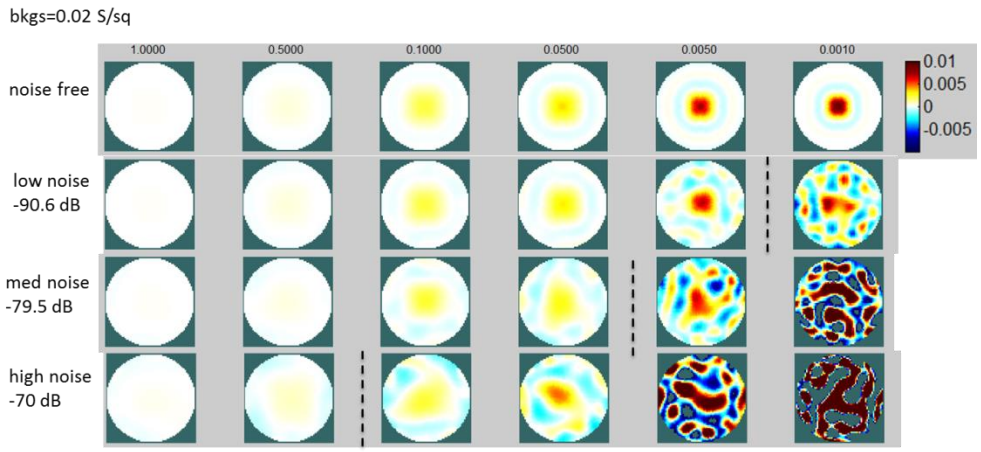

(b)

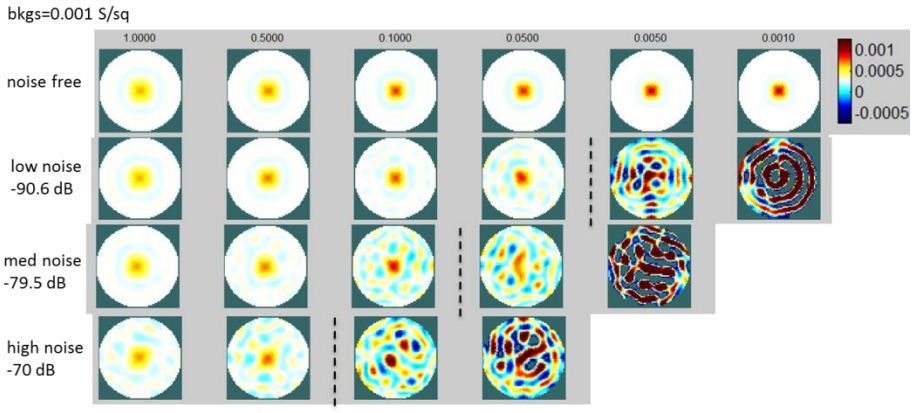

Figure G.1: Reconstructed images while using different hyperparameters for background conductivities of (a) 0.02 S/sq and (b) 0.001 S/sq in cases of noise free, low noise, medium noise, and high noise.

G 2 Optimal Hyperparameter and Feature of Stimulus

Optimal hyperparameter at different noise levels has been investigated for a stimulus with a specific intensity in the main chapter. Optimal hyperparameters for stimuli of different intensities are studied here.

Three intensities of stimuli were selected, represented by relative conductivity decrease of 0.3, 0.4, and 0.5. Number of artifacts were obtained for a range of hyperparameters covering optimal hyperparameter. Cases of low, medium, and high noise were simulated, and the definition for noise levels has been described in session 5.3.1. Same simulation setups were for all cases, including radius of stimulus (r = 0.2) and background conductivity ($S_0 = 0.01\ S/sq$).

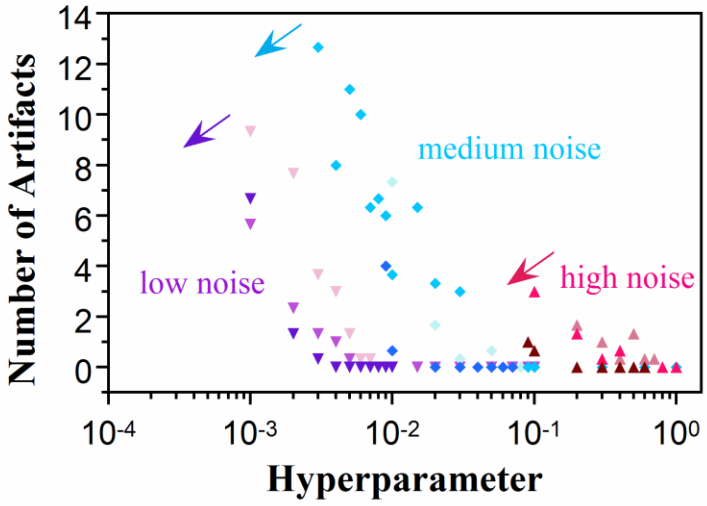

Figure G.2: Number of artifacts versus hyperparameter for different intensity of stimulus at low, medium, and high noise levels. The arrows indicate the increasing intensities, coded by lighter to darker color.

Figure G.2 shows number of artifacts as a function of hyperparameters for increasing intensity of stimulus at three noise levels. At each noise level, the number of artifacts for a stimulus with

higher intensity decreases sooner to zero with increasing hyperparameters. This means the stronger the stimulus, the smaller optimal hyperparameter is required. Data points obtained from this simulation in general are separated by different noise levels.

Optimal hyperparameter is affected by not only noise level but also features of stimuli. Stimulus with higher intensity requires smaller optimal hyperparameter. It is expected that stimulus with bigger contact area also requires smaller optimal hyperparameter. For the range of intensity investigated in this session, optimal hyperparameters for stimuli with different intensities fall in separate regions.

G 3 Discussion on EIT Spatial Performance

The spatial performance presented in the main text is along one radial direction. To investigate the dependency upon different radial directions, this session presented spatial performance for both intensity and size obtained from different radial directions.

The spatial performance is obtained in simulation using EIDORS toolbox. Figure G.3 demonstrates the definition of radial directions over a circular sensing medium. The radial direction is defined by the angle Φ. Since the sensing medium is symmetric, only radial directions inside the first quadrant are investigated. To compare spatial performance for radial directions pointing to and not pointing to electrodes, performance along radial directions $\Phi = 0$, 5, 10, 15, and 22.5 degree are investigated. Note that $\Phi = 0$ and 22.5 degree are two directions

pointing to two adjacent electrodes. To compare spatial performance for radial directions pointing to different electrodes, spatial performance along radial directions Φ = 0, 22.5, 45, 67.5, and 90 degree are investigated. 33 data points within radial positions 0 – 0.8 are selected. A stimulus is centered at each data point, with a stimulus radius of 0.2 and relative conductivity change of ds = -0.4 S_0. Background conductivity is $S_0 = 0.01\ S/sq$.

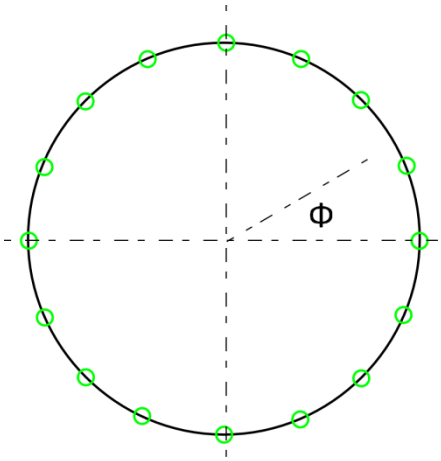

Figure G.3: Schematic for radial directions over a circular sensing medium. Radial direction is indicated by the angle Φ. Green circles indicate point electrodes.

Figure G.4 shows the spatial performance of a) intensity (peak value) and b) size along radial directions Φ = 0, 5, 10, 15, and 22.5 degree. Intensity curves within radial position 0-0.7 are identical for all directions. Small split occurs when position is approaching 0.8. Spatial curves are closer for radial directions pointing closer to electrodes or away from electrodes. Size curves demonstrate similar performance as the intensity curves. Performance along different directions within radial position of 0-0.7 is identical, and the difference close to edge (radial position 0.8) is not significant.

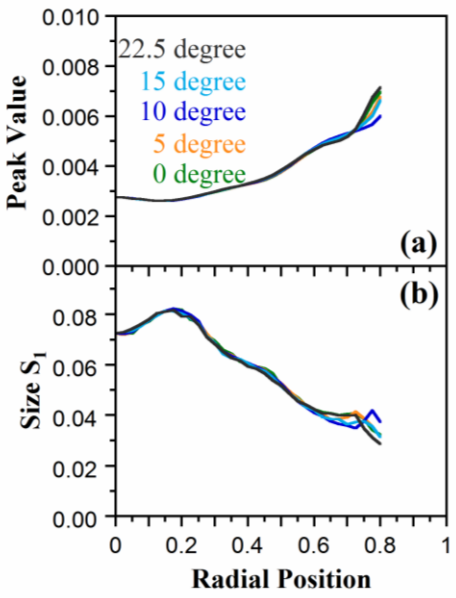

Figure G.4: Comparison of spatial performance of a) intensity (peak value) and b) size along radial directions pointing to (0 and 22.5 degree)and not pointing to (5, 10, and 15 degree) electrodes.

Figure G.5 shows the spatial performance of a) intensity (peak value) and b) size along radial directions Φ = 0, 22.5, 45, 67.5, and 90 degree. Spatial performance for both intensity and size are identical along radial directions pointing to different electrodes.

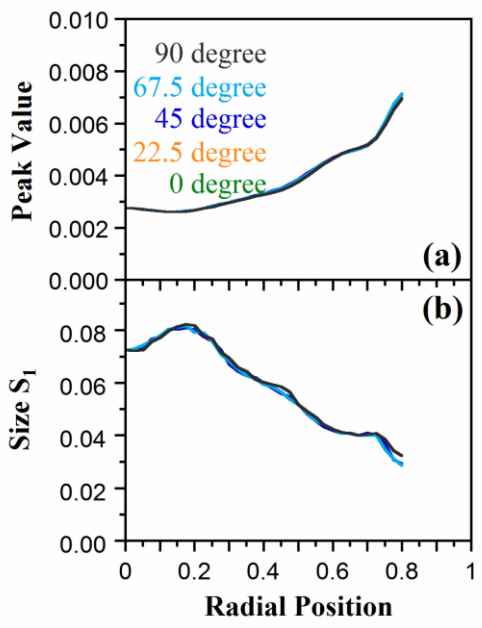

Figure G.5: Comparison of spatial performance of a) intensity and b) size along radial directions pointing to different electrodes (0, 22.5, 45, 67.5, and 90 degree).

The investigation shown in this session validates the usage of performance along one radial direction in the main Chapter. Considering that the radial directions during experiments were all pointing to electrodes, the split effect close to position = 0.8 does not affect the spatial correction method described in Chapter 5.3.3.

Bibliography

1. A. Shukla and H. Karki, "Application of robotics in onshore oil and gas industry-A review Part I," Robot. Auton. Syst., 75**,** 490-507 (2016).

2. T. Brogårdh, "Present and future robot control development - An industrial perspective," Annu. Rev. Control, 31 (1)**,** 69-79 (2007).

3. A. Bechar and C. Vigneault, "Agricultural robots for field operations: Concepts and components," Biosyst. Eng., 149**,** 94-111 (2016).

4. H. B. Yan, M. H. Ang, and A. N. Poo, "A survey on perception methods for human-robot interaction in social robots," Int. J. Soc. Robot., 6 (1)**,** 85-119 (2014).

5. L. Bruzzone and G. Quaglia, "Review article: locomotion systems for ground mobile robots in unstructured environments," Mech. Sci., 3 (2)**,** 49-62 (2012).

6. T. Arnold and M. Scheutz, "The tactile ethics of soft robotics: designing wisely for human-robot interaction," Soft Robotics, 4 (2)**,** 81-87 (2017).

7. B. D. Argall and A. G. Billard, "A survey of tactile human robot interactions," Robot. Auton. Syst., 58 (10)**,** 1159 (2010).

8. RIKEN - Bio-Mimetic Control Research Center, "Ri-Man", http://rtc.nagoya.riken.jp/RI-MAN/index_us.html.

9. T. Minato, Y. Yoshikawa, T. Noda, S. Ikemoto, H. Ishiguro, and M. Asada, "CB2: A child robot with biomimetic body for cognitive developmental robotics," in IEEE-RAS Int'l. Conf. on Humanoid Robots of the series IEEE-RAS International Conference on Humanoid Robots, p. 557-+ (2007).

10. H. Ishiguro, T. Ono, M. Imai, T. Maeda, T. Kanda, and R. Nakatsu, "Robovie: an interactive humanoid robot," Industrial Robot, 28 (6)**,** 498-503 (2001).

11. T. Tajika, T. Miyashita, H. Ishiguro, and N. Hagita, "Reducing influence of robot's motion on tactile sensor based on partially linear model," in IEEE Int'l. Conf. on Intelligent Robots and Systems (IROS), p. 512-517 (2008).

12. T. Yoshikai, M. Hayashi, Y. Ishizaka, T. Sagisaka, and M. Inaba, "Behavior integration for whole-body close interactions by a humanoid with soft sensor flesh," in IEEE-RAS Int'l. Conf. on Humanoid Robots of the series IEEE-RAS International Conference on Humanoid Robots, p. 109-114 (2007).

13. W. D. Stiehl, J. Lieberman, C. Breazeal, L. Basel, L. Lalla, and M. Wolf, "Design of a therapeutic robotic companion for relational, affective touch," ROMAN 2005. IEEE International Workshop on Robot and Human Interactive Communication, 2005., (IEEE), p. 408-415 (2005).

14. G. Westling and R. S. Johansson, "Factors influencing the force control during precision grip," Exp. Brain Res., 53 (2)**,** 277-284 (1984).

15. M. H. Lee and H. R. Nicholls, "Tactile sensing for mechatronic - a state of the art survey," Mechatronics, 9 (1)**,** 1-31 (1999).

16. T. Mukai, M. Onishi, T. Odashima, and S. Hirano, "Development of the tactile sensor system of a human-interactive robot "RI-MAN"," IEEE Trans. Robot., 24**,** 505-512 (2008).

17. Y. Ohmura and Y. Kuniyoshi, "Humanoid robot which can lift a 30kg box by whole body contact and tactile feedback," IEEE Int'l. Conf. on Intelligent Robots and Systems (IROS)**,** 1136-1141 (2007).

18. R. Dahiya, P. Mittendorfer, and M. Valle, "Directions toward effective utilization of tactile skin: a review," IEEE Sensors J., 13 (11)**,** 4121-4138 (2013).

19. R. S. Fearing, "Tactile sensing mechanisms," Int. J. Robotics Res., 9 (3)**,** 3-23 (1990).

20. A. Chortos, J. Liu, and Z. A. Bao, "Pursuing prosthetic electronic skin," Nat. Mater., 15 (9)**,** 937-950 (2016).

21. M. L. Hammock, A. Chortos, B. C. K. Tee, J. B. H. Tok, and Z. A. Bao, "25th Anniversary Article: The evolution of electronic skin (E-skin): a brief history, design considerations, and recent progress," Adv. Mater., 25 (42)**,** 5997-6037 (2013).

22. N. S. Lu and D. H. Kim, "Flexible and stretchable electronics paving the way for soft robotics," Soft Robotics, 1 (1)**,** 53-62 (2014).

23. S. Stassi, V. Cauda, G. Canavese, and C. F. Pirri, "Flexible tactile sensing based on piezoresistive composites: a review," Sensors, 14 (3)**,** 5296-5332 (2014).

24. M. Inaba, Y. Hoshino, K. Nagasaka, T. Ninomiya, S. Kagami, and H. Inoue, "A full-body tactile sensor suit using electrically conductive fabric and strings," IEEE Int'l. Conf. on Intelligent Robots and Systems (IROS), Osaka, Japan, p. 450-457 (Nov 4-8, 1996).

25. A. Schmitz, P. Maiolino, M. Maggiali, L. Natale, G. Cannata, and G. Metta, "Methods and technologies for the implementation of large-scale robot tactile sensors," IEEE Trans. Robot., 27 (3)**,** 389-400 (2011).

26. M. W. Strohmayr, H. Wörn, and G. Hirzinger, "The DLR artificial skin step I: Uniting sensitivity and collision tolerance," IEEE Int'l. Conf. on Robot. and Autom. (ICRA), Karlsruhe, Germany, p. 1012-1018 (May 6-10, 2013).

27. R. S. Dahiya and M. Valle, "Robotic Tactile Sensing : Technologies and System" (Springer, Dordrecht, 2013).

28. S. J. Lederman, "Skin and touch" in Encyclopedia of human biology; Vol. 7, edited by R. Dulbecco (Academic, San Diego, CA, 1991), p. 51-63.

29. Y. Park, B. Chen, and R. J. Wood, "Design and fabrication of soft artificial skin using embedded microchannels and liquid conductors," IEEE Sensors J., 12 (8), 2711-2718 (2012).

30. W. Zeng, L. Shu, Q. Li, S. Chen, F. Wang, and X.-M. Tao, "Fiber-based wearable electronics: a review of materials, fabrication, devices, and applications," Adv. Mater. , 26 (31), 5310-5336 (2014).

31. G. H. Büscher, R. Koiva, C. Schuermann, R. Haschke, and H. J. Ritter, "Flexible and stretchable fabric-based tactile sensor," Robot. Auton. Syst., 63, 244-252 (2015).

32. T. Yamada, Y. Hayamizu, Y. Yamamoto, Y. Yomogida, A. Izadi-Najafabadi, D. N. Futaba, and K. Hata, "A stretchable carbon nanotube strain sensor for human-motion detection," Nat. Nanotechnol., 6 (5), 296-301 (2011).

33. D. J. Lipomi, M. Vosgueritchian, B. C. K. Tee, S. L. Hellstrom, J. A. Lee, C. H. Fox, and Z. N. Bao, "Skin-like pressure and strain sensors based on transparent elastic films of carbon nanotubes," Nature Nanotechnology, 6 (12), 788-792 (2011).

34. R. D. Howe and M. R. Cutkosky, "Dynamic tactile sensing - perception of fine surface-features with stress rate sensing," IEEE Trans. Robot. Autom., 9 (2), 140-151 (1993).

35. H. Vandeparre, D. Watson, and S. P. Lacour, "Extremely robust and conformable capacitive pressure sensors based on flexible polyurethane foams and stretchable metallization," Appl. Phys. Lett., 103 (20), 204103 (2013).

36. J. A. Fan, W. H. Yeo, Y. W. Su, Y. Hattori, W. Lee, S. Y. Jung, Y. H. Zhang, Z. J. Liu, H. Y. Cheng, L. Falgout, M. Bajema, T. Coleman, D. Gregoire, R. J. Larsen, Y. G. Huang, and J. A. Rogers, "Fractal design concepts for stretchable electronics," Nature Communications, 5 (2014).

37. X. Huang, Y. H. Liu, H. Y. Cheng, W. J. Shin, J. A. Fan, Z. J. Liu, C. J. Lu, G. W. Kong, K. Chen, D. Patnaik, S. H. Lee, S. Hage-Ali, Y. G. Huang, and J. A. Rogers, "Materials and designs for wireless epidermal sensors of hydration and strain," Adv. Funct. Mater., 24 (25), 3846-3854 (2014).

38. S.-J. Park, J. Kim, M. Chu, and M. Khine, "Highly flexible wrinkled carbon nanotube thin film strain sensor to monitor human movement," Adv. Mater. Technol., 1 (5) (2016).

39. J. Kost and M. Narkis, "Resistivity behavior of carbon-black-filled silicone rubber in cyclic loading experiments," J. Appl. Polym. Sci., 29 (12)**,** 3937-3946 (1984).

40. M. Shimojo and A. Namiki, "A tactile sensor sheet using pressure conductive rubber with electrical-wires stitched method," IEEE Sensors J., 4 (5)**,** 589-596 (2004).

41. T. Ding, L. Wang, and P. Wang, "Changes in electrical resistance of carbon-black-filled silicone rubber composite during compression," J. Polym. Sci. B 45 (19)**,** 2700-2706 (2007).

42. N. Lu, C. Lu, S. Yang, and J. Rogers, "Highly sensitive skin-mountable strain gauges based entirely on elastomers," Adv. Funct. Mater., 22 (19)**,** 4044-4050 (2012).

43. M. Y. Cheng, C. M. Tsao, Y. Z. Lai, and Y. J. Yang, "The development of a highly twistable tactile sensing array with stretchable helical electrodes," Sens. Act. A, 166 (2)**,** 226-233 (2011).

44. N. Hu, Y. Karube, C. Yan, Z. Masuda, and H. Fukunaga, "Tunneling effect in a polymer/carbon nanotube nanocomposite strain sensor," Acta Mater., 56 (13)**,** 2929-2936 (2008).

45. M. Amjadi, Y. J. Yoon, and I. Park, "Ultra-stretchable and skin-mountable strain sensors using carbon nanotubes-Ecoflex nanocomposites," Nanotechnology, 26 (37) (2015).

46. L. Chen, G. H. Chen, and L. Lu, "Piezoresistive behavior study on finger-sensing silicone rubber/graphite nanosheet nanocomposites," Adv. Funct. Mater., 17 (6)**,** 898-904 (2007).

47. M. Kujawski, J. D. Pearse, and E. Smela, "Elastomers filled with exfoliated graphite as compliant electrodes," Carbon, 48 (9)**,** 2409-2417 (2010).

48. J. Wissman, A. Perez-Rosado, A. Edgerton, B. M. Levi, Z. N. Karakas, M. Kujawski, A. Philipps, N. Papavizas, D. Fallon, H. A. Bruck, and E. Smela, "New compliant strain gauges for self-sensing dynamic deformation of flapping wings on miniature air vehicles," Smart Mater. Struct., 22 (8)**,** 085031 (2013).

49. M. K. Abyaneh and S. K. Kulkarni, "Giant piezoresistive response in zinc-polydimethylsiloxane composites under uniaxial pressure," J. Phys. D, 41 (13) (2008).

50. A. Charalambides, "Microfabricated elastomer tactile sensors for robotic fingertip systems," Doctor of Philosophy, Mechanical Engineering, University of Maryland - college park (2016).

51. M. P. Kujawski, "Polymer Composites For Sensing And Actuation," Doctor of Philosophy, Material Science and Engineering, University of Maryland, College Park (2011).

52. S. Kirkpatrick, "Percolation and conduction," Rev. Mod. Phys., 45 (4), 574-588 (1973).

53. J. Kost, A. Foux, and M. Narkis, "Quantitative model relating electrical resistance, strain, and time for carbon black loaded silicone rubber," Polym. Eng. Sci., 34 (21), 1628-1634 (1994).

54. University of Auckland, "An introduction to solid mechanics: viscoelasticity", http://homepages.engineering.auckland.ac.nz/~pkel015/SolidMechanicsBooks/, 2015.

55. W. N. Findley, Creep and Relaxation of Nonlinear Viscoelastic Materials with An Introduction to Linear Viscoelasticity, Vol. 18, North-Holland Series in Applied Mathematics and Mechanics (Elsevier Science, Amsterdam, NETHERLANDS, 1976).

56. M.-A. Lacasse, V. Duchaine, and C. Gosselin, "Characterization of the electrical resistance of carbon-black-filled silicone: application to a flexible and stretchable robot skin," IEEE Conf. on Robotics and Automation (ICRA), Anchorage, AK, p. 4842-4848 (May 3-8, 2010).

57. L. Chen and G. Chen, "Relaxation behavior study of silicone rubber crosslinked network under static and dynamic compression by electric response," Polym. Compos., 30 (1), 101-106 (2009).

58. L. Wang, T. Ding, and P. Wang, "Research on stress and electrical resistance of skin-sensing silicone rubber/carbon black nanocomposite during decompressive stress relaxation," Smart Mater. Struct., 18 (6), 065002 (2009).

59. K. Yoshimura, K. Nakano, and Y. Hishikawa, "Flexible tactile sensor materials based on carbon microcoil/silicone-rubber porous composites," Compos. Sci. Technol., 123, 241-249 (2016).

60. O. Atalay, A. Atalay, J. Gafford, and C. Walsh, "A highly sensitive capacitive-based soft pressure sensor based on a conductive fabric and a microporous dielectric layer," Adv. Mater. Technol., 3 (1) (2018).

61. H. Tian, Y. Shu, X.-F. Wang, M. A. Mohammad, Z. Bie, Q.-Y. Xie, C. Li, W.-T. Mi, Y. Yang, and T.-L. Ren, "A graphene-based resistive pressure sensor with record-high sensitivity in a wide pressure range," Sci. Rep., 5, 8603 (2015).

62. K. B. Shimoga and A. A. Goldenberg, "Soft robotic fingertips part I: a comparison of construction materials," Int. J. Robot. Res., 15 (4), 320-334 (1996).

63. P. Maiolino, F. Galantini, F. Mastrogiovanni, G. Gallone, G. Cannata, and F. Carpi, "Soft dielectrics for capacitive sensing in robot skins: performance of different elastomer types," Sens. Act. A, 226**,** 37-47 (2015).

64. I. Jung, M. Lee, H. Lim, E. Smela, and J. Ko, "Microbumpers maintain superhydrophobicity of nanostructured surfaces upon touch," Appl. Surf. Sci., 349**,** 705-714 (2015).

65. J. T. Dennerlein, E. Diao, C. Mote, and D. M. Rempel, "In vivo finger flexor tendon force while tapping on a keyswitch," J. Orthop. Res., 17 (2)**,** 178-184 (1999).

66. R. Johansson and G. Westling, "Roles of glabrous skin receptors and sensorimotor memory in automatic control of precision grip when lifting rougher or more slippery objects," Exp. Brain Res., 56 (3)**,** 550-564 (1984).

67. R. G. Radwin, S. Oh, T. R. Jensen, and J. G. Webster, "External finger forces in submaximal five-finger static pinch prehension," Ergonomics, 35 (3)**,** 275-288 (1992).

68. A. D. Astin, "Finger force capability: measurement and prediction using anthropometric and myoelectric measures," Master of Science, Industrial and Systems Engineering, Virginia Polytechnic Institute and State University, Blacksburg, Virginia (1999).

69. A. Didomenico and M. A. Nussbaum, "Measurement and prediction of single and multi-digit finger strength," Ergonomics, 46 (15)**,** 1531-1548 (2003).

70. K. Kroemer, "Push forces exerted in sixty-five common working positions," DTIC Document, Aerospace Medical Division, (1969).

71. M. Smith, R. Dyson, T. Hale, and L. Janaway, "Development of a boxing dynamometer and its punch force discrimination efficacy," J. Sports Sci., 18 (6)**,** 445-450 (2000).

72. Canadian Centre for Occupational Health and Safety, "OSH Answers Fact Sheets", http://www.ccohs.ca/oshanswers/ergonomics/push1.html, 1997.

73. N. Wettels, V. J. Santos, R. S. Johansson, and G. E. Loeb, "Biomimetic tactile sensor array," Adv. Robot., 22 (8)**,** 829-849 (2008).

74. J. Ulmen and M. Cutkosky, "A robust, low-cost and low-noise artificial skin for human-friendly robots," IEEE Int'l. Conf. on Robot. and Autom. (ICRA), Alaska, USA, p. 4836-4841 (May 3-8, 2010).

75. S. Guo, Y. Kato, H. Ito, and T. Mukai, "Development of rubber-based flexible sensor sheet for care-related apparatus," SEI Technical Review, 75**,** 125-131 (2012).

76. I. Rosenberg and K. Perlin, "The UnMousePad: an interpolating multi-touch force-sensing input pad," ACM Transactions on Graphics (TOG), (ACM), vol. 28, p. 65 (2009).

77. A. Charalambides and S. Bergbreiter, "A novel all-elastomer MEMS tactile sensor for high dynamic range shear and normal force sensing," J. Micromech. Microeng., 25 (9), 095009 (2015).

78. H. A. Bruck, E. Smela, M. Yu, J. Tigue, O. Popkov, G. Ocel, and Y. Chen, "Compliant artificial skins to enable robotic sensing and training by touch," in Mechanics of Composite and Multifunctional Materials, Vol. 7 of the series conference proceedings of the Society for Experimental Mechanics, p. 31-40 (Springer International Publishing, 2016).

79. H. B. Wu, J. P. Chen, Y. X. Su, Z. J. Li, and J. H. Ye, "New tactile sensor for position detection based on distributed planar electric field," Sens. Act. A, 242, 146-161 (2016).

80. M. Y. Shi, J. X. Zhang, H. T. Chen, M. D. Han, S. A. Shankaregowda, Z. M. Su, B. Meng, X. L. Cheng, and H. X. Zhang, "Self-powered analogue smart skin," ACS Nano, 10 (4), 4083-4091 (2016).

81. D. Petkovic, M. Issa, N. D. Pavlovic, and L. Zentner, "Electrical properties estimation of conductive silicone rubber for tactile sensing structure," Sensor Review, 33 (2), 114-124 (2013).

82. S. Yoshimoto, M. Imura, and O. Oshiro, "Unobtrusive tactile sensing based on electromechanical boundary estimation," 2015 37th Annual International Conference of the IEEE Engineering in Medicine and Biology Society (EMBC), p. 4375-4378 (25-29 Aug. 2015, 2015).

83. M. Shimojo, T. Araki, M. Aigou, and M. Ishikawa, "A ZMP sensor for a biped robot," IEEE Int'l. Conf. on Robot. and Autom. (ICRA), Florida, USA, p. 1200-1205 (15-19 May, 2006).

84. P. Piacenza, Y. C. Xiao, S. Park, I. Kymissis, and M. Ciocarlie, "Contact localization through spatially overlapping piezoresistive signals" in Int'l. Conf. on Intelligent Robots and Systems (IROS) (Daejeon, Korea, 2016), p. 195-201.

85. M. Shimojo, T. Arakil, M. Teranishi, A. Ming, and M. Ishikawa, "A net-structure tactile sensor covering freeform surface with reduced wiring," SICE Annual Conference, Japan, p. 904-909 (20-22 Aug., 2008).

86. Z. X. Pan and Z. Q. Zhu, "Flexible full-body tactile sensor of low cost and minimal output connections for service robot," Ind. Robot., 32 (6), 485-491 (2005).

87. B. Rigaud and J. Morucci, "Bioelectrical impedance techniques in medicine. Part III: Impedance imaging. First section: general concepts and hardware," Crit. Rev. Biomed. Eng., 24 (4-6)**,** 467-597 (1995).

88. L. Borcea, "Electrical impedance tomography," Inverse Problems, 18 (6)**,** R99-R136 (2002).

89. D. S. Holder, Ed., Electrical Impedance Tomography: Methods, Histroty, and Applications, Medical physics and biomedical engineering (Institute of Physics Publishing, Bristol, UK, 2005).

90. V. Chitturi and F. Nagi, "Spatial resolution in electrical impedance tomography: A topical review," Journal of Electrical Bioimpedance, 8 (1)**,** 66 (2017).

91. J. Morucci and P. Marsili, "Bioelectrical impedance techniques in medicine. Part III: Impedance imaging. Second section: reconstruction algorithms," Crit. Rev. Biomed. Eng., 24 (4-6)**,** 599-654 (1995).

92. Trek Inc, "Surface resistivity and surface resistance measurements using a concentric ring probe technique", http://www.trekinc.com/pdf/1005_Resistivity_Resistance.pdf, 2013.

93. J. Hadamard, "Sur les problèmes aux dérivées partielles et leur signification physique," Princeton University Bulletin**,** 49-52 (1902).

94. M. Vauhkonen, "Electrical Impedance Tomography and Prior Information," Ph.D., Department of Applied Physics, University of Kuopio (1997).

95. B. H. Brown, "Electrical impedance tomography (EIT): a review," J. Med. Eng. Technol., 27 (3)**,** 97-108 (2003).

96. A. k. Björck, Numerical Methods for Least Squares Problems, (SIAM, Philadelphia, 1996).

97. R. A. Horn and C. R. Johnson, Matrix Analysis, (Cambridge University Press, Cambridge, 1985).

98. A. Kirsch, An Introduction to the Mathematical Theory of Inverse Problems, Vol. 120, Applied Mathematical Sciences, 2nd ed. (Springer, New York, 2011).

99. B. Graham and A. Adler, "Objective selection of hyperparameter for EIT," Physiol. Meas., 27 (5)**,** S65 (2006).

100. N. Polydorides and W. R. B. Lionheart, "A Matlab toolkit for three-dimensional electrical impedance tomography: a contribution to the Electrical Impedance and Diffuse Optical Reconstruction Software project," Meas. Sci. Technol., 13**,** 1871-1883 (2002).

101. M. Vauhkonen, W. R. Lionheart, L. M. Heikkinen, P. J. Vauhkonen, and J. P. Kaipio, "A MATLAB package for the EIDORS project to reconstruct two-dimensional EIT images," Physiol. Meas., 22 (1), 107-111 (2001).

102. A. Adler and W. R. B. Lionheart, "Uses and abuses of EIDORS: an extensible software base for EIT," Physiol. Meas., 27 (5), S25-42 (2006).

103. C. Venkatratnam and N. Farrukh, "Electrode considerations, excitation methods and measurement techniques for electrical impedance tomography," in Int'l. Conf. for Innovation in Biomedical Engineering and Life Sciences, Vol. 56 of the series IFMBE Proceedings, p. 1-5 (2016).

104. J. M. Ye, H. G. Wang, and W. Q. Yang, "Evaluation of effect of number of electrodes in ERT sensors on image quality," in IEEE Int'l. Conf. on Imag. Syst. and Tech. of the series IEEE International Conference on Imaging Systems and Techniques, p. 19-24 (2013).

105. D. Isaacson, "Distinguishability of conductivities by electric-current computed-tomography," IEEE Trans. Med. Imag., 5 (2), 91-95 (1986).

106. A. Adler, P. O. Gaggero, and Y. Maimaitijiang, "Adjacent stimulation and measurement patterns considered harmful," Physiol. Meas., 32 (7) (2011).

107. P. Hua, E. J. Woo, J. G. Webster, and W. J. Tompkins, "Improved methods to determine optimal currents in electrical impedance tomography," IEEE Trans. Med. Imag. , 11 (4), 488-495 (1992).

108. D. G. Gisser, D. Isaacson, and J. C. Newell, "Electric-current computed-tomography and eigenvalues," SIAM J. Appl. Math., 50 (6), 1623-1634 (1990).

109. N. Polydorides and H. McCann, "Electrode configurations for improved spatial resolution in electrical impedance tomography," Meas. Sci. Technol., 13 (12), 1862-1870 (2002).

110. P. Wang, B. L. Guo, and N. Li, "Multi-index optimization design for electrical resistance tomography sensor," Measurement, 46 (8), 2845-2853 (2013).

111. H. Alirezaei, A. Nagakubo, and Y. Kuniyoshi, "A highly stretchable tactile distribution sensor for smooth surfaced humanoids," IEEE/RAS Int'l. Conf. on Humanoid Robots, Pittsburgh, PA, p. 167-173 (Nov. 29-Dec. 01, 2007).

112. Y. Kato, T. Mukai, T. Hayakawa, and T. Shibata, "Tactile sensor without wire and sensing element in the tactile region based on EIT method" in 6th IEEE Conf. on Sensors; Vol. 1-3 (IEEE, Atlanta, GA, 2007), p. 792-795.

113. D. Tawil, D. Rye, and M. Velonaki, "Improved image reconstruction for an EIT-based sensitive skin with multiple internal electrodes," Robotics, IEEE Transactions on, 27**,** 425-435 (2011).

114. G. Pugach, V. Khomenko, A. Melnyk, A. Pitti, P. Henaff, and P. Gaussier, "Electronic hardware design of a low cost tactile sensor device for physical human-robot interactions," Electronics and Nanotechnology (ELNANO), 2013 IEEE XXXIII International Scientific Conference, (IEEE), p. 445-449 (2013).

115. A. Yao, C. L. Yang, J. K. Seo, and M. Soleimani, "EIT-based fabric pressure sensing," Computational and mathematical methods in medicine, 2013**,** 405325 (2013).

116. T. Tallman, S. Gungor, K. Wang, and C. Bakis, "Tactile imaging and distributed strain sensing in highly flexible carbon nanofiber/polyurethane nanocomposites," Carbon, 95**,** 485-493 (2015).

117. D. S. Tawil, D. Rye, and M. Velonaki, "Interpretation of the modality of touch on an artificial arm covered with an EIT-based sensitive skin," Int. J. Robot. Res., 31 (13)**,** 1627-1641 (2012).

118. F. Visentin, P. Fiorini, and K. Suzuki, "A deformable smart skin for continuous sensing based on electrical impedance tomography," Sensors, 16 (11)**,** 1928 (2016).

119. H. Lee, D. Kwon, H. Cho, I. Park, and J. Kim, "Soft nanocomposite based multi-point, multi-directional strain mapping sensor using anisotropic electrical impedance tomography," Sci. Rep., 7 (2017).

120. H. Alirezaei, A. Nagakubo, and Y. Kuniyoshi, "A tactile distribution sensor which enables stable measurement under high and dynamic stretch," 2009 IEEE Symposium on 3D User Interfaces**,** 87-93 (2009).

121. S. Russo, S. Nefti-Meziani, N. Carbonaro, and A. Tognetti, "A quantitative evaluation of drive pattern selection for optimizing EIT-based stretchable sensors," Sensors, 17 (9)**,** 1999 (2017).

122. J.-B. Chossat, H.-S. Shin, Y.-L. Park, and V. Duchaine, "Soft tactile skin using an embedded ionic liquid and tomographic imaging," Journal of Mechanisms and Robotics, 7 (2)**,** 021008 (2015).

123. D. S. Tawil, D. Rye, M. Soleimani, and M. Velonaki, "Electrical impedance tomography for artificial sensitive robotic skin: a review," IEEE Sensors J., 15 (4)**,** 2016 (2015).

124. A. Yao and M. Soleimani, "A pressure mapping imaging device based on electrical impedance tomography of conductive fabrics," Sensor Review, 32**,** 310-317 (2012).

125. M. Calisti, A. Arienti, F. Renda, G. Levy, B. Hochner, B. Mazzolai, P. Dario, and C. Laschi, "Design and development of a soft robot with crawling and grasping capabilities," IEEE Int'l. Conf. on Robotics and Automation (ICRA), Minnesota, USA, p. 4950-4955 (14-18 May, 2012).

126. S. W. Kwok, S. A. Morin, B. Mosadegh, J. H. So, R. F. Shepherd, R. V. Martinez, B. Smith, F. C. Simeone, A. A. Stokes, and G. M. Whitesides, "Magnetic assembly of soft robots with hard components," Adv. Funct. Mater., 24 (15)**,** 2180-2187 (2014).

127. S. Sanan, M. H. Ornstein, and C. G. Arkeson, "Physical human interaction for an inflatable manipulator," IEEE EMBS, Boston, MA, p. 7401-7404 (Aug. 30 - Sep. 3, 2011).

128. M. Shimojo, "Mechanical filtering effect of elastic cover for tactile sensor," IEEE Trans. Robot. Autom., 13 (1)**,** 128-132 (1997).

129. M. H. Lee, "Tactile sensing: new directions, new challenges," Int. J. Robot. Res., 19 (7)**,** 636-643 (2000).

130. H. Yousef, M. Boukallel, and K. Althoefer, "Tactile sensing for dexterous in-hand manipulation in robotics - a review," Sens. Act. A, 167**,** 171-187 (2011).

131. H.-J. Kwon, J.-H. Kim, and W.-C. Choi, "Development of a flexible three - axial tactile sensor array for a robotic finger," Microsys. Technol., 17 (12)**,** 1721-1726 (2011).

132. A. Fassler and C. Majidi, "Liquid-phase metal inclusions for a conductive polymer composite," Adv. Mater., 27 (11)**,** 1928-1932 (2015).

133. A. Charalambides, C. Jian, L. Teng, and S. Bergbreiter, "3-axis all elastomer MEMS tactile sensor," IEEE Int'l. Conf. on MEMS, Estoril, Portugal, p. 726-729 (18-22 Jan., 2015).

134. S. Gorgutsa, J. F. Gu, and M. Skorobogatiy, "A woven 2D touchpad sensor and a 1D slide sensor using soft capacitor fibers," Smart Mater. Struct., 21 (1)**,** 015010 (2012).

135. S. Laflamme, H. S. Saleem, B. K. Vasan, R. L. Geiger, D. Chen, M. R. Kessler, and K. Rajan, "Soft elastomeric capacitor network for strain sensing over large surfaces," IEEE/ASME Trans. Mechatronics, 18 (6)**,** 1647-1654 (2013).

136. R. Koiva, M. Zenker, C. Schurmann, R. Haschke, and H. J. Ritter, "A highly sensitive 3D-shaped tactile sensor," IEEE/ASME Int'l. Conf. on Advanced Intelligent Mechatronics (AIM), Wollongong, Australia, p. 1084-1089 (9-12 July, 2013).

137. T. Someya, Y. Kato, T. Sekitani, S. Iba, Y. Noguchi, Y. Murase, H. Kawaguchi, and T. Sakurai, "Conformable, flexible, large-area networks of pressure and thermal sensors with organic transistor active matrixes," PNAS, 102 (35)**,** 12321-12325 (2005).

138. T. Someya, T. Sekitani, S. Iba, Y. Kato, H. Kawaguchi, and T. Sakurai, "A large-area, flexible pressure sensor matrix with organic field-effect transistors for artificial skin applications," PNAS, 101 (27)**,** 9966-9970 (2004).

139. M. Acer, M. Salerno, K. Agbeviade, and J. Paik, "Development and characterization of silicone embedded distributed piezoelectric sensors for contact detection," Smart Mater. Struct., 24 (7)**,** 075030 (2015).

140. A. Kadowaki, T. Yoshikai, M. Hayashi, and M. Inaba, "Development of soft sensor exterior embedded with multi-axis deformable tactile sensor system," IEEE Int'l. Symp. on Robot and Human Interactive Communication, Toyama, Japan, p. 1093-1098 (Sep. 27 - Oct. 2, 2009).

141. H. P. Wang, D. B. Zhou, and J. G. Cao, "Development of a skin-like tactile sensor array for curved surface," IEEE Sensors J., 14 (1)**,** 55-61 (2014).

142. S. Stassi, G. Canavese, F. Cosiansi, R. Gazia, C. Fallauto, S. Corbellini, M. Pirola, and M. Cocuzza, "Smart piezoresistive tunnelling composite for flexible robotic sensing skin," Smart Mater. Struct., 22 (12)**,** 125039 (2013).

143. M. Vatani, E. D. Engeberg, and J. W. Choi, "Detection of the position, direction and speed of sliding contact with a multi-layer compliant tactile sensor fabricated using direct-print technology," Smart Mater. Struct., 23 (9)**,** 095008 (2014).

144. S. Kharroub, S. Laflamme, C. H. Song, D. J. Qiao, B. Phares, and J. Li, "Smart sensing skin for detection and localization of fatigue cracks," Smart Mater. Struct., 24 (6)**,** 065004 (2015).

145. S. K. Hwang and H. Y. Hwang, "Development of a tactile sensing system using piezoelectric robot skin materials," Smart Mater. Struct., 22 (5)**,** 055004 (2013).

146. ExpertPages http://expertpages.com/news/standard_care_absorbing2.htm, "A new standard of care in absorbing and dissipating forces", http://expertpages.com/news/standard_care_absorbing2.htm, 2003.

147. L. J. Gibson and M. F. Ashby, Cellular solids: structure and properties, Vol. 5, Cambridge Solid State Science Series, 2nd ed. (Cambridge University Press, Cambridge, 1997).

148. L. Gong, S. Kyriakides, and W. Y. Jang, "Compressive response of open-cell foams part I: morphology and elastic properties," Int. J. Solids Struct., 42 (5-6)**,** 1355-1379 (2005).

149. M. Hayashi, T. Sagisaka, and M. Inaba, "Development of functional whole-body flesh with distributed three-axis force sensors to enable close interaction by humanoids," IEEE/RSJ Int'l Conf. on Intelligent Robots and Systems, San Diego, p. 3610-3615 (Oct. 29 - Nov. 2, 2007).

150. J.-J. Cabibihan, S. Pattofatto, M. Jom âa, A. Benallal, and M. C. Carrozza, "Towards humanlike social touch for sociable robotics and prosthetics: comparisons on the compliance, conformance and hysteresis of synthetic and human fingertip skins," Int. J. Soc. Robot., 1 (1)**,** 29-40 (2008).

151. G. Berselli, M. Piccinini, G. Palli, and G. Vassura, "Engineering design of fluid-filled soft covers for robotic contact interfaces: guidelines, nonlinear modeling, and experimental validation," IEEE Trans. Robot., 27 (3)**,** 436-449 (2011).

152. E. Sauerbrunn, Y. Chen, J. Didion, M. Yu, E. Smela, and H. A. Bruck, "Thermal imaging using polymer nanocomposite temperature sensors," Phys. Status Solidi A, 212 (10)**,** 2239-2245 (2015).

153. L. J. van der Pauw, "A method of measuring specific resistivity and Hall effect of discs of arbitrary shape," Philips Res. Rep., 13 (1)**,** 1-9 (1958).

154. B. Pan, K. Qian, H. Xie, and A. Asundi, "Two-dimensional digital image correlation for in-plane displacement and strain measurement: a review," Meas. Sci. Technol., 20 (6)**,** 062001 (2009).

155. H. A. Bruck, S. R. McNeill, M. A. Sutton, and W. H. Peters III, "Digital image correlation using Newton-Raphson method of partial differential correction," Exp. Mech., 29 (3)**,** 261-267 (1989).

156. M. Sutton, W. Wolters, W. Peters, W. Ranson, and S. McNeill, "Determination of displacements using an improved digital correlation method," Image Vision Comp., 1 (3)**,** 133-139 (1983).

157. P. F. Luo, Y. J. Chao, M. A. Sutton, and W. H. Peters, "Accurate measurement of three-dimensional deformations in deformable and rigid bodies using computer vision," Exp. Mech., 33 (2)**,** 123-132 (1993).

158. J. Cernosek, "Three-dimensional photoelasticity by stress freezing," Exp. Mech., 20 (12)**,** 417-426 (1980).

159. F. Schneider, T. Fellner, J. Wilde, and U. Wallrabe, "Mechanical properties of silicones for MEMS," J. Micromech. Microeng., 18 (6)**,** 065008 (2008).

160. J. S. Bergstrom and M. C. Boyce, "Constitutive modeling of the large strain time-dependent behavior of elastomers," J. Mech. Phys. Solids, 46 (5)**,** 931-954 (1998).

161. M. S. H. Fatt and L. Chen, "A viscoelastic damage model for hysteresis in PVC H100 foam under cyclic loading," J. Cell. Plast., 51 (3)**,** 269-287 (2015).

162. Y. Ahn, S. Song, and K. S. Yun, "Woven flexible textile structure for wearable power-generating tactile sensor array," Smart Mater. Struct., 24 (7)**,** 075002 (2015).

163. L. M. Castano and A. B. Flatau, "Smart fabric sensors and e-textile technologies: a review," Smart Mater. Struct., 23 (5)**,** 053001 (2014).

164. F. Wang, B. Zhu, L. Shu, and X. M. Tao, "Flexible pressure sensors for smart protective clothing against impact loading," Smart Mater. Struct., 23 (1)**,** 015001 (2014).

165. Y. Q. Fan, C. R. Liao, G. L. Liao, R. B. Tan, and L. Xie, "Capacitive pressure-sensitive composites using nickel-silicone rubber: experiments and modeling," Smart Mater. Struct., 26 (7)**,** 075003 (2017).

166. B. Li, Y. Gao, A. Fontecchio, and Y. Visell, "Soft capacitive tactile sensing arrays fabricated via direct filament casting," Smart Mater. Struct., 25 (7)**,** 075009 (2016).

167. E. L. White, M. C. Yuen, J. C. Case, and R. K. Kramer, "Low-cost, facile, and scalable manufacturing of capacitive sensors for soft systems," Adv. Mater. Technol., 2 (9)**,** 1700072 (2017).

168. S. Gong, W. Schwalb, Y. Wang, Y. Chen, Y. Tang, J. Si, B. Shirinzadeh, and W. Cheng, "A wearable and highly sensitive pressure sensor with ultrathin gold nanowires," Nat. Commun., 5**,** 3132 (2014).

169. C. Pang, G.-Y. Lee, T.-i. Kim, S. M. Kim, H. N. Kim, S.-H. Ahn, and K.-Y. Suh, "A flexible and highly sensitive strain-gauge sensor using reversible interlocking of nanofibres," Nat. Mater., 11 (9)**,** 795-801 (2012).

170. L. Pan, A. Chortos, G. Yu, Y. Wang, S. Isaacson, R. Allen, Y. Shi, R. Dauskardt, and Z. Bao, "An ultra-sensitive resistive pressure sensor based on hollow-sphere microstructure induced elasticity in conducting polymer film," Nat. Commun., 5**,** 3002 (2014).

171. S. Kang, J. Lee, S. Lee, S. Kim, J. K. Kim, H. Algadi, S. Al-Sayari, D. E. Kim, D. Kim, and T. Lee, "Highly sensitive pressure sensor based on bioinspired porous structure for real-time tactile sensing," Adv. Electron. Mater., 2 (12)**,** 1600356 (2016).

172. B.-Y. Lee, J. Kim, H. Kim, C. Kim, and S.-D. Lee, "Low-cost flexible pressure sensor based on dielectric elastomer film with micro-pores," Sens. Act. A, 240**,** 103-109 (2016).

173. D. Kwon, T. I. Lee, J. Shim, S. Ryu, M. S. Kim, S. Kim, T. S. Kim, and I. Park, "Highly sensitive, flexible, and wearable pressure sensor based on a giant piezocapacitive effect of three-dimensional microporous elastomeric dielectric layer," ACS Appl. Mater. Interfaces, 8 (26)**,** 16922-16931 (2016).

174. Y. Li, S. D. Luo, M. C. Yang, R. Liang, and C. C. Zeng, "Poisson ratio and piezoresistive sensing: a new route to high-performance 3D flexible and stretchable sensors of multimodal sensing capability," Adv. Funct. Mater., 26 (17)**,** 2900-2908 (2016).

175. Y. Chen, M. Yu, H. A. Bruck, and E. Smela, "Stretchable touch-sensing skin over padding for co-robots," Smart Mater. Struct., 25 (5)**,** 055006 (2016).

176. M. Weigel, T. Lu, G. Bailly, A. Oulasvirta, C. Majidi, and J. Steimle, "iSkin: flexible, stretchable and visually customizable on-body touch sensors for mobile computing," Proceedings of the 33rd Annual ACM Conference on Human Factors in Computing Systems, Seoul, Korea, p. 2991-3000 (April 18-23, 2015).

177. Y. C. Lai, B. W. Ye, C. F. Lu, C. T. Chen, M. H. Jao, W. F. Su, W. Y. Hung, T. Y. Lin, and Y. F. Chen, "Extraordinarily sensitive and low-voltage operational cloth-based electronic skin for wearable sensing and multifunctional integration uses: a tactile-induced insulating-to-conducting transition," Adv. Funct. Mater., 26 (8)**,** 1286-1295 (2016).

178. Y. H. Zhang, "Sensitivity enhancement of a micro-scale biomimetic tactile sensor with epidermal ridges," J. Micromech. Microeng., 20 (8)**,** 085012 (2010).

179. B. W. Zhu, Z. Q. Niu, H. Wang, W. R. Leow, H. Wang, Y. G. Li, L. Y. Zheng, J. Wei, F. W. Huo, and X. D. Chen, "Microstructured Graphene Arrays for Highly Sensitive Flexible Tactile Sensors," Small, 10 (18)**,** 3625-3631 (2014).

180. B. C. K. Tee, A. Chortos, R. R. Dunn, G. Schwartz, E. Eason, and Z. Bao, "Tunable flexible pressure sensors using microstructured elastomer geometries for intuitive electronics," Adv. Funct. Mater., 24 (34)**,** 5427-5434 (2014).

181. M. Ha, S. Lim, J. Park, D. S. Um, Y. Lee, and H. Ko, "Bioinspired interlocked and hierarchical design of ZnO nanowire arrays for static and dynamic pressure-sensitive electronic skins," Adv. Funct. Mater., 25 (19)**,** 2841-2849 (2015).

182. R. S. Johansson and G. Westling, "Roles of glabrous skin receptors and sensorimotor memory in automatic-control of precision grip when lifting rougher or more slippery objects," Exp. Brain Res., 56 (3)**,** 550-564 (1984).

183. M. Segev-Bar, A. Landman, M. Nir-Shapira, G. Shuster, and H. Haick, "Tunable touch sensor and combined sensing platform: toward nanoparticle-based electronic skin," ACS Appl. Mater. Interfaces, 5 (12)**,** 5531-5541 (2013).

184. S. Chun, Y. Kim, H.-S. Oh, G. Bae, and W. Park, "A highly sensitive pressure sensor using a double-layered graphene structure for tactile sensing," Nanoscale, 7 (27)**,** 11652-11659 (2015).

185. R. Li, B. Nie, P. Digiglio, and T. Pan, "Microflotronics: a flexible, transparent, pressure-sensitive microfluidic film," Adv. Funct. Mater., 24 (39)**,** 6195-6203 (2014).

186. E. Choi, O. Sul, S. Hwang, J. Cho, H. Chun, H. Kim, and S.-B. Lee, "Spatially digitized tactile pressure sensors with tunable sensitivity and sensing range," Nanotechnology, 25 (42)**,** 425504 (2014).

187. K.-W. Liao, M. T. Hou, H. Fujita, and J. A. Yeh, "Liquid-based tactile sensing array with adjustable sensing range and sensitivity by using dielectric liquid," Sens. Act. A, 231**,** 15-20 (2015).

188. C. X. Gu, W. T. Liu, P. Yu, X. Y. Cheng, and X. Fu, "Smart structure with elastomeric contact surface for prosthetic fingertip sensitivity development," Smart Mater. Struct., 26 (9)**,** 095041 (2017).

189. H. Shinoda, N. Morimoto, and S. Ando, "Tactile sensing using tensor cell," in Proc. IEEE Intl. COnf. Robotics and Automation, Vol. 1-3 of the series Ieee International Conference on Robotics and Automation, p. 825-830 (1995).

190. R. Russell, "Compliant-skin tactile sensor," Proc. IEEE Int'l. Conf. Robotics and Automation, vol. 4, p. 1645-1648 (Mar 1987, 1987).

191. Tekscan, "Body Pressure Measurement System (BPMS) - Research", https://www.tekscan.com/products-solutions/systems/body-pressure-measurement-system-bpms-research, 2017.

192. SynTouch, "Sensor Technology", https://www.syntouchinc.com/en/sensor-technology/, 2017.

193. J. A. Fishel, G. E. Loeb, R. A. Peck, C.-H. Lin, B. Matulevich, and V. Pandit, "Compliant tactile sensor with fluid-filled, sponge-like material," US 20140069212A1 (US) (2014).

194. A. B. Vallbo and R. S. Johansson, "Properties of cutaneous mechanoreceptors in the human hand related to touch sensation," Human Neurobiol., 3 (1)**,** 3-14 (1984).

195. R. S. Dahiya, G. Metta, M. Valle, and G. Sandini, "Tactile sensing - from humans to humanoids," IEEE Trans. Robot., 26 (1)**,** 1-20 (2010).

196. M. R. Cutkosky and J. Ulmen, "Dynamic tactile sensing," in Human Hand As An Inspiration For Robot Hand Development, Vol. 95 of the series Springer Tracts in Adv. Robotics, p. 389-403 (Springer International Publishing, Switzerland, 2014).

197. C. Edwards and R. Marks, "Evaluation of biomechanical properties of human skin," Clin. Dermatol., 13 (4)**,** 375-380 (1995).

198. E. M. Barnett, J. J. Lofton, M. Yu, H. A. Bruck, and E. Smela, "Targeted feature recognition using mechanical spatial filtering with a low-cost compliant strain sensor," Sci. Rep., 7**,** 5118 (2017).

199. R. W. Ogden and D. G. Roxburgh, "A pseudo-elastic model for the Mullins effect in filled rubber," Proc. Royal Soc. A - Math. Phys. Eng. Sci., 455 (1988)**,** 2861-2877 (1999).

200. S. L. Yu, D. R. Chang, L. C. Tsao, W. P. Shih, and P. Z. Chang, "Porous nylon with electro-active dopants as flexible sensors and actuators" in Proc. IEEE 21st Int'l. Conf. on Micro Electro Mechanical Systems (MEMS) (IEEE, Tucson, AZ, 2008), p. 908-911.

201. T. B. Xu, W. B. Wang, X. L. Bian, X. X. Wang, X. Z. Wang, J. K. Luo, and S. R. Dong, "High resolution skin-like sensor capable of sensing and visualizing various sensations and three dimensional shape," Sci. Rep., 5 (2015).

202. J. C. Doll and B. L. Pruitt, "Sensitivity, Noise and Resolution," in Piezoresistor Design and Applications, Vol. 1, p. 51-83 (Springer, New York, New York, NY, 2013).

203. K. L. Johnson, Contact Mechanics, (Cambridge University, 1985).

204. Rethink Robotics, "Collaborative Robots", http://www.rethinkrobotics.com/smart-collaborative-difference/, 2018.

205. J. Tegin and J. Wikander, "Tactile sensing in intelligent robotic manipulation – a review," Indust. Robot, 32**,** 64-70 (2005).

206. S. A. Napper and R. L. Seaman, "Applications of robots in rehabilitation," Robot. Auton. Syst., 5 (3)**,** 227-239 (1989).

207. P. Dario, E. Guglielmelli, V. Genovese, and M. Toro, "Robot assistants: Applications and evolution," Robot. Auton. Syst., 18 (1-2)**,** 225-234 (1996).

208. R. H. Krishnan and S. Pugazhenthi, "Mobility assistive devices and self-transfer robotic systems for elderly, a review," Intel. Serv. Robot., 7 (1)**,** 37-49 (2014).

209. D. Trivedi, C. D. Rahn, W. M. Kier, and I. D. Walker, "Soft robotics: biological inspiration, state of the art, and future research," Appl. Bionics Biomech., 5 (3) (2008).

210. S. Kim, C. Laschi, and B. Trimmer, "Soft robotics: a bioinspired evolution in robotics," Trends Biotechnol., 31 (5), 23-30 (2013).

211. C. Majidi, "Soft robotics: a perspective - current trends and prospects for the future," Soft Robotics, 1 (1), 5-11 (2014).

212. D. Rus and M. T. Tolley, "Design, fabrication and control of soft robots," Nature, 521 (7553), 467-475 (2015).

213. K. Suita, Y. Yamada, N. Tsuchida, K. Imai, H. Ikeda, and N. Sugimoto, "A failure-to-safety "Kyozon" system with simple contact detection and stop capabilities for safe human-autonomous robot coexistence" in Proc. IEEE Intl. Conf. Robotics and Automation (Nagoya, Japan, 1995), p. 3089-3096.

214. G. A. Pratt and M. M. Williamson, "Series elastic actuators," IEEE/RSJ Int. Conf. Intelligent Robots and Systems, Pittsburgh, PA, (IEEE), vol. 1, p. 399-406 (Aug 5-9, 1995, 1995).

215. N. B. Yu, W. L. Zou, W. Tan, and Z. Yang, "Augmented virtual stiffness rendering of a cable-driven SEA for human-robot interaction," IEEE/CAA J. Automat. Sin., 4 (4), 714-723 (2017).

216. H. R. Nicholls and M. H. Lee, "A survey of robot tactile sensing technology," Int. J. Robot. Res., 8 (3), 3-30 (1989).

217. N. Yogeswaran, W. Dang, W. T. Navaraj, D. Shakthivel, S. Khan, E. O. Polat, S. Gupta, H. Heidari, M. Kaboli, L. Lorenzelli, G. Cheng, and R. Dahiya, "New materials and advances in making electronic skin for interactive robots," Adv. Robot., 29 (21), 1359-1373 (2015).

218. M. Amjadi, K. U. Kyung, I. Park, and M. Sitti, "Stretchable, skin-mountable, and wearable strain sensors and their potential applications: a review," Adv. Funct. Mater., 26 (11), 1678-1698 (2016).

219. R. Tajima, S. Kagami, M. Inaba, and H. Inoue, "Development of soft and distributed tactile sensors and the application to a humanoid robot," Adv. Robot., 16, 381-397 (2002).

220. B. Borovac, D. Seslija, and S. Stankovski, "Soft sensored grippers in assembly process" in IEEE Int'l Conf. on Robotics and Automation : Proceedings, Vols 1-3 (Nice, France, 1992), p. 1283-1288.

221. S. Fujino, H. Yamazaki, A. Hosoki, and K. Watanabe, "A flexible tactile sensitive sheet using a hetero-core fiber-optic sensor" in 23rd Int'l Conf. on Optical Fibre Sensors; Vol. 9157 (Santander, Spain, 2014).

222. A. Charalambides and S. Bergbreiter, "Rapid manufacturing of mechanoreceptive skins for slip detection in robotic grasping," Adv. Mater. Technol., 2 (1)**,** 1600188 (2017).

223. B. H. Pubols and L. M. Pubols, "Tactile receptor discharge and mechanical-properties of glabrous skin," Fed. Proc., 42 (9)**,** 2528-2535 (1983).

224. G. Shi, Z. H. Zhao, J. H. Pai, I. Lee, L. Q. Zhang, C. Stevenson, K. Ishara, R. J. Zhang, H. W. Zhu, and J. Ma, "Highly sensitive, wearable, durable strain sensors and stretchable conductors using graphene/silicon rubber composites," Adv. Funct. Mater., 26 (42)**,** 7614-7625 (2016).

225. G. Pullin and A. Gammie, "Current capabilities of rehabilitation robots," J. Biomed. Eng., 13 (3)**,** 215-216 (1991).

226. J. C. Yeo, Z. Liu, Z. Q. Zhang, P. Zhang, Z. Wang, and C. T. Lim, "Wearable mechanotransduced tactile sensor for haptic perception," Adv. Mater. Technol., 2 (6) (2017).

227. W. G. Li, J. H. Guo, and D. L. Fan, "3D graphite-polymer flexible strain sensors with ultrasensitivity and durability for real-time human vital sign monitoring and musical instrument education," Adv. Mater. Technol., 2 (6) (2017).

228. O. Atalay, A. Atalay, J. Gafford, H. Q. Wang, R. Wood, and C. Walsh, "A highly stretchable capacitive-based strain sensor based on metal deposition and laser rastering," Adv. Mater. Technol., 2 (9) (2017).

229. N. Besse, S. Rosset, J. J. Zarate, and H. Shea, "Flexible active skin: large reconfigurable arrays of individually addressed shape memory polymer actuators," Adv. Mater. Technol., 2 (10) (2017).

230. M. Kaboli, A. Long, and G. Cheng, "Humanoids learn touch modalities identification via multi-modal robotic skin and robust tactile descriptors," Adv. Robot., 29 (21)**,** 1411-1425 (2015).

231. F. Naya, J. Yamato, and K. Shinozawa, "Recognizing human touching behaviors using a haptic interface for a pet-robot," IEEE Int'l. Conf. on Systems, Man, and Cybernetics, Tokyo, (IEEE), vol. 2, p. 1030-1034 (1999).

232. S.-y. Koo, J. G. Lim, and D.-s. Kwon, "Online touch behavior recognition of hard-cover robot using temporal decision tree classifier," 17th IEEE International Symposium on Robot and Human Interactive Communication, Munich, Germany, (IEEE), p. 425-429 (August 1-3, 2008, 2008).

233. S. Aoyagi, T. Tanaka, and M. Minami, "Recognition of contact state of four layers arrayed type tactile sensor by using neural network" in 2006 IEEE Int'l Conf. on Information Acquisition, Vols 1 and 2 (Weihai, Shandong, China, 2006), p. 393-397.

234. Y. Chen, M. Yu, H. A. Bruck, and E. Smela, "Characterization of a compliant multilayer system for tactile sensing with enhanced sensitivity and range," Smart Mater. Struct., 27 (6)**,** 065005 (2018).

235. A. E. Block, "How should robots hug?," Master of Science, Mechanical Engineering and Applied Science, University of Pennsylvania, Philadelphia (2017).

236. S. Russo, S. Nefti-Meziani, N. Carbonaro, and A. Tognetti, "Development of a high-speed current injection and voltage measurement system for electrical impedance tomography-based stretchable sensors," Technologies, 5 (3)**,** 5030048 (2017).

237. E. H. L. Falcao, R. G. Blair, J. J. Mack, L. M. Viculis, C. W. Kwon, M. Bendikov, R. B. Kaner, B. S. Dunn, and F. Wudl, "Microwave exfoliation of a graphite intercalation compound," Carbon, 45 (6)**,** 1367-1369 (2007).

238. T. Wei, Z. J. Fan, G. L. Luo, C. Zheng, and D. S. Xie, "A rapid and efficient method to prepare exfoliated graphite by microwave irradiation," Carbon, 47 (1)**,** 337-339 (2009).

239. A. Adler, R. Amyot, R. Guardo, J. Bates, and Y. Berthiaume, "Monitoring changes in lung air and liquid volumes with electrical impedance tomography," J. Appl. Physiol., 83 (5)**,** 1762-1767 (1997).

240. A. Nagakubo, H. Alirezaei, and Y. Kuniyoshi, "A deformable and deformation sensitive tactile distribution sensor," IEEE/ROBIO Int'l Conf. on Robotics and Biomimetics, p. 1301-1308 (15-18 Dec. 2007, 2007).

241. F. Braun, M. Proenca, J. Sola, J. P. Thiran, and A. Adler, "A versatile noise performance metric for electrical impedance tomography algorithms," IEEE Trans. Biomed. Eng., 64 (10)**,** 2321-2330 (2017).

242. A. Adler and R. Guardo, "Electrical impedance tomography: Regularized imaging and contrast detection," IEEE Trans. Med. Imaging, 15 (2)**,** 170-179 (1996).

243. A. Adler, J. H. Arnold, R. Bayford, A. Borsic, B. Brown, P. Dixon, T. J. C. Faes, I. Frerichs, H. Gagnon, Y. Garber, B. Grychtol, G. Hahn, W. R. B. Lionheart, A. Malik, R. P. Patterson, J. Stocks, A. Tizzard, N. Weiler, and G. K. Wolf, "GREIT: a unified approach to 2D linear EIT reconstruction of lung images," Physiol. Meas., 30 (6)**,** S35-S55 (2009).

244. M. X. Tang, W. Wang, J. Wheeler, M. McCormick, and X. Z. Dong, "The number of electrodes and basis functions in EIT image reconstruction," Physiol. Meas., 23 (1)**,** 129-140 (2002).

245. J. L. Wheeler, W. Wang, and M. X. Tang, "A comparison of methods for measurement of spatial resolution in two-dimensional circular EIT images," Physiol. Meas., 23 (1)**,** 169-176 (2002).

246. B. Grychtol and A. Adler, "Uniform background assumption produces misleading lung EIT images," Physiol. Meas., 34 (6)**,** 579 (2013).

247. J. Scheibert, S. Leurent, A. Prevost, and G. Debregeas, "The role of fingerprints in the coding of tactile information probed with a biomimetic sensor," Science, 323 (5920)**,** 1503-1506 (2009).

248. Y. Chen, B. W. Lu, Y. H. Chen, and X. Feng, "Breathable and stretchable temperature sensors inspired by skin," Sci. Rep., 5 (2015).